

THEORETICAL MODELS OF NONTHERMAL PROCESSES
IN THE
ATMOSPHERES OF VENUS, EARTH AND MARS

By

Gregory G. Arkos

B.Sc. Hons. (Geophysics), University of Manitoba, 1990.

A THESIS SUBMITTED IN PARTIAL FULFILLMENT OF
THE REQUIREMENTS FOR THE DEGREE OF
DOCTOR OF PHILOSOPHY

in

THE FACULTY OF GRADUATE STUDIES
DEPARTMENT OF EARTH AND OCEAN SCIENCES (GEOPHYSICS)

We accept this thesis as conforming
to the required standard

THE UNIVERSITY OF BRITISH COLUMBIA

August 1997

© Gregory G. Arkos, 1997

In presenting this thesis in partial fulfilment of the requirements for an advanced degree at the University of British Columbia, I agree that the Library shall make it freely available for reference and study. I further agree that permission for extensive copying of this thesis for scholarly purposes may be granted by the head of my department or by his or her representatives. It is understood that copying or publication of this thesis for financial gain shall not be allowed without my written permission.

Department of Earth and Ocean Sciences (Geophysics)
The University of British Columbia
2219 Main Mall
Vancouver, BC, Canada
V6T 1Z4

Date: August, 1997.

Abstract

The present state of planetary exospheres is determined largely by satellite and ground based observations which are predominantly measurements of the emissions of exospheric constituents. Such observations are responsible for the growing recognition of the importance of nonthermal collisional processes in determining the distribution and escape of species in planetary exospheres. Nonthermal processes provide an important enhanced escape mechanism for lighter species such as hydrogen. They may also make escape possible for heavier species, such as oxygen, nitrogen and carbon, for which thermal escape is very small. Nonthermal processes have been employed in order to understand discrepancies in the terrestrial helium budget. They have also been used to reconcile discrepancies between observed and calculated escape fluxes for hydrogen on Earth. Nonthermal processes have also been utilized to explain features observed in the exospheres of other planets. These include the measured deuterium-to-hydrogen ratio on Venus and the extended hot oxygen corona on Mars. Given the importance of nonthermal processes it is clear that exospheric conditions are determined to a large extent by collisional processes and that the collisionless model must be reconsidered.

The formation of translationally energetic (or hot) oxygen coronae via the nonthermal process of dissociative recombination of O_2^+ in the atmospheres of Venus and Mars is examined using both hydrodynamic and kinetic theory approaches. Of interest is the distribution of hot oxygen at altitude resulting from production and transport from lower altitudes. It is found that an extended hot oxygen corona can be predicted from either approach, although the magnitude and extent of the predicted coronae vary significantly.

Product velocity distribution functions describing the rate of production of hot atoms

for the atomic systems H-H^+ , D-H^+ , O-H , and O-D are calculated for a variety of nonthermal processes, including direct-elastic and charge-exchange collisions. The calculations are carried out using a kinetic theory approach, and utilize direct numerical integration techniques. The calculations incorporate realistic, quantum-mechanical collision cross sections for each system so as to accurately describe the kinematics of the collision process. Energy exchange rate coefficients for each of the atomic systems are calculated and compared with results obtained using a more complicated Monte Carlo approach. The product velocity distribution functions are also used to estimate the escaping fractions of H and D as a result of nonthermal direct elastic energization by hot oxygen atoms. These kinetic theory calculations are compared to work done by other workers using Monte Carlo methods incorporating approximate and quantum mechanical cross sections. The calculations show that the fraction of hot deuterium produced via direct energization by hot oxygen, while less than the fraction of hot hydrogen, is not negligible as previously believed.

An altitude dependent, kinetic theory approach is used to calculate the rate of escape of atmospheric constituents, in the context of escape resulting from energization of neutral atmospheric species via nonthermal processes. The reduction of the escape rate by the ambient atmosphere is included through an altitude dependent parameter describing the probability of escape, although the effect of thermalization via collisions with the background is neglected. Temperature and density profiles used in the calculations are taken from available atmospheric data and from atmospheric models, and escape fluxes of hydrogen and deuterium are estimated for Venus and Earth.

Table of Contents

Abstract	ii
List of Tables	vii
List of Figures	ix
Acknowledgements	xii
1 Introduction and Basic Theory	1
1.1 Introduction	1
1.2 An Overview of the Exospheric Problem: Basic Theory	3
1.3 Nonthermal Processes	10
1.4 Kinetic Theory and the Boltzmann Equation	16
1.5 An Overview of the Thesis	17
2 Diffusion and Boltzmann Equation Models of Hot Oxygen Coronae	22
2.1 Introduction	22
2.2 Constant Temperature Model	31
2.3 Non-constant Temperature Model	41
2.4 The Linear Boltzmann Equation Model	54
2.4.1 Discretization Procedure and Solution	58
2.5 Collisional and Diffusional Timescales	77
2.6 Summary	80

3	Nonthermal Production of Energetic Hydrogen and Deuterium	83
3.1	Introduction	83
3.2	Collision Cross Sections	92
3.2.1	Quantum Mechanical Scattering	93
3.2.2	Calculation of the Phase Shifts	95
3.2.3	Cross Sections for H^+ -H and D^+ -H	96
3.2.4	Cross Sections for O-H and O-D	101
3.3	Energy Exchange Rate Coefficients	107
3.3.1	Theory	109
3.3.2	Time Evolution of the Average Test Particle Energy	114
3.3.3	Results and Discussion	116
3.4	Product Velocity Distribution Functions	137
3.4.1	Theory	137
3.4.2	Total Collision Rates	144
3.4.3	Rate of Production of Escaping Atoms	145
3.4.4	Results and Discussion	146
3.5	Summary	177
4	Kinetic Theory Calculations of Nonthermal Escape Fluxes	179
4.1	Theory	182
4.2	Summary	189
5	Summary and Suggestions for Future Research	195
A	Density Profiles in a Collisionless Exosphere	199
B	Details from Chapter 2	206
B.1	Modified Fourier's Law	206

B.2	Symmetrization of the Collision Kernel	208
B.3	Symmetrization of the Discretized Collision Operator	210
B.4	Solution of the Eigenvalue Problem	212
C	The Differential Collision Cross Section	215
D	Scattering Theory	219
D.1	Quantum Mechanical Scattering	219
D.2	Calculation of the Phase Shifts	223
D.3	Semi-Classical (WKB) Phase Shift Approximation	228
E	Details of the Production of Hot Atoms	230
E.1	Derivation of $\xi_1'^2 - \xi_1^2$	230
E.2	Derivation of $\xi_1^2 + \xi_2^2$	231
E.3	Transformation from $d\xi_1 d\xi_2$ to $d\Xi d\xi$	231
E.4	Transformation from χ to the scattering angle θ	232
E.5	Derivation of the hard sphere product velocity distribution function . . .	233
E.6	Interpolation scheme for the calculation of integrals over reduced energy .	238
F	Derivation of the Hard Sphere Collision Frequency	240
	Bibliography	244

List of Tables

1.1	Planetary escape velocities and energies	8
1.2	Planetary exospheric values for hydrogen escape	8
2.3	Diffusional versus collisional timescales for Mars	78
2.4	Diffusional versus collisional timescales for Venus	79
3.5	Energy exchange rate coefficients for $H^+ - H$	117
3.6	Energy exchange rate coefficients for $H^+ - H$ from Hodges and Breig . . .	117
3.7	Energy exchange rate coefficients for $H^+ - D$	124
3.8	Energy exchange rate coefficients for $O - H$ and $O - D$	129
3.9	Timescales for the time evolution of the average energy for H	133
3.10	Timescales for the time evolution of the average energy for H^+	134
3.11	Comparison of timescales for the time evolution of the average energy . .	136
3.12	Energy exchange rate coefficients for $H^+ - H$	159
3.13	Energy exchange rate coefficients for $H^+ - D$	160
3.14	Energy exchange rate coefficients for $O - H$ and $O - D$	161
3.15	Comparison of energy exchange rate coefficients for hard spheres	161
3.16	Rate of production of escaping H on Venus	164
3.17	Rate of production of escaping H on Earth	165
3.18	Rate of production of escaping H on Mars	166
3.19	Rate of production of escaping H on Earth from Hodges & Breig	169
3.20	Rate of production of escaping D on Venus	170
3.21	Rate of production of escaping D on Earth	170

3.22	Rate of production of escaping D on Mars	171
3.23	Rate of production of escaping H on Venus from O-H and OD interactions	172
3.24	Rate of production of escaping H on Earth from O-H and OD interactions	172
3.25	Rate of production of escaping H on Mars from O-H and OD interactions	173
3.26	Escape fraction for hot H from O-H elastic collisions on Venus	176
3.27	Escape fraction for hot H and hot D from elastic collisions with O	176
A.28	Exospheric particle classes	203

List of Figures

1.1	Stratification of the terrestrial atmosphere	4
2.2	Observed Martian density profiles	27
2.3	Observed Venusian density profiles	28
2.4	Stratification of the atmosphere by collisional property	29
2.5	Martian hot oxygen density (diffusion equation)	35
2.6	Venusian hot oxygen density (diffusion equation)	36
2.7	Martian hot oxygen density temperature dependence (diffusion equation)	38
2.8	Venusian hot oxygen density temperature dependence (diffusion equation)	39
2.9	Hot oxygen densities at large altitudes for Venus and Mars	40
2.10	Solutions of the collisionless, sourceless momentum conservation equation	48
2.11	Time dependence of hot oxygen density and temperature on Mars	63
2.12	Time dependence of hot oxygen density and temperature on Venus . . .	64
2.13	Time evolution of the Martian exospheric distribution function	66
2.14	Time evolution of the Venusian exospheric distribution function	67
2.15	Energy distribution function of hot oxygen on Mars	68
2.16	Energy distribution function of hot oxygen on Venus	69
2.17	Maxwellian fit of the energy density distribution	71
2.18	Maxwellian fit of the Venusian energy density distribution	72
2.19	Hot oxygen density profile for Mars derived from ballistic component . .	73
2.20	Hot oxygen density profile for Venus derived from ballistic component . .	74
3.21	Schematic of the charge-exchange and LTA	91

3.22	Interaction potentials for H^+-H	97
3.23	Differential cross sections for H^+-H	98
3.24	Differential cross sections for D^+-H	99
3.25	Total elastic collision cross sections	100
3.26	Interaction potentials for $O-H$	102
3.27	Total elastic collision cross sections	104
3.28	Total elastic collision cross sections	105
3.29	Differential cross sections for $O-H/O-D$	106
3.30	Fits to the LTA momentum transfer cross section	120
3.31	Temperature dependence of k_E for the LTA	121
3.32	Dependence of energy exchange rate coefficients on bath temperature for H^+-H	122
3.33	Dependence of energy exchange rate coefficients on bath temperature for D^+-H	126
3.34	Details of the integrand in calculation of the energy exchange rate coefficient	127
3.35	Convergence of the energy exchange rate coefficient	128
3.36	Time evolution of the average energy in a relaxing H^+-H system	131
3.37	Time evolution of the average energy in a heating H^+-H system	132
3.38	Comparison of the time evolution of the average proton energy	135
3.39	Schematic of an elastic binary collision	138
3.40	Coordinate system for the calculation of collisional production	141
3.41	Product velocity distributions for the DPE cross section for H^+-H	148
3.42	Product velocity distributions for the CE cross section for H^+-H	149
3.43	Product velocity distributions for the LTA cross section for H^+-H	150
3.44	Product velocity distributions for H^+-H	152
3.45	Product velocity distributions for the DIR cross section for H^+-D	154

3.46	Product velocity distributions for the CE cross section for D^+H	155
3.47	Product velocity distributions for the DIR cross section for $O-H$	156
3.48	Product velocity distributions for the DIR cross section for $O-D$	157
3.49	Dependence of charge exchange rate coefficients on bath temperature for D^+H	163
3.50	Product velocity distribution functions for $O-H$ and $O-D$ escape producing collisions.	175
4.51	Geometry for a plane-parallel atmosphere	190
4.52	Temperature and density profiles used as input for flux calculations on Venus	191
4.53	Density profiles used as input for flux calculations on Earth	192
4.54	Density profiles used as input for flux calculations on Earth	193
4.55	Temperature profile used as input for flux calculations on Earth	194
A.56	Graphical illustration of exospheric particle classes	202
C.57	Typical scattering configuration	216
D.58	Wave function scattering by a central potential	222
E.59	Geometry of the dynamics of an elastic collision	233

Acknowledgments

I would like to acknowledge the support, patient advice, and many helpful suggestions of Dr. B. D. Shizgal throughout the course of my graduate studies. His input and guidance have contributed greatly to this work. I would like to acknowledge the members of my supervisory committee, Dr. D. Oldenburg, Dr. G. Fahlman, and Dr. R. F. Snider, for their constructive comments and advice during the writing of this work.

I also thank the many graduate students and post-doctoral researchers who took time from their own work to discuss various aspects of this work, to help out with the specifics of computer code, or just commiserate when things weren't working. Ki, Andrew, Duncan, Heli, François, and Gianpiero - your support was much appreciated.

I would also like to thank my sister, Julia, and my entire family for their unconditional support and encouragement throughout my graduate work. Their unwavering support and love helped me to focus on completion of this work through some difficult and tumultuous times. Without them, I am certain that I would not have been able to successfully complete this work.

I wish to acknowledge the Chemistry Department and the computing resources which were made available to me throughout the course of this work.

Finally, I would like to gratefully acknowledge the sources of financial support throughout my graduate studies. To the Natural Sciences and Engineering Research Council, the Canadian Society of Exploration Geophysicists Trust Fund, Canadian National Scholarship Program, the Department of Geophysics and Astronomy, and Dr. B. D. Shizgal I extend my many thanks for making my graduate studies possible.

Chapter 1

Introduction and Basic Theory

1.1 Introduction

The understanding of the composition, dynamics, and evolution of planetary atmospheres is important in many fields, including geophysics, astronomy, and atmospheric science. A critical part in the determination of the overall behaviour of planetary atmospheres is the behaviour of the exosphere. The exosphere is the high altitude region of a planetary atmosphere characterized by vanishingly small gas densities.¹ As densities are so low, the mean free path of particles in the exosphere are exceedingly long, and gas kinetic energies may be sufficient to permit atoms to escape the planetary gravitational potential. The altitude where the mean free path is equal to the scale height, defined later, is the bottom of the exosphere, known as the exobase. Below the exosphere, the atmosphere is predominantly turbulent, well mixed, and dense enough to be collision dominated. In this region of the atmosphere, hydrodynamic or fluid theory is often used to characterize gas behaviour. Above the exobase, in the exosphere, densities are low, collisions are rare, and gases are distributed primarily according to diffusive equilibrium rather than turbulent mixing. Under such conditions, the kinetic theory of gases is more appropriate to describe the behaviour and character of exospheric species.

In the real atmosphere, the transition from one regime to the other is gradual and continuous. However, early exospheric models considered the exobase as a discontinuous division between collisional and collisionless regions of the atmosphere. Despite

this unrealistic treatment of the atmosphere, the discontinuous exobase model has been extensively employed in the interpretation of observations of Lyman- α and Balmer- α emissions of atomic hydrogen in the exosphere.²⁻⁸

Atoms in a range of altitudes above and below the exobase can attain speeds in excess of the planetary escape speed and escape from the planetary atmosphere. The escape process may thus be viewed as an 'evaporative' process where high energy particles are preferentially removed from the atmosphere. This thermal picture of escape was formulated by Jeans,⁹ and the escape flux resulting from this evaporative escape process is known as Jeans flux. Comparison of escape fluxes inferred from satellite measurements to those predicted by Jeans based on neutral exospheric temperatures clearly indicated that the thermal escape process alone was insufficient. It was suggested by Cole¹⁰ that excitation of 'cold' atmospheric species could take place via nonthermal processes such as charge exchange. Such translationally energetic (or 'hot') nonthermal product atoms would then have sufficient energy to escape from the planetary atmosphere. Such hot atom populations have been observed by satellite and ground based techniques in the Earth's exosphere,^{11,12} and inferred from measurements made of Venus^{13,4} and Mars.^{6,14}

The interest in hot atoms in the atmospheres of Venus and Mars is motivated by several factors. A thorough understanding of the hot atom populations is necessary to understand observations of emissions in planetary exospheres made by instruments aboard spacecraft and from the ground. The long term evolution of planetary atmospheres, including the loss of hydrogen and oxygen related to the removal of water, requires an understanding of the transport and distribution of atomic species in the upper atmospheres of the planets. Accurate calculation of escape fluxes requires an understanding of the magnitude and extent of planetary hot atom populations. Such a description is also important in understanding and describing the interaction of planetary atmospheres

with the solar wind. For example, the effect of photoionization of energetic atoms in planetary exospheres and the subsequent interaction with the solar wind (pick-up, knock-on, and precipitation of photo-ions). There is also the 'direct' interaction of the solar wind 'striking' the upper atmospheres of Venus and Mars, since these planets do not have (very strong) magnetic fields to deflect or slow the solar wind.

A good overview of basic exospheric physics which emphasizes nonthermal escape was given in a recent paper by Shizgal and Arkos.¹⁵ The review by Chamberlain¹⁶ provides a very detailed theoretical description of the collisionless exosphere. Additional reviews dealing with the problem of the description of exospheric processes have been written by Hunten and Donahue,¹⁷ Tinsley,¹⁸ Fahr and Shizgal¹ and more recently by Hunten,^{19,20} and Mahajan and Kar.²¹

1.2 An Overview of the Exospheric Problem: Basic Theory

The basic concepts of planetary atmospheric escape were given by Jeans⁹ and extended to the conventional collisionless thermal escape model by Chamberlain.¹⁶ A picture of the stratification of the atmosphere is illustrated in Figure 1.1.

The lower region of the atmosphere where turbulent mixing of gases leads to a homogeneous composition is called the homosphere. Above this region, turbulence ceases and the vertical distribution of individual atmospheric gases is determined by their respective masses. In this region, called the heterosphere, the density profile $n_i(r)$ of the i^{th} constituent is determined by the balance of gravity and gas pressures. When these two opposing forces are equal we have the condition of hydrostatic equilibrium, given by²²

$$\begin{aligned}\frac{\partial p_i}{\partial r} &= n_i m_i g \\ &= -kT_i \frac{\partial n_i}{\partial r}\end{aligned}\tag{1.2.1}$$

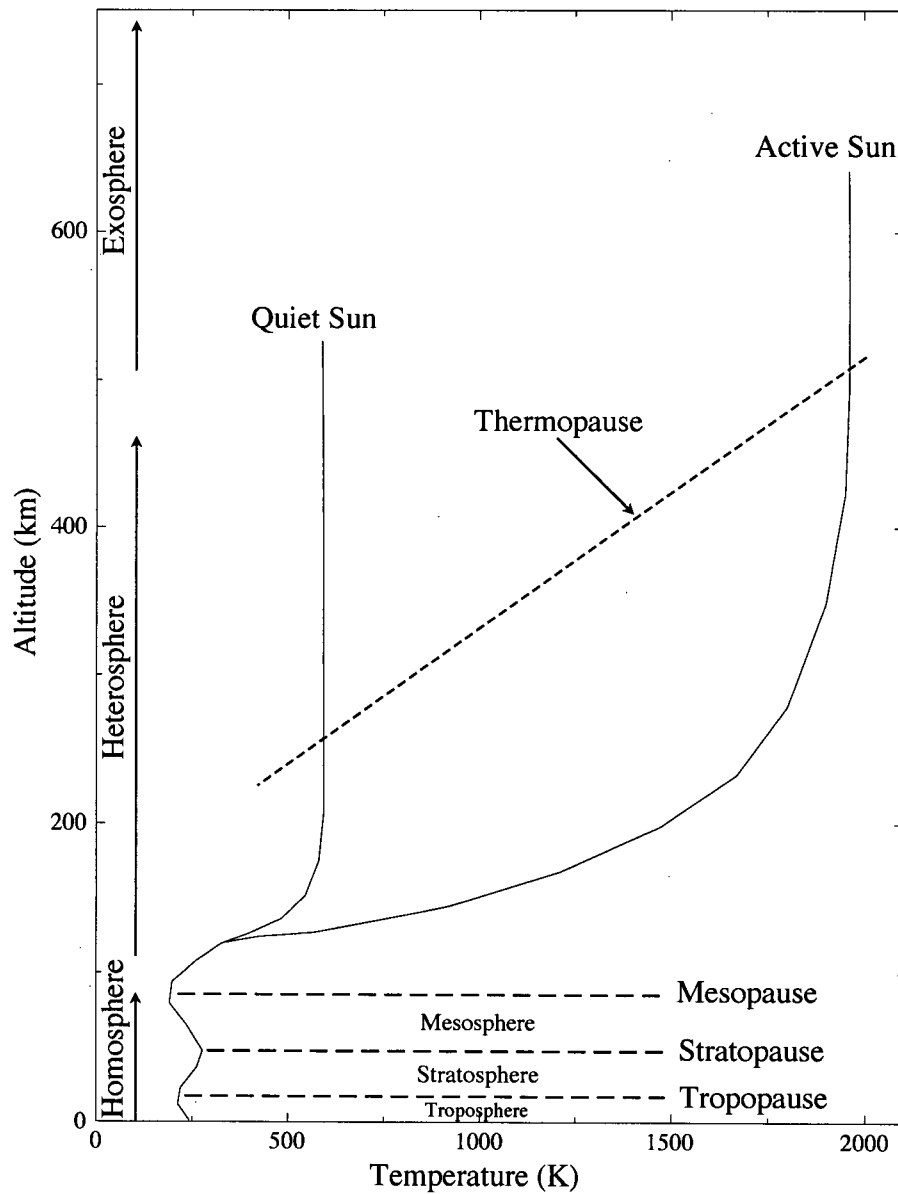


Figure 1.1: Atmospheric divisions as a function of altitude for the terrestrial atmosphere. Indicated are the various divisions of the atmosphere, including the homosphere, heterosphere, and exosphere. The curves represent average temperature profiles for the bulk neutral atmosphere for quiet and active solar periods. From Banks & Kockarts.²²

where $g = GM/r^2$ is the gravitational acceleration, m_i and T_i are the mass and (constant) temperature of the i^{th} constituent, k is the Boltzmann constant, G is the universal gravitational constant, M is the planetary mass, and $p_i = n_i k T_i$ is the (partial) hydrostatic pressure as given by the ideal gas law. If we substitute for g in equation (1.2.1) we have

$$kT_i \frac{\partial n_i}{\partial r} = -n_i m_i \frac{GM}{r^2}$$

Integrating both sides yields

$$\begin{aligned} \int_{n_{io}}^{n_i} \frac{dn_i}{n_i} &= \frac{GMm_i}{kT_i} \int_{r_o}^r -\frac{dr}{r^2} \\ \ln(n_i/n_o) &= \frac{GMm_i}{kT_i} (1/r - 1/r_o) \\ n_i(r) &= n_o \exp[r/H_i(r) - r_o/H_i(r_o)] \end{aligned} \quad (1.2.2)$$

where r_o is some reference level, n_o is the density of species i at r_o , and where we have defined the scale height for species i as

$$H_i(r) = \frac{kT_i r^2}{GMm_i} = \frac{kT_i}{m_i g(r)} \quad (1.2.3)$$

Equation (1.2.2) is the barometric or hydrostatic density distribution. It is important to note that while we have included the correct radial dependence of the gravitational acceleration in deriving equation (1.2.2) the result is nonphysical in that the density $n_i(r)$ is finite as $r \rightarrow \infty$. This is a result of the fact that our assumption of hydrostatic equilibrium is no longer valid. As the density becomes vanishingly small, collisions become extremely rare and hydrodynamics breaks down.

If we write $z = r - r_o$, we have

$$\begin{aligned} n_i(r) &= n_o \exp \left[\frac{GMm_i}{kT_i} (1/(r_o + z) - 1/r_o) \right] \\ &= n_o \exp \left[\frac{GMm_i}{kT_i r_o} (1/(1 + z/r_o) - 1) \right] \end{aligned}$$

Assuming that $z/r_o \ll 1$, we have that $g \approx g(r_o)$, constant, we may expand the first term of the exponential, yielding

$$\begin{aligned} n_i(r) &= n_o \exp \left[-\frac{GMm_i}{kT_i r_o^2} z \right] \\ &= n_o \exp \left[-\frac{z}{H_i(r_o)} \right] \end{aligned} \quad (1.2.4)$$

The barometric density distribution given by equation 1.2.4 now vanishes as $r \rightarrow \infty$, as we would physically expect, although we no longer correctly account for the radial dependence of the gravitational acceleration.

The exobase or critical level, r_c , is defined as the altitude for which the mean free path, the average distance between particle collisions, given by

$$\ell = \frac{1}{\sqrt{2}N\sigma} \quad (1.2.5)$$

is equal to the barometric scale height of the heaviest constituent, that is, $\ell(r_c) = H(r_c)$. In equation (1.2.5), σ is the energy independent total elastic collision cross section for the diffusing species and the background and $N = \sum_i n_i$ is the total density.

In the standard Chamberlain model,^{9,16} the atmosphere is considered collisionless above the exobase and collision dominated below it. Particles that reach the exobase from below and move upwards with speeds in excess of the escape speed, given by

$$c_{esc} = \sqrt{\frac{2GM}{r}} \quad (1.2.6)$$

will escape from the gravitational field of the planet. This model assumes that above the exobase the particles move on collision free trajectories determined by the planetary gravitational field. The classification of exospheric species into classes of particles such as ballistic, satellite, and escaping based on this model is discussed at length by Chamberlain,¹⁶ and Fahr and Shizgal,¹ and is summarized in Appendix A. In these

models a Maxwellian distribution of particle velocities

$$f^{max}(c) = n \left(\frac{m}{2\pi kT} \right)^{\frac{3}{2}} \exp \left[-\frac{mc^2}{2kT} \right] \quad (1.2.7)$$

is assumed to exist at the exobase. The escape flux of particles moving radially outward with speeds in excess of the escape velocity (at the critical level) is determined by averaging over the outward directed velocity for speeds greater than the escape speed, that is

$$F_J = 2\pi \int_{c_{esc}}^{\infty} \int_{\theta=\pi/2}^{\theta=0} f^{max} \cos \theta c^3 d(\cos \theta) dc \quad (1.2.8)$$

so that the thermal or Jeans escape flux is given by⁹

$$F_J = \frac{n_c}{2} \sqrt{\frac{2kT_c}{m\pi}} (1 + \lambda_c) e^{-\lambda_c} \quad (1.2.9)$$

In equation (1.2.9), T_c and n_c are the temperature and density of the escaping species at the exobase respectively, and the escape parameter, λ_c , is defined by

$$\lambda_c = \frac{E_{esc}}{kT_c} \quad (1.2.10)$$

where the total energy for escape is $E_{esc} = \frac{1}{2}mc_{esc}^2$. The escape speeds and escape energies for hydrogen, deuterium, and oxygen from the terrestrial planets are shown in Table 1.1. Mars, the least massive of the three planets, has the lowest escape energy. The escape flux is determined by the ratio of the escape energy relative to the thermal energy, that is, by λ_c in equation (1.2.10). Table 1.2 compares the values of λ_c for the terrestrial planets; the very large value for Venus, arising from the low exospheric temperature, is evident. For Venus, thermal escape is insignificant at present, and nonthermal processes play a dominant role. However, Donahue²³ has discussed the escape of primordial atmospheres from planetesimals for which λ_c is small and Jeans flux is significant.

It is important to note that in equation (1.2.8) the three dimensional velocity integral is carried out only over the upper half of the velocity space ($\theta \geq 0$). Since the

Planet	c_{esc}^{exo} (km/sec)	E_{esc}^H (eV)	E_{esc}^D (eV)	E_{esc}^O (eV)
Earth	10.8	0.61	1.22	9.69
Venus	10.2	0.54	1.08	8.60
Mars	4.8	0.12	0.25	1.91

Table 1.1: Planetary escape velocities and energies. The values given are for an altitude corresponding to the exobase level for each planet (see Table 1.2). Neutral atmospheric temperatures are taken from Niemann et al.,²⁴ Banks and Kockarts²² and Fox and Dalgarno²⁵ for Venus, Earth and Mars, respectively.

Planet	r_c (km)	T_c ($^{\circ}K$)	λ_c	F_J/n_c (cm/sec)
Earth	500	1000	7.06	7.94×10^2
Venus	200	275	22.89	1.65×10^{-4}
Mars	250	300	4.65	3.39×10^2

Table 1.2: Planetary exospheric values for hydrogen escape. The exobase or critical level is at the altitude given by r_c , the exobase temperature is given by T_c , and the escape parameter at the exobase by λ_c . The Jeans' flux F_J is given with respect to the exobase density n_c of hydrogen.

Maxwellian distribution function is isotropic, the flux would be zero if the lower hemisphere of the velocity space were not artificially removed. This model of atmospheric escape is an oversimplification. The actual distribution function at the exobase is not Maxwellian, because the escape process preferentially removes energetic atoms and non-thermal processes introduce them. The distribution that leads to an outward flow must be anisotropic, that is

$$f(\mathbf{r}, \mathbf{c}) = f^{max}(\mathbf{r}, c) + f^{aniso}(\mathbf{r}, c, \theta) \quad (1.2.11)$$

where θ is the angle between the velocity \mathbf{c} and the outward radial direction. Since the average of the Maxwellian distribution over all velocities is zero, the drift velocity is given by

$$\mathbf{u}(r) = \int f^{aniso}(\mathbf{r}, \mathbf{c}) \mathbf{c} d\mathbf{c} \quad (1.2.12)$$

It is reasonable to expect that escaping particles originate not only from the exobase but from a range of radial positions in the vicinity of the exobase. Hence, the differential escape flux found using equation (1.2.12), $\mathbf{F}(r)dr = n(r)\mathbf{u}(r)$, depends on the radial position. The *net* escape flux is determined by the integral of $\mathbf{F}(\mathbf{r})d\mathbf{r}$ over a range of radial distances in the vicinity of the exobase.²⁶ This picture of atmospheric escape, as detailed by Lindinfeld and Shizgal²⁶ and Shizgal and Blackmore,²⁷ which considers both thermal and nonthermal escape as collisionally induced phenomena is discussed in Chapter 4.

For rarified regions, such as in the exosphere, the behaviour of gases is best described by the kinetic theory of gases. Of principle interest to most workers in exospheric physics is the description of the bulk physical properties of the exospheric constituents, including the density, temperature, and heat conductivity. An important problem in this calculation of the bulk physical properties is the proper treatment of the transition between

the collision dominated lower atmosphere and the nearly collisionless upper exosphere. A quantity which categorizes kinetic theory problems in the exosphere is the Knudsen number, Kn , defined as the ratio of the mean free path of the gas and the local scale height,

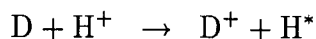
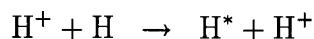
$$Kn = \frac{\ell}{H}$$

For small values of the Knudsen number, $Kn \ll 1$, the system is considered to be collision dominated, and hydrodynamic equations such as the Navier-Stokes equation,²⁸ are valid. In the other limit, $Kn \gg 1$, the system is considered nearly collisionless, and it is necessary to employ kinetic theory in order to properly characterize the behaviour of gases. If the velocity distribution function of the system constituents is considered to be close to equilibrium, it is possible to use 'standard' methods such as the Chapman-Enskog method,²⁹ to study the transport properties of the gas. Far from equilibrium systems, such as frequently encountered in atmospheric physics, are more difficult. Such systems are of interest in the present work. The region between the two Knudsen limits is considered a transition region with regard to the collisional properties of the system. It is here that hydrodynamics begins to break down. Kinetic theory remains valid for *all* Knudsen values (e.g. the hydrodynamic equations are readily derived from the equations of kinetic theory), although the generation of a rigorous kinetic theory solution valid over the entire range of Knudsen values is a formidable problem.

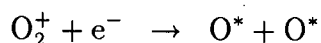
1.3 Nonthermal Processes

Nonthermal processes generally refer to collisional processes between exospheric species and translationally energetic species (both ions and electrons), generally of ionospheric origin. This includes processes such as charge exchange between hot plasmaspheric protons and neutral exospheric hydrogen or deuterium (thought to be important for both

Earth and Venus),



The products of such processes, labelled with an asterisk (*) are translationally energetic and incompletely thermalized. The result is the conversion of translationally energetic protons to translationally energetic hydrogen atoms, H^* , with speeds in excess of the escape speed. An important nonthermal process in the Martian exosphere is the dissociative recombination of O_2^+ with electrons, that is,



The dissociation energy of the ion is divided between the product oxygen atoms which become translationally excited. Hot oxygen atoms may explain the maintenance of the nighttime terrestrial ionosphere by increasing the flux of energetic hydrogen from the plasmasphere via elastic collisions. In addition, hot oxygen in the plasmasphere coupled with charge exchange could provide an important source for plasmaspheric O^+ and heating of plasmaspheric ions.³⁰

The present state of planetary exospheres is determined largely by satellite and ground based observations which are predominantly measurements of the emissions of exospheric constituents. These include Lyman- α and Lyman- β emissions of atomic hydrogen at 121.6 nm and 102.6 nm, respectively, emission of helium at 58.4 nm, and emission of atomic oxygen at 130.5 nm. Such observations are responsible for the growing recognition of the importance of nonthermal processes in planetary exospheres. For example, the existence of a population of energetic H atoms on Venus was confirmed by emission observations by the ultraviolet photometer on Mariner 5.^{13,2} Lyman- α emission indicated an exospheric altitude dependence characterized by two very different scale heights corresponding to thermal and hot H components not predicted by the Jeans' model. Evidence

of a similar hot corona of atomic oxygen in the Martian and terrestrial exospheres has also been discovered.^{31,7,32,6,33,34} Another observation not predicted by calculations of thermal escape rates are the mass spectrometer measurements by the Pioneer Venus Orbiter, which recorded an enrichment of the deuterium to hydrogen (D/H) ratio in the exosphere of Venus by a factor of 100 relative to the terrestrial value.³⁵⁻³⁷ This enrichment of deuterium relative to hydrogen is believed to arise from the enhanced escape of hydrogen relative to deuterium. Observations of terrestrial H escape flux also conflict with predictions based on thermal escape. The thermal Jeans' flux increases with exospheric temperature, in contrast to the results by Liu and Donahue³⁸⁻⁴⁰ and Hunten and Strobel,⁴¹ which demonstrated that the flux of hydrogen in all forms is equal to approximately $1.5 \times 10^8 \text{ cm}^{-2}\text{s}^{-1}$ independent of exospheric temperature. It was consequently shown that a nonthermal charge-exchange model could account for the discrepancy between the calculated H escape flux and the predicted thermal H escape flux.⁴²⁻⁴⁵

Nonthermal processes provide an important enhanced escape mechanism for lighter species such as H. They may also make escape possible for heavier species, such as oxygen, nitrogen and carbon, for which thermal escape is very small. Nonthermal processes have been employed in order to understand a discrepancy in the terrestrial helium budget.^{46,47} The production of ^4He is predominantly from the radioactive decay of ^{238}U , with an estimated flux of $F_{\text{prod}} \approx (0.9 - 1.9) \times 10^6 \text{ cm}^{-2}\text{sec}^{-1}$.⁴⁸ For helium, the exospheric escape energy on Earth is approximately 2.5 eV; with typical exobasic conditions ($n_c = 10^6 \text{ cm}^{-3}$, $T_c = 1000\text{K}$) the thermal Jeans flux is $F_J = 0.4 \text{ cm}^{-2}\text{sec}^{-1}$, yielding a ratio of $F_{\text{prod}}/F_J \approx (2-4) \times 10^6$ (the abundance of ^3He is almost entirely extraterrestrial in nature, and does not affect the ^4He flux balance). Clearly, the calculated rate of outgassing of ^4He is far greater than the loss due to thermal Jeans escape and the atmospheric helium content should be far above what is observed. In order to reconcile this, there must exist additional loss processes which remove helium from the atmosphere. Furthermore, as

helium is chemically inert there are no reactive processes to account for the observed discrepancy. Some sort of enhanced nonthermal escape mechanism is required in order to supplement the required remaining escape flux. Lie-Svendsen et al.⁴⁷ and Rees and Lie-Svendsen⁴⁹ recently studied several potential nonthermal mechanisms and suggested that the exothermic charge exchange reaction



originally proposed by Maier⁵⁰ could produce He atoms of sufficient energy for escape.

The impact of nonthermal processes in planetary exospheres in the development of evolutionary models is extremely important. The Pioneer Venus Orbiter measurements of D/H enrichment on Venus mentioned previously have lead to the suggestion of a layer of water tens to hundreds of meters thick in the distant past.^{51,52} For Mars, a similar history of past water abundance has been suggested⁵³ based on estimates from surface morphology from satellite data,⁵⁴ Earth based spectroscopy of HDO,⁵⁵ and measurements of isotopic fractionation¹ of gases trapped in Shergottite-Nakhlite-Chassignite (SNC) meteorites.^{56,57} However, the nonthermal processes which may have contributed to the loss of water on Mars and Venus appear to be different. Venus probably had its water primarily in the form of water vapour⁵⁸ because of the higher atmospheric and surface temperatures. This large amount of atmospheric water vapour would have created a dense population of atomic hydrogen via photodissociation, and conditions would have been favorable for bulk hydrodynamic loss. This process has been suggested to explain both the observed isotopic fractionation of noble gases and removal of large amounts of hydrogen (and thus, possibly, water). Unless exospheric temperatures were higher in the past than today, it appears that thermal escape is, in general, negligible on Venus. On Mars, nonthermal and thermal processes may have both played a large role in removing much

¹This refers to the preferential removal of lighter isotopes of a gas, leading to a modification of the expected isotopic ratio

of the original water, possibly aided by impact erosion early in the planet's history.^{58,53} A fair amount of water, in the form of ice, may still be trapped in the Martian regolith and polar caps. A mechanism for removal of the excess oxygen following dissociation of water and loss of hydrogen is still not definitively identified.

The noble gases are another important constraint for models of planetary atmospheric evolution. Neutral noble gases atoms are chemically inert and do not have sinks due to interaction with crustal or other atmospheric species. Removal of noble gas atoms at the present time requires transformation of the neutrals to ionic species which can then take part in reactions similar to that specified for He previously. Removal of the noble gases in the distant past may have been achieved by bulk hydrodynamic flow, but would have required significantly higher densities of hydrogen in planetary atmospheres.⁵⁹ Either method (or both) may lead to the observed patterns of isotopic fractionation found in the noble gases of the terrestrial atmospheres. Other isotopic fractionations, such as the enrichment of ¹⁵N over ¹⁴N on Mars, can be explained on the basis of nonthermal processes similar to those described for oxygen. For example, the dissociative recombination process



can create a population of energetic nitrogen on Mars.^{6,33,8,60} The mass spectrometers on the Viking landers measured an isotopic ratio $^{15}\text{N}/^{14}\text{N} = 6.0 \times 10^{-3}$, which is about 1.62 times the terrestrial value of 3.68×10^{-3} . This isotopic enhancement (or fractionation) of the heavier isotope with respect to the lighter one is due to the fact that the energy given to the products of a reaction such as (1.3.1) is just enough for the ¹⁴N to escape but too small for the heavier ¹⁵N. Measurements of such isotopic fractionations, including the fractionation of the noble gases and their deviation from the patterns found in the solar wind and meteorites, yield significant information about early planetary volatile budgets and atmospheric evolution and form important constraints on the development

of evolutionary models of the terrestrial atmospheres.^{61, 59, 62, 56, 63-65, 30}

The study of the Martian exosphere is particularly timely in light of the upcoming international effort to observe both the surface and atmosphere of Mars. The Martian neutral atmosphere, ionosphere, and the solar wind plasma interaction will be measured by instruments aboard satellites to Mars toward the end of the decade; these include Planet B (Japan), and Mars 98 (Russia and ESA). Some of the planned missions to Mars involve experiments to obtain signatures of the hot atom populations in the Martian exosphere.⁷ Some information on the magnitude of this population has already been derived from solar wind deceleration measurements made by instruments aboard the Phobos 2 spacecraft in the late 1980's.¹⁴ Additional measurements concerning the atmosphere and surface of Mars will be obtained with the Hubble Space Telescope and instruments aboard the Mars Surveyor and Pathfinder orbiter/lander pairs, launched in the late 1990's. All of these studies will collectively yield important information and constraints for models of nonthermal processes, and will provide the impetus for the further development of models of atmospheric evolution and planetary climate change.

Given the importance of nonthermal collisional processes it is clear that exospheric conditions are determined to a large extent by collisional processes and that the collisionless models must be reconsidered. A primary goal of this thesis is the description of the effect of nonthermal collisional processes on exospheric escape. Escape rates provide important boundary conditions for processes in the lower atmosphere, including reactive processes, diffusive transport, planetary outgassing, and photochemical effects. For example, of tremendous importance to models predicting terrestrial atmospheric evolution is the transport and escape of hydrogenous compounds injected into the atmosphere at the Earth's surface. Gases such as methane, carbon dioxide, and water vapour are involved in several chemical reactions as they are transported higher into the atmosphere.⁶⁶ The

effect of these reactions, in addition to solar radiation induced photo-ionization and dissociation, is to break down the original gases and eventually leave molecular and atomic hydrogen at the highest altitudes. The rate of the escape of hydrogen is extremely important in the understanding and prediction of the long term stability and concentration of these compounds in the terrestrial atmosphere.

1.4 Kinetic Theory and the Boltzmann Equation

For the description of gas behaviour in dense systems, the use of hydrodynamics and fluid mechanics is appropriate and adequate. However, when a system becomes rarified and collisions become infrequent, such descriptions are no longer valid.⁶⁷ For such cases, the state of a gas is described by the velocity distribution function, $f(\mathbf{r}, \mathbf{c}, t)$. In general the distribution function is a function of seven independent variables; the position, the time, and the velocity. The distribution function is defined as the number of particles per unit volume at a position \mathbf{r} and time t with velocities in the range \mathbf{c} to $\mathbf{c} + d\mathbf{c}$. The total density at a given \mathbf{r} and t is found by integrating over all velocities

$$n(\mathbf{r}, t) = \int f(\mathbf{r}, \mathbf{c}, t) d\mathbf{c}$$

The evolution of the distribution function is described by gas kinetic theory. The equation that specifies the distribution function for a dilute gas is the Boltzmann equation,^{29,68}

$$\frac{\partial f}{\partial t} + \mathbf{c} \cdot \nabla_{\mathbf{r}} f + \frac{\vec{F}}{m} \cdot \nabla_{\mathbf{c}} f = \sum_n J_n[f] \quad (1.4.1)$$

where \vec{F} represents all external forces acting on the system and the sum \sum_n is taken over all collision partners. The collision operator J_n is given by²⁹

$$J_n[f] \equiv \iint (f' f'_n - f f_n) \sigma(g, \Omega) g d\Omega d\mathbf{c}_n \quad (1.4.2)$$

where g is the relative velocity of the colliding pair, Ω is the scattering angle giving the orientation of the final relative velocity vector, \mathbf{g}' , relative to \mathbf{g} , and $\sigma(g, \Omega)$ is the differential scattering cross section describing the details of the binary collision. The square brackets $[f]$ indicate that the distribution function f is the argument of the operator J_n . The primed distribution functions in equation (1.4.2) are pre-collisional values and the unprimed distribution functions are post-collisional values.

1.5 An Overview of the Thesis

Chapter 2 examines the creation of extended hot oxygen distributions ('coronae') in the exospheres of the terrestrial planets. Calculations of hot atom densities based on the so called two-stream model have been carried out by Nagy et al.^{69,7} The two-stream model splits the distribution function in a plane parallel atmosphere into two parts; one, $f^+(r, v)$, represents particles moving upwards, whereas the other, $f^-(r, v)$, represents particles moving downwards. This is a very simplified description of the actual anisotropic velocity distribution function. In the first paper, these workers considered a two-stream approximation as well as a diffusion approach to model the production and thermalization of hot oxygen in the Venus exosphere. The thermalization is with the ambient CO_2 , O and H, and modeled by a hard sphere cross section. Uncertainties in their model included the energy distribution of the product oxygen atoms from dissociative recombination and the ion and electron densities and temperatures. Their calculations clearly indicated that there is an extended oxygen corona on Venus.

Ip^{6,33} and Lammer and Bauer⁸ carried out Monte-Carlo simulations of the dissociative recombination process to model the oxygen corona on Mars. There are many uncertainties in the dynamical and atmospheric parameters and these calculations are only estimates of the actual exosphere. Nevertheless, the existence of an extended oxygen corona on

both Venus and Mars is clear. It is far more extended on Mars than on Venus owing to the smaller gravitational field.

Shematovich et al.^{34,70} presented a detailed kinetic theory analysis of the formation of the oxygen geocorona from dissociative recombination of O_2^+ , resonant charge exchange with hot plasmaspheric oxygen ions, and other sources. They begin with a set of Boltzmann-type kinetic equations and considered a stochastic/Monte-Carlo method of solution, and showed that the oxygen geocorona is formed primarily by energization of the thermal oxygen component with superthermal $O(^1D)$ and $O(^1S)$ atoms produced from O_2 photodissociation and dissociative recombination of O_2^+ and NO^+ .

The primary motivation of Chapter 2 is to achieve a qualitative description of the hot exospheric oxygen distribution, and assess the importance of collisional processes in determining the final hot oxygen density distribution. Several new approaches to modeling of the hot oxygen corona are considered. A hydrodynamic model based on the solution of the constant-temperature diffusion equation is used to describe transport of the translationally energetic ('hot') exospheric oxygen atoms through a thermal, stationary background gas. This model is based on the time-independent continuity equation, and includes a hot atom source term. As its name suggests, the temperature of the hot atoms is set to some (arbitrary) fixed value, and densities are calculated from the resulting diffusion equation. This model is extended to include a self-consistent temperature profile in order to more accurately determine the effect of thermalization on the density profile of the hot oxygen atoms.

A method of deriving exospheric atom densities based on solutions of the local Boltzmann equation is also examined. Rather than calculating the density, drift velocity, and temperature, this method solves directly for the hot oxygen velocity distribution function. The distribution function implicitly includes information about the density and temperature in a self-consistent fashion. However, as the local form of the Boltzmann

equation is used, it is necessary to make several assumptions in order to extract altitude profiles for the density of the hot oxygen. The first assumption made is that it is possible to transform linearly between time and altitude via a (fixed) bulk drift velocity for the hot oxygen atoms. This restricts the model to a range of altitudes over which the distribution function does not change too appreciably. Hence, it is necessary to calculate the distribution function close to the exobase level, and then calculate the hot oxygen density for altitudes above the exobase using methods employed in collisionless models.¹⁶

Chapter 3 describes the production of hot hydrogen and deuterium by nonthermal processes. In particular, it focuses on the production of hot hydrogen via charge exchange reactions with protons and deuterium and the formation of hot deuterium via charge exchange reactions with hydrogen. Realistic quantum mechanical differential collision cross sections are used to describe the kinematics of these collisional systems. The examination of these processes using quantum mechanical cross sections has been done previously. Shizgal⁷¹ and Clarke and Shizgal⁷² calculated collision cross sections for the hydrogen-proton system, and examined the resulting escape rate of hydrogen from Venus and the relaxation dynamics of hot protons in a bath of thermal hydrogen, respectively. Hodges and Breig⁷³ used Monte Carlo integration to examine energization of hydrogen via nonthermal collisional processes with hot protons. They later⁷⁴ examined the effect of similar processes on the production of hot deuterium.

The energization of hydrogen and deuterium via elastic collisions with energetic oxygen atoms is also examined. A particular motivation for a detailed examination of the differential energization of deuterium and hydrogen by this process is that it has been suggested by several groups as a possible explanation for the observed enrichment of the deuterium/hydrogen ratio measured on Venus. McElroy and co-workers³⁵ considered such an energization process, although they assumed that scattering proceeded as an isotropic process. They found that energization of thermal hydrogen to energies above the escape

energy of Venus was possible via direct elastic collisions with hot atomic oxygen, but that the same process for deuterium was negligible, hence explaining the enhancement of the D/H ratio. This result was questioned by Cooper et al.⁷⁵ and Gurwell and Yung,⁷⁶ who used more realistic anisotropic quantum mechanical cross sections. They found that the production of escaping hydrogen was overestimated by the isotropic model, and that production of escaping deuterium was not negligible.

The current work extends the results of the previous work on nonthermal processes. The rate at which energy is transferred between colliding species for a variety of nonthermal processes is calculated using both a hydrodynamic and kinetic theory approach. The product velocity distribution function (PVDF), which gives the distribution of velocities of the product atom as a result of a collisional interaction, is calculated and used to derive escape fractions for a variety of nonthermal processes and atomic systems. Quantum mechanical cross sections are calculated in order to accurately describe the kinematics of the collisional processes. All of the calculations of the current work are formulated so as to avoid resorting to Monte Carlo simulations or integrations as in many of the previous works. This reduces computational times and computer resources required, and also eliminates the need to fit or smooth results to remove statistical fluctuations.

In Chapter 4 we utilize the results of Chapter 3 to calculate nonthermal escape fluxes. The problem of escape of hydrogen from Earth has been examined by many workers. Lindenfeld and Shizgal⁴⁵ employed a simple collisional model to obtain an expression of the charge exchange induced flux and showed that the total of the charge exchange and Jeans' hydrogen escape flux was roughly constant. This was consistent with the results of Liu and Donahue,³⁸⁻⁴⁰ who demonstrated that the escape flux should be approximately $1.8 \times 10^8 \text{ cm}^{-2} \text{ s}^{-1}$. Maher and Tinsley⁷⁷ estimated the hydrogen escape rate on Earth at $1.5 \times 10^8 \text{ cm}^{-2} \text{ s}^{-1}$, while Yung and co-workers⁷⁸ used a one dimensional photochemical model to calculate total and charge-exchange escape fluxes of $3.02 \times 10^8 \text{ cm}^{-2} \text{ s}^{-1}$ and

$1.41 \times 10^8 \text{ cm}^{-2} \text{ s}^{-1}$ for hydrogen, and $3.5 \times 10^4 \text{ cm}^{-2} \text{ s}^{-1}$ and $5.4 \times 10^3 \text{ cm}^{-2} \text{ s}^{-1}$ for deuterium, respectively.

Escape rates for hydrogen on Venus have also been examined in some detail. McElroy et al.^{79,35} found hydrogen escape via collisions with hot oxygen atoms from dissociative recombination of O_2^+ yielded fluxes of $8 \times 10^6 \text{ cm}^{-2} \text{ sec}^{-1}$ for hydrogen. Shizgal⁷¹ used a kinetic theory treatment to calculate escape rates of 1.1 and $6.2 \times 10^7 \text{ cm}^{-2} \text{ s}^{-1}$ for hydrogen on the dayside and nightside exosphere, respectively. Hunten²⁰ has reviewed published estimates of globally averaged escape rates for hydrogen from nonthermal processes, and reports that current values are in the range of $(0.2\text{-}2.7) \times 10^7 \text{ cm}^{-2} \text{ s}^{-1}$.

Lammer and Bauer⁸ employed a Monte Carlo technique to simulate the thermalization and transport of hot oxygen atoms produced by dissociative recombination of O_2^+ on Mars. They estimated an escape flux of $6 \times 10^6 \text{ cm}^{-2} \text{ s}^{-1}$, corresponding to a mass loss of oxygen atoms at a rate of 0.14 kg/s. Other estimates of the oxygen escape rate are given by Fox⁸⁰ at $3 \times 10^6 \text{ cm}^{-2} \text{ s}^{-1}$, and by McElroy⁸¹ at $(6\text{-}7) \times 10^6 \text{ cm}^{-2} \text{ s}^{-1}$.

In the current work, the escape flux is determined by integration of the hot atom product velocity distribution function over all speeds above the escape speed. The escape flux is considered to occur over a range of altitudes, and so an altitude integration is performed to determine the net escape flux. This integration proceeds over all altitudes at which nonthermal production of escaping atoms is non-negligible. The model thus incorporates altitude dependent production of translationally energetic atoms via charge exchange/direct elastic collisions. It does not account for thermalization of the hot species by elastic collisions with the background gas, which would involve a solution of the full, altitude dependent Boltzmann equation. It does, however, include realistic quantum mechanical collision cross sections to describe the kinematics of the interaction between colliding pairs of particles.

Chapter 2

Diffusion and Boltzmann Equation Models of Hot Oxygen Coronae

2.1 Introduction

Direct observation and theoretical modeling have combined to demonstrate the existence of an extended, enhanced population (or corona) of translationally energetic ('hot') oxygen atoms in the exospheres of the terrestrial planets. On Earth, Yee¹¹ used airglow measurements of twilight radiative emission from the transition between the states $O^+(^2P)$ and $O^+(^2D)$ at 732-33 nm^{11,31} to observe nonthermal oxygen above the terrestrial exobase. Hedin¹² showed that a significant population of hot oxygen can be inferred by comparing data available from mass spectrometer measurements and in-situ satellite drag observations, with values of $1-3 \times 10^4 \text{ cm}^{-3}$ at 1100 km and $1-3 \times 10^5 \text{ cm}^{-3}$ at 550 km for low to moderate solar conditions, and $1-4 \times 10^5 \text{ cm}^{-3}$ at 925 km for high solar activity. Direct rocket based observations have also been made of the geocorona. Analysis of the photometric measurements of oxygen emissions at 557.7 nm during rocket flights in 1980⁸² showed a variable increase in the concentration of atomic oxygen as compared to MSIS (mass-spectrometer/incoherent scatter) models. The Berkeley EUV airglow rocket spectrometer made measurements of the atomic oxygen dayglow emissions at 98.9-135.6 nm between the altitudes of 150 and 960 km,⁸³ and inferred a peak value of the geocorona of 10^6 cm^{-3} at 550 km, with a temperature of 4000 K.

Theoretical modeling of the Earth's oxygen geocorona has been relatively extensive. While the current work does is not concerned with calculations of the oxygen geocorona,

a brief description of theoretical work done by others is included for completeness and for comparison with Venus and Mars. Early theoretical results showing the formation of a hot oxygen geocorona were calculated by Rohrbaugh and Nisbet⁸⁴ using dissociative recombination of O_2^+ and NO^+ as sources. Their results showed hot oxygen concentrations on the order of 10^4 cm^{-3} at approximately 750 km, and 10^2 cm^{-3} at 3000 km. Shizgal and Lindenfeld⁸⁵ employed a kinetic theory treatment in the calculation of the energy distribution of hot O^3P atoms, and found that the distribution function was strongly perturbed at higher energies from the equilibrium Maxwellian, although the total number density of hot oxygen atoms produced was still too low to compete with thermalization at low altitudes. Yee¹¹ calculated hot oxygen densities from dissociative recombination sources using a two-stream transport code. He found that above altitudes of approximately 1200 km that nonthermal oxygen atoms dominate the thermal, ambient oxygen population, with a density of the order of 10^4 - 10^5 cm^{-3} . A dissociative recombination source was also considered by Schmitt and workers,⁸⁶ who calculated thermal and non-thermal O^1D density profiles coupled by a thermalization cross section. They used the 630 nm airglow measurements made by the Visible Airglow Experiment aboard the Atmosphere Explorer Satellite-C to normalize the thermalization cross section and arrived at hot atom densities on the order of 0.1 - 1 cm^{-3} at 750 km. Richards and workers³⁰ examined other potential sources of hot atoms in the thermosphere. They found that quenching of metastable species could provide significant new sources of hot oxygen beyond the previously considered dissociative recombination sources, although they only examined local production and did not address the transport of the hot atoms into the exosphere. More recently, Shematovich and workers³⁴ use a Monte Carlo model based on a non-linear Boltzmann equation to examine the thermal and nonthermal components of the oxygen geocorona. They find that a hot population of $O(^3P)$ atoms is indicated, with a density of about 10^4 cm^{-3} and temperature of 4100 K at 600 km.

For Venus, the suggestion of a corona of hot oxygen came from interpretation of observations made by the ultraviolet photometer on Mariner 5² and the objective grating spectrometer on Mariner 10,^{87,88} in 1967 and 1974, respectively. These results were more recently clearly confirmed by optical measurements made by extreme ultraviolet spectrometers on Venera 11 and 12⁸⁹ in 1978 and measurement of the 130.4 nm dayglow by the Pioneer Venus Orbiter Ultraviolet Spectrometer in 1978.^{4,69}

To explain the existence of a hot oxygen corona about Venus, Nagy et al.⁶⁹ used the two-stream transport model of Yee¹¹ in their interpretation of the Pioneer Venus data. They found daytime hot oxygen concentrations on the order of 10^4 cm^{-3} at 1600 km altitude. That study used preliminary ion density data which were higher than currently accepted values, and so the predicted hot oxygen concentrations were relatively high. A radiative transfer model by McElroy et al.⁷⁹ predicted values of similar but smaller magnitude, with differences between the two models attributed to a different choice of the primary dissociative recombination branch of O_2^+ , exobase level, and ion density profile. Paxton⁹⁰ also managed to get reasonable agreement with observed dayglow emission values by adjusting the branching ratios for dissociative recombination of O_2^+ . Calculation of the hot oxygen density on Venus was repeated by Nagy and Cravens⁷ using updated densities, and densities on the order of 10^2 - 10^3 cm^{-3} at 1600 km altitude were found, a factor of ten or more less than the previous calculation.

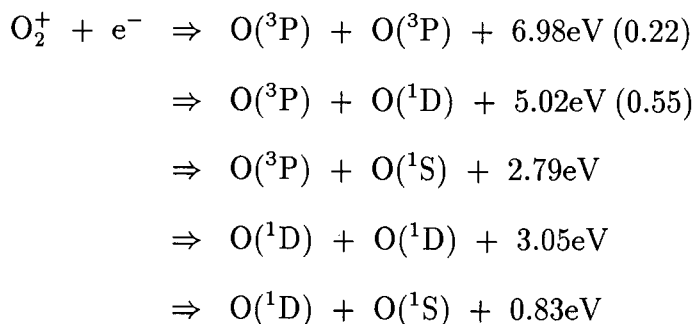
Modeling based on density profiles collected by the Viking Mission to Mars in 1977 has indicated that a hot oxygen corona should exist out to many Martian radii.^{7,6,8,32} Ip^{6,33} and Lammer & Bauer⁸ use a Monte Carlo simulation to model the diffusion and thermalization of hot oxygen up to the exobase in order to derive the hot oxygen energy density distribution at the exobase. They then assume a collisionless exosphere in order to apply Liouville's theorem to calculate the hot oxygen density profile for the upper exosphere. Their results give hot oxygen densities of the order of 0.5 - $2 \times 10^3 \text{ cm}^{-3}$ at

1600 km, depending on the choice of dissociative recombination coefficient. The existence of a hot oxygen corona on Mars has been largely verified by Phobos and Phobos 2 missions to Mars in 1989,³³ although the interpretation of the magnitude and extent of the corona is somewhat uncertain.⁹¹ Recent analysis by Kotova et al.¹⁴ of solar wind plasma and magnetic data obtained by Phobos 2 lead them to suggest that the Martian hot oxygen coronae densities could be even higher than those predicted by the Monte Carlo calculations of previous workers.

Most workers assume that the source of the hot oxygen atoms for both Mars and Venus is due to dissociative recombination of O_2^+ , which has the general form



This energy, ΔE , which is liberated by the dissociation of the O_2^+ molecule, is available to the product oxygen atoms. The amount of dissociation energy available depends on the final state of the product atoms, as the dissociative recombination of O_2^+ can take place along a number of branches or channels,^{69,80}



It is assumed that the available energy is split between the two product atoms equally. From Table 1.1, the O escape energy for oxygen at the Venusian and Martian exobases is approximately 8.6 and 1.9 eV, respectively. Thus, only the first two dissociation channels provide enough energy (3.99 eV and 2.51 eV per oxygen atom, respectively) to permit

direct escape from Mars, and none of the above channels provide sufficient energy for direct escape of oxygen from Venus.

The branching ratios for the O_2^+ dissociative recombination process are still only poorly known.⁹²⁻⁹⁴ That is, the relative populations of the various product states of atomic oxygen, in addition to translational energy available to each product atom, are poorly constrained. An estimate of the branching ratios of two channels which give rise to product atoms with sufficient energy to escape from Mars is given in brackets next to the appropriate reaction.⁹⁰ We assume that all dissociation takes place along the (dominant) second channel only, with a dissociative recombination coefficient $\alpha_{DR} = 3.0 \times 10^{-7} \text{ cm}^3 \text{ sec}^{-1}$.^{6,8} The source of hot oxygen is then given by

$$\begin{aligned} S(z) &= \alpha_{DR} [O_2^+][e^-] \\ &= \alpha_{DR} [O_2^+]^2 \end{aligned} \quad (2.1.2)$$

where the square brackets $[A]$ represent the density of species A . Following prior convention, we have assumed that the electron density is equal to the O_2^+ density.⁶ Altitude profiles of the O_2^+ density and the background gas densities are taken from available atmospheric profiles collected by planetary missions to Mars^{95,25,6} and Venus,^{96,24} and are illustrated in Figures 2.2 and 2.3 respectively. The densities are extrapolated beyond the tabulated values assuming that they follow a barometric distribution, as given by equation (1.2.4).

A representation of the process of hot oxygen atom creation and subsequent diffusion giving rise to exospheric coronae is given by Figure 2.4. Production of hot oxygen atoms occurs primarily in the lower atmosphere where the density of O_2^+ is sufficiently high that dissociative recombination is frequent. As can be seen in Figures 2.2 and 2.3, the density of O_2^+ peaks near 140 km altitude and decays rapidly above and below the peak altitude. The translationally energetic product oxygen atoms diffuse upward from their

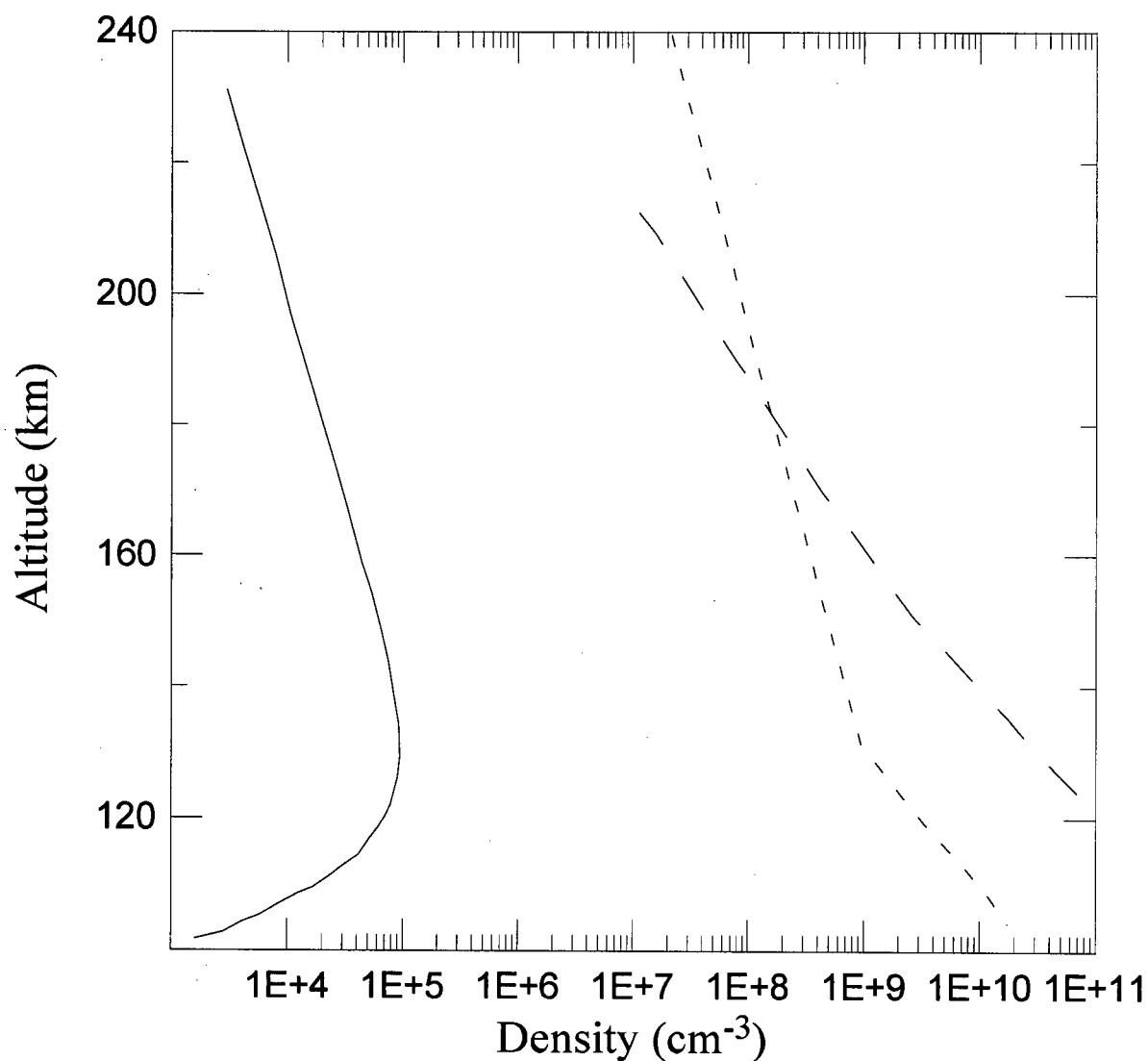


Figure 2.2: Observed Martian density profiles. The data are from Viking missions of 1977. The solid curve is the O_2^+ density profile, the dotted curve is the background oxygen density profile, and the dashed curve the background carbon-dioxide density profile. From Fox and Dalgarno.²⁵

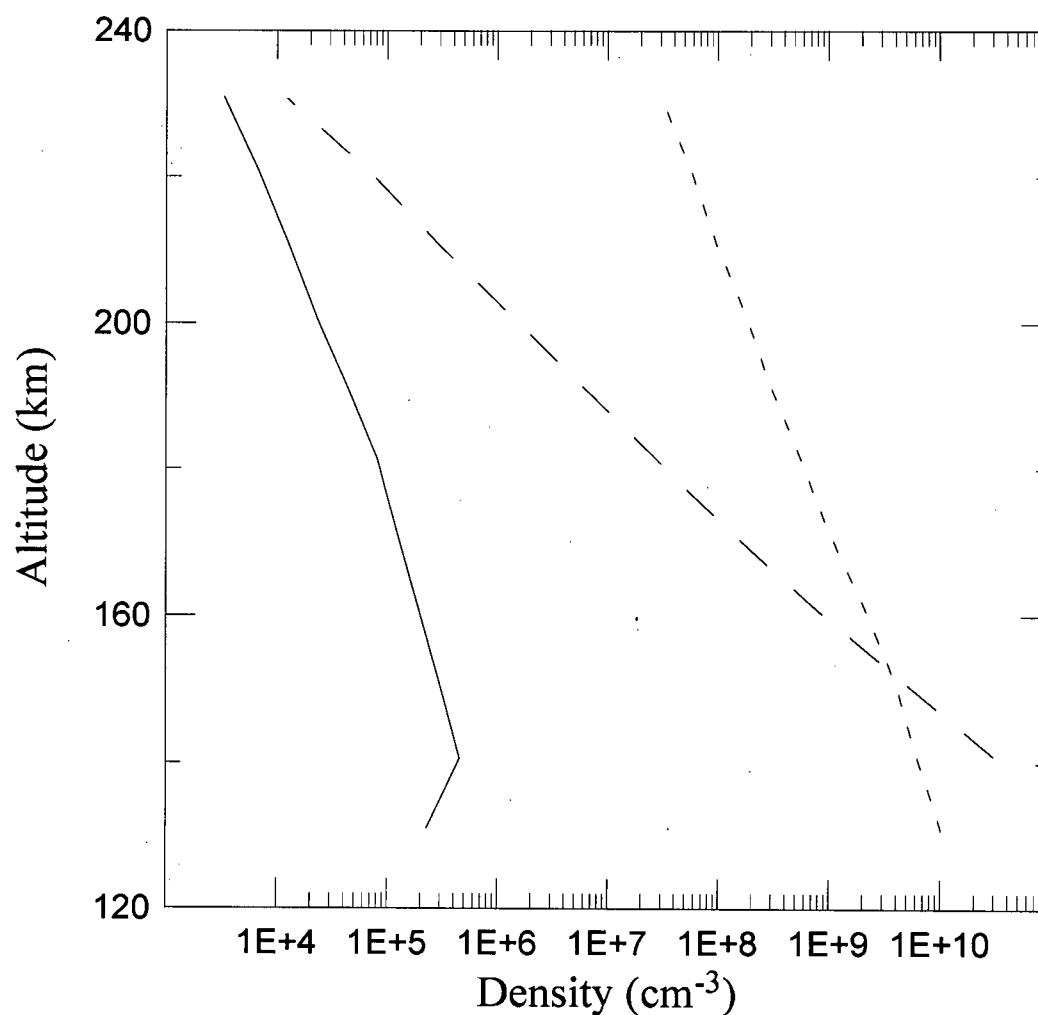


Figure 2.3: Observed Venusian density profiles. The data are from observations made by the Pioneer Venus orbiter and probe. The solid curve is the O₂⁺ density profile, the dotted curve is the background oxygen density profile, and the dashed curve the background carbon-dioxide density profile. From Nagy and Cravens.⁷

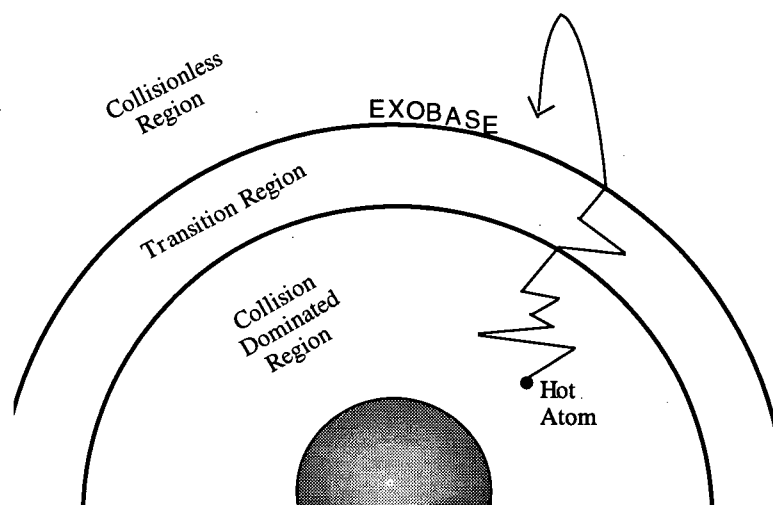


Figure 2.4: Stratification of the atmosphere by collisional property. In the collisionally dominated and transition regions, collisions drive energetic atoms toward equilibrium with the thermal background. Above the exobase, in the 'collisionless' region, particles move in trajectories solely under the affect of the planetary gravitational field. Hot atoms in this region have extremely long mean free paths and so may form an extremely extended corona of energetic atoms. A typical hot particle's path is shown on the right hand side of the figure.

altitude of creation until they achieve diffusive equilibrium. However, as the background density is still substantial at lower altitudes, the hot oxygen atoms have a high probability to suffer thermalizing collisions. Above the exobase, densities are sufficiently low that collisions are practically negligible, and atoms are free to move in accordance with their translational energy. The formation of an extended hot oxygen corona is thus a problem of the description of production and transport of hot atoms at low altitudes to above the exobase.

This chapter examines of the creation of hot oxygen 'coronae' in the exospheres of Venus and Mars using two new approaches to the production and diffusion of hot oxygen in planetary exospheres. The first model for the formation of the hot oxygen coronae is

given by solution of the diffusion equation, which describes diffusion of the translationally energetic exospheric oxygen atoms through a cold background gas. The general diffusion equation for a minor species of density n diffusing through a background is given by²²

$$\frac{\partial n}{\partial t} = \frac{\partial}{\partial z} \left[D(z) \left\{ \frac{\partial n}{\partial z} + \frac{n}{H(z)} \right\} \right] + S(z) \quad (2.1.3)$$

where $D(z)$ is the diffusion coefficient, given by²²

$$D(z) = \frac{kT_{hot}}{m_{hot}\nu(z)} \quad (2.1.4)$$

and $S(z)$, the source of the hot oxygen atoms due to dissociative recombination of O_2^+ , is given previously by equation (2.1.2). It is assumed that the collisional interaction between the hot oxygen and background gases is described by a hard sphere model. The collision frequency and average relative speed are thus given, respectively, by

$$\begin{aligned} \nu(z) &= n_{back}(z)\sigma_{hs}V_{ave} \\ V_{ave} &= \sqrt{\frac{8k}{\pi} \left(\frac{T_{hot}}{m_{hot}} + \frac{T_{back}}{m_{back}} \right)} \end{aligned} \quad (2.1.5)$$

where n_{back} is the thermal oxygen altitude density profile, T_{hot} and T_{back} are the hot oxygen and thermal oxygen temperature profiles, and σ_{hs} is the hard sphere collision cross section. The collision frequency and average velocity in equation (2.1.5) have assumed that the colliding species' distribution functions are Maxwellian. The diffusion coefficient is thus determined by the altitude dependent temperature of the hot oxygen atoms and density profile of the background thermal oxygen. For the first model examined in this chapter, we assume an altitude independent (constant) temperature for the hot oxygen atoms. This is equivalent to assuming that there is no thermalization or energy exchange between the diffusing hot oxygen and the background gas. The simple diffusion model is then extended by incorporating an altitude dependent temperature, which is calculated

self-consistently using coupled density and energy equations based on standard hydrodynamic theory.^{97,98} The incorporation of an energy equation accounts for the effect of thermalization or energy transfer between the hot oxygen and the background.

A model of hot atom densities based on solutions of the local Boltzmann equation is also examined. The velocity distribution function of the hot oxygen atoms are calculated at the altitude of the exobase and hot oxygen density profiles are then generated using Liouville's theorem.¹⁶ The Boltzmann collision operator rigorously accounts for the thermalizing effect of (elastic) collisions, and so temperature and density profiles are calculated in a self-consistent fashion. As for the other models in this chapter, we assume the use of 'hard sphere' or energy independent collision cross sections.

The models introduced in this chapter are relatively simple descriptions of the production and transport of hot atoms. Our goal is thus to investigate whether such models are sufficient to qualitatively describe the altitude distribution of densities of hot exospheric oxygen and to compare with similar studies using more complicated models by other workers.^{11,69,79,7,6,33,32,8} There are many uncertainties to consider in contrasting and comparing results between the various models. Poor constraints on the values of the dissociative recombination branching ratios, the dissociative recombination coefficient, neutral temperature and density altitude profiles, and the hot oxygen-background collision cross section contribute greatly to discrepancies between the various approaches. They also degrade the accuracy of the predictions of hot atom densities.

2.2 Constant Temperature Model

As illustrated in Figure 2.4 the generation of an enhanced population of hot atoms at high altitudes in the exosphere requires transporting hot atoms from their altitude of production. It was of interest to determine whether simple diffusion of energetic atoms

through a stationary thermal background was capable of producing qualitative agreement with densities inferred from satellite and ground based emission studies and calculated by other workers using Monte Carlo and other techniques.

If it is assumed that the density of the minor species has reached a steady-state value, the time derivative on the left-hand side of equation (2.1.3) may be set to zero to yield the steady state diffusion equation

$$\frac{\partial}{\partial z} \left[D(z) \left\{ \frac{\partial n}{\partial z} + \frac{n}{H(z)} \right\} \right] + S(z) = 0 \quad (2.2.1)$$

where $D(z)$ is the diffusion coefficient given previously by equation (2.1.4). Equation (2.2.1) is then integrated in altitude from z_o to z to yield

$$\frac{\partial n}{\partial z} + \frac{n}{H(z)} = -\frac{1}{D(z)} \int_{z_o}^z S(z') dz' + C_1 \quad (2.2.2)$$

where C_1 is the constant of integration. This equation is a linear first-order differential equation, and may be solved by use of an integrating factor,⁹⁹ $\exp(h(z))$, where

$$h(z) = \int_{z_o}^z \frac{1}{H(z')} dz'$$

The integrating factor is applied to equation (2.2.2), and after some rearrangement and collecting of constants, we find

$$n(z) = e^{-h(z)} \int_{z_o}^z e^{h(z')} \{P(z') + C_1\} dz' + C_2 e^{-h(z)} \quad (2.2.3)$$

where for clarity we have defined

$$P(z) \equiv -\frac{1}{D(z)} \int_{z_o}^z S(z') dz' \quad (2.2.4)$$

The two constants in equation (2.2.3) may be evaluated easily if boundary conditions are applied at the lower ($z = z_o$) boundary. From equations (2.2.2) and (2.2.3), with $z \equiv z_o$, we thus find

$$\begin{aligned} C_1 &= \frac{\partial n(z_o)}{\partial z} + \frac{n(z_o)}{H(z_o)} \\ C_2 &= n(z_o) e^{h(z_o)} \end{aligned} \quad (2.2.5)$$

For the case of a constant scale height, $H(z) = H(z_o)$, and no source, $S(z) = 0$, equation (2.2.3) reduces to the barometric solution given by equation (1.2.4),

$$n(z) = n(z_o) \exp \left[\frac{-(z - z_o)}{H(z_o)} \right] \quad (2.2.6)$$

Similarly, for a constant temperature but radially dependent gravitational acceleration, with the scale height given by

$$H(z) = \frac{kT}{mg(z)}$$

we find after some algebraic manipulation that the argument of the integrating factor is given by

$$h(z) = \frac{R + z_o}{H(z_o)} - \frac{R + z}{H(z)}$$

where R is the planetary radius. Substituting this result in equation (2.2.3) we arrive at

$$n(z') = n(z'_o) \exp \left[\frac{-(z' - z'_o)}{H(z'_o)} \right] \quad (2.2.7)$$

which is identical in form to the barometric density equation except it is a function of a 'reduced altitude' (or 'geopotential height')

$$z' - z'_o = (z - z_o) / \left(1 + \frac{z - z_o}{R + z_o} \right)$$

rather than altitude.

To determine the hot oxygen density using equation (2.2.3) it is necessary to provide a temperature profile for the hot oxygen in order to calculate the altitude dependent scale height. For this model, some (arbitrary) constant temperature T_o is chosen. There is no *a priori* justification for a particular choice of this (constant) temperature, other than the physical argument that it should be between the background thermal oxygen temperature and the temperature equivalent to the initial hot oxygen dissociation energy.

The solution of equation (2.2.3) involves a double integral. The integrations are done using a Simpson's Rule with 150 altitude steps. In order to accurately calculate the integrated hot atom source density, $P(z)$, we do a 250 point Simpson's Rule integration between *each* pair of altitude points from the Simpson's Rule integration over z' in equation (2.2.3), and simply add the contributions from each to yield $P(z_i)$. This is necessary as the altitudes of interest span several thousand kilometers and so a straightforward integration of the source over the entire span of z' requires excessive numbers of integration points (and time). The initial altitude is (arbitrarily) chosen below the exobase level, and is 90 km for Mars and 100 km for Venus. As a check of the accuracy of the numerical solution of equation (2.2.3), as detailed above, it was compared to the analytic solutions given by equations (2.2.6) and (2.2.7) for the case where the source is set to zero, and the scale height is constant or dependent only on the gravitational acceleration, respectively.

Once the accuracy of the numerical solution of equation (2.2.3) was verified for the above test cases, the effect of an altitude dependent scale height (via equation (1.2.3)) and/or diffusion coefficient on the density profile of the hot oxygen was examined. A value of 8500 K was chosen as the (constant) temperature for the hot atoms.⁸ For the background thermal oxygen on Mars, a (constant) temperature of 180 K was inferred from the thermal oxygen density profile of Figure 2.2, given the assumption of barometric behaviour. A temperature of 280 K was derived similarly for the thermal oxygen temperature on Venus. A hard sphere (total) collision cross section of $2.0 \times 10^{-15} \text{ cm}^2$ is used. The solutions for the hot oxygen density profiles for Mars and Venus are shown in Figures 2.5 and 2.6.

The density profiles are physically reasonable given the changes in the scale height and the diffusion coefficient. The solid curve in both figures indicates the case where both the scale height and diffusion coefficient are held constant. The curve marked with open triangles illustrates the case where only the scale height is allowed to vary

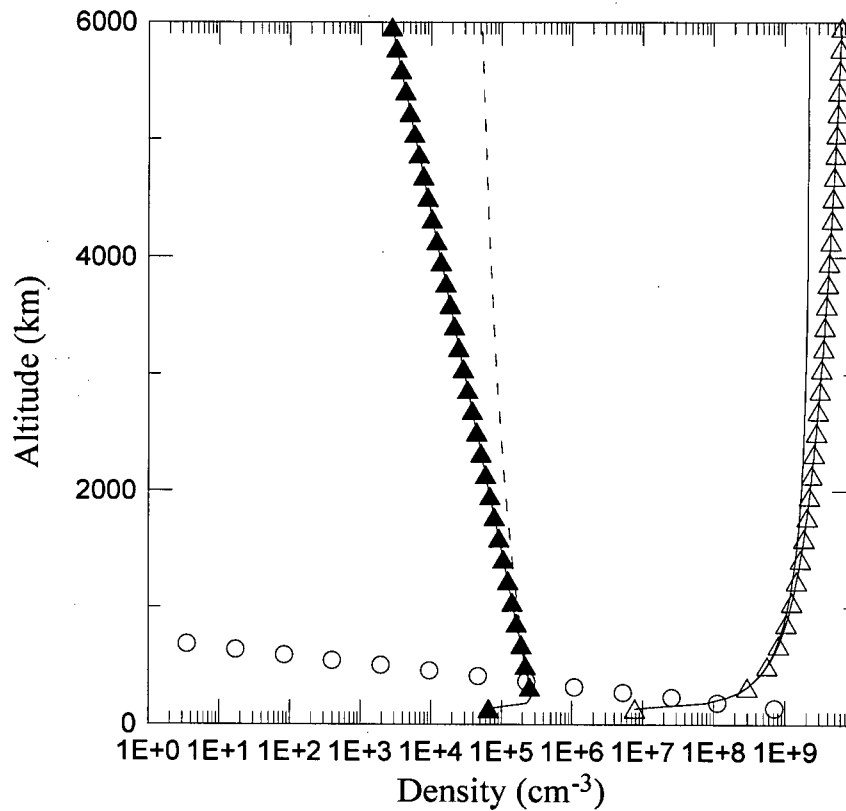


Figure 2.5: Martian hot oxygen density profiles derived from solutions of the diffusion equation. The hot oxygen temperature is taken to be a (constant) 8500 K, and the background temperature is a (constant) 180 K. The various curves depict the behaviour of the hot oxygen density to the variation of gravity g and diffusion coefficient D . The solid curve is for both g and D constant with altitude, the open triangle marked curve is for variation of g (and thus scale height) only with altitude, the filled triangle marked curve is for variation of D only with altitude, and the dashed curve is for the density with both g and D varying with altitude. The open circle symbols indicate the background ('cold') oxygen density.

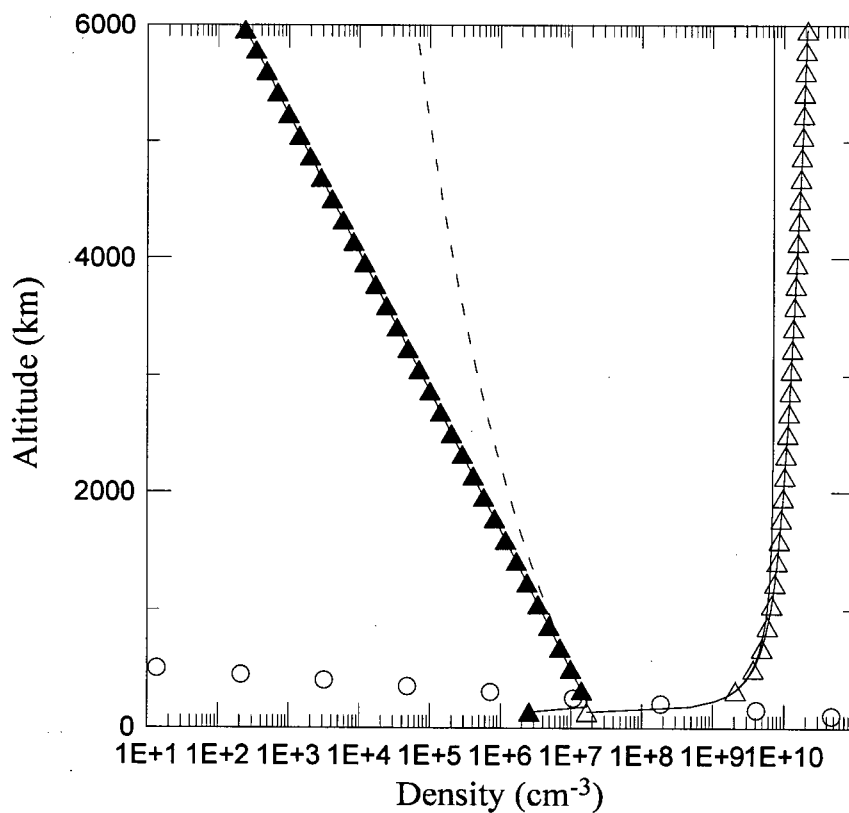


Figure 2.6: Venusian hot oxygen density profiles derived from solutions of the diffusion equation. The hot oxygen temperature is taken to be a (constant) 8500 K, and the background temperature is a (constant) 280 K. The labeling of the curves is as for Figure 2.5.

with altitude. For this case, the hot atom density is maximal at altitude. Physically, this is expected given that the scale height increases with altitude as the gravitational acceleration decreases, all other parameters held constant. The case where only the diffusion coefficient is allowed to vary with altitude is indicated by the curve marked with solid triangles. The integrated hot atom source density, $P(z)$, given in equation (2.2.4) depends inversely on the diffusion coefficient, which depends inversely on the collision frequency. Since the background density is decreasing with altitude, from equation (2.1.5) we have that $P(z)$ decreases with an altitude dependent diffusion coefficient, and so the density at altitude decreases. The rate of decrease is larger for Venus, where the background density (and hence collision frequency) decreases more rapidly with altitude. If both the scale height and diffusion coefficient vary with altitude, as indicated by the dashed curves in the figure, the density profile lies between the values produced when only one or the other is allowed to vary.

The density profiles are shown out to an altitude of 6000 km, well beyond the limited altitude range of input density profiles as given in Figure 2.2. There are several reasons for an interest in hot atom densities for such large altitudes. The first is that the enormous enhancement of the hot atom density over the thermal background does not become apparent until above approximately 500 km on Mars. Additionally, the hot atom densities at high altitude are important in determining the nature and magnitude of interactions with the solar wind.¹⁴

The dependence of the hot atom density profile on temperature was also examined, and the results are illustrated in Figures 2.7 and 2.8 for Mars and Venus, respectively. Since we do not have any detailed information on the hot atom temperature profile, a constant temperature profile was used, with the value varied between 500 and 8500 K. An increase of hot atom density at higher altitudes is visible with an increase in the hot temperature, for both Mars and Venus. The effect becomes less pronounced above 5000

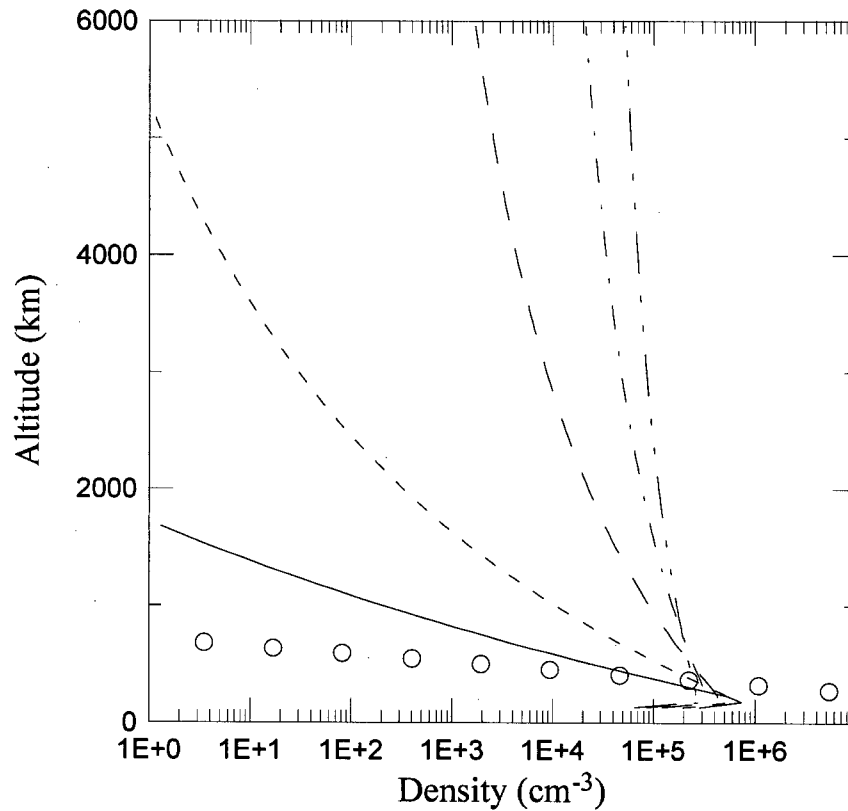


Figure 2.7: Martian hot oxygen density temperature dependence. The (constant) hot oxygen temperature was varied between 500 and 8500 K, and the scale height (gravity) and diffusion coefficient were allowed to vary with altitude. The solid, short-dashed, long-dashed, dot-dashed, and dot-dot-dashed curves represent hot oxygen temperatures of 500 K, 1000 K, 2500 K, 5000 K, and 8500 K, respectively. The open circle symbols indicate the background ('cold') oxygen density.

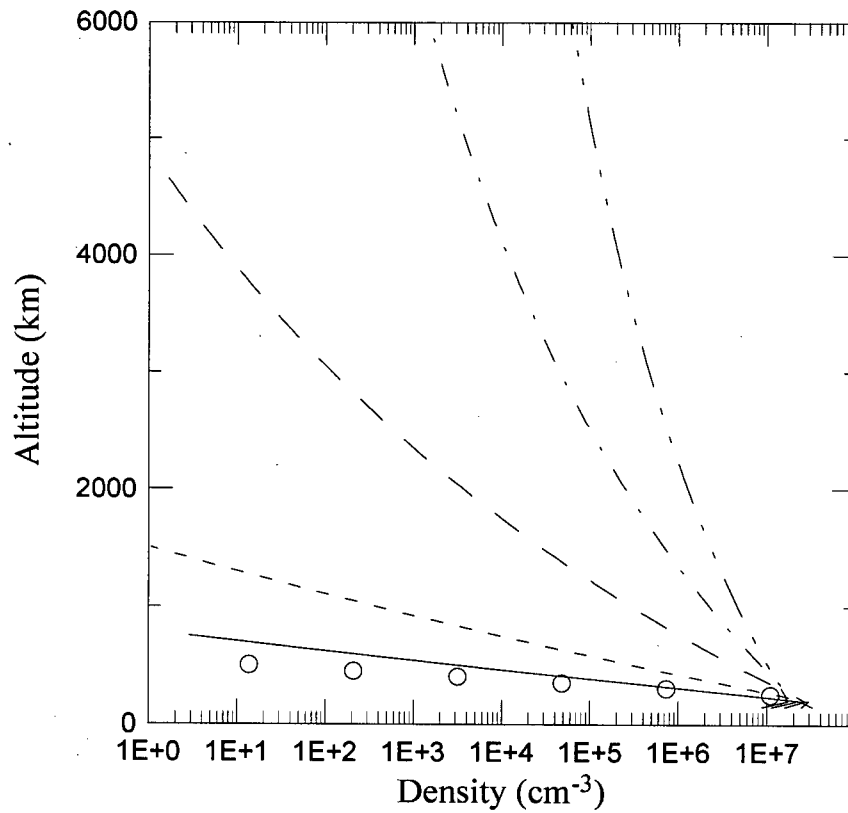


Figure 2.8: Venusian hot oxygen density temperature dependence. The (constant) hot oxygen temperature was varied between 500 and 8500 K, and the scale height (gravity) and diffusion coefficient were allowed to vary with altitude. The labeling is as in Figure 2.7.

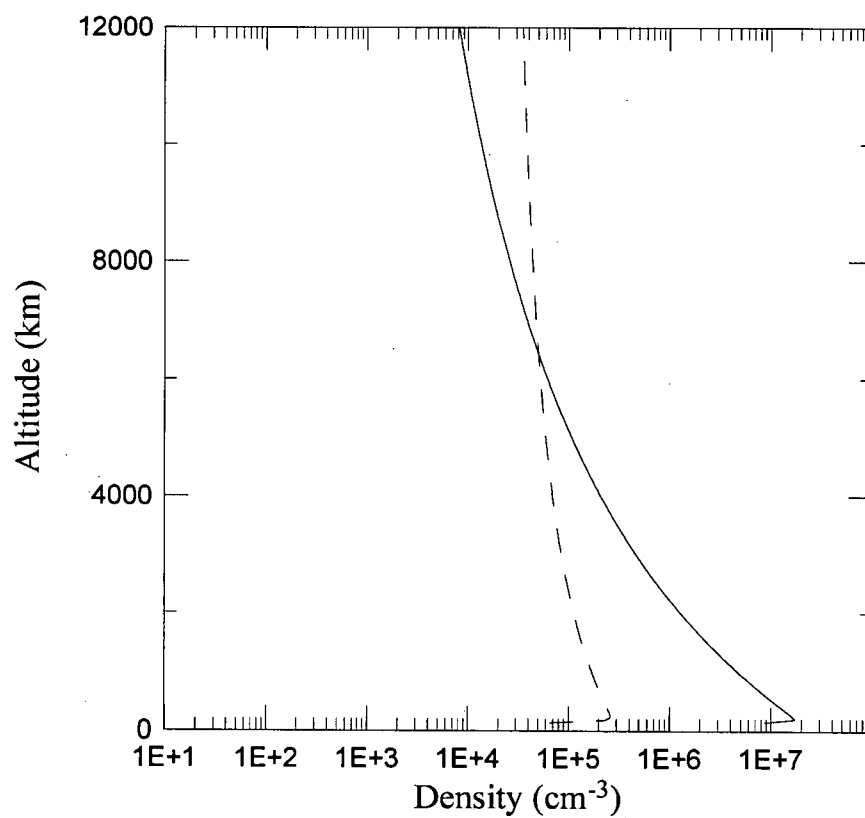


Figure 2.9: Hot oxygen densities at large altitudes for Venus and Mars. The solid and dashed lines indicate the hot oxygen densities for Venus and Mars, respectively. The hot atom temperature is fixed at 8500 degrees for both planets.

K, especially for Mars, where the low gravitational acceleration and high temperatures combine to yield scale heights of the order of thousands of kilometers. The effect of the stronger gravitational acceleration on Venus is most apparent for temperatures below 8500 K, where hot atom densities are lower than their Martian counter-parts at altitudes above approximately 1000 km.

When comparing the hot oxygen density profiles of the two planets, we see that they are remarkably similar in magnitude at the 6000 km altitude of Figures 2.7 and 2.8. The hot oxygen density is greater below this altitude on Venus than Mars. The stronger dissociative recombination source at low altitudes on Venus appears to offset the effect of a lower gravitational acceleration and hence much larger scale height for the hot oxygen on Mars for altitudes up to approximately 6000 km. The hot oxygen density profiles are plotted together for altitudes up to 12 000 km in Figure 2.9. It is clear that for altitudes greater than roughly the planetary radius of Venus that the hot oxygen corona of Mars decays much more slowly due to the lower gravity, and is thus much more extensive, despite the stronger dissociative recombination source on Venus.

2.3 Non-constant Temperature Model

In the previous section we assumed that the hot oxygen atoms were at some (arbitrary) constant temperature. This is equivalent to neglecting energy transfer between the diffusing hot oxygen and the thermal background. In order to extract information about the altitude dependence of the temperature of the hot oxygen atoms in the planetary coronae, we must account for the partial thermalization of the hot atoms as they collide with the thermal background. To extend the model of the previous section to allow for temperature variation with altitude, we employ a standard hydrodynamic approach commonly used in analysis of particle transport and temperature distribution in the middle

and upper atmosphere.

As previously, we consider a system of hot atomic oxygen diffusing through a thermal background of oxygen. The thermal oxygen is assumed to be at diffusive equilibrium. We are interested in the transport of the translationally energetic, nonequilibrium hot oxygen, and the steady-state altitude dependence of its density and temperature. Following standard hydrodynamic theory used for the solar wind^{100,101} we rewrite equations (1.4.1) and (1.4.2) in terms of the the random velocity, multiply by 1, $m_s \mathbf{c}_s$ and $\frac{1}{2} m_s c_s^2$, and then integrate over velocity space to obtain the continuity, momentum and energy transport equations for the hot oxygen (denoted by the subscript s):

Continuity:

$$\frac{\partial n_s}{\partial t} + \nabla \cdot (n_s \mathbf{u}_s) = \frac{\delta n_s}{\delta t} + N \quad (2.3.1)$$

Momentum:

$$n_s m_s \frac{\partial \mathbf{u}_s}{\partial t} + n_s m_s \mathbf{u}_s \cdot \nabla (\mathbf{u}_s) + \nabla \cdot \mathbf{P}_s - n_s m_s \mathbf{G} = \frac{\delta \mathbf{M}_s}{\delta t} + M \quad (2.3.2)$$

Energy:

$$\frac{\partial \frac{3}{2} p_s}{\partial t} + \mathbf{u}_s \cdot \nabla \left(\frac{3}{2} p_s \right) + \frac{3}{2} p_s (\nabla \cdot \mathbf{u}_s) + \nabla \cdot \mathbf{q}_s + \mathbf{P}_s : \nabla \mathbf{u}_s = \frac{\delta E_s}{\delta t} + E \quad (2.3.3)$$

In equations (2.3.1)-(2.3.3), n_s , \mathbf{u}_s , T_s , \mathbf{q}_s , and \mathbf{P}_s are the hot oxygen density, drift (average) velocity, temperature, heat flow, and (anisotropic) pressure tensor, respectively. We have also defined N, M, E as the (altitude dependent) production terms for the hot oxygen number density, momentum, and energy, respectively. The terms $\frac{\delta n_s}{\delta t}$, $\frac{\delta \mathbf{M}_s}{\delta t}$ and $\frac{\delta E_s}{\delta t}$ on the right-hand side of equations (2.3.1)-(2.3.3) correspond to the moments of the Boltzmann collision integral, equation (1.4.2), and represent changes of density, momentum, and energy as a result of collisions. They are not shown explicitly as they depend on the type of interaction between colliding particles (e.g. hard sphere) and on

the form of the distribution functions of the interacting species. In our coupled system of transport equations, we have ignored external force terms except for that due to the gravitational acceleration, \mathbf{G} .

At lower altitudes, collisions with background species are plentiful and the velocity distribution functions for diffusing species are generally considered to be close to the equilibrium Maxwellian distribution. As collisions decrease with altitude, larger temperature and diffusion velocity differences can be maintained by diffusing species, and the distribution function can depart from the equilibrium Maxwellian distribution of the thermal background gas. At the lowest level of approximation, we assume that the distribution function of the diffusing hot species is completely described by the first five moments of the hot atom distribution function: the density, n_s , the three components of the drift velocity \mathbf{u}_s , and the temperature, T_s . We assume the pressure tensor is isotropic (off diagonal elements are zero), and that the stress tensor, heat flow, and higher order moments are zero. Thus, the system of transport equations reduces to

$$\frac{\partial n_s}{\partial t} + \nabla \cdot (n_s \mathbf{u}_s) = \frac{\delta n_s}{\delta t} + N(z) \quad (2.3.4)$$

$$n_s m_s \frac{\partial \mathbf{u}_s}{\partial t} + n_s m_s \mathbf{u}_s \cdot \nabla (\mathbf{u}_s) + \nabla p_s - n_s m_s \mathbf{G} = \frac{\delta \mathbf{M}_s}{\delta t} + \mathbf{M}(z) \quad (2.3.5)$$

$$\frac{\partial \frac{3}{2} p_s}{\partial t} + \mathbf{u}_s \cdot \nabla \left(\frac{3}{2} p_s \right) + \frac{5}{2} p_s (\nabla \cdot \mathbf{u}_s) = \frac{\delta E_s}{\delta t} + E(z) \quad (2.3.6)$$

The collision terms on the right-hand side of equations (2.3.4)-(2.3.6) may be evaluated rigorously for arbitrary interactions between species for the case where both species' distribution functions are Maxwellian. In this case, for arbitrarily large differences in drift velocities and temperatures, we have

$$\frac{\delta n_s}{\delta t} = 0$$

$$\frac{\delta \mathbf{M}_s}{\delta t} = n_s m_s \nu_{st} (\mathbf{u}_t - \mathbf{u}_s) \Phi_{st}$$

$$\frac{\delta E_s}{\delta t} = \frac{n_s m_s \nu_{st}}{m_s + m_t} \left[3k(T_t - T_s) \Psi_{st} + m_t (\mathbf{u}_s - \mathbf{u}_t)^2 \Phi_{st} \right]$$

where Φ_{st} and Ψ_{st} are velocity dependent ‘correction factors’ given for hard spheres by^{97,98}

$$\begin{aligned}\Phi_{st} &= \frac{3\sqrt{\pi}}{8} \left[\epsilon_{st} + \frac{1}{\epsilon_{st}} - \frac{1}{4\epsilon_{st}^3} \right] \text{erf}(\epsilon_{st}) + \frac{3}{8} \left[1 + \frac{1}{2\epsilon_{st}^2} \right] \exp(-\epsilon_{st}^2) \\ \Psi_{st} &= \frac{\sqrt{\pi}}{2} \left[\epsilon_{st} + \frac{1}{2\epsilon_{st}} \right] \text{erf}(\epsilon_{st}) + \frac{1}{2} \exp(-\epsilon_{st}^2)\end{aligned}$$

and where the subscript t denotes a parameter for the background species, which is taken to be thermal atomic oxygen. In the equations above, $\text{erf}()$ is the error function,

$$\text{erf}(x) \equiv \frac{2}{\sqrt{\pi}} \int_0^x e^{-t^2} dt$$

ν_{st} is the momentum transfer collision frequency,

$$\nu_{st} \equiv \frac{8}{3\sqrt{\pi}} \frac{n_t \mu_{st}}{m_s} V_{th} \sigma_{HS}$$

and T_{st} and μ_{st} are the reduced temperature and mass, respectively, defined as

$$\begin{aligned}T_{st} &\equiv \frac{m_s T_t + m_t T_s}{m_s + m_t} \\ \mu_{st} &\equiv \frac{m_s m_t}{m_s + m_t}\end{aligned}$$

The hard sphere collision cross section is denoted by σ_{HS} . The parameter ϵ_{st} is the ratio of the magnitude of the difference in drift velocities to the average ‘thermal’ speed, that is

$$\epsilon_{st} \equiv \frac{|\mathbf{u}_s - \mathbf{u}_t|}{V_{th}}$$

where

$$V_{th} \equiv \sqrt{\frac{2kT_{st}}{\mu_{st}}}$$

is defined as the ‘average’ thermal speed of the gas mixture. We choose to set the background drift velocity to zero (e.g. a stationary background gas). Our problem is thus reduced to finding the density, drift, and temperature profile of the diffusing species.

If we assume that all motion is along the vertical (z) direction, and look for steady-state solutions, our transport equations reduce to

$$\frac{\partial}{\partial z}(n_s u_s) = N(z) \quad (2.3.7)$$

$$n_s m_s u_s \frac{\partial u_s}{\partial z} + k \frac{\partial}{\partial z}(n_s T_s) + n_s m_s g = -n_s m_s \nu_{st} u_s \Phi_{st} \quad (2.3.8)$$

$$\frac{3}{2} u_s k \frac{\partial}{\partial z}(n_s T_s) + \frac{5}{2} n_s k T_s \frac{\partial u_s}{\partial z} = E(z) - \frac{n_s \mu_{st} \nu_{st}}{m_t} \times [3k(T_s - T_t) \Psi_{st} - m_t u_s^2 \Phi_{st}] \quad (2.3.9)$$

where we have defined the gravitational acceleration as $\mathbf{G} \equiv -g\hat{k}$. If it is assumed that the drift speed is much less than the average ‘thermal’ speed of the gas mixture, so that $\epsilon_{st} \ll 1$, it may be shown that

$$\Phi_{st} = 1$$

$$\Psi_{st} = 1$$

In addition, we must specify the production terms $N(z), M(z), E(z)$. We assume, as in the previous section, that dissociative recombination of O_2^+ is the only source of energetic hot oxygen atoms, so that

$$N(z) = \alpha_{DR} [\text{O}_2^+]^2 \quad (2.3.10)$$

where $\alpha_{DR} \approx (1-3) \times 10^{-7} \text{ cm}^3/\text{sec}$ and the units of N are $\text{cm}^{-3}\text{sec}^{-1}$. The dissociative recombination reaction is assumed to be ‘single channel’, with the product 5.02 eV of energy for the dissociation branch shared equally between the two product oxygen atoms. The product atoms will thus have an initial temperature T_{prod} given by⁶⁷

$$\frac{3}{2} k T_{prod} = 2.5 \text{ eV} \quad (2.3.11)$$

and that the average energy per atom will be

$$E_{av} = \frac{3}{2} k T_{prod} \quad (2.3.12)$$

The energy source term $E(z)$ is then simply given by $N(z) \times E_{av}$, with units of $\text{ergs cm}^{-3} \text{ sec}^{-1}$. We also assume that the distribution of hot atom trajectories following the dissociation reaction is isotropic; in this case, hot atoms are equally likely to have upward motion as downward, and the net momentum gain is zero ($M(z) \equiv 0$).

As an example of such singularities, and in an attempt to gain insight into their physical meaning, we rewrite our original coupled system of transport equations, equations (2.3.7)-(2.3.9), assumed a 1-D plane parallel atmospheric geometry, steady state, and neglected sources and collisions, yielding

$$\frac{\partial}{\partial z}(n_s u_s) = 0 \quad (2.3.13)$$

$$n_s m_s u_s \frac{\partial u_s}{\partial z} + k \frac{\partial}{\partial z}(n_s T_s) + n_s m_s g = 0 \quad (2.3.14)$$

$$\frac{3}{2} u_s k \frac{\partial}{\partial z}(n_s T_s) + \frac{5}{2} n_s k T_s \frac{\partial u_s}{\partial z} = 0 \quad (2.3.15)$$

If we now assume a constant temperature and gravitational acceleration, we may write equation (2.3.14) as

$$\frac{\partial n_s}{\partial z} = -\frac{n_s}{H - C^2/(n_s^2 g)} \quad (2.3.16)$$

where we have used, from the continuity equation, that $n_s u_s = C$, constant, and that $\frac{\partial u_s}{\partial z} = -C \frac{\partial n_s}{\partial z} / n_s^2$. We have also defined a (constant) scale height, $H = kT_s/m_s g$. To solve for the density profile, we rewrite equation (2.3.16) as

$$-dz = \frac{H - C^2/(n_s^2 g)}{n_s^3 g} dn \quad (2.3.17)$$

Integrating both sides,

$$\begin{aligned} -\int_{z_o}^z dz &= \int_{n_o}^n \frac{H - C^2/(n_s^2 g)}{n_s^3 g} dn \\ -(z - z_o)/H &= \ln(n_s/n_o) + \frac{C^2}{2gH} \left(\frac{1}{n_s^2} - \frac{1}{n_o^2} \right) \\ y \exp(A/y^2) &= \exp\left(-\frac{(z - z_o)}{H} + A\right) \end{aligned} \quad (2.3.18)$$

where $A = C^2/(2gHn_o^2) = u_o^2/(2gH)$ and $y = n_s/n_o$. The final result is transcendental for y . For fixed values of A , plots of $y \exp(A/y^2)$ vs. y (or $\exp(-\frac{(z-z_o)}{H} + A)$ vs. z) may be drawn. Examples are given in Figure 2.10. The gravitational acceleration and scale height are held constant at 3.3 m/s^2 and 30 km , respectively, and are chosen to represent typical values near the Martian exobase for atomic oxygen. The flow speed u_o is chosen to be 300 m/s and 30 m/s , respectively, for curves labeled A and B, yielding values of the parameter A equal to 0.454 and 4.54×10^{-3} , respectively.

The curve defined by equation (2.3.18) has a minimum at $y_{min} = \sqrt{2A}$. Using this value in equation (2.3.18), we may solve for $z = z_{max}$,

$$z_{max} = \left[A - \ln(\sqrt{2A}e) \right] H + z_o$$

Thus, for given values of the hot oxygen density, n_s , and A , there are altitudes above which the solution to equation (2.3.18) *does not exist*, and forcing the numerical algorithm past these altitudes results in meaningless solutions. Graphically, this is illustrated in Figure 2.10 by the continuation of the solid curves (the RHS of equation (2.3.18)) below the minimum of the dashed curves (the LHS of equation (2.3.18)).

We may rewrite our conservation equations for the above case in a slightly different form in order to gain further insight into the source of the singularity. For the case of no sources, no collisions and constant temperature, we had conservation and momentum equations given by :

$$\begin{aligned} \frac{\partial}{\partial z}(n_s u_s) &= 0 \\ n_s m_s u_s \frac{\partial u_s}{\partial z} + k \frac{\partial}{\partial z}(n_s T_s) &= -n_s m_s g \end{aligned}$$

Substituting the continuity equation into the momentum equation, we have

$$\left(n_s m_s u_s - \frac{k T_s C}{u_s^2} \right) \frac{\partial u_s}{\partial z} = -n_s m_s g$$

where we have made use of

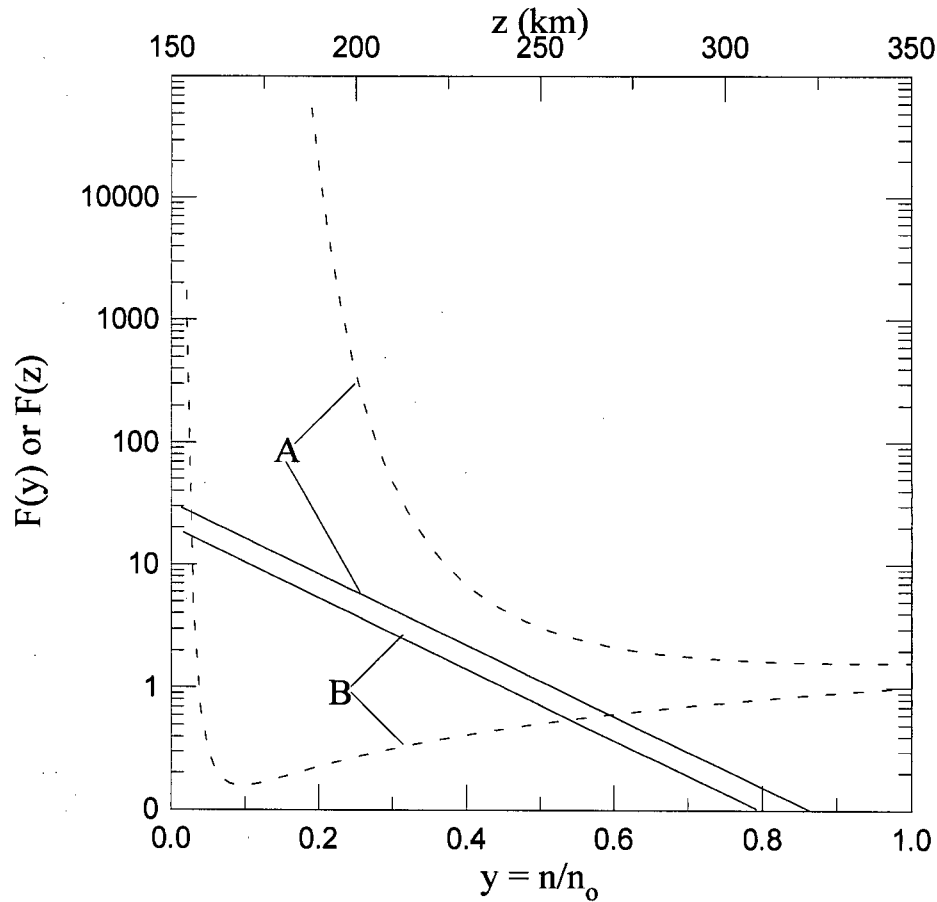


Figure 2.10: Solutions of the collisionless, sourceless momentum conservation equation for a plane parallel geometry. The gravitational acceleration and scale height are held constant at 3.3 m/s^2 and 30 km , respectively, and are chosen to represent typical values near the Martian exobase for atomic oxygen. The flow speed u_o is chosen to be 300 m/s and 30 m/s , respectively, for curves labeled A and B. The solid lines represent plots of $\exp(-\frac{(z-z_o)}{H} + A)$ vs. z from equation (2.3.18), with the z axis given by the top horizontal axis. The dashed lines represent plots of $y \exp(A/y^2)$ vs. y from equation (2.3.18), with the y axis given by the bottom horizontal axis. The vertical axis is common to both plots.

$$n_s u_s = C, \quad \frac{\partial u_s}{\partial z} = -C \frac{\partial n_s}{\partial z} / n_s^2$$

After further manipulation, we may rewrite our momentum equation in the form

$$\left(u_s^2 - \frac{kT_s}{m_s} \right) \frac{\partial u_s}{\partial z} = -u_s g \quad (2.3.19)$$

The important point to note from equation (2.3.19) is that while the left-handside may vanish for either $du/dz \equiv 0$ or $u^2 = kT/m$, the right-handside vanishes only if $u \equiv 0$. That is, the zeroes on the LHS are not balanced on the RHS, and the two sides vanish independently of each other. This imbalance may be resolved by following the approach used in the examination of the solar wind.^{102,100,101} Rewriting our conservation equations in spherical coordinates, we have

$$\begin{aligned} \frac{1}{r^2} \frac{\partial}{\partial r} (n_s u_s r^2) &= 0 \\ n_s m_s u_s \frac{\partial u_s}{\partial r} + k \frac{\partial}{\partial r} (n_s T_s) &= -n_s m_s g - n_s m_s \nu_{st} u_s \\ \frac{3}{2} u_s k \frac{\partial}{\partial r} (n_s T_s) + \frac{5}{2} \frac{n_s k T_s}{r^2} \frac{\partial u_s r^2}{\partial r} &= -\frac{n_s m u_{st} \nu_{st}}{m_t} 3k(T_s - T_t) \end{aligned}$$

For the case of no sources, no collisions and constant temperature, we may rewrite our momentum equation as for the plane parallel case, yielding

$$\left(u_s^2 - \frac{kT_s}{m_s} \right) \frac{\partial u_s}{\partial r} = u_s \left(-g + \frac{2kT_s}{m_s r} \right)$$

We may now *force* the left- and right-hand sides to vanish identically by requiring that $u_s^2 = kT/m$ at the point $r = \frac{2kT_s}{m_s g}$. This point is known as the ‘critical point’ of the solution of the flow velocity. As we add more parameters to our system of conservation equations (e.g. temperature, heat flow) we alter the nature of such singularities, removing some and adding others.¹⁰³

The system of equations given by (2.3.7)-(2.3.9) have excluded such physical processes as heat flow (conduction). As the conductivity (and hence the heat flow) in the upper

atmosphere is large, it may be that heat flow terms cannot simply be discarded from the energy equation. In fact, such terms may dominate the drift terms, and it was decided that a model which incorporated heat flow should be investigated. We choose to close the transport equations including the heat flow with phenomenologic laws rather than with the introduction of another, higher order transport equation. For example, the phenomenologic heat flow equation (Fourier's Law) may be written,^{98,104}

$$\mathbf{q}_s = -\lambda_{st}\nabla T_t - \lambda'_{ts}\nabla T_s + R_{st}(\mathbf{u}_s - \mathbf{u}_t) \quad (2.3.20)$$

where the various coefficients are detailed in Appendix B, and are strongly dependent on the form of the interaction between species in the gas mixture. It has been shown¹⁰⁵ that for a range of altitudes spanning the thermosphere and above, the Navier-Stokes (Fourier's Law) expression for the heat flow vector

$$\mathbf{q}_s = -\lambda_{st}\nabla T_t \quad (2.3.21)$$

may be used in place of equation (2.3.20). Inserting this term into the energy equation, and neglecting nonlinear flow terms in the momentum and energy equations as 'small', our system of equations now becomes

$$\frac{\partial}{\partial z}(n_s u_s) = N(z) \quad (2.3.22)$$

$$k \frac{\partial}{\partial z}(n_s T_s) = -n_s m_s g - n_s m_s \nu_{st} u_s \quad (2.3.23)$$

$$-\frac{\partial}{\partial z} \left(\lambda \frac{\partial T_s}{\partial z} \right) = -\frac{n_s \mu_{st} \nu_{st}}{m_t} 3k(T_s - T_t) + E(z) \quad (2.3.24)$$

Previously, we looked for a solution of the continuity equation for the density, given fixed temperature, for the case where the flux was given by the expression for a minor species diffusing in a background and neglecting thermal diffusion, that is equation (2.2.1),

$$\begin{aligned} \frac{\partial \phi_s}{\partial z} &= N(z) \\ \phi_s &= -D_{st} \left[\frac{\partial n_s}{\partial z} + \frac{n_s}{H_s} \right] \end{aligned} \quad (2.3.25)$$

where D_{st} is the mutual diffusion coefficient, and H_s is the scale height for species s .

It may be shown that when nonlinear terms in the momentum equation are ignored that our coupled system of equations (2.3.22)-(2.3.24) reduce to equation (2.3.25) for the case where the temperature of the diffusing species is constant with altitude. From equation (2.3.8), we have for this case that

$$u_s = -D_{st} \left[\frac{n'_s}{n_s} + \frac{1}{H_s} \right] \quad (2.3.26)$$

where the flux is defined as $\phi_s = n_s u_s$, and the mutual diffusion coefficient D_{st} and scale height H_s are defined as

$$D_{st} = \frac{kT_s}{m_s \nu_{st}}$$

$$H_s = \frac{kT_s}{m_s g}$$

respectively. Multiplying equation (2.3.26) by the density n_s yields the result of the previous section, equation (2.3.25). Similarly, from inspection it is seen that in the case where heat-flow is retained and nonlinear flow terms are discarded, that the momentum equation (2.3.23) also reduces to equation (2.3.26).

The continuity, momentum, and energy equations given by equations (2.3.7)-(2.3.9) form a coupled system of simultaneous differential equations. As both the scale height and diffusion coefficient are temperature dependent, they become altitude dependent if the temperature is not held constant. We considered solving the system using a simple 'stepping' finite differencing; that is, we rewrite the equations so that a simple first order forward-difference gave us the value of either the density, drift, or temperature at the next altitude step in terms of the values of the other parameters at the previous (current) altitude step. Thus, given a set of input values at the 'bottom' of the atmosphere, one could simply 'step' up in altitude to get the new values of each parameter, governed by the transport equations. The difficulty in this method appeared to be a

strong instability/discontinuity at an altitude where the drift velocity became equal to some equation-dependent 'sonic' speed, analogous to the singular point(s) in the solar wind momentum equation. It appears such singularities are inherent to the truncated transport equations used in transport theory,¹⁰³ and that there is some difficulty (in general) in the determination of the singular points and integrating/stepping a solution past them.

In recasting the equations with the inclusion of the heat flow (and exclusion of the nonlinear drift terms), we hoped to avoid the particular singularity which hampered the direct 'stepping' method. The equations given by (2.3.22)-(2.3.24) can be put in the non-dimensional form

$$\frac{\partial F}{\partial \xi} = \tilde{N}(\xi) \quad (2.3.27)$$

$$\frac{\partial N}{\partial \xi} = -\frac{N}{T} \frac{m_s g z_o}{k T_o} - \frac{F}{T} \frac{m_s u_o z_o \nu_{st}}{k T_o} - \frac{N}{T} V \quad (2.3.28)$$

$$\frac{\partial T}{\partial \xi} = V \quad (2.3.29)$$

$$\frac{\partial V}{\partial \xi} = \frac{3 k n_o z_o^2 \mu_{st} \nu_{st}}{\lambda(T) m_t} N (T - T_t / T_o) - \frac{E(z) z_o^2}{\lambda(T) T_o} - \frac{V^2}{\lambda(T)} T_o \frac{\partial \lambda}{\partial T_s} \quad (2.3.30)$$

where we have used

$$N = n_s / n_o$$

$$U = u_s / u_o$$

$$T = T_s / T_o$$

$$\xi = z / z_o$$

$$F = N \cdot U$$

$$V = \frac{\partial T}{\partial \xi}$$

$$\tilde{N} = \frac{N(z) z_o}{u_o n_o}$$

$$\lambda(T_s) = C T_s^\beta$$

We now have the four unknowns F, N, T, V , where $F \equiv N * U$. It should be noted that we have chosen to solve for F , and not U as it simplifies the form of the equations by eliminating the appearance of derivatives on the RHS of equation (2.3.27).

The set of 'heat-flow' equations was integrated using a standard fourth-order Runge Kutta integrator, with a set of initial conditions specified at the lower boundary only. The lower boundary altitude was selected such that we could assume that there was no production of hot atoms; hence, N, U, F at the lower boundary were set to zero. The temperature T was set equal to the background temperature. The source terms are the same as for the previous coupled transport equation case. When the temperature was set to a constant it was found that the system yielded results for the density profile that were in rough agreement with those found by direct integration of the diffusion equation (as for the constant temperature model results earlier in this chapter).

Transport models based on moment equations derived from the Boltzmann equation are regularly used to address flow problems in planetary atmospheres and in the solar wind. These transport models consist of truncated sets of coupled differential equations involving moments of the distribution function of the flowing species. As the number of moments retained in the expansion increases, large departures from equilibrium for the distribution function can be treated more accurately. However, the choice of the level of truncation also determines the number of singular points in the system of equations. These points are of importance in both steady-state and time-dependent systems.¹⁰³ While some of these singular points are well known (e.g the sonic point in the 'solar wind' equations¹⁰⁰), in general they must be investigated uniquely for each particular system. These singular points cannot be integrated over using standard methods, and require special attention, which again must be applied on a system-by-system basis.¹⁰³ For simpler systems, it may be possible to easily identify the singular points (e.g. equation (2.3.19)), but for more complex system such a simple treatment does not necessarily

stabilize the numerical system. It is clear from the behaviour observed when numerically integrating equations, although the nature of the singularity/singularities and their treatment is not certain.

2.4 The Linear Boltzmann Equation Model

The problem of thermalization of translationally energetic particles in a moderator of atomic or molecular constituents is a well known problem in nuclear physics.¹⁰⁶ An example is the problem of the moderation of high energy neutrons resulting from fission reactions. Energetic neutrons are created with a narrow range of initial energies, and diffuse through a moderator, losing energy through collisions with the moderator nuclei. If the moderator is composed of nuclei of moderate to high mass, the average spread of final energies between individual neutrons after some number of collisions is relatively small, and it is possible to characterize the movement of a large number of neutrons through the moderator by means of some average velocity. The loss of energy to the moderator is then viewed as a continuous process, since it is assumed that the average energy (velocity) change due to collisions with moderator nuclei at any given time is minimal. The approximation of thermalization as a continuous process is known as the Continuous Slowing Down Approximation, or CSDA. Application of the CSDA is not limited to neutron moderation; its validity has been explored in electron degradation problems as well.^{107,108}

We may model the diffusion of hot oxygen atoms resulting from the dissociative recombination of O_2^+ ions in a manner similar to the CSDA for neutrons in a moderator. The height distribution of the hot oxygen atoms and their thermalization through collisions with the ambient background atmosphere is analagous to the 'depth of penetration'

and rate of thermalization of energetic neutrons moving through a moderator. The density and temperature of the hot oxygen atoms may be self-consistently calculated as moments of the distribution function of the hot oxygen atoms. The hot oxygen distribution function is given by the Boltzmann equation, equation (1.4.1). In the current work, we choose to neglect external force fields (such as magnetic and gravitational fields). In addition, with the CSDA the velocity appearing in the second (or diffusion) term on the left-hand side of equation 1.4.1) is assumed to be constant, with a value equal to the average speed of the hot atoms. The time and diffusion terms may thus be combined to yield an equation of the form

$$\frac{\partial f}{\partial t} = J[f] + S \quad (2.4.1)$$

where S is the (steady) source of the translationally energetic atoms, J is the Boltzmann collision operator, given by equation (1.4.2), describing elastic collisions between the hot and (single) background species, and $f = f(\mathbf{c}, t)$ is the velocity distribution function for the hot species. Equation (2.4.1) is a local model for the time evolution of the distribution function at some (fixed) altitude. We have assumed that the moderating background gas is in equilibrium and is distributed with a Maxwellian distribution of velocities. In applications of the CSDA to nuclear physics, hot particle energies are of the order of keV-MeV, and the distribution function of the hot atoms remains sharply peaked about the average velocity. For the present case, the hot particle energies are of the order of eV, and so we expect that there will be some broadening of the hot atom distribution function as a result of collisions with the background.

The Boltzmann equation given by equation (2.4.1) yields the hot oxygen distribution function as a function of time, at some particular altitude. This altitude is a parameter in the model, and dictates the strength of the source of hot oxygen atoms, the background densities, and other physical parameters for the model. If we assume, as in the CSDA,

that there is limited thermalization of the hot oxygen atoms and that their distribution function remains relatively narrow, then the average velocity of the hot oxygen atoms is approximately constant. Thus, the time dependent distribution function may be transformed to an 'altitude dependent' distribution function through the linear transformation given by

$$z = v_{hot} t \quad (2.4.2)$$

where v_{hot} is an average velocity characterizing the motion of the hot atoms. With this transformation, we may consider the time variation of the distribution function as an altitude variation. However, since the CSDA requires that the hot atom distribution function not thermalize (or broaden) 'too much', we are limited to altitudes 'close' to the true altitude chosen to parameterize the local Boltzmann equation. In order to extend the model to yield the altitude distribution of hot atom densities high into the exosphere, we adopt the method used in many collisionless models of the exosphere,¹⁶ detailed shortly.

The form of the hot oxygen source distribution is largely unknown,^{6,8} and is assumed to be a narrow Gaussian centered about the O_2^+ dissociative recombination energy of 2.5 eV per atom. The altitude dependent source strength is given by equation (2.1.2). The normalization of the source function is chosen equal to the source strength. The initial ($t = 0$) hot atom distribution function is set equal to a Gaussian of the same form as the source Gaussian, and is normalized to 1. With our steady source of hot atoms, we expect that any final steady state solution should exhibit a departure from Maxwellian.

We may rewrite the collision operator J in equation (2.4.1) in its kernel representation,^{109,110} yielding

$$\frac{\partial f}{\partial t} = \int_0^\infty dx' \{K(x, x')f(x', t)\} - Z(x)f(x, t) + S(x) \quad (2.4.3)$$

where $x = m_{hot}c^2/2kT_b$ is the hot atom energy normalized to the background energy, and $K(x, x')$ is the non-symmetric collision kernel (that is, $K(x', x) \neq K(x, x')$). The

(elastic) collision frequency between hot atoms and the background, $Z(x)$, is given by

$$Z(x) = \int_0^\infty K(x, x') dx' \quad (2.4.4)$$

or by

$$Z(x) \equiv \iint f \sigma(g, \Omega) g d\Omega d\mathbf{c}$$

in order to ensure that detailed-balance or conservation of particle number is satisfied.

Integrating equation (2.4.1) over x , we find that

$$\frac{\partial n}{\partial t} \equiv S \quad (2.4.5)$$

where

$$\int_0^\infty S(x) dx \equiv S$$

Integration of equation (2.4.5) yields

$$n(t) = S t \quad (2.4.6)$$

This model gives a density that is linearly increasing with time, with a rate of increase directly proportional to the strength of the source at the altitude of interest. The density may also be calculated directly from the normalization of the velocity distribution function,

$$n(t) = \int_0^\infty f(x, t) dx \quad (2.4.7)$$

Similarly, it may be shown that the average reduced hot atom energy is given by

$$E(t) = \int_0^\infty x f(x, t) dx \quad (2.4.8)$$

2.4.1 Discretization Procedure and Solution

We solve the Boltzmann equation using the quadrature discretization method (QDM), the basis of which is described in detail elsewhere¹¹¹. The method involves the determination of the velocity distribution function, $f(y)$, at a discrete grid of points, $\{y_i\}$. The grid points correspond to a set of quadrature points which are the roots of a set of orthogonal polynomials based on the weight function $w(y) = y^2 \exp[-y^2]$. We may thus write

$$\int_0^\infty e^{-y^2} y^2 g(y) dy = \sum_{m=1}^N w_m g(y_m)$$

or

$$\int_0^\infty g(y) dy = \sum_{m=1}^N W_m g(y_m)$$

where

$$W_m = w_m e^{y_m^2} / y_m^2$$

We rewrite equation (2.4.3) as a function of reduced speed $y \equiv \sqrt{x}$, noting the change in the volume element from dx to $2y dy$, and then apply our QDM discretization to yield

$$\frac{\partial f_i(y_l^2, t)}{\partial t} = \sum_{m=1}^N W_m 2y_m K(y_m^2, y_l^2) f_i(y_l^2, t) - Z(y^2) f_i(y_l^2, t) + S(y_l^2) \quad (2.4.9)$$

If the grid of points y_l at which the distribution function is evaluated are chosen to coincide with our grid of speed points y_m then equation (2.4.9) is reduced to a set of linear equations which may be represented in vector form as

$$\frac{\partial \mathbf{f}}{\partial t} = \mathbf{M} \cdot \mathbf{f} + \mathbf{S} \quad (2.4.10)$$

where

$$M_{m,l} = W_m 2y_m K^{ns}(y_m^2, y_l^2) - Z(y_l) \delta(y_m - y_l)$$

For a hard sphere collision model, $K^{ns}(x, x')$ is the well known^{109,112} non-symmetric Wigner-Wilkins kernel,

$$K^{ns}(x, x') = \frac{1}{2} A Q^2 \sqrt{\frac{\pi}{x}} \{ \text{erf}(Q\sqrt{x'} + R\sqrt{x}) + e^{x-x'} \text{erf}(R\sqrt{x'} + Q\sqrt{x}) \\ \pm [\text{erf}(Q\sqrt{x'} - R\sqrt{x}) + e^{x-x'} \text{erf}(R\sqrt{x'} - Q\sqrt{x})] \} \quad (2.4.11)$$

where the $+$ ($-$) sign refers to $x > x'$ ($x < x'$), and

$$Q \equiv \frac{1}{2} \left[\frac{1}{\sqrt{\gamma}} + \sqrt{\gamma} \right] \\ R \equiv \frac{1}{2} \left[\frac{1}{\sqrt{\gamma}} - \sqrt{\gamma} \right] \\ \gamma \equiv m_{back}/m_{hot} \\ A \equiv \sigma_{tot}^{hs} n_{back} \sqrt{\frac{2kT_{back}}{\pi m_{hot}}}$$

with $\text{erf}(x)$ the standard error function. It can be shown (see Appendix B.2) that the non-symmetric kernel in equation (2.4.11) may be defined in terms of a symmetric kernel $K^s(x, x')$,

$$K^{ns}(x, x') = \sqrt{\frac{(x')^{\frac{1}{2}}}{x^{\frac{1}{2}}}} e^{x-x'} K^s(x, x') \quad (2.4.12)$$

Transforming to speed, we then have

$$K^{ns}(y_m^2, y_l^2) = \sqrt{\frac{y_m}{y_l}} e^{y_l^2 - y_m^2} K^s(y_m^2, y_l^2) \quad (2.4.13)$$

To complete the symmetrization of \mathbf{M} requires that we make a few further changes to the form of equation (2.4.10). These are detailed in Appendix B.3, with the result that equation (2.4.10) becomes

$$\frac{\partial \hat{\mathbf{f}}}{\partial \tau} = \hat{\mathbf{B}} \cdot \hat{\mathbf{f}} + \tilde{\mathbf{S}} \quad (2.4.14)$$

where

$$\tilde{\mathbf{S}} \equiv \sqrt{\frac{W_i}{e^{-y_i^2}}} \hat{\mathbf{S}}$$

and $\hat{\mathbf{B}}$ is a symmetric matrix defined by equations (B.3.11) and (B.3.13). In equation (2.4.14), we have defined a dimensionless 'time'

$$\tau \equiv At$$

and where

$$\hat{f}_i = \sqrt{\frac{W_i}{e^{-y_i^2}}} f_i \quad (2.4.15)$$

The solution of equation (2.4.14) is relatively straightforward, and is detailed in Appendix B.4. The final result is

$$\hat{f}_i(\tau) = U_{i,1} [F_1(0) + Q_1\tau] + \sum_{j=2}^N U_{i,j} \left(F_j(0) e^{-\lambda_j\tau} + Q_j \frac{[1 - e^{-\lambda_j\tau}]}{\lambda_j} \right) \quad (2.4.16)$$

where

$$\mathbf{U}^{-1} = \mathbf{U}^T$$

$$\mathbf{Q} = \mathbf{U}^T \tilde{\mathbf{S}}$$

$$\lambda_j \geq 0$$

$$F_i(\tau) = \mathbf{U}^T \hat{f}_i(\tau)$$

and equation (2.4.15) is used to transform between \hat{f} and f .

As mentioned previously, to determine the altitude density profile, as given by equations (2.4.17)-(2.4.19), we require the Maxwellian distribution function for the hot atoms at the exobase level. Hence, we need to determine the change in the distribution function between the altitude of production of the hot atoms and the exobase. To accomplish this, we make a transformation from time to altitude in equation (2.4.16). An initial altitude near the production peak and below the exobase is selected to parameterize the local Boltzmann equation. Equation (2.4.16) is then used to find the time dependent velocity distribution function for the hot atoms produced at this altitude. The timescale

over which we follow the development of the distribution function is dependent on the distance between the production altitude and the exobase (that is, we assume that using our transformation from time to altitude approximates following hot atoms from their production at some initial altitude to the exobase altitude). The distribution function at the exobase level is fitted to a Maxwellian distribution function parameterized by some density and temperature, which are used to calculate the density profile as a function of altitude above the exobase as follows.

In the absence of collisions, particles moving through an exosphere follow trajectories determined by the direction and magnitude of their velocities and the strength of the gravitational field. Based on the various types of possible trajectories, classes of particles may be defined. Of interest in our particular case are those classes of particles which can give rise to an extended population of hot atoms. The exospheric density profile is calculated by partial integration of the hot atom Maxwellian distribution function at the exobase. The integration is carried out over the permitted ranges of velocity and angle corresponding to those particle classes which lead to extended hot atom populations. The details of the particle classifications and the calculation of the densities is discussed by Chamberlain^{16,43} and reviewed in detail by Fahr and Shizgal,¹ and is detailed in Appendix A. The resulting expressions for the densities of the various exospheric components are

$$n_b = \frac{2}{\sqrt{\pi}} n_{bar} \left\{ \gamma(3/2, \lambda_c y) - \sqrt{1-y^2} \exp \left[\frac{-\lambda_c y^2}{1+y} \right] \gamma(3/2, \lambda_c y/(1+y)) \right\} \quad (2.4.17)$$

$$n_e = \frac{n_{bar}}{\sqrt{\pi}} \left\{ [\Gamma(3/2) - \gamma(3/2, \lambda_c y)] - \sqrt{1-y^2} \exp \left[\frac{-\lambda_c y^2}{1+y} \right] [\Gamma(3/2) - \gamma(3/2, \lambda_c y/(1+y))] \right\} \quad (2.4.18)$$

$$n_{bs} = \frac{2}{\sqrt{\pi}} n_{bar} \gamma(3/2, \lambda_c y) \quad (2.4.19)$$

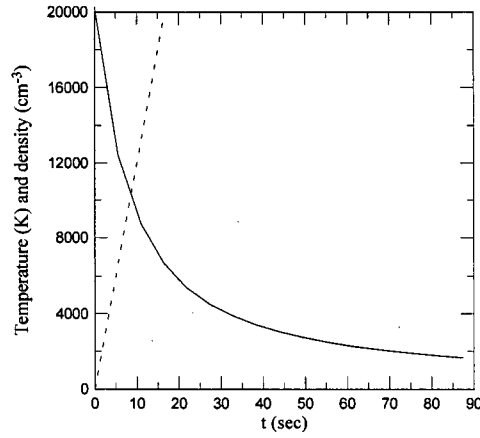
where $y = r_c/r$, the ratio of exobase position to the exospheric radial position being considered, $\lambda_c = E_{esc}/(kT_c)$ is the exobase escape parameter given previously by equation

(1.2.10), $n_{bar} = n_c \exp[-\lambda_c(1 - y)]$ is the barometric density distribution given previously by equation (1.2.4), and Γ and γ are the standard gamma and incomplete gamma functions, respectively. The subscripts b , s , e refer to ballistic, satellite, and escaping components, respectively.

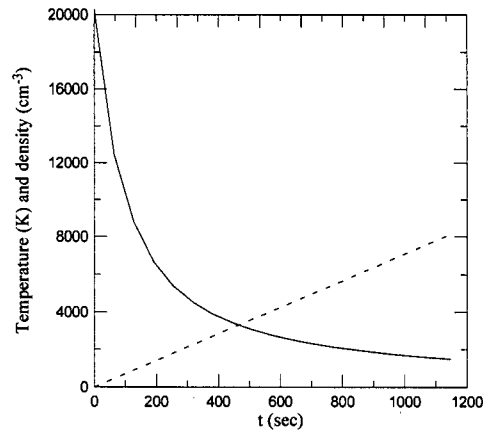
In order to calculate a time dependent hot oxygen density and temperature, we solve for the hot oxygen distribution function, from equation (2.4.16), and then take the appropriate moments of the distribution function (equations (2.4.7) and (2.4.8), respectively). The integrations are done numerically using the QDM points and weights mentioned previously. A hard sphere (total) collision cross section of $2.0 \times 10^{-15} \text{ cm}^2$ is used. These calculations are carried out for both Venus and Mars. Figure 2.11 shows the time dependent hot oxygen density and temperature for Mars, as calculated for two different altitudes, 150 and 220 km. The time dependent hot oxygen density and temperature for Venus, as calculated for the altitudes of 150 and 180 km, are shown in Figure 2.12.

For both cases, we note that the density is a linear function of time, as predicted by equation (2.4.6) for a steady source. We also note the sharp exponential decay of the temperature from the initial value of 2.5 eV toward the background oxygen value of 180 K and 280 K for Mars and Venus, respectively. In both cases, the rate of decrease of the temperature of the hot atoms is greater for the lower altitude. Physically, this conforms to our expectation that the background atoms thermalize the hot atoms via elastic collisions much more quickly at lower altitudes, where the background density is higher. Note that while the initial drop in temperature for the hot oxygen atoms is large, the temperature does not fully equilibrate with the background because energy is continually added to the hot oxygen population via the steady dissociative recombination source.

The distribution functions are shown at both altitudes for several times in Figure 2.13 for Mars and Figure 2.14 for Venus. The total number of particles will grow (linearly)

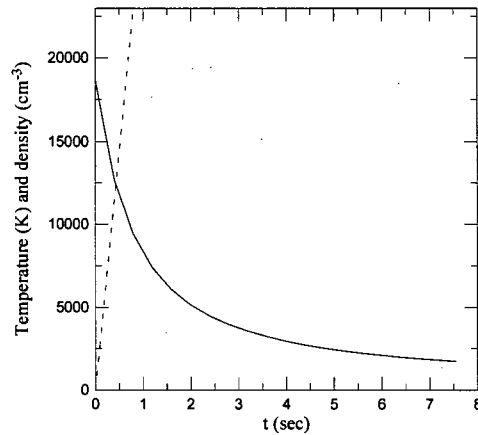


(a)

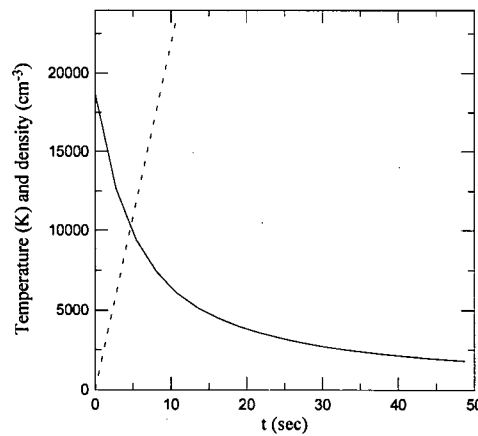


(b)

Figure 2.11: Time dependence of hot oxygen density and temperature on Mars. The graphs are for altitudes of (a) 150 km and (b) 220 km. The time t is calculated from $t = \tau/A$, where $A \equiv \pi d^2 n_{back} \sqrt{\frac{2kT_{back}}{\pi m_{hot}}}$ is altitude dependent. The value of A and the source strength are (a) 0.0183 & 1199.2 and (b) 0.00157 & 7.08, in units of sec^{-1} and $\text{cm}^{-3} \text{sec}^{-1}$, respectively. The solid and dashed curves indicate the time dependent temperature and density, respectively.



(a)



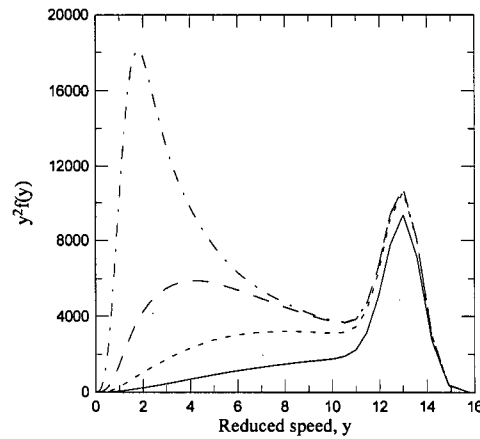
(b)

Figure 2.12: Time dependence of hot oxygen density and temperature on Venus. The graphs are for altitudes of (a) 150 km and (b) 180 km. The time t is calculated from $t = \tau/A$, where $A \equiv \pi d^2 n_{back} \sqrt{\frac{2kT_{back}}{\pi m_{hot}}}$ is altitude dependent. The value of A and the source strength are (a) 0.25 & 28747.7 and (b) 0.037 & 2187.5, in units of sec^{-1} and $\text{cm}^{-3} \text{sec}^{-1}$, respectively. The solid and dashed curves indicate the time dependent temperature and density, respectively.

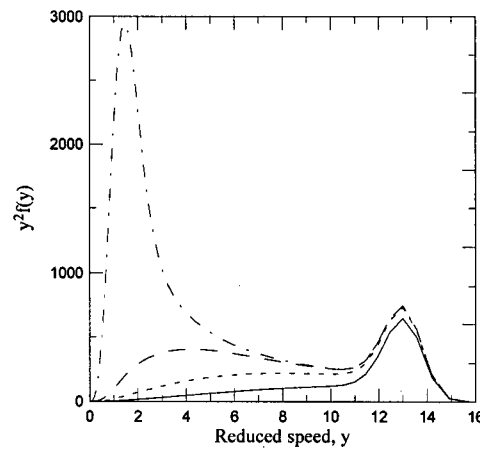
with time due to the steady hot oxygen source. The much higher O_2^+ density on Venus results in a significantly higher rate of production of hot oxygen particles; however, the background thermal oxygen density is also larger, and so thermalization is also increased. The distribution function near the equilibrium (background) energy grows rapidly on both planets, once production and thermalization of hot oxygen atoms reaches steady-state. The steady-state distribution function will thus be bi-modal, with a peak about the production energy and a peak about the thermal energy. The degradation in energy of atoms from their initial hot production energy to a peak about the thermal (background) energy is clearly visible. The shape of the distribution function as it evolves in time is similar for the two altitudes illustrated. However, the rate of evolution of the hot oxygen distribution function and the number density of hot oxygen atoms (as given by the area under the distribution function curve) varies significantly between the two altitudes for both planets, as is clear from Figures 2.13 and 2.14.

Previous workers^{11,7,6,33,8} employed Monte Carlo simulations and their energy distribution functions are plotted as histograms for energy 'bins' of discrete widths of 0.05 eV. We compare with their results by taking the value of our distribution (as a function of energy) at the midpoint of a given energy bin and multiplying by the bin width. This yields the hot atom density per bin width at the exobase, as shown in Figures 2.15 and 2.16. It should be noted that a residual 'peak' remains at the dissociation energy of the hot oxygen, 2.5 eV. This is because we consider a constant source of hot atoms.

A Maxwellian (or sum of Maxwellians) is fitted to the energy distribution, yielding an exobase temperature and density. The best fit for the altitude of 150 km for both Mars and Venus is shown in Figures 2.17 and 2.18. For Mars, the fit is comprised of two Maxwellians, a cold one with density $3\,500\text{ cm}^{-3}$ and temperature 800 K, and a hot one with density 800 cm^{-3} and temperature 7 500 K. For Venus, the fit is also comprised of two Maxwellians, a cold one with density $10\,000\text{ cm}^{-3}$ and temperature 800 K, and a

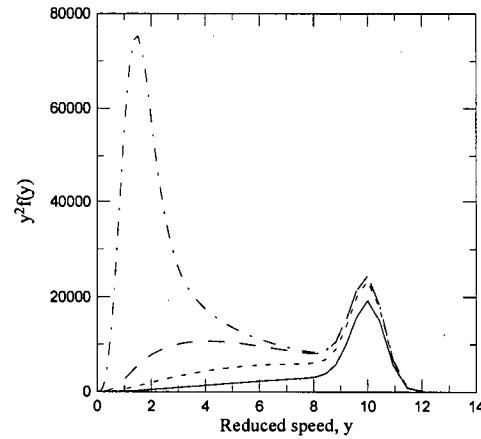


(a)

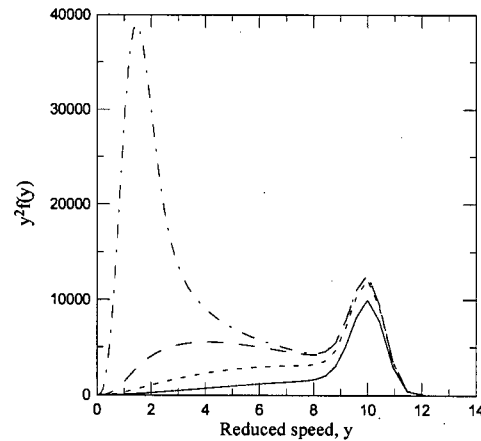


(b)

Figure 2.13: Time evolution of the Martian hot oxygen distribution function from an initial Gaussian distribution at 2.5 eV due to a steady source at that same point. The graphs are for altitudes of (a) 150 km and (b) 220 km. The solid, short dashed, long dashed, and dot-dashed curves correspond to dimensionless times of $\tau = 0.1, 0.2, 0.4$, and 1.0 in (a) and $\tau = 0.1, 0.2, 0.4$, and 1.9 in (b). The time t is calculated as described in Figure 2.11.

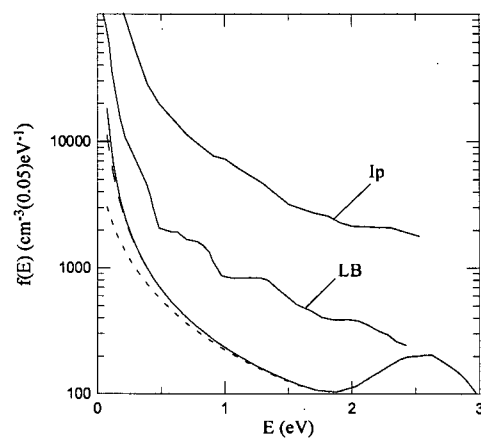


(a)

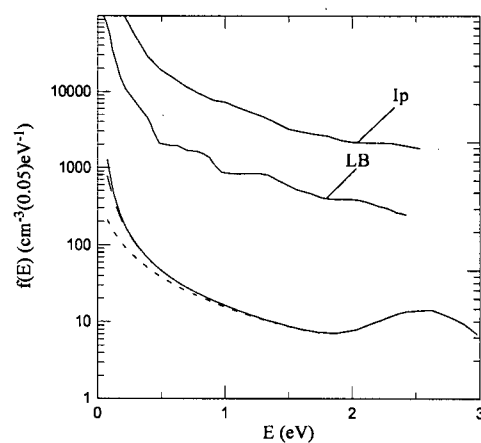


(b)

Figure 2.14: Time evolution of the Venusian hot oxygen distribution function from an initial Gaussian distribution at 2.5 eV due to a steady source at that same point. The graphs are for altitudes of (a) 150 km and (b) 180 km. The solid, short dashed, long dashed, and dot-dashed curves correspond to dimensionless times of $\tau = 0.1, 0.2, 0.4$, and 1.0 in (a) and $\tau = 0.1, 0.2, 0.4$, and 1.9 in (b). The time t is calculated as described in Figure 2.12.

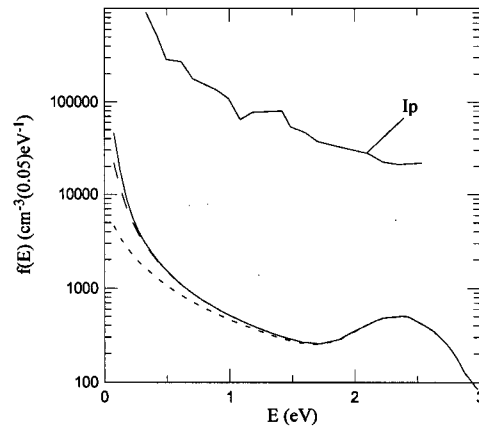


(a)

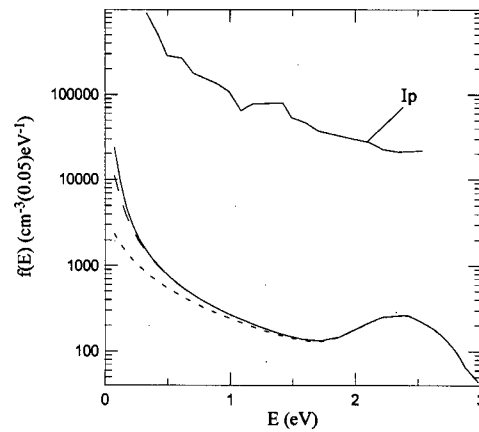


(b)

Figure 2.15: Energy distribution of hot oxygen on Mars. The graphs are for altitudes of (a) 150 km and (b) 220 km. The dotted, dashed, and solid curves are for dimensionless times $\tau = 0.4, 1.0$, and 1.9 , respectively. The results of Ip⁶ and Lammer and Bauer⁸ are shown for comparison.



(a)



(b)

Figure 2.16: Energy distribution of hot oxygen on Venus. The graphs are for altitudes of (a) 150 km and (b) 180 km. The dotted, dashed, and solid curves are for dimensionless times $\tau = 0.4, 1.0$, and 1.9 , respectively. The result of I_p^6 is shown for comparison.

hot one with density $1\,200\,\text{cm}^{-3}$ and temperature $7\,500\,\text{K}$. We use equation (2.4.17) to calculate the hot atom density profile for altitudes above the exobase.

The results for the ballistic component are shown in Figure 2.19 for Mars, together with the results of Ip⁶ and Lammer and Bauer,⁸ and in Figure 2.20 for Venus, together with the results of Ip⁶ and Nagy and Cravens.⁷

The difference in predicted hot atom densities between Venus and Mars originates in the escape parameter, λ_c , which is the controlling parameter in the collisionless exospheric model, equations (2.4.17)-(2.4.19). From the Maxwellian fits to the energy distributions, we extracted a hot component temperatures of $7500\,\text{K}$ for hot oxygen on Venus and Mars, respectively. Referring to Table 1.1 for escape energies for oxygen from Venus and Mars, we thus find that the escape parameter, $\lambda_c = E_{esc}/(kT_c)$, is approximately 13.3 for Venus and 3.0 for Mars. This is crucial since the exospheric density profile is approximately given as a barometric distribution with an exponential decay parameterized by λ_c . Thus, even though the hot oxygen density on Venus is higher at the exobase level, it decays much more rapidly with altitude due to the much higher escape parameter, yielding the observed discrepancy between predicted hot oxygen densities for the two planets. This discrepancy would be expected to grow significantly larger at higher altitudes.

For both Mars and Venus there is a discrepancy between the currently calculated exospheric densities and the profiles of previously published results. The discrepancy is on the order of 2-10 times smaller than other densities for Mars, and of the order of 2-30 times smaller for Venus. It should be noted, however, that order of magnitude differences exist between models of previous workers. In order to assess possible reasons for the discrepancies between the current model results for the hot oxygen densities and those of previous workers, it is first important to compare and contrast the assumptions and input parameters for each. The input density profiles are identical for each, as is the choice and magnitude of a hard sphere collision cross section between the hot oxygen atoms

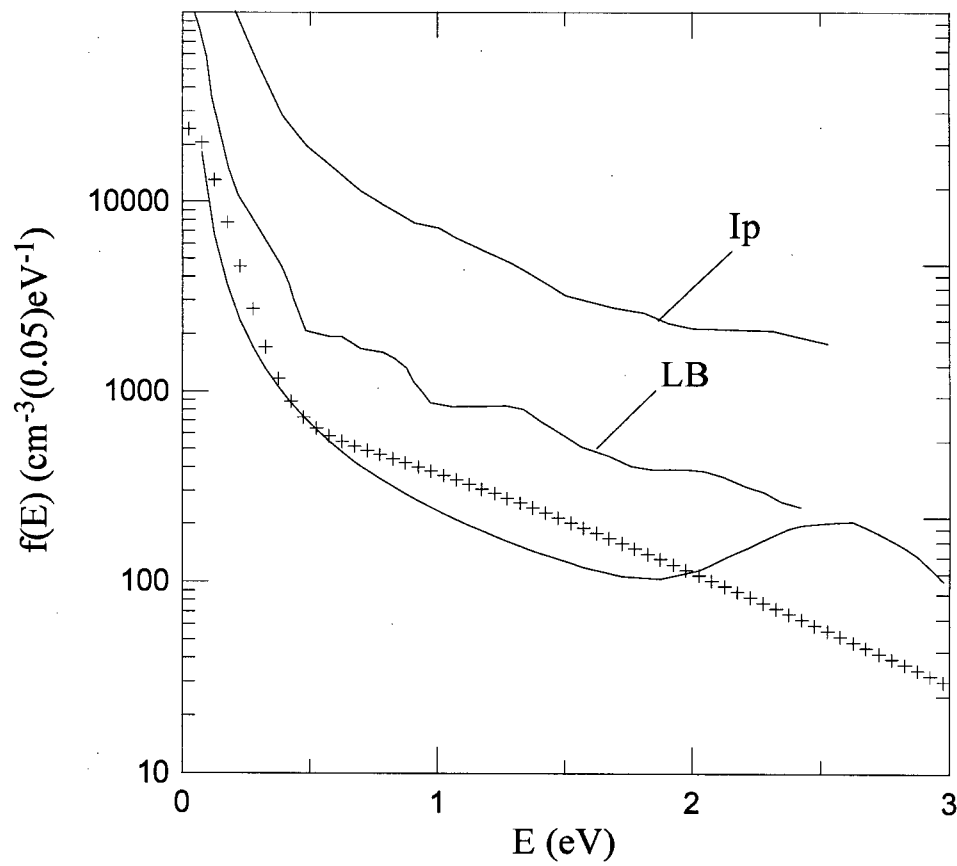


Figure 2.17: Maxwellian fit to the hot oxygen energy distribution function at 150 km. The fit, indicated by the plus symbols, is composed of two separate Maxwellians, a cold one with density $3.5 \times 10^5 \text{ cm}^{-3}$ and temperature 800 K, and a hot one with density $8 \times 10^4 \text{ cm}^{-3}$ and temperature 7500 K. The results of Ip⁶ and Lammer and Bauer⁸ are shown for comparison.

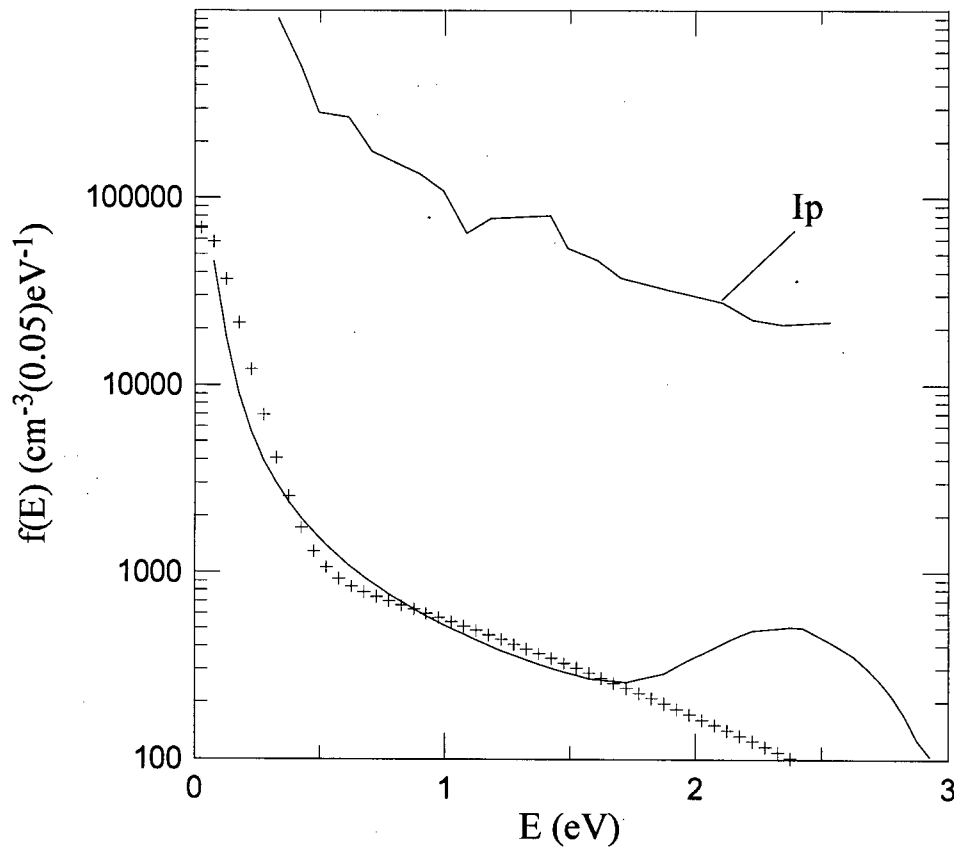


Figure 2.18: Maxwellian fit to the Venusian hot oxygen energy distribution function at 150 km. The fit, indicated by the plus symbols, is composed of two separate Maxwellians, a cold one with density $10\,000\text{ cm}^{-3}$ and temperature 800 K, and a hot one with density $1\,200\text{ cm}^{-3}$ and temperature 7 500 K. The result of Ip^6 is shown for comparison.

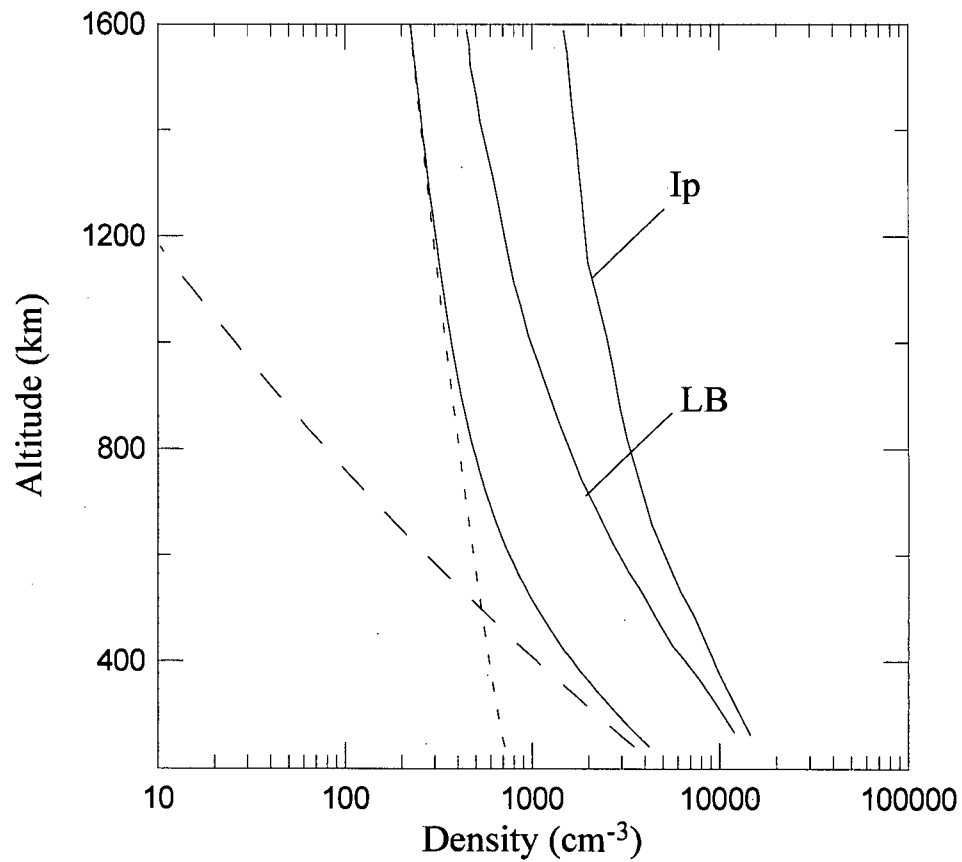


Figure 2.19: The hot oxygen density profile for Mars derived from the ballistic component calculated from the Maxwellian fits to the energy distribution function at 150 km. The densities resulting from the 'hot' and 'cold' Maxwellian fits are given by the short and long dashed curves, and their sum, the total density of the fit, is given by the solid curve. See Figure 2.17 for details on the fit parameters. The results of I_p^6 (IP) and Lammer and Bauer⁸ (LB) are shown for comparison.

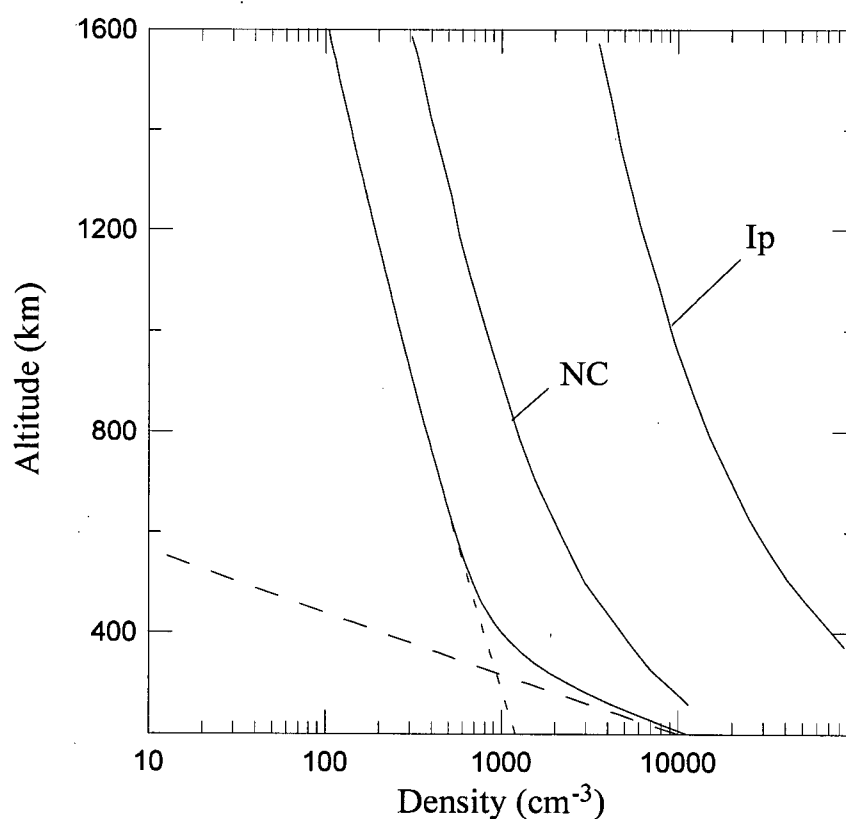


Figure 2.20: The hot oxygen density profile for Venus derived from the ballistic component calculated from the Maxwellian fits to the energy distribution function at 150 km. The densities resulting from the 'hot' and 'cold' Maxwellian fits are given by the short and long dashed curves, and their sum, the total density of the fit, is given by the solid curve. See Figure 2.18 for details on the fit parameters. The results of Ip^6 (IP) and Nagy and Cravens^{7,32} (NC) are shown for comparison.

and the background. The exobase altitudes are identical. The Monte Carlo and present models both approximate the source as fixed at a single altitude, with a dissociation energy of 2.5 eV available to each hot product oxygen atom. The current model assumes a Gaussian spread of dissociation energies about the dissociation energy while the Monte Carlo work utilizes a delta function at the dissociation energy. The current model utilizes the Boltzmann collision operator to account for thermalization of the hot oxygen atoms by the thermal background; in the Monte Carlo work, collisions and the amount of energy exchanged between the hot atom and the background per collision are treated as stochastic processes, and are calculated using random number generators and altitude dependent background density profiles. In neither the work of Ip⁶ or Lammer and Bauer⁸ is there a detailed description of the statistics used in generation of their final energy density distribution functions and densities, so it is not possible to comment further on the specifics of their simulations.

In the current model, as well as in the two stream models of Nagy and Cravens⁷ and Monte Carlo models of Ip⁶ and Lammer and Bauer,⁸ the exospheric density profile for the hot oxygen atoms is assumed to be given by the ballistic component of the collisionless exospheric density model, equation (2.4.17). The density and temperature of the hot oxygen distribution function fit to a Maxwellian distribution at the exobase level is required in order to calculate this ballistic density profile. Aside from the present work, only Lammer and Bauer explicitly indicate fitting the exobase distribution function with a Maxwellian distribution in order to extract an altitude density profile. Their work is also the only work to give the exobase altitude density and temperature used as input for the collisionless ballistic density profile, citing a two component fit consisting of a hot component ($2\,000\text{ cm}^{-3}$ and temperature $7\,500\text{ K}$) and a cold component ($15\,000\text{ cm}^{-3}$ and temperature 850 K).

The current model calculates the collisionless exospheric densities using equation

(2.4.17). The accuracy of this formulation was checked numerically for Earth against previously published results in Fahr and Shizgal¹ and Chamberlain,¹⁶ and excellent agreement was attained. We were also able to reproduce the results of Lammer and Bauer⁸ for the Martian hot oxygen density profile using their exobase density and temperature fit parameters. It was thus concluded that the calculation of the exospheric densities from equation (2.4.17) was not in error in the current work.

The most probable remaining source of error is the collision model used to describe the thermalization of the hot oxygen atoms. The probabilistic approach of Monte Carlo is replaced in our kinetic theory method by the time dependent Boltzmann equation. We generate the exobase altitude energy distribution function without need for fitting. The model calculates the time dependent variation of the velocity distribution function at a *single*, fixed altitude and uses the linear transformation given by equation (2.4.2) to approximate altitude variation of the distribution function. The effect of thermalization is exaggerated since the background density remains fixed at the chosen altitude, ignoring the decrease in background density with altitude. While the Boltzmann equation model does account for collisional thermalization of the hot atoms with the background it does not properly describe diffusive transport of hot atoms over the range of altitudes over which production is non-negligible. The true exobase velocity distribution function of the hot atoms includes the effect of hot atom production from a range of altitudes. In addition, since our transformation between time and altitude is linear, with a proportionality constant given by the (constant) average velocity, we require that the hot atoms not thermalize 'too much' (and thus change their average velocity). This limits the model to regions 'close' (in a mean free path sense) to the exobase. As seen from Figure 2.11 for Mars, and especially in Figure 2.12 for Venus, even with these limitations the thermalization (and thus change in the average velocity) of the hot atoms is not negligible, and so the simple linear transform of equation (2.4.2) does not adequately describe the

diffusion process of the hot oxygen atoms.

A significant approximation in both this model and in the Monte Carlo simulations is that the atmosphere above the exobase level is collisionless, and that equations (2.4.17)-(2.4.19) adequately describe the altitude distribution of hot atom densities in the exosphere. The validity of this approximation is examined in the following section by a simple comparison of timescales describing the rate at which diffusion and thermalization proceed.

2.5 Collisional and Diffusional Timescales

In order for the hot atoms to form a planetary corona, they must travel from their place of creation (generally low in the atmosphere) into the upper parts of the exosphere. This requires transport from a generally collisional regime near the production peak to a (nearly) collisionless one in the upper exosphere. Diffusion acts to transport hot atoms away from the source region while collisions thermalize the hot atoms.

The relative strength of these processes can be compared by examining timescales representative of the speed at which they take place. A collisional timescale is given by

$$\tau_{coll}(z) = 1/\nu \quad (2.5.1)$$

where ν , the hot atom-background collision frequency, is defined previously in equation (2.1.5). A measure of the 'diffusive timescale' is given by

$$\tau_{diff}(z) = H^2(z)/D(z) \quad (2.5.2)$$

As ν increases, $\tau_{coll}(z)$ decreases, but $D(z)$ decreases, and $\tau_{diff}(z)$ increases. An example of how these processes compare is given in Table 2.3 for Mars and Table 2.4 for Venus. The first column of the tables shows the altitude, the second and third the timescales

Altitude (km)	τ_{coll} (sec)	τ_{diff} (sec)	τ_{coll}/τ_{diff}
150.0	3.94e+00	9.64e+04	4.08e-05
200.0	2.49e+01	1.61e+04	1.55e-03
250.0	1.28e+02	3.30e+03	3.90e-02
300.0	7.31e+02	6.12e+02	1.19e+00
350.0	4.16e+03	1.14e+02	3.66e+01
400.0	2.36e+04	2.11e+01	1.12e+03
450.0	1.34e+05	3.90e+00	3.45e+04
500.0	7.65e+05	7.23e-01	1.06e+06
550.0	4.35e+06	1.34e-01	3.25e+07
600.0	2.47e+07	2.47e-02	1.00e+09
650.0	1.41e+08	4.57e-03	3.08e+10
700.0	8.01e+08	8.44e-04	9.49e+11
750.0	4.55e+09	1.56e-04	2.92e+13
800.0	2.59e+10	2.87e-05	9.02e+14
850.0	1.47e+11	5.29e-06	2.78e+16
900.0	8.38e+11	9.75e-07	8.59e+17
950.0	4.77e+12	1.80e-07	2.65e+19

Table 2.3: Diffusional versus collisional timescales for Mars. The values are for 8500 K oxygen diffusing through a background of 180 K oxygen. A hard sphere (total) collision cross section of 2.0×10^{-15} cm² is used. The Martian exobase for oxygen is located at approximately 250 km.

for collisions and diffusion, respectively, and the final column shows the ratio of the timescales.

From the tables it is clear that at low altitudes collisions are extremely important in altering the hot atom distribution before there is much chance to diffuse from the source region. For both Mars and Venus, the ratio of the timescales for collisions is less than or equal to the the diffusional timescale for altitudes exceeding the exobase level. We would thus expect that thermalization of the hot atom population would continue beyond the exobase level, and that the final hot atom energy distribution should be somewhat more thermalized than the collisionless exosphere models would predict.

Altitude (km)	τ_{coll} (sec)	τ_{diff} (sec)	τ_{coll}/τ_{diff}
150.0	3.55e-01	1.74e+05	2.03e-06
200.0	7.75e+00	8.25e+03	9.40e-04
250.0	1.34e+02	4.93e+02	2.71e-01
300.0	2.00e+03	3.41e+01	5.86e+01
350.0	3.03e+04	2.32e+00	1.30e+04
400.0	4.59e+05	1.58e-01	2.91e+06
450.0	6.96e+06	1.07e-02	6.47e+08
500.0	1.05e+08	7.31e-04	1.44e+11
550.0	1.60e+09	4.97e-05	3.22e+13
600.0	2.42e+10	3.38e-06	7.17e+15
650.0	3.68e+11	2.30e-07	1.60e+18
700.0	5.57e+12	1.56e-08	3.57e+20
750.0	8.45e+13	1.06e-09	7.97e+22
800.0	1.28e+15	7.20e-11	1.78e+25
850.0	1.94e+16	4.89e-12	3.97e+27
900.0	2.94e+17	3.32e-13	8.86e+29
950.0	4.46e+18	2.25e-14	1.98e+32

Table 2.4: Diffusional versus collisional timescales for Venus. The values are for 8500 K oxygen diffusing through a background of 280 K oxygen. A hard sphere (total) collision cross section of $2.0 \times 10^{-15} \text{ cm}^2$ is used. The Venusian exobase for oxygen is located at approximately 200 km.

The strength of the dissociative recombination reaction is directly proportional to the density of ambient O_2^+ . Since the O_2^+ density peaks relatively low in the both the Venusian and Martian atmospheres (about 140 km for both) and decays rapidly with altitude, the production of hot oxygen is non-negligible only over a very small region of altitudes. Thus, for both Venus and Mars we would expect that the predominant source of exospheric hot oxygen from dissociative recombination would be near 140 km (see Figures 2.2 and 2.3). However, it is important to consider the collisional and diffusional timescales when examining production of hot atoms. If the bulk of the hot atoms are produced over altitudes where collisions are dominant (or τ_{coll} is small), we would expect relatively few hot atoms to escape full or partial thermalization. This would result in a much reduced coronal temperature and extent.

2.6 Summary

The formation of hot oxygen coronae in the atmospheres of Venus and Mars via the nonthermal process of dissociative recombination of O_2^+ was examined using both hydrodynamic and kinetic theory approaches. Both methods predicted an extended hot oxygen corona. The constant temperature hydrodynamic model predicted hot oxygen densities in the order of 3×10^3 - 4×10^5 cm^{-3} at an altitude of about 1500 km on Mars for hot product temperatures between 1000-8500 K. For a similar altitude on Venus, the predicted hot oxygen densities are of the order of 10 - 2×10^6 cm^{-3} . Variation of the temperature, especially below 5000 K, produced sizable differences in the predicted hot atom density profile, and showed how sensitive the final density profile was to the choice of hot oxygen temperature.

A time dependent Boltzmann equation was used to include the effect of thermalization of the hot oxygen atoms through collisions with the cold background and include

the hot oxygen temperature in a consistent manner. The time dependent hot oxygen velocity distribution function was then calculated, with energy degradation described by the Boltzmann collision operator. A simple linear transformation was used to derive the hot atom distribution function as a function of altitude. The distribution at the exobase level was fitted using hot and cold Maxwellian distributions, which yielded exobase temperature and densities. These parameters were used in the collisionless theory of Jeans and Chamberlain to calculate hot atom densities at altitudes above the exobase. The present calculations yielded hot oxygen densities of the order of 10^2 at an altitude of about 1500 km on both Mars and Venus. The hot product temperature for both planets was 7 500 K. The predicted hot atom densities calculated in this way differ from Monte Carlo derived values by a factor of approximately 2-10 on Mars, and 2-30 on Venus, although the predicted hot oxygen densities are still well above measured thermal oxygen densities for both planets. The current and previous models use common input profiles, collision cross sections, source distributions, exobase altitudes, and a collisionless model to generate exospheric densities, so these factors cannot account for the discrepancy. It should be noted, however, that there are differences of up to an order of magnitude between the results of previous workers due to small changes in model parameters, and so the magnitude of the deviation of the current results are not unreasonable.

The CSDA, which requires a roughly constant average velocity in order to legitimize the use of a linear transformation, is less applicable on Venus than on Mars, where there are higher background densities and hence higher rates of thermalization of the hot oxygen atoms. This is particularly true for our model, which fixes the background density at the source altitude despite the fact that we transform from time to space in our local Boltzmann equation. The Monte Carlo simulations, which follow particle motions in altitude directly, account for the change in background density, and so would be expected to yield lower levels of thermalization (that is, a higher population of energetic oxygen

atoms). This is confirmed for both Mars and Venus through comparison with results of previous workers.

Chapter 3

Nonthermal Production of Energetic Hydrogen and Deuterium

3.1 Introduction

The present state of our understanding of the distribution of hydrogen in planetary exospheres is determined predominantly by measurements of the emissions of exospheric hydrogen. These include Lyman- α and Lyman- β emissions of atomic hydrogen at 121.6 nm and 102.6 nm, respectively.

For the terrestrial exosphere, hydrogen densities have typically been inferred by fitting observed emission rates to calculated intensities based on a spherically symmetric exospheric density distribution.⁶⁶ Information about hydrogen densities near the exobase have been provided by measurements of Lyman- α by low-altitude satellites such as OSO-4, OGO-4,^{113,114} and OGO-6.¹¹⁵ There have also been ground based resonant fluorescent measurements of the geocoronal Balmer- α spectral line at 656.3 nm,¹¹⁶ although there has been some difficulty in filtering out contamination in the measured emissions from multiple scattering.¹¹⁷ He et al.¹¹⁸ have used a radiative transfer model to attempt to reconcile theoretical models of the thermospheric and exospheric hydrogen density with these data. In all cases, it has been determined that an extended population of hot hydrogen exists about the Earth.

The first measurements of Lyman- α emissions which indicated the presence of a hot hydrogen corona around Venus were made by the ultraviolet photometer on Mariner 5¹³

during the flyby of 1967. The data indicated two, distinct, exospheric scale heights. Initially it was thought that the scale heights were indicative of two different species, such as atomic and molecular hydrogen or atomic hydrogen and deuterium. This explanation was reconsidered by several workers^{2,5} who suggested instead that the Mariner 5 data were more consistent with a two-temperature hydrogen exosphere. Photodissociation of molecular hydrogen was suggested as the source of the hot hydrogen atoms. Analysis of data collected by the ultraviolet spectrometer on Mariner 10^{87,88} during its Venus flyby in 1974, in addition to data obtained by the Lyman- α photometers on the Venera 9 and 10 orbiters³ in 1975 and Venera 11 and 12⁸⁹ in 1978, supported the theory of a two temperature hydrogen exosphere. High quality data available from the ultraviolet spectrometer aboard the Pioneer Venus Orbiter,⁴ which reached Venus in 1978, confirmed the result. It appears that more likely sources of the hot hydrogen are the nonthermal interactions of ionospheric protons with exospheric oxygen and hydrogen or elastic collisions of hydrogen with hot oxygen.³²

Although data is less extensive for Mars, Lyman- α emissions similar to those measured on Venus have been recorded in the Martian exosphere by ultraviolet spectrometers aboard Mariner 6 and Mariner 7^{119,120} in 1969 and aboard Mariner 9¹²¹ in 1971. Calculations of the hot hydrogen distribution about Mars indicate that the hydrogen corona is much less extensive than that of Venus,³² about a factor of 100 times smaller. While such calculations are limited by the lack of available information on ionospheric densities and temperatures involved in the production of the hot hydrogen, the lack of a strong Lyman- α signature for hot hydrogen about Mars is consistent with the relatively large thermal hydrogen population inferred from available data.^{120,95}

These observations of the exosphere together with insitu mass spectrometric measurements provide density and temperature profiles of neutral and charged constituents. For example, the mass spectrometer on the Pioneer Venus Orbiter measured an enrichment

of the deuterium to hydrogen (D/H) ratio in the exosphere of Venus by a factor of 100 relative to the terrestrial value. This enrichment of deuterium relative to hydrogen is believed to arise from the enhanced escape of hydrogen due to nonthermal processes.

Nonthermal processes refer to collisions between exospheric species and translationally energetic species (both ions and electrons), generally of ionospheric or plasmaspheric origin. This includes processes such as the collision of hot plasmaspheric protons with exospheric hydrogen,



which effectively converts the energetic protons to translationally excited hydrogen atoms, H^* , with speeds in excess of the escape speed. This nonthermal process is of great importance in reconciling discrepancies between predictions of hydrogen escape fluxes utilizing the thermal Jeans' flux and observations. Models of the chemistry and transport processes of the terrestrial mesosphere Liu and Donahue,³⁸⁻⁴⁰ Hunten and Strobel⁴¹ and Maher and Tinsley⁷⁷ demonstrated that the flux of hydrogen in all forms is equal to approximately $1.5\text{--}1.8 \times 10^8 \text{ cm}^{-2}\text{s}^{-1}$, independent of the exospheric temperature. However, the Jeans escape flux calculations predict that the hydrogen escape flux should increase with an increase in the hydrogen temperature at the exobase, T_c . The nonthermal charge exchange process given by equation (3.1.1) was first suggested by Cole¹⁰ in order to reconcile this discrepancy. It has since received a great deal of attention by many others.^{122,42,43,123,26,44,5,45,78} The energetic protons for this process are produced by photodissociation of hydrogenous compounds in the ionosphere. It has been verified by several workers^{43,45,66} that the charge exchange induced escape flux decreases with the hydrogen exobase temperature, T_c , and that the sum of the nonthermal and Jeans' fluxes is constant, independent of exospheric temperature and consistent with the mesospheric models. This has been demonstrated very clearly by Shizgal and Lindenfeld,⁴⁵

who employed a simple hard sphere collisional model to obtain an analytic expression of the charge exchange induced flux. They showed that the charge exchange induced escape, F_{ce} , is given by

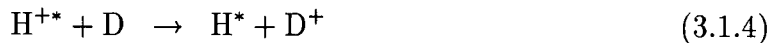
$$\begin{aligned} F_{ce} &= n_{H+} \sqrt{2kT_c/\pi m_H} e^{-\lambda_c} [(1 + \tau) - \sqrt{1 + \tau} e^{-\lambda_c \tau}] / \tau \\ &= 2k_{ce} n_{H+} n_H \end{aligned} \quad (3.1.2)$$

where the important parameter is $\tau = T_c/T_{H+} - 1$, and n_{H+} is an effective density. For sufficiently large T_{H+}/T_c temperature ratios, equation (3.1.2) gives a rate coefficient of the form

$$k_{ce} = 3.6 \times 10^{-6} \text{ s}^{-1} / (1 - T_c/T_{H+}) \quad (3.1.3)$$

For temperature values of $T_{H+} = 4000$ K and $T_c = 1000$ K, this gives a value of $4.8 \times 10^{-6} \text{ s}^{-1}$ close to the estimate obtained by others.⁴² Despite the approximate nature of equation 3.1.2, this result has still been found very useful in the interpretation of ground based Balmer- α observations of geocoronal hydrogen.^{124,118,66} It is of considerable interest to extend the work of Shizgal and Lindenfeld to more realistic charge exchange cross sections.

In the Venusian exosphere, the charge exchange process is essentially the dominant escape mechanism since the thermal escape is very slow because of the low exospheric temperature (see equation (1.2.9) and Table 1.2). Some important nonthermal charge-exchange processes of importance, in addition to reaction (3.1.1) are reactions involving deuterium ions,



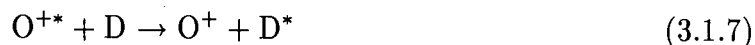
It is believed that the enhanced escape of hydrogen due to these and other nonthermal processes may have had significant bearing on the history of possible water loss on Venus.

Current interpretations of the deuterium/hydrogen ratio measured by the Pioneer Venus Orbiter appear indicative of the relative importance of nonthermal loss of hydrogen on Venus in the past.^{58,51,52} A difficulty with interpretations suggesting the loss of an 'Earth equivalent ocean' of water is that mechanisms yielding enhanced escape of hydrogen do not wholly account for removal of water;³⁷ oxygen must also be removed at a rate consistent with the stoichiometry of water. This is particularly difficult on Venus where the escape energy of such massive constituents is high (see Table 1.1). Mechanisms including incorporation of excess oxygen into crustal rocks or early magmas,^{125,37,126} enhanced nonthermal escape of hot oxygen,¹²⁷ and tectonic resurfacing⁵⁸ have been suggested, although at this time it is still unclear whether any or all of these processes could have been sufficiently vigorous over geologic timescales to absorb the required excess oxygen.

Another important process in the energization of hydrogen is the 'resonant' charge exchange process between oxygen and hydrogen,



and the equivalent process for deuterium,



Both reaction (3.1.6) and (3.1.7) have been considered as important mechanisms for the enhancement of hydrogen escape.³⁵ Reaction (3.1.6) is able to proceed rapidly in either direction with the overall direction of reaction depending strongly on the relative rate of production of H^+ and O^+ at the altitude of interest.

It is also possible to produce hot hydrogen and deuterium through momentum transfer collisions with hot exospheric oxygen. Such energization of atomic hydrogen via elastic collisions with translationally energetic oxygen is of the form



where the hot oxygen may or may not become thermalized completely in the collision. This process also acts as a sink for hot exospheric oxygen. The analogous process for deuterium would be of the form



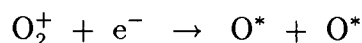
This energy transfer process was suggested in the early 70's by Brinkmann.¹²⁸ McElroy et al.³⁵ employed this mechanism to demonstrate that H would readily escape from Venus whereas D would not, thus providing the enhancement of D over H consistent with the Pioneer Venus mass spectrometer measurements.

Cooper et al.⁷⁵ employed the quantum mechanical differential elastic cross sections for O-H collisions to calculate the energy transfer and the velocity distributions of the product hot hydrogen. They also determined the escape fraction of hydrogen by this process and demonstrated that the angular distribution of the differential cross section is important. They showed that the fraction of product H atoms above the escape speed is 8.5% with the quantum cross sections and 18.8% if isotropic scattering is assumed. The value of this fraction calculated by McElroy et al.³⁵ for isotropic scattering is 15%.

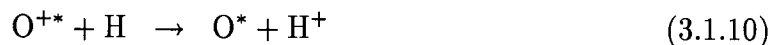
Hodges¹²⁹ recently recalculated the differential cross sections and found some errors in the scattering calculations of Cooper et al.. Hodges did not report any results for escape for either H or D. Gurwell and Yung⁷⁶ reconsidered the enhanced escape of H over D with this same mechanism. Instead of the actual quantum cross sections, they employed Henyey-Greenstein¹³⁰ analytic fits to the cross sections. They calculated product velocity distribution functions for both H and D, and calculate that the fraction of H atoms above the escape energy for isotropic scattering is 15.8%, in agreement with McElroy et al. However, they calculate that the fraction of H atoms above the escape energy with the actual differential cross sections is 4.6% in disagreement with Cooper et al.. They did their calculations with the background gas at both 0K and 300K. For the cold gas

case, the product distributions can be determined analytically whereas with the thermal background, they carry out their calculations with a Monte Carlo simulation.

Nonthermal processes provide an important escape mechanism for heavier species, such as oxygen, nitrogen and carbon, for which the thermal escape is negligible. An important nonthermal process in the Martian exosphere is the dissociative recombination of O_2^+ with electrons, mentioned in Chapter 2 by equation (2.1.1); that is,



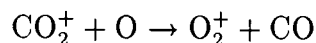
with the product oxygen atoms translationally excited. This process produces a large population of energetic (or 'hot') atoms, and there is evidence of such hot coronae of atomic oxygen in the Martian and terrestrial exospheres.^{11,31,7,32,6,33,34} If the hot oxygen atoms do not escape and are ionized in the upper atmosphere, they may in turn excite other species via charge exchange reactions. An example of such resonant charge exchange reactions of hot ionospheric atomic oxygen with neutral atomic hydrogen and oxygen are given by



Reaction (3.1.10) may also act as a sink for both thermal and hot hydrogen. Dissociative recombination of O_2^+ , as given previously above, is believed to be the main mechanism for the production of a hot oxygen corona on Mars,⁶⁻⁸ although with its high atmospheric concentration of carbon-dioxide, the dissociative recombination reaction



may also be important in the formation of hot oxygen on Mars,³² although its effectiveness in producing hot oxygen may be limited by the reduction of CO_2^+ via reactions such as

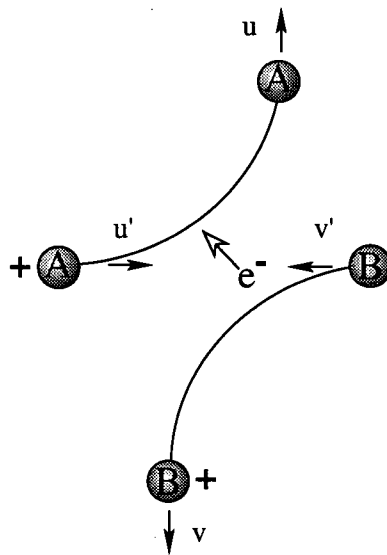


The representation of the dynamics of nonthermal processes is given by the collision cross sections used to approximate the physics of such processes. In many past works examining the role of charge exchange in the production of hot species,^{77,43,5,44,45} the so called 'Linear Trajectory Approximation' (or LTA) has been used. This approximation assumes that exospheric charge exchange takes place with no momentum transfer, in effect simply exchanging the incoming velocities of the two collision partners to arrive at their post-collisional values.^{131,73} The difference between the actual charge-exchange process and the LTA are illustrated schematically in Figure 3.21.

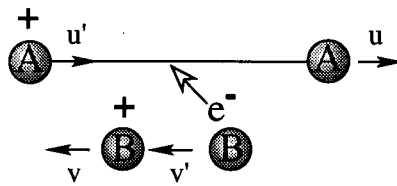
While the LTA of the charge exchange cross section has made detailed (and even analytic) analysis of this process possible, it has been shown that the approximation appears to overestimate the effect of charge exchange on the exospheric escape flux of the hot product.¹³¹ More accurate and realistic representation of the collision dynamics between ions and atoms in the charge exchange process is of great interest, and has been examined in some detail for certain systems, such as H-H^+ and D-H^+ .^{71,73,74,72} In addition, the velocity distribution function (VDF) of the product hot atom, and hence the escape flux, is sensitive to the form of the collision cross section, it is vital that it accurately reflect the physics of the process, and that these cross sections be included in models describing the escape process.

Given the importance of nonthermal collisional processes in the exosphere, it is clear that the standard collisionless models have to be reconsidered. For this reason, our goal is to calculate the non-equilibrium and nonthermal VDF of the product hot atoms resulting from nonthermal collisional processes. A consistent description of these product velocity distribution functions (PVDFs) is required to, ultimately, accurately estimate escape fluxes resulting from nonthermal mechanisms. This is done in Chapter 4.

The current chapter is concerned with the calculation of the PVDFs for several atomic



(a)



(b)

Figure 3.21: Schematic of the charge-exchange and LTA. The charge-exchange collisional process is illustrated in (a), where an electron is transferred from the neutral to the ion, and momentum is transferred from the ion to the neutral. The LTA is shown in (b), where again an electron is transferred from the neutral to the ion, but no momentum is transferred between the ion and neutral. The result is that the collision appears simply to have switched the initial velocities of the ion and neutral, $u = v'$ and $v = u'$, with no change in direction.

systems and nonthermal processes. In section 3.4 we investigate a kinetic theory description of the production of nonequilibrium, hot products resulting from nonthermal processes. To calculate these PVDFs, we require an accurate representation of the energy and angle dependence of various nonthermal collision processes. As mentioned previously, this entails the calculation of quantum mechanical differential and total collision cross sections. We detail the calculation and form of realistic quantum mechanical collision cross sections in section 3.2. The systems examined include direct-plus-exchange (DPE) elastic collisions, direct elastic (DIR) collisions, charge exchange (CE) and LTA collisions for H-H^+ and D-H^+ , and direct elastic collisions for O-H and O-D . The resulting PVDFs are used to calculate energy exchange rate coefficients, which are compared to calculations using a simple hydrodynamic approach. The energy exchange rate coefficients are used to examine the time evolution of the average energy for hot products resulting from nonthermal processes as well as providing a check on our kinetic theory approach of the same calculation. The PVDFs are also used to calculate the escaping fractions of the hot products, and compare these results with those of previous workers.^{131, 71, 73, 74, 76}

3.2 Collision Cross Sections

As mentioned in the introduction to this chapter, early work in the field approximated the charge exchange mechanism by considering the transfer of momentum during the charge exchange collision to be minimal (i.e. the LTA). If the pre- and post- collisional velocities of the ion and atom are indicated by the pairs $(\mathbf{c}'_i, \mathbf{c}'_a)$ and $(\mathbf{c}_i, \mathbf{c}_a)$, this is equivalent to the simple interchange of particle labels, that is $\mathbf{c}'_i = \mathbf{c}_a$ and $\mathbf{c}'_a = \mathbf{c}_i$. Alternately, this is also equivalent to a charge exchange cross section which is a delta function in the backward scattering direction, $\theta = \pi$, and that there is no contribution from elastic scattering during the collision.

In order to more accurately represent the details of the kinematics of the collision process, it is necessary to calculate the collision cross section using quantum mechanical methods. The importance of the angle and energy dependence of real, quantum cross sections was noted by Cooper et al.⁷⁵ in their study of OH. This has been demonstrated by Shizgal^{131,71} for hydrogen-proton and hydrogen-deuterium systems and was recently re-confirmed by Hodges and Breig^{73,74} and Hodges.¹²⁹

3.2.1 Quantum Mechanical Scattering

The procedure for the calculation of quantum mechanical (QM) differential cross sections is well known. A detailed description of these calculations is given in Appendix D.1, standard textbooks on quantum mechanics,¹³²⁻¹³⁴ and in the literature,^{135,136,73,72} here we simply summarize the important results.

The collision of a pair of particles of masses m_1, m_2 may be reduced to the motion of a single particle of reduced mass $\mu = m_1 m_2 / (m_1 + m_2)$ moving in a potential due to the scattering center, given by $V(r)$. In quantum mechanics, this scattering problem involves the solution of the Schrödinger wave equation. The amplitude of the scattered wave, denoted by \mathcal{F} , may be related to the differential collision cross section by (see Appendix D.2)

$$\mathcal{F}(\theta) = \frac{1}{k} \sum_{l=0}^{\infty} (2l+1) P_l(\cos \theta) e^{i\delta_l} \sin \delta_l \quad (3.2.1)$$

and so, from equation (D.1.14), the differential elastic cross section is

$$\sigma(E, \theta) = \frac{1}{k^2} \left| \sum_{l=0}^{\infty} (2l+1) P_l(\cos \theta) e^{i\delta_l} \sin \delta_l \right|^2 \quad (3.2.2)$$

From equation (C.0.5), the total elastic cross section is given by

$$\sigma_{tot}(E) = \frac{4\pi}{k^2} \sum_{l=0}^{\infty} (2l+1) \sin^2 \delta_l \quad (3.2.3)$$

Equations (3.2.2) and (3.2.3) above assume only single channel scattering (that is, a single interaction potential describes the particle interaction). For most real systems of atoms and molecules, there are several elastic scattering channels for any given energy. In such cases, the elastic differential scattering cross sections are given by combining the contributions of each channel according to their quantum mechanical statistical weight.^{137,129}

The momentum transfer cross section is defined as a weighted integral of the differential cross section over all angles, or

$$\sigma_{mt}(E) = \int \sigma(E, \theta) (1 - \cos \theta) d\Omega \quad (3.2.4)$$

It appears in the final form of the energy exchange rate coefficient, discussed later in this chapter. In addition, the momentum transfer collision cross section is often used in aeronomical calculations.¹³⁷

The linear trajectory approximation (or LTA) cross section is often used to approximate the charge-exchange process. As was mentioned briefly in the introduction to this section, this model cross section is the equivalent of a charge exchange cross section which is a delta function in the backward scattering direction, $\theta = \pi$, and assumes that there is no contribution from elastic scattering during the collision. The definition for the LTA cross section is⁷²

$$\sigma_{LTA}(\theta) = \frac{\sigma_{tot}^{HS}}{2\pi} \frac{\delta(\theta - (\pi - \epsilon))}{\sin(\pi - \epsilon)} \quad (3.2.5)$$

where ϵ is a positive number between 0 and π , and σ_{tot}^{HS} is some (arbitrary, energy independent) total hard sphere cross section; the LTA approximation is given in the limit $\epsilon \rightarrow 0+$. Another definition of the LTA, which incorporates energy dependence, is given by⁷³

$$\sigma_{LTA}(E, \theta) = \frac{\sigma_{tot}^{ce}(E)}{2\pi} \delta(\theta - \pi) \quad (3.2.6)$$

where $\sigma_{tot}^{ce}(E)$ is some (energy dependent) total cross section for charge exchange. It is easy to show using equation (C.0.5) that the total LTA cross section is given by σ_{tot}^{HS} and $\sigma_{tot}^{ce}(E)$, respectively; similarly, using equation (3.2.4), the momentum transfer LTA cross section is given by $2\sigma_{tot}^{HS}$ and $2\sigma_{tot}^{ce}(E)$, respectively. The LTA and the overestimation of energy transfer resulting from the neglect of momentum transfer in this approximation to the charge exchange process, is discussed later in this chapter.

3.2.2 Calculation of the Phase Shifts

This phase difference between asymptotic solutions of the radial wave equation with and without the potential is known as the phase shift, denoted δ_l . In general, the phase shifts are calculated by finding the nodes r_o of R_l from equation (D.2.18), yielding

$$\tan \delta_l = \frac{j_l(kr_o)}{n_l(kr_o)} \quad (3.2.7)$$

The solutions R_l are found by direct integration of the radial Schrödinger equation using a Runge-Kutta-Gill (Adam-Bashforth, Milne) method. This method is accurate and relatively quick for the small number of phase shifts required at low energies. For higher energies, more phase shifts are required, and if the collision pair has several interaction potentials (such as for $O-O^+$), direct numerical integration may require on the order of a day to calculate all the required phase shifts. For these energies, the phase shifts can be calculated using the Wentzel-Kramers-Brillouin (WKB) or semi-classical approximation.¹³³ A brief outline of the WKB formulation for the phase shifts is given in Appendix D.3. In general, the WKB approximation is appropriate for those energies above the centrifugal barrier for the effective potential (see equation (D.2.18) in Appendix D.1), where there is no orbiting and only a single classical turning point.¹³³ For energies falling between the QM and WKB regimes, the lower-order phase shifts are calculated quantum mechanically and the higher-order phase shifts are calculated with the WKB method. The transition

from QM to WKB calculations is made when agreement is reached between phase shifts calculated by the two methods.

3.2.3 Cross Sections for H^+ -H and D^+ -H

The quantum description for the collisional process between hydrogen and protons is well established. For the range of energies of interest in this work, approximately 1×10^{-4} to 10 eV, values for the elastic and charge exchange cross sections have been calculated by Hunter and Kuriyan,¹³⁵ Davis and Thorson,¹³⁶ Hodges and Breig,^{73,74} and Clarke and Shizgal.⁷² As in Clarke and Shizgal,⁷² we use the interaction potentials given by Peek¹³⁸ and Wind,¹³⁹ interpolated using a cubic spline to ensure a smooth fit. The potentials are shown in Figure 3.22.

At collision energies below the first excited state of hydrogen (10.2 eV), the scattering process for H - H^+ involves only two electronic states of the H_2^+ ion. These states, labeled by the subscripts u and g , are known as the gerade ($1S\sigma_g$) and ungerade ($2P\sigma_u$) states. From equation (3.2.3), for the H - H^+ system, we thus have

$$\sigma_d(E, \theta) = \frac{1}{4} |\mathcal{F}_+(\theta) + \mathcal{F}_-(\theta)|^2 \quad (3.2.8)$$

for the differential ‘direct’ elastic scattering cross section, and

$$\sigma_{ce}(E, \theta) = \frac{1}{4} |\mathcal{F}_+(\pi - \theta) - \mathcal{F}_-(\pi - \theta)|^2 \quad (3.2.9)$$

for the charge exchange cross section, where \mathcal{F}_+ and \mathcal{F}_- refer to scattering amplitudes derived from phase shifts calculated using the potential for the gerade or singlet state ($1S\sigma_g$) and the ungerade or triplet state ($2P\sigma_u$), respectively. Both equations (3.2.8) and (3.2.9) assume that the particles are distinguishable. The total cross sections for the ‘direct plus exchange’ (DPE) and charge exchange (CE) cross sections are given by

$$\sigma_{tot}^{dpe}(E) = 2\pi \int_0^\pi \{\sigma_d(E, \theta) + \sigma_{ce}(E, \theta)\} \sin \theta d\theta$$

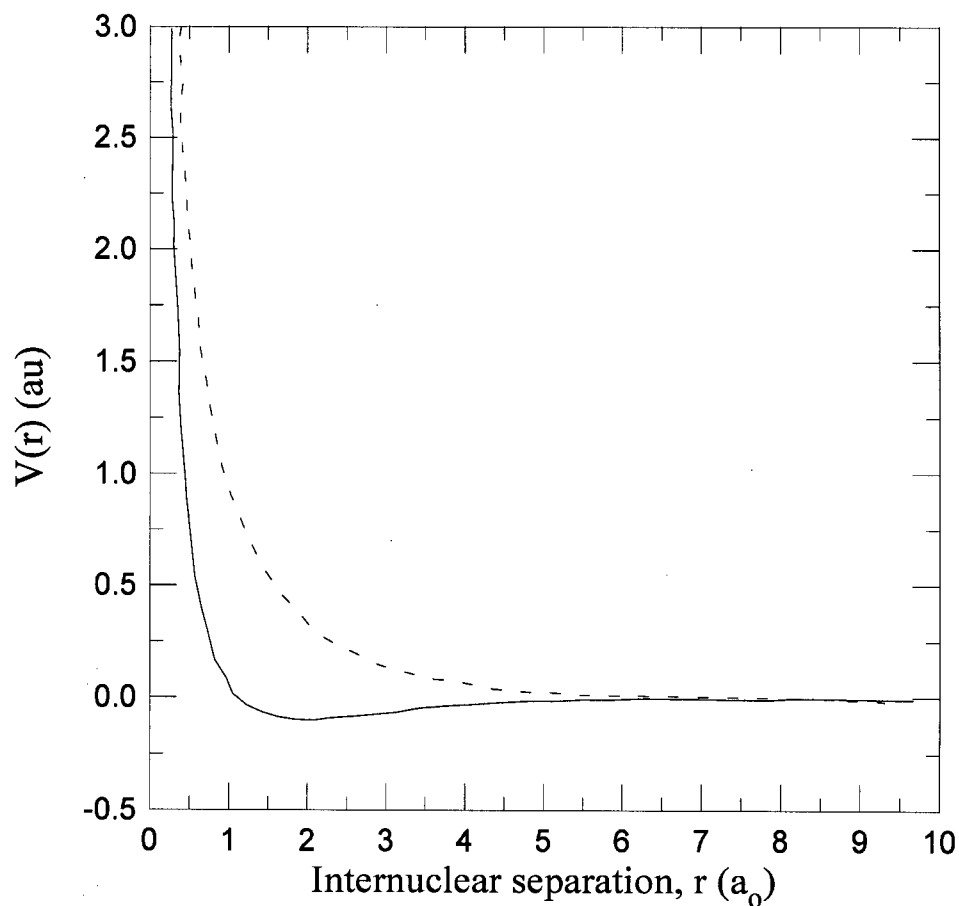


Figure 3.22: Interaction potentials for H^+-H . The solid curve is for the gerade or $1S_g$ state, and the dashed curve is for the ungerade or $2P_u$ state. The unit of energy for $V(r)$ is the ionization energy of atomic hydrogen, while the unit of internuclear separation is the Bohr radius, $a_0 = 0.5292$ cm.

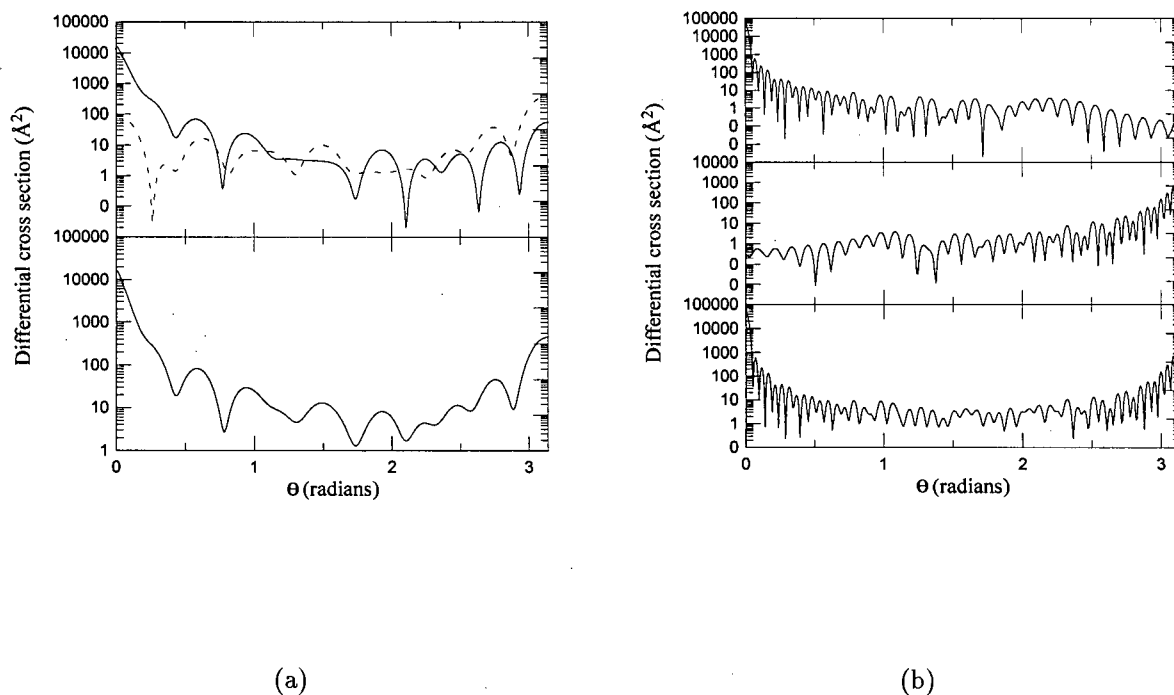


Figure 3.23: Differential cross sections for $\text{H}^+\text{-H}$. The differential scattering cross sections, in square Angstroms, are shown for fixed energy as a function of the scattering angle, θ . In (a), the energy is 0.01 eV; the top part of the figure shows the differential cross sections for direct (solid line) and charge exchange (dashed line) cross sections, and the bottom part of the figure shows the direct plus exchange (DPE) differential elastic cross section. In (b), the energy is 1.0 eV; the top part of the figure shows the differential cross sections for direct elastic scatter, the middle portion shows the differential elastic cross section for the charge exchange cross section, and the bottom figure shows the direct plus exchange (DPE) differential elastic cross section.

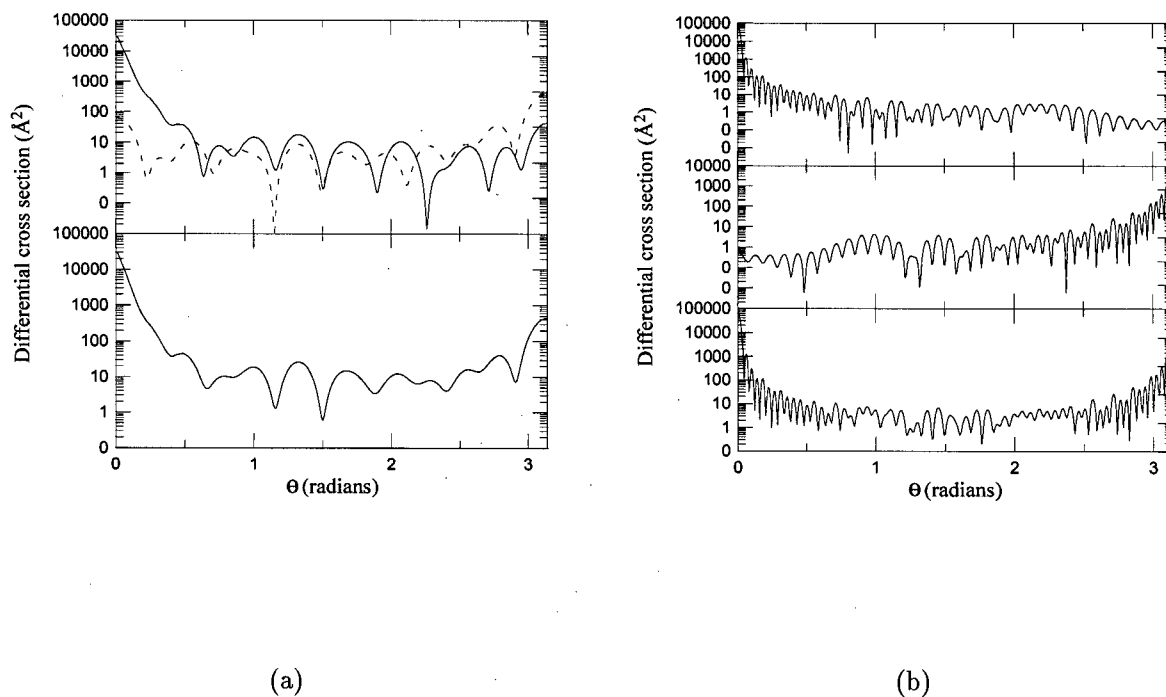


Figure 3.24: Differential cross sections for $\text{D}^+\text{-H}$. The differential scattering cross sections, in square Angstroms, are shown for fixed energy as a function of the scattering angle, θ . In (a), the energy is 0.01 eV; the top part of the figure shows the differential cross sections for direct (solid line) and charge exchange (dashed line) cross sections, and the bottom part of the figure shows the direct plus exchange (DPE) differential elastic cross section. In (b), the energy is 1.0 eV; the top part of the figure shows the differential cross sections for direct elastic scatter, the middle portion shows the differential elastic cross section for the charge exchange cross section, and the bottom figure shows the direct plus exchange (DPE) differential elastic cross section.

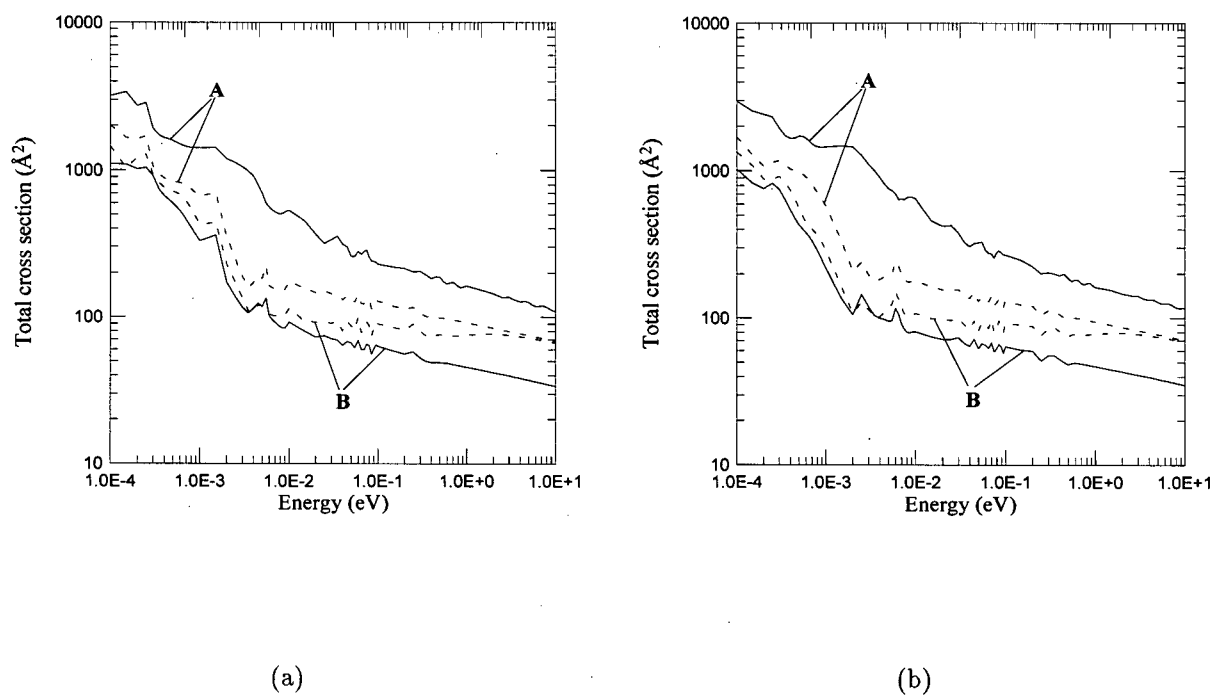


Figure 3.25: Total elastic collision cross sections. Figure (a) is for H⁺-H, Figure (b) is for H⁺-D. In both (a) and (b), A denotes total cross sections for direct plus exchange (DPE) and B denotes total cross sections for charge exchange (CE). The solid lines are for the standard total elastic cross section and the dashed lines are for the momentum transfer cross sections for each respective type of cross section (DPE or CE).

$$= \frac{2\pi}{k^2} \sum_{l=0}^{\infty} (2l+1) \{ \sin^2 \delta_{l,+} + \sin^2 \delta_{l,-} \} \quad (3.2.10)$$

and

$$\begin{aligned} \sigma_{tot}^{ce}(E) &= 2\pi \int_0^\pi \sigma_{ce}(E, \theta) \sin \theta d\theta \\ &= \frac{\pi}{k^2} \sum_{l=0}^{\infty} (2l+1) \sin^2(\delta_{l,+} - \delta_{l,-}) \end{aligned} \quad (3.2.11)$$

respectively, where again + or - refers to a value calculated using either the gerade or ungerade potential. Some examples of differential cross sections for hydrogen-proton scattering calculated as described here are illustrated in Figure 3.23, with total cross sections shown in Figure 3.25.

We assume that the potentials of Figure 3.22 and equations (3.2.8)-(3.2.11) are applicable to deuterium-proton scattering when the reduced mass for the $D^+ - H$ system is used in the calculation of the phase shifts. This is equivalent to ignoring the 'coupling coefficient' between the lowest two electronic states of $D^+ - H$, and appears justified given that the coupling potential is four orders of magnitude smaller than the other interaction potentials.⁷⁴ Differential cross sections for deuterium-proton scattering are illustrated in Figure 3.24 and total cross sections are shown in Figure 3.25.

3.2.4 Cross Sections for O-H and O-D

As discussed previously, an important nonthermal mechanism on Mars and Venus is the production of translationally energetic oxygen atoms from dissociative recombination and the subsequent energy transfer to H and D, equations (3.1.8) and (3.1.9).

The present work considers the use of quantum mechanical collision cross sections for O-H and O-D and the determination of the enhanced product velocity distributions of hot H and D. The collision cross sections were evaluated as detailed previously in this chapter, with the primary difference being that in this case there are four interactions

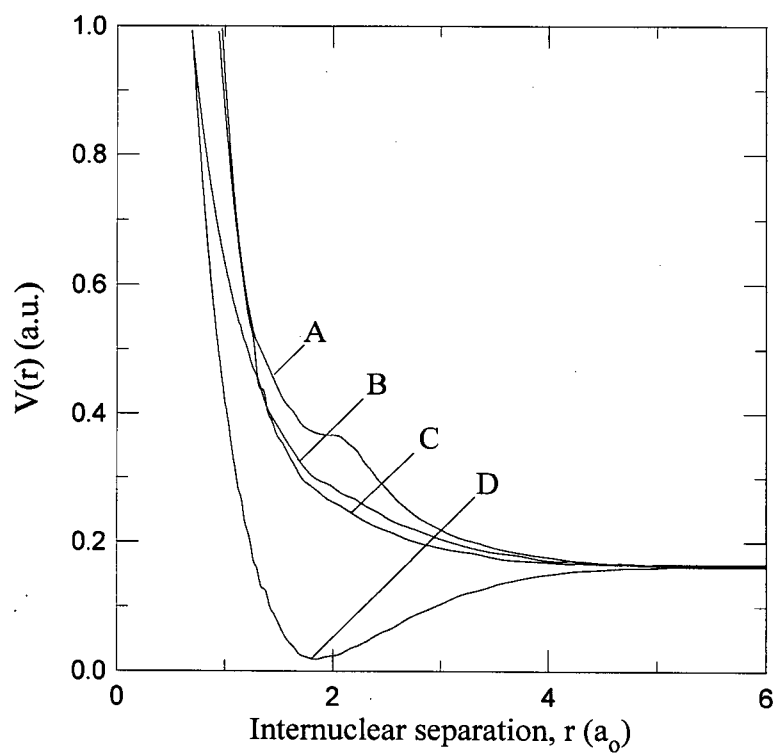


Figure 3.26: Interaction potentials for O-H. The labels A, B, C, and D denote the curves for the $^4\Pi$, $^2\Sigma$, $^4\Sigma$, and $^2\Pi$ states, respectively. The unit of energy for $V(r)$ is the ionization energy of atomic hydrogen, while the unit of internuclear separation is the Bohr radius, $a_0 = 0.5292$ cm.

potentials, or four scattering channels, corresponding to the electronic states $^4\Pi$, $^2\Sigma^-$, $^4\Sigma^-$ and $^2\Pi$. These potential energy curves were taken from Figure 1 of Hodges,¹²⁹ and are shown in Figure 3.26. We assume that deuterium-oxygen collisions are governed by the hydrogen-oxygen interaction potentials, with the only change being the reduced mass of the system.

The potentials for the $^2\Pi$ and $^2\Sigma^-$ are also listed in Table 1 of van Dishoeck et al.^{140,141} The bound state potential $^2\Pi$ was fitted to a Morse potential of the form,

$$V(r) = D_e[1 - \exp(-\beta x)]^2$$

where $x = r - r_e$ and $\beta = \beta_0(1 + \lambda_1 x + \lambda_2 x)$.^{142,143} We chose the values $D_e = 4.582$, $r_e = 1.838$, $\beta_0 = 1.239$, $\lambda_1 = 0.001$ and $\lambda_2 = 0.037$. The other three potentials were digitized from the work of Hodges,¹²⁹ and a spline fit was used to interpolate in the table. An important part of the potentials is their asymptotic forms for large r . These are of the form $9.13/r^6$ (in au) for the Σ states and $9.22/r^6$ for the Π state,⁷⁵ and represent the long range interaction of the two polarizable atoms as dipoles. The way in which the tabulated potential functions are made to go over to these long range forms is somewhat arbitrary. It is not known at what radial positions these asymptotic forms become valid and it appears that the tabulated potentials do not extend into this region. Consequently a rather arbitrary merging of the tabulated potentials with the asymptotic portion is made. Hodges alludes to this difficulty in attempting to reconcile some differences between his cross sections and those reported by Cooper et al. The actual forms of the potentials in the intermediate range (6-10 au) will have to await further quantum mechanical calculations. At short range, the potentials are fitted with polynomials of the form $a/r + b + cr$, as in Hodges.¹²⁹

These potential functions were used to calculate four sets of phase shifts and four sets of cross sections. The cross section for O-H and O-D collisions are the sum of these cross

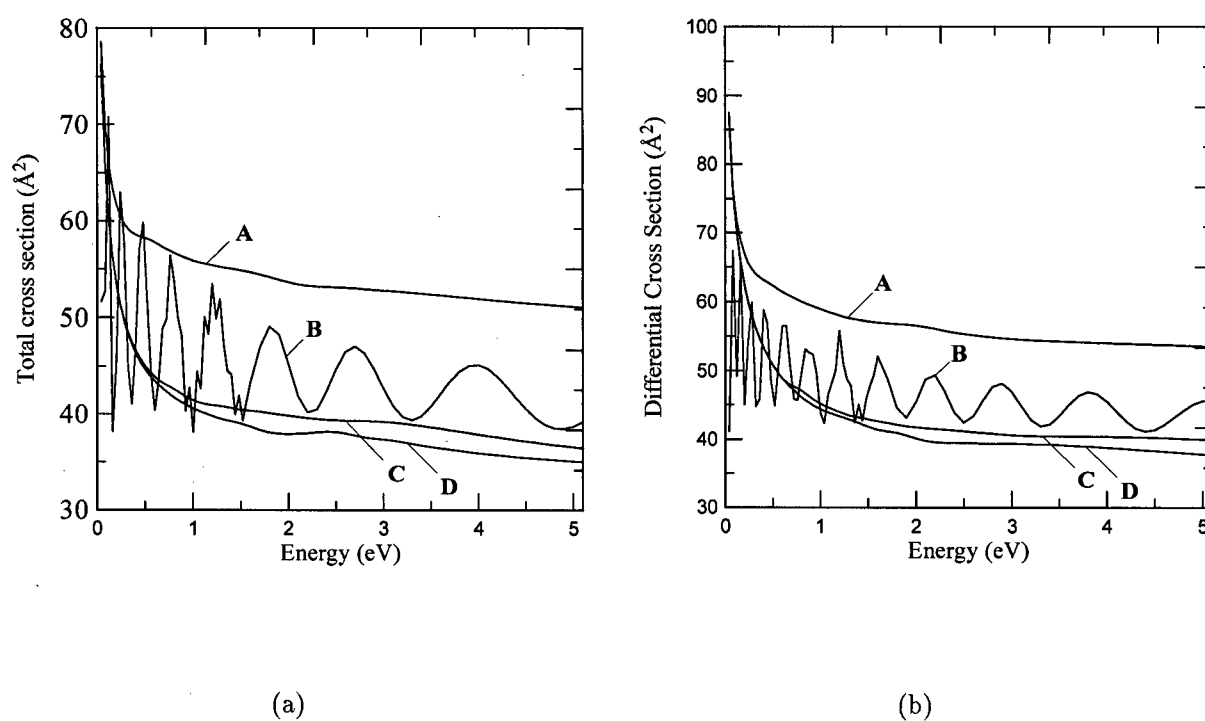


Figure 3.27: Total elastic collision cross sections. Figure (a) is for O-H, Figure (b) is for O-D. The labels A, B, C, and D denote the total cross sections corresponding to the $^4\Pi$, $^2\Sigma$, $^4\Sigma$, and $^2\Pi$ states, respectively.

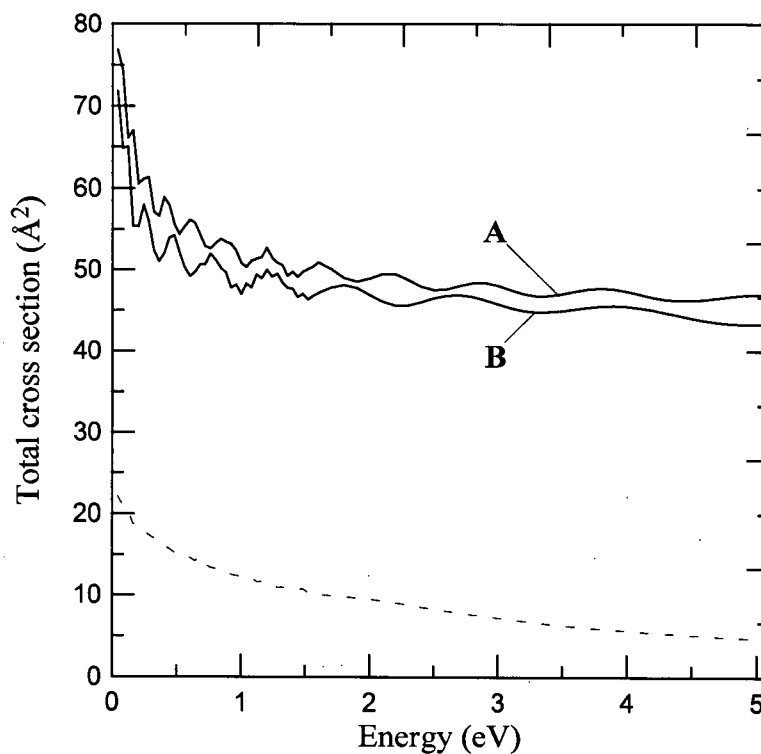


Figure 3.28: Total elastic collision cross sections. The labels A and B for the solid curves denote the total elastic cross sections for O-D and O-H, respectively, as given by the weighted average of the total cross sections for each of the 4 states of O-D/O-H. The dashed curve indicates the analogous elastic momentum transfer cross section; at this scale, it is identical for O-H and O-D.

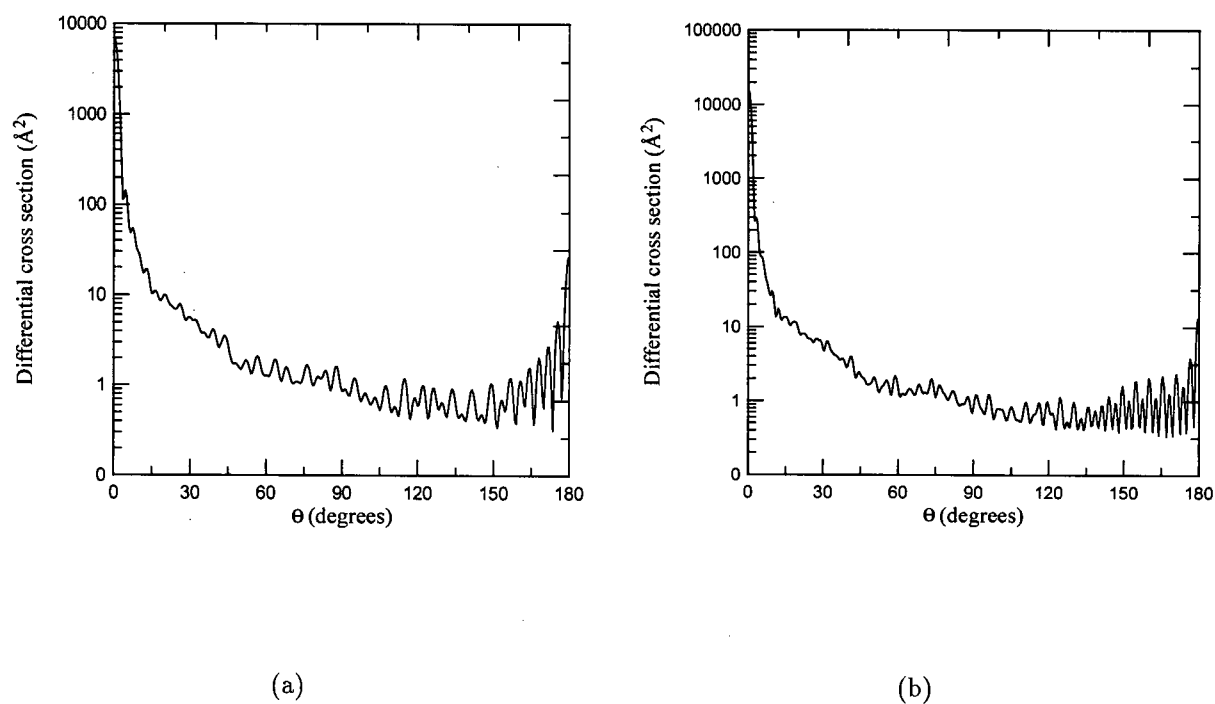


Figure 3.29: Differential cross sections for (a) O-H and (b) O-D. The differential scattering cross sections, in square Angstroms, are shown for fixed energy as a function of the scattering angle, θ . The differential cross sections are shown for an energy of 1.0 eV, are a weighted sum of the four states for each system.

sections weighted by the statistical weights, w_i , determined from the degeneracies of the electronic states, that is,

$$\sigma(E) = \sum_i w_i \sigma_i(E)$$

where i denotes one of the four channels. The energy variation of the total cross sections for O-H and O-D collisions are shown in Figure 3.27. While similar, the results are slightly different for the two systems. The oscillatory curve is for the $^2\Pi$ state, while the smooth curves correspond to the $^4\Pi$, $^2\Sigma^-$, and $^4\Sigma^-$ states. Hodges found that the cross sections for the $^2\Sigma^-$ and $^4\Sigma^-$ states (the two lowest curves in the figure) are indistinguishable, whereas here we find a slight difference. Cooper et al.⁷⁵ reported a significant difference between these two cross sections.

It would appear that the manner in which the potentials at small r are merged to the asymptotic form is responsible for slight differences in the cross section but probably not the large difference noted in the results of Cooper et al., as discussed by Hodges. We agree with his conclusion that the large difference that they report is unreasonable. The statistically weighted cross sections for H-O and D-O collisions are shown in Figure 3.28, along with the momentum transfer cross section for elastic scatter. There is a small but real difference between the weighted total elastic cross sections, in contrast with Hodges' supposition that these cross sections are the same. This is important since the object of these calculations is to study the enhancement of escape of H over D. Differential cross sections for both types of collisions at 1.0 eV are illustrated in Figure 3.29. The large forward scattering peak is evident in both cross sections.

3.3 Energy Exchange Rate Coefficients

An aspect of interest in the production of hot atoms involved in the nonthermal escape process is the rate at which energy is transferred between various atmospheric

constituents. Calculation of the energy exchange rate coefficients enable us to compare the relative efficiency with which various nonthermal processes operate. We may also use them to study the time evolution of the average energy of between species of differing (initial) temperatures.

Energy exchange rate coefficients are reported by Hodges and Breig,⁷³ who examine charge exchange and momentum transfer effects in hydrogen-proton collisions. They carry out quantum mechanical calculations of hydrogen-proton cross sections for both processes. However, they choose to use Monte Carlo integration techniques to treat the Boltzmann collision operator, citing complexities in the relationships of pre- and post-collisional encounter velocities produced by wide-ranging variations in the collision cross section.

We show in this section that such Monte Carlo techniques are not required for the calculation of the energy exchange rate coefficients. We follow the method and notation of Shizgal and Fitzpatrick¹⁴⁴⁻¹⁴⁶ and Shizgal.¹⁴⁷

The derivation of the energy exchange rate coefficient involves the calculation of the energy moment of the Boltzmann equation. This yields the rate of change of the average energy of particles of species 1. In general, the energy exchange rate coefficient depends in a complicated way on the details of the differential collision cross section and the form of the velocity distribution functions of both species involved in the collision process. This involves solving an equation containing the Boltzmann collision operator, as detailed in equation (1.4.2). It was demonstrated by Shizgal and Fitzpatrick^{144,145} that it is possible with some simplifying assumptions to reduce the problem of the calculation of the energy exchange rate coefficients to a single integral over the total momentum transfer collision cross section.

3.3.1 Theory

The rate at which species 1 transfers energy to the background, species 2, for a uniform system in the absence of external forces is given by the energy moment of the collision operator in the Boltzmann equation, that is

$$\begin{aligned}
 R_E \equiv \frac{\partial E}{\partial t} &= \int \frac{1}{2} m_1 c_1^2 \frac{\partial f_1}{\partial t} d\mathbf{c}_1 \\
 &= n_1(r) n_2(r) \iiint \{f_1(r, \mathbf{c}'_1) f_2(r, \mathbf{c}'_2) - f_1(r, \mathbf{c}_1) f_2(r, \mathbf{c}_2)\} \times \\
 &\quad \frac{1}{2} m_1 c_1^2 g \sigma(g, \Omega) d\Omega d\mathbf{c}_2 d\mathbf{c}_1
 \end{aligned} \tag{3.3.1}$$

where the Boltzmann collision term was given by equation (1.4.2). We assume that both velocity distribution functions are Maxwellian distributions at *different* temperatures,

$$f_i^M(c_i) = \left(\frac{m_i}{2\pi k T_i} \right)^{\frac{3}{2}} \exp \left[-\frac{m_i c_i^2}{2k T_i} \right]$$

If primed/unprimed velocities in the collision integral in equation (3.3.1) are interchanged, we have that

$$\iint f'_1 f'_2 \frac{1}{2} m_1 c_1^2 g \sigma d\Omega d\mathbf{c}_2 d\mathbf{c}_1 = \iint f_1 f_2 \frac{1}{2} m_1 c_1'^2 g \sigma d\Omega d\mathbf{c}_2 d\mathbf{c}_1$$

where²⁹

$$g' \sigma(g', \Omega') d\Omega' d\mathbf{c}'_1 d\mathbf{c}'_2 = g \sigma(g, \Omega) d\Omega d\mathbf{c}_1 d\mathbf{c}_2$$

and where we have also used microscopic reversibility; that is, we assume that every forward collision has a corresponding inverse collision. Since summing over all possible collisions is equivalent to summing over all possible inverse collisions, the value of the integration is unchanged by the interchange of primed and unprimed variables. Equation (3.3.1) can thus be written

$$R_E = n_1 n_2 \iiint f_1^M f_2^M \frac{1}{2} m_1 (c_1'^2 - c_1^2) g \sigma d\Omega d\mathbf{c}_2 d\mathbf{c}_1 \tag{3.3.2}$$

With the transformation to dimensionless velocity coordinates,

$$\begin{aligned}\xi_i &\equiv \left(\frac{m_i}{2kT_i}\right)^{\frac{1}{2}} \mathbf{c}_i \\ d\xi_i &= \left(\frac{m_i}{2kT_i}\right)^{\frac{3}{2}} d\mathbf{c}_i\end{aligned}\quad (3.3.3)$$

equation (3.3.2) becomes

$$R_E = \frac{n_1 n_2}{\pi^3} kT_1 \iiint e^{-\xi_1^2 - \xi_2^2} (\xi_1'^2 - \xi_1^2) g \sigma d\Omega d\xi_2 d\xi_1 \quad (3.3.4)$$

Hodges and Breig⁷³ evaluate equation (3.3.4), an eight dimensional integral, using Monte Carlo integration. They cite, as justification for resorting to Monte Carlo techniques, that direct integration of equation (3.3.4) is 'impractical'. However, the techniques for the reduction of equation (3.3.4) to a one dimensional integral over a total cross section are well known,¹⁴⁴⁻¹⁴⁶ and are outlined below.

The center of mass velocity and relative velocity are given, respectively, by²⁹

$$\begin{aligned}\mathbf{g} &= \mathbf{c}_2 - \mathbf{c}_1 \\ \mathbf{G} &= M_1 \mathbf{c}_1 + M_2 \mathbf{c}_2\end{aligned}\quad (3.3.5)$$

where

$$\begin{aligned}M_i &\equiv m_i/m_o \\ m_o &\equiv m_1 + m_2\end{aligned}$$

We have standard relations²⁹ between particle velocities and the center of mass and relative velocities, namely

$$\begin{aligned}\mathbf{c}_1 &= \mathbf{G} - M_2 \mathbf{g} \\ \mathbf{c}_2 &= \mathbf{G} + M_1 \mathbf{g} \\ \mathbf{c}_1' &= \mathbf{G}' - M_2 \mathbf{g}' \\ \mathbf{c}_2' &= \mathbf{G}' + M_1 \mathbf{g}'\end{aligned}\quad (3.3.6)$$

We may define a reduced center of mass velocity, Ξ , and relative velocity ξ ,

$$\begin{aligned}\Xi &\equiv \mathcal{M}_1^{\frac{1}{2}}\xi_1 + \mathcal{M}_2^{\frac{1}{2}}\xi_2 \\ \xi &\equiv \mathcal{M}_1^{\frac{1}{2}}\xi_2 - \mathcal{M}_2^{\frac{1}{2}}\xi_1\end{aligned}\quad (3.3.7)$$

where

$$\begin{aligned}\mathcal{M}_1 &\equiv \frac{M_1 T_2}{M_1 T_2 + M_2 T_1} \\ \mathcal{M}_2 &\equiv \frac{M_2 T_1}{M_1 T_2 + M_2 T_1}\end{aligned}$$

We may relate Ξ and ξ to \mathbf{G} and \mathbf{g} by¹⁴⁴

$$\begin{aligned}\Xi &= (m_1/2kT_1 + m_2/2kT_2)^{\frac{1}{2}} \left[\mathbf{G} + M_1 M_2 (T_1 - T_2) / (M_1 T_2 + M_2 T_1)^{\frac{1}{2}} \mathbf{g} \right] \\ \xi &= \left[\frac{\mu}{2kT_{eff}} \right]^{\frac{1}{2}} \mathbf{g}\end{aligned}\quad (3.3.8)$$

where $\mu = m_1 m_2 / m_o$ is the normal reduced mass, and $T_{eff} \equiv (M_1 T_2 + M_2 T_1) / m_o$ is the effective temperature. Inverting equation (3.3.7), we have

$$\begin{aligned}\xi_1 &= \mathcal{M}_1^{\frac{1}{2}}\Xi - \mathcal{M}_2^{\frac{1}{2}}\xi \\ \xi_2 &= \mathcal{M}_2^{\frac{1}{2}}\Xi + \mathcal{M}_1^{\frac{1}{2}}\xi\end{aligned}\quad (3.3.9)$$

We note that equations (3.3.7) and (3.3.8) are valid for the pre-collisional (primed) velocities by simply replacing variables with their primed counterparts.

For elastic collisions, we also have²⁹

$$\mathbf{g}' = \mathbf{g} - 2(\mathbf{g} \cdot \mathbf{k}) \mathbf{k} \quad (3.3.10)$$

where the unit vector \mathbf{k} is the 'apse line' or line joining the two particles at the point of closest approach during a collision; it corresponds to the external bisector of the angle between the relative velocities before and after the collision, \mathbf{g}' and \mathbf{g} (see Figure E.59).

Equation (3.3.10) is a result of the principles of conservation of momentum and energy. From equations (3.3.6) and (3.3.10) we have

$$\mathbf{c}'_1 = \mathbf{G} - M_2 \mathbf{g} + 2M_2(\mathbf{g} \cdot \mathbf{k})\mathbf{k} \quad (3.3.11)$$

where by conservation of momentum $\mathbf{G}' \equiv \mathbf{G}$. Using the primed analogue to equation (3.3.9), and utilizing equation (3.3.11), we then have

$$\xi'_1 = \mathcal{M}_1^{\frac{1}{2}} \Xi - \mathcal{M}_2^{\frac{1}{2}}(1 + \alpha)\xi' + \mathcal{M}_2^{\frac{1}{2}}\alpha\xi \quad (3.3.12)$$

where $\alpha \equiv M_1(T_1/T_2 - 1)$. After some algebra (see Appendix E), we find

$$\xi_1'^2 - \xi_1^2 = 4(\mathcal{M}_1\mathcal{M}_2)^{\frac{1}{2}}(1 + \alpha)(\xi \cdot \mathbf{k})(\Xi \cdot \mathbf{k}) + 4\mathcal{M}_2\alpha(1 + \alpha)(\xi \cdot \mathbf{k})^2 \quad (3.3.13)$$

From conservation of energy (see Appendix E), we have that

$$\begin{aligned} \xi_1^2 + \xi_2^2 &= \Xi^2 + \xi^2 \\ d\xi_1 d\xi_2 &= d\Xi d\xi \end{aligned} \quad (3.3.14)$$

and so equation (3.3.4) becomes

$$\begin{aligned} R_E &= \frac{n_1 n_2}{\pi^3} kT_1 \iiint \left[4(\mathcal{M}_1\mathcal{M}_2)^{\frac{1}{2}}(1 + \alpha)(\xi \cdot \mathbf{k})(\Xi \cdot \mathbf{k}) + 4\mathcal{M}_2\alpha(1 + \alpha)(\xi \cdot \mathbf{k})^2 \right] \times \\ &\quad e^{-\Xi^2 - \xi^2} \left(\frac{2kT_{eff}}{\mu} \right)^{\frac{1}{2}} \xi \sigma d\Omega d\Xi d\xi \end{aligned} \quad (3.3.15)$$

The first term in equation (3.3.15) is odd in the cosine of the angle between \mathbf{k} and Ξ , and so vanishes when integrated over $d\Xi$; that is, if we choose our coordinate system such that the polar direction is along Ξ , then $d\Xi = \sin\theta d\theta d\phi \Xi^2 d\Xi$, and so $\mathbf{k} \cdot \Xi \equiv k\Xi \cos\theta$, which means that $\int k\Xi \cos\theta d(\cos\theta) \equiv 0$. Thus, equation (3.3.15) becomes

$$\begin{aligned} R_E &= \frac{n_1 n_2}{\pi^3} kT_1 4\mathcal{M}_2\alpha(1 + \alpha) \left(\frac{2kT_{eff}}{\mu} \right) \int e^{-\Xi^2} d\Xi \iint (\xi \cdot \mathbf{k})^2 e^{-\xi^2 \frac{1}{2}} \xi \sigma d\Omega d\xi \\ &= \frac{n_1 n_2}{\pi^3} kT_1 4\mathcal{M}_2\alpha(1 + \alpha) \left(\frac{2kT_{eff}}{\mu} \right)^{\frac{1}{2}} 4\pi \int_0^\infty e^{-\Xi^2} \Xi^2 d\Xi \times \\ &\quad \iint (\xi \cdot \mathbf{k})^2 e^{-\xi^2} \xi \sigma d\Omega d\xi \end{aligned}$$

The integral over $d\Xi$ may be done analytically,

$$4\pi \int_0^\infty e^{-\Xi^2} \Xi^2 d\Xi = \pi^{\frac{3}{2}}$$

and we have

$$R_E = \frac{n_1 n_2}{\pi^{\frac{3}{2}}} kT_1 4\mathcal{M}_2 \alpha (1 + \alpha) \left(\frac{2kT_{eff}}{\mu} \right)^{\frac{1}{2}} 4\pi \iint (\xi \cos \chi)^2 e^{-\xi^2} \xi^5 \sigma d\Omega d\xi$$

where we have defined χ as the angle between \mathbf{k} and $\boldsymbol{\xi}$. With the transformation (see Figure E.59)

$$\cos^2 \chi = \frac{1}{2}(1 - \cos \theta)$$

and the definition of the momentum transfer cross section, equation (3.2.4), we thus have

$$R_E = N(T_1, T_2) \int_0^\infty e^{-\xi^2} \xi^5 \sigma_{mt} d\xi \quad (3.3.16)$$

The momentum transfer cross section is a function of energy through the relative velocity between the colliding pair, i.e. $\sigma_{mt} = \sigma_{mt}(\xi)$, where the physics of the collision process is given by the energy *and* angle dependence of the differential cross section $\sigma(\xi, \theta)$ used to calculate σ_{mt} . We note that σ_{mt} is implicitly a function of the effective temperature, T_{eff} ; explicitly the dependence is

$$\sigma_{mt}(\xi) = \sigma_{mt}\left(\sqrt{\frac{\mu}{2kT_{eff}}} \mathbf{g}\right)$$

The factor in front of the integral in equation (3.3.16) is defined by

$$N(T_1, T_2) = \frac{8n_1 n_2 \mu}{\pi m_o} \sqrt{\frac{2\pi kT_{eff}}{\mu}} k(T_2 - T_1)$$

It is clear from the form of the coefficient N that as the temperature difference between the two species diminishes that the rate of energy transfer also decreases, becoming zero when the temperatures are equal. In practice, the integral in equation (3.3.16) is done

numerically. For the hard sphere cross section, $\sigma_{diff} = d^2/4$, where d is the atomic diameter, we may carry out the integration in equation (3.3.16) analytically, yielding

$$R_E = \frac{8n_1n_2d^2\mu}{m_o} \sqrt{\frac{2\pi kT_{eff}}{\mu}} k(T_2 - T_1) \quad (3.3.17)$$

If we make the substitution $E = 3kT/2$, the above result is identical to that obtained by Shizgal and Fitzpatrick.¹⁴⁶

We may rewrite equation (3.3.16) in the form of a rate equation,

$$\frac{\partial E_1}{\partial t} = n_1n_2k_E k(T_2 - T_1) \quad (3.3.18)$$

where

$$k_E = \frac{8\mu}{\pi m_o} \sqrt{\frac{2\pi kT_{eff}}{\mu}} \int_0^\infty e^{-\xi^2} \xi^5 \sigma_{mt} d\xi \quad (3.3.19)$$

is the energy exchange rate coefficient, with units $\text{cm}^3 \text{s}^{-1}$. It should be noted that while the energy exchange between the two species goes to zero as the temperatures equilibrate ($T_2 \approx T_1$), the energy exchange rate coefficient is still well defined and non-zero.

3.3.2 Time Evolution of the Average Test Particle Energy

The calculation of the energy exchange rate coefficients is motivated by two points. First, it provides a check on the calculation of the more complex double integral calculation of the product velocity distribution functions (PVDFs, calculated in the next section of this chapter). Second, we may calculate the time evolution of the average energy per test particle (species 1), given some initial energy and some (constant) background or bath temperature. Studying the time evolution for different momentum transfer cross sections allows us to compare how efficient various collision processes are in transferring energy.

We may re-write equation (3.3.18) as

$$\frac{1}{n_1n_2} \frac{\partial E_1}{\partial t} = k_E k(T_2 - T_1) \quad (3.3.20)$$

where E_1 is the total energy of all particles of species 1. We define $\hat{E}_1 = E_1/n_1 \equiv \frac{3}{2}kT_1$ as the average energy per particle (of species 1), and also define $E_{thermal} = \hat{E}_2$ as the (constant) average energy per particle (of species 1) at the background (species 2) temperature. Then, defining the ratio $E^* = \hat{E}_1/E_{thermal}$, we may write our energy evolution equation as

$$\frac{1}{n_2} \frac{\partial E^*}{\partial t} = \frac{k_E}{E_{thermal}} k(T_2 - T_1)$$

Since $E_{thermal} = \frac{3}{2}kT_2$, we find that this reduces to

$$\frac{1}{n_2} \frac{\partial E^*}{\partial t} = \frac{2}{3}k_E (1 - T_1/T_2)$$

Defining a dimensionless energy exchange rate coefficient $\hat{k}_E = k_E/k_o$, where k_o is some (arbitrary) reference value, and a dimensionless time, $\tau = At = n_2 k_o t$, our time dependent equation thus becomes

$$\frac{\partial E^*}{\partial \tau} = \frac{2}{3}\hat{k}_E (1 - E^*)$$

where we have used $E^* = \hat{E}_1/E_{thermal} = T_1/T_2$. This result may be discretized using a first order forward difference to yield

$$\begin{aligned} E_{i+1}^* &= E_i^* + \Delta\tau \frac{2}{3}\hat{k}_E (1 - E_i^*) \\ &= E_i^* + \Delta E_i^* \end{aligned} \tag{3.3.21}$$

Clearly, when $T_1 > T_2$, $\Delta E^* < 0$, and energy is transferred from species 1 to species 2, the background, and vice versa. As well, we note that when $T_1 \equiv T_2$, $\Delta E^* = 0$, and there is no further energy exchange (equilibrium). Thus, depending on the initial temperatures (energies) of the interacting species, we can have either relaxation (cooling) or excitation (heating) of species 1.

3.3.3 Results and Discussion

The calculation of the energy exchange rate coefficient, using equation (3.3.16), involves a single integral over the reduced relative velocity ξ . From a computational standpoint, this one-dimensional integral is much more efficient and accurate than the original triple integral of equation (3.3.1). The momentum transfer cross section(s) required for the ξ integration are calculated at 91 energies, from 1×10^{-4} to 10 eV, and at 361 angles (half degree increments), and are illustrated in Figure 3.25. The integral over $d\xi$ is done using a transformation to reduced energy, $z = \xi^2$, or

$$\int_0^\infty e^{-\xi^2} \xi^5 \sigma_{mt} d\xi = \frac{1}{2} \int_0^\infty e^{-z} z^2 \sigma_{mt} dz$$

and applying an interpolation scheme with z points located at the 91 energies used when calculating the differential cross section (the interpolation scheme is detailed in Appendix E).

We compute values of k_E , in units of cm^3s^{-1} , for several momentum transfer cross sections, corresponding to differential cross sections for elastic direct (DIR), charge exchange (CE), and the linear trajectory approximation (LTA) for the charge-exchange cross section. The temperatures of the ion-neutral pairs are chosen to approximate the observed or estimated range of temperatures for exospheric conditions on the terrestrial planets (Venus, Earth and Mars).^{5,148}

For hydrogen-proton collisions, Table 3.5 summarizes the results for the DIR, CE, and LTA cross sections for several combinations of hydrogen and proton temperatures. We note that the LTA cross section overestimates the energy exchange rate coefficient for charge exchange by approximately 30% for all combinations of proton and hydrogen temperatures. We observe a uniformly monotonic increase in the energy exchange rate coefficient for all cross sections as the hydrogen temperature is increased for a fixed proton temperature except for the direct (DIR) elastic interaction, which remains roughly

T[H ⁺]	Cross Section	T[H]		
		500	1000	1500
6000	DIR	2.30	2.29	2.28
	CE	8.87	9.19	9.51
	LTA	11.12	11.43	11.74
4000	DIR	2.27	2.29	2.30
	CE	7.47	7.84	8.19
	LTA	9.67	10.06	10.43
2000	DIR	2.07	2.14	2.19
	CE	5.82	6.27	6.69
	LTA	7.80	8.33	8.81

Table 3.5: Energy exchange rate coefficients for several H⁺-H cross sections. The temperatures of both hydrogen and the protons, in degrees Kelvin, are indicated in the table. The tabulated values of the energy exchange rate coefficients are in units of 10⁻⁹ cm³ s⁻¹.

T[H ⁺]	Cross Section	T[H]		
		500	1000	1500
6000	DIR	20.78	20.48	19.90
	LTA	22.07	21.27	20.99
4000	DIR	17.67	17.77	17.50
	LTA	18.58	18.16	18.08
2000	DIR	13.23	13.70	16.02
	LTA	13.71	14.02	16.72

Table 3.6: Energy exchange rate coefficients for several H⁺-H cross sections as reported by Hodges and Breig.⁷³ The temperatures of both hydrogen and the protons, in degrees Kelvin, are indicated in the table. The tabulated values of the energy exchange rate coefficients have been converted to units of 10⁻⁹ cm³ s⁻¹ for comparison with Tables 3.5 and 3.12.

constant for all temperatures considered.

The results for hydrogen-proton collisions may also be compared with the work of Hodges and Breig,⁷³ which is summarized in Table 3.6. Comparing tabulated values for the LTA we note that there is a discrepancy between their results and the present work, on the order of a factor of roughly 1.6 to 1.9. It should also be noted that while Hodges and Breig designate the elastic cross section as the regular 'direct' elastic collision cross section, it appears that they have mislabelled it, and in fact those results are for the DPE collision cross section. If we sum the DIR and CE rate coefficients in Table 3.5 to yield the DPE result, we get a similar discrepancy as with the LTA. The calculation of the energy exchange rate coefficients is repeated in an independent calculation later in this chapter, and the same discrepancy is observed; it is unclear as to its origin. It may be a systematic statistical problem with their Monte Carlo integration scheme, but without repeating their calculation exactly this is difficult to determine absolutely. The cross sections from both works have been compared and show excellent agreement, so that cannot be the source of the discrepancy. In addition, their LTA results exhibit strange variation as the hydrogen temperature is changed for a fixed proton temperature. For a proton temperature of 2000 K, the LTA rate coefficient appears to increase with increasing hydrogen temperature; however, for a proton temperature of 4000 K, the rate coefficient appears to increase then decrease, and for a proton temperature of 6000 K the rate coefficient decreases. The results of the current work show a uniform increase in the energy exchange rate coefficient as the hydrogen temperature is increased, regardless of the proton temperature or the cross section used, with exception of the DIR interaction. In order to determine which behaviour was correct, we fitted the momentum transfer cross section for the LTA with a power law of the form

$$\sigma_{mt}(E) = aE^p$$

where E is the energy in eV, and $\sigma_{mt}(E)$ is in \AA^2 . Several sets of parameters were assessed to fit $\sigma_{mt}(E)$, and are illustrated in Figure 3.30. The solid curve is the true LTA momentum transfer cross section. The short dashed, long dashed, and dot-dashed curves represent values of a and p corresponding to 83/-0.28, 80/-0.35, and 40/-0.45 respectively. These fits attempt to account for the sharp increase in the LTA cross section at low energy. A fourth fit, given by the dot-dot-dashed curve and corresponding to fit parameters of 91/-0.12, respectively, fits only the high energy portion of the cross section.

With this form of the momentum transfer cross section, the integral in equation (3.3.19) may be carried out analytically to yield an energy exchange rate coefficient of the form

$$k_E = \frac{4\mu}{\pi m_o} \sqrt{\frac{2\pi k T_{eff}}{\mu}} A (k T_{eff})^p \Gamma(p+3)$$

where Γ is the standard gamma function. The energy exchange rate coefficients as a function of the effective temperature, T_{eff} , are plotted in Figure 3.31.

Regardless of the fit, it appears that for the LTA cross section we find that the energy exchange rate coefficient increases monotonically with an increase in the effective temperature, T_{eff} , verifying the pattern seen in Table 3.5.

The dependence of the rate coefficients with the bath and test particle temperatures, T_2 and T_1 , is shown in Figure 3.32. The solid curve is for the DPE cross section and the dashed curve is for the CE cross section. A (constant) value of $T_1 = 1500$ K is used for both curves. The values of $k_E(T_1, T_2)$ are normalized by the value of $k_E(T_2 = T_1)$, and so the relative magnitudes of the DPE and CE curves cannot be compared directly. From the figure we see that the energy exchange rate coefficients increase almost uniformly.

The disparate masses of the two collision partners makes the identification of the hot atom and background important for deuterium-proton collisions. The energy exchange rate coefficient, as given by equation (3.3.19), is explicitly dependent on the effective

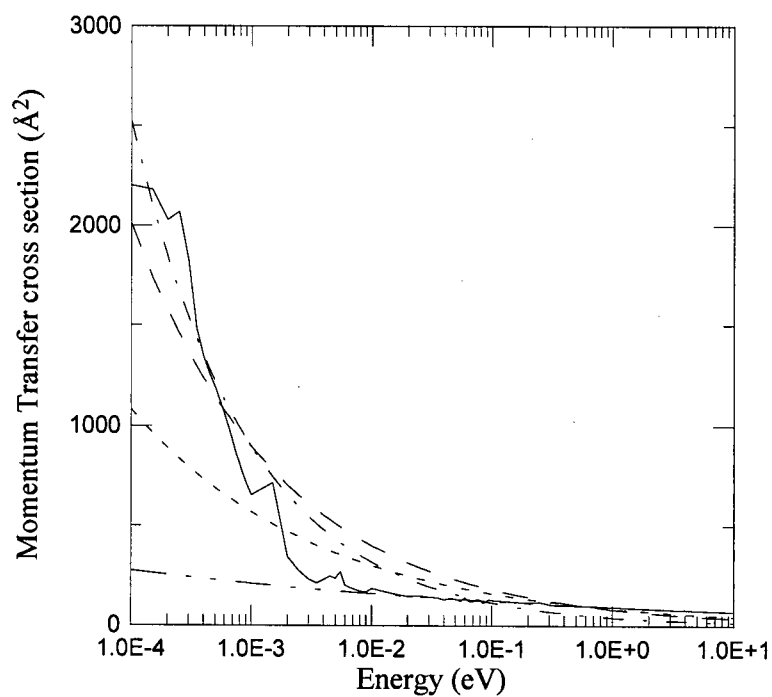


Figure 3.30: Fits to the LTA momentum transfer cross section. The solid curve is the true LTA momentum transfer cross section. The short dashed, long dashed, dot-dashed and dot-dot-dashed curves represent fit parameters a and p corresponding to 83/-0.28, 80/-0.35, 40/-0.45 and 91/-0.12 respectively.

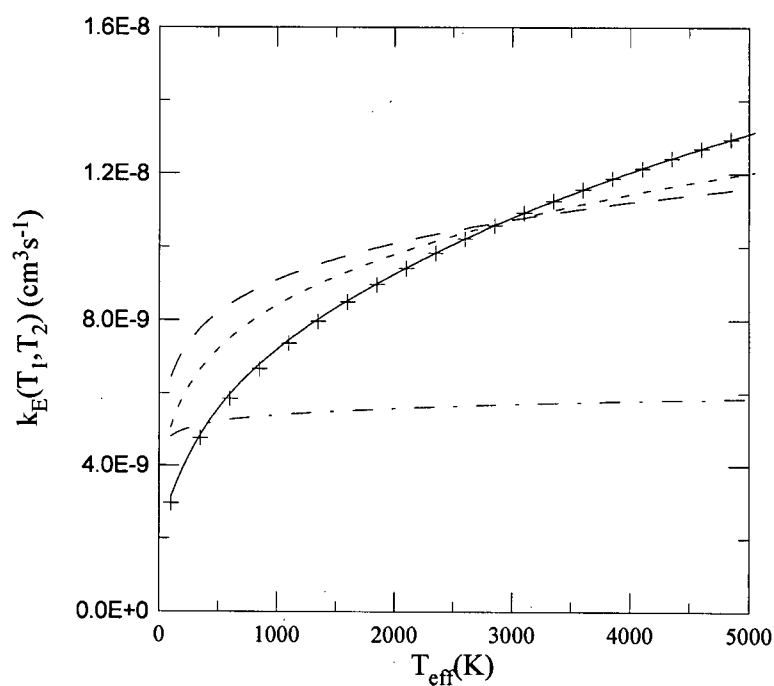


Figure 3.31: Temperature dependence of k_E for the LTA . The solid curve is the true LTA momentum transfer cross section. The short dashed, long dashed and dot-dashed curves represent fit parameters a and p corresponding to 83/-0.28, 80/-0.35 and 40/-0.45 respectively. The plus symbols correspond to a fit with parameters 91/-0.12.

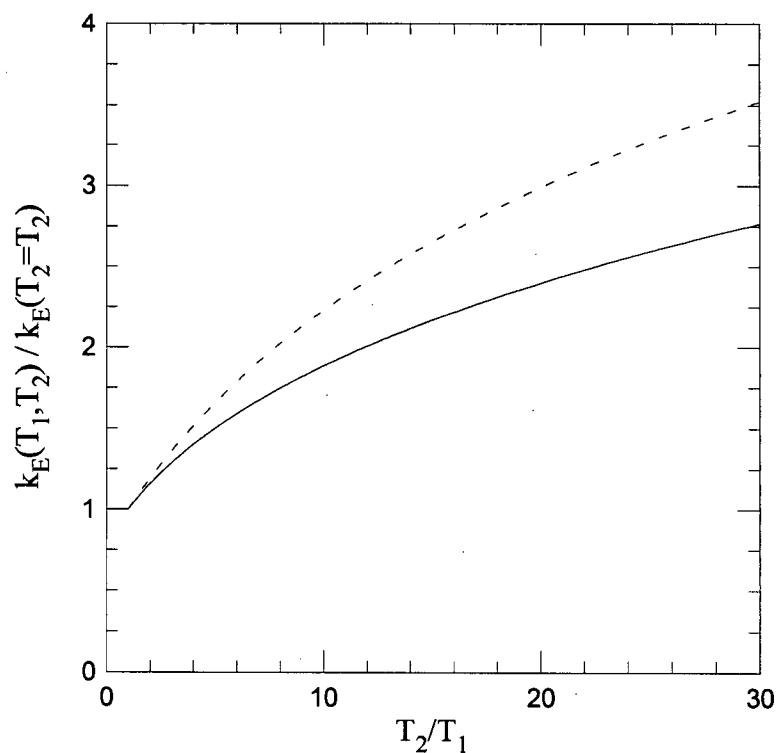
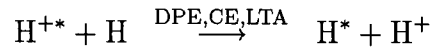


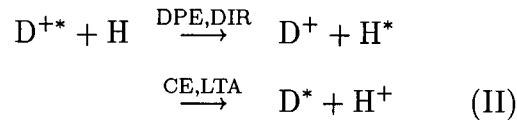
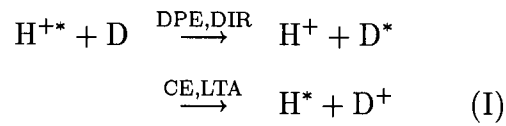
Figure 3.32: Dependence of energy exchange rate coefficients on bath temperature for H^+-H . The value of $k_E(T_1, T_2)$ is plotted relative to the value of $k_E(T_2 = T_1)$ as a function of T_2 for fixed values of T_1 . The solid curve is for the direct-plus-exchange (DPE) cross section, dashed curve for the charge exchange (CE) cross section. A constant temperature $T_1 = 1500$ K is used for both curves.

temperature, T_{eff} through the factor $\sqrt{\frac{2\pi k T_{eff}}{\mu}}$. In addition, k_E is implicitly dependent on the effective temperature through the definition of ξ , as mentioned in connection with the momentum transfer cross section appearing in equation (3.3.19).

For hydrogen-proton collisions, we had merely to consider a single process for the formation of hot hydrogen, as given by equation (3.1.1),



However, to produce hot deuterium, we have from processes given in equations (3.1.4) and (3.1.5) that



where the labels DPE, DIR, CE, LTA indicate the types of processes which produce the products on the right-hand side of the reaction. In each case, we consider the neutral reactant as species 1 (test particle) and the ion reactant as species 2 (bath). Thus, process I above can have two different sets of products, depending on the type of cross section considered; the same is true for process II.

We tabulate the energy exchange rate coefficients for the above processes in Table 3.7. Columns labeled 'I' refer to the reaction given by the processes labeled I above, while columns labeled 'II' refer to the reaction given by the processes labeled II above. Thus, a DIR reaction which is labeled 'I' refers to the first branch of process I, while a CE reaction labeled 'II' refers to the second branch of process II. It should be noted that entries for DIR 'II' and CE/LTA 'I' are thus representative of the transfer of energy to

T[ion]	Cross Section	T[neutral]					
		500		1000		1500	
		I	II	I	II	I	II
6000	DIR	1.741	1.76	1.731	1.78	1.72	1.78
	CE	8.026	6.098	8.812	6.482	8.336	6.850
	LTA	9.714	7.790	9.861	8.193	10.00	8.568
4000	DIR	1.78	1.69	1.781	1.73	1.78	1.76
	CE	6.667	5.259	6.849	5.691	7.027	6.097
	LTA	8.382	6.870	8.567	7.351	8.745	7.789
2000	DIR	1.663	1.55	1.691	1.63	1.72	1.69
	CE	5.027	4.241	5.258	4.784	5.478	5.258
	LTA	6.606	5.693	6.868	6.327	7.116	6.869

Table 3.7: Energy exchange rate coefficients for several H^+ -D cross sections. The temperatures of both deuterium and the protons, in degrees Kelvin, are indicated in the table. Values under columns marked 'I' are for reactions where the test particle is the deuterium atom, with a bath of hot protons; values under columns marked 'II' are for reactions where the test particle is hydrogen, with a bath of hot deuterium ions. The tabulated values of the energy exchange rate coefficients are in units of $10^{-9} \text{ cm}^3 \text{ s}^{-1}$.

produce hot hydrogen atoms, rather than hot deuterium atoms, via reactions with hot deuterium ions.

Comparing values from Tables 3.5 and 3.7, we observe that energy exchange rate coefficients corresponding to production of hot deuterium via DIR collisions with protons are approximately 80-90% of the corresponding value for hydrogen-proton production of hot hydrogen. For CE/LTA collisions, the deuterium energy exchange rate coefficients are approximately 70-80% of the hydrogen-proton values. We believe this is due to the less efficient transfer of energy between particles of disparate masses.

The dependence of the rate coefficients with the bath and test particle temperatures, T_2 and T_1 , for deuterium and hydrogen is shown in Figure 3.33. The solid curve is for the

DIR cross section and the dashed curves is for the CE cross section. A constant value of $T_1 = 500$ K is used in the calculation of both curves. The values of $k_E(T_1, T_2)$ are normalized by the value of $k_E(T_2 = T_1)$. From a comparison with Figure 3.32, we can see that the behaviour of the DIR curve is very different from that for the hydrogen-proton system. At first it was thought that the curvature of the DIR curve was due to numerical error, such as poor convergence in the integration of equation 3.3.19. To eliminate this possibility, the details of the integrands and convergence of the integration yielding the rate coefficients were examined. The results are shown in Figures 3.34 and 3.35. Since the integrands are well behaved and the convergence of the integral is smooth, we deduce that the result is in fact physical and not numeric. It may simply be a result of the change in efficiency of energy transfer for colliding partners of disparate mass.

The energy exchange rate coefficients for O-H and O-D direct elastic collisions are tabulated in Table 3.8. We can see immediately that the energy exchange is much less efficient for these systems than for hydrogen-proton and deuterium-proton systems, owing to the very large difference in mass between the O-H and O-D colliding pairs. The energy exchange rate coefficients for O-D are larger than those for O-H, reflecting the larger mass of deuterium and the larger reduced mass of the O-D system.

We may, as mentioned in the preceding section, calculate the time evolution of the average energy of species 1 using equation (3.3.21). We chose three temperature pairs from those used for the calculation of the energy exchange rate coefficient: $T_{H^+} = 6000$ K/ $T_H = 500$ K, $T_{H^+} = 4000$ K/ $T_H = 1000$, and $T_{H^+} = 2000$ K/ $T_H = 1500$. These were chosen as they represented the full range of possible temperature ratios previously considered. In addition, we have examined both the case where, initially, $T_1 > T_2$ and where $T_2 > T_1$. In plotting the results, we have used dimensionless time units

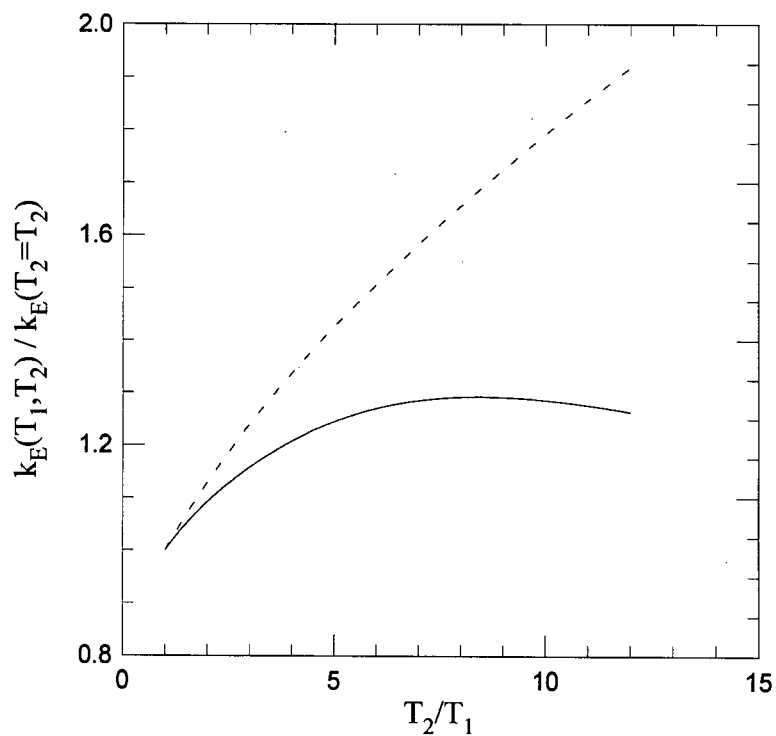


Figure 3.33: Dependence of energy exchange rate coefficients on bath temperature for D^+-H . The value of $k_E(T_1, T_2)$ is plotted relative to the value of $k_E(T_2 = T_1)$ as a function of T_2 for a fixed value of $T_1 = 500$ K. The solid curve is for the direct elastic (DIR) cross section, the dashed curve for the charge exchange (CE) cross section.

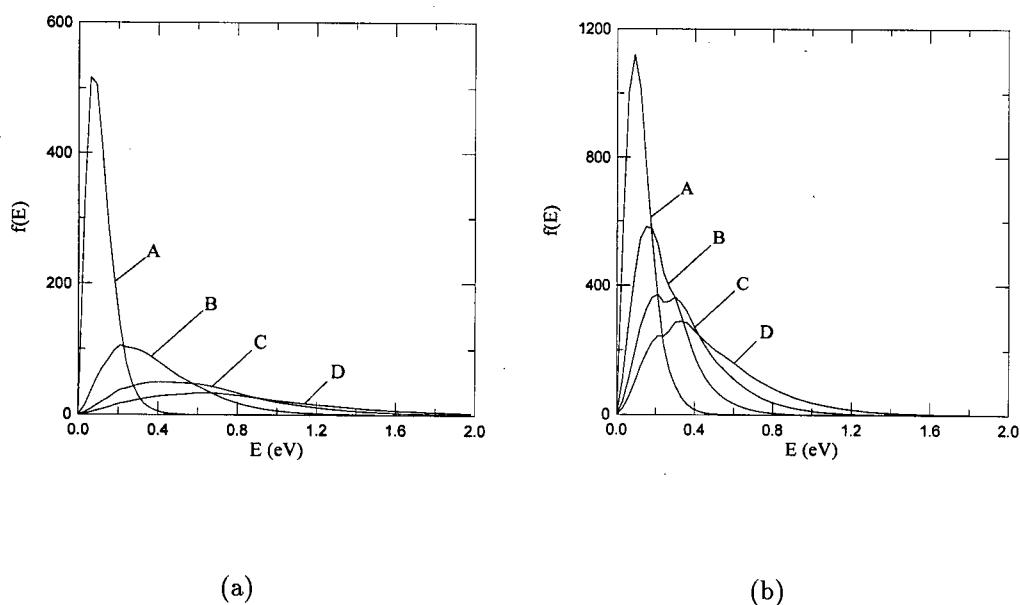


Figure 3.34: Details of the integrand in calculation of the energy exchange rate coefficient for DH^+ . The neutral temperature, T_1 , is in both cases fixed at 500 K. In (a), the deuterium ion temperature is fixed at values of 500, 1875, 3250 and 4625 K, corresponding to the labels A-D, respectively. In (b), the proton temperature is fixed at 500, 2333, 4166 and 6000 K, corresponding to the labels A-D, respectively.

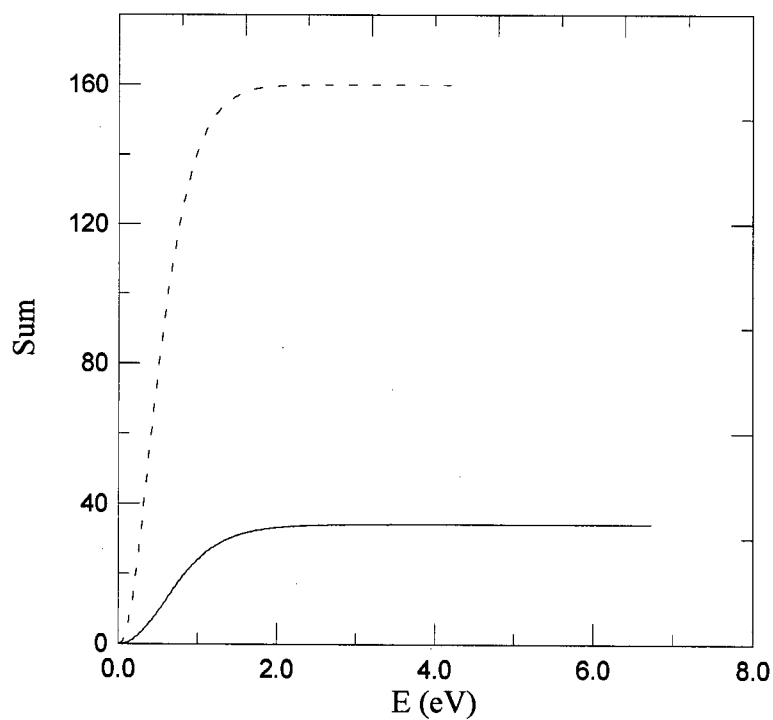


Figure 3.35: Convergence of the energy exchange rate coefficient for DH^+ . The solid curve is for the DIR cross section, the dashed curve for CE. The sum of the integration to calculate the energy exchange rate coefficient, as a function of energy, is shown for the highest T_2 temperatures of Figure 3.34.

T[O]	Cross Section	T[H] or T[D]		
		500	1000	1500
6000	OH	0.179	0.207	0.226
	OD	0.258	0.284	0.303
4000	OH	0.170	0.201	0.222
	OD	0.241	0.272	0.294
2000	OH	0.159	0.194	0.217
	OD	0.219	0.258	0.284

Table 3.8: Energy exchange rate coefficients for O-H and O-D direct elastic cross sections. The temperatures of O and H/D, in degrees Kelvin, are indicated in the table. The tabulated values of the energy exchange rate coefficients are in units of $10^{-9} \text{ cm}^3 \text{ s}^{-1}$.

corresponding to those used by Clarke and Shizgal,⁷²

$$\tau_{cs} = A t$$

where

$$A = n_2 \sigma_o \sqrt{32\pi k T_2 / m}$$

and where $\sigma_o = 1 \text{ cm}^2$. If we choose $n_2 = 1 \text{ cm}^{-3}$, then for a background of hydrogen at 500, 1000, and 1500 K we find values of A corresponding to 2.04, 2.88 and $3.53 \times 10^6 \text{ s}^{-1}$; hence, a unit of τ is of the order of sub-microseconds of real time for these choices of parameters.

Comparing the definition with that given for τ in equation (3.3.21), we immediately see that

$$\tau_{cs} = \frac{\tau \sigma_o}{k_o} \sqrt{32\pi k T_2 / m}$$

For the case of $T_1 > T_2$, we choose the protons as species 1, and hydrogen as the bath. The results are plotted in Figure 3.36. For the case of $T_1 > T_2$, we choose hydrogen

as species 1, and the proton as the bath; the results are plotted in Figure 3.37. It is clear from the figures that the rate of energy transfer depends on the initial temperature (energy) ratio; as is indicated by the energy exchange rate coefficients of Table 3.5, as the temperature disparity becomes more pronounced, the rate at which energy is exchanged between the components increases, and the rate at which cooling or heating occurs is greater than for smaller temperature differences.

As in Clarke and Shizgal,⁷² we define two timescales to better quantify the time evolution process. For a cooling (relaxation) system, we define $\tau_{1/e}$ as the time required for the energy ratio, $E/E_{thermal}$, to decay to $1/e$ of its original value, and $\tau_{1.1}$ as the time it takes for the energy ratio to decay to 1.1. For a heating (excitational) system, we define $\tau_{1/e}$ as the time for the energy ratio to increase to e times its original value, and $\tau_{1.1}$ as the time it takes for the energy ratio to reach $1/1.1 = 0.91$. These timescales are tabulated for both cases in Tables 3.9 and 3.10.

As a check of our time evolution calculations, we compared energy relaxation times for protons with initial energies of 0.646eV (4993 K) and 1.27eV (9816 K) in a hydrogen bath at 298K, using both the cross sections given previously in this chapter and those used by Clarke and Shizgal.⁷² The time evolution results are illustrated in Figure 3.38, while a comparison of relaxation times is given in Table 3.11.

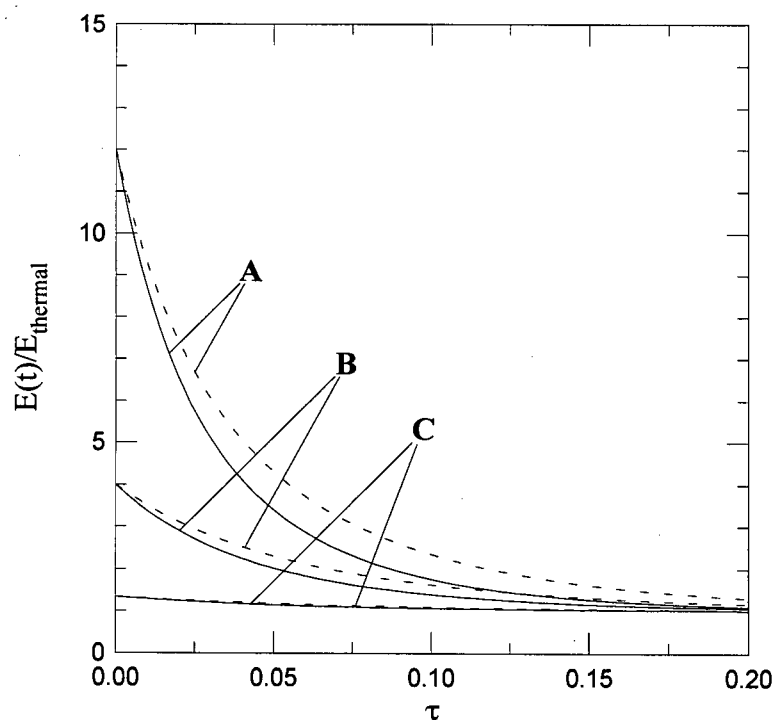


Figure 3.36: Time evolution of the average energy in a relaxing H^+ -H system. Solid curves are for the direct-plus-exchange (DPE) cross section, dashed curves for the charge exchange (CE) cross section. Time is in reduced dimensionless units τ , corresponding to those used by Clarke and Shizgal.⁷² The labels A, B, and C correspond to proton/hydrogen temperatures of 6000 K/500 K, 4000 K/1000 K, 2000 K/1500 K, respectively.

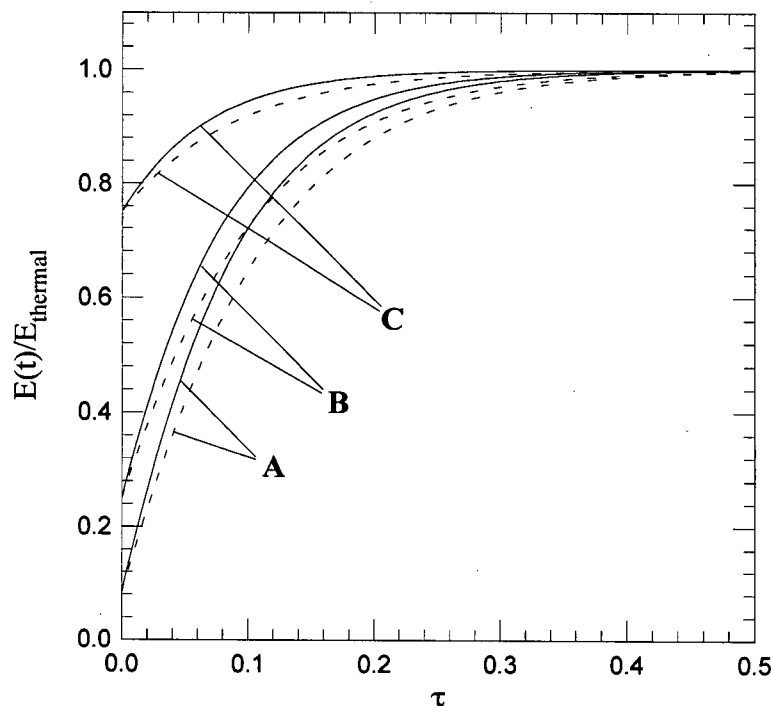


Figure 3.37: Time evolution of the average energy in a heating $\text{H}^+\text{-H}$ system. Solid curves are for the direct-plus-exchange (DPE) cross section, dashed curves for the charge exchange (CE) cross section. Time is in reduced dimensionless units τ , corresponding to those used by Clarke and Shizgal.⁷² The labels A, B, and C correspond to proton/hydrogen temperatures of 6000 K/500 K, 4000 K/1000 K, 2000 K/1500 K, respectively.

T[H ⁺]	Cross Section	T[H]					
		500		1000		1500	
		$\tau_{1/e}$	$\tau_{1.1}$	$\tau_{1/e}$	$\tau_{1.1}$	$\tau_{1/e}$	$\tau_{1.1}$
6000	DPE	0.0158	0.188				
	CE	0.0197	0.226				
	LTA	0.0158	0.189				
4000	DPE			0.0680	0.162		
	CE			0.0864	0.203		
	LTA			0.0684	0.162		
2000	DPE					n/a	0.0683
	CE					n/a	0.0904
	LTA					n/a	0.0688

Table 3.9: Timescales for the time evolution of the average energy of H for several H⁺-H cross sections. The temperatures of both hydrogen and the protons, in degrees Kelvin, are indicated in the table. The tabulated values are timescales, in dimensionless units, for H being heated by H⁺ (i.e. timescales are for the time evolution of the average energy of the hydrogen). An entry of 'n/a' means that the particular timescale is not applicable for those particular temperatures. The timescales are defined in the text. The dimensionless time units are those of Clarke and Shizgal,⁷² $\tau = A t$, where A is defined in the text and is of the order of $2.04 - 3.53 \times 10^6 \text{ s}^{-1}$.

T[H ⁺]	Cross Section	T[H]					
		500		1000		1500	
		$\tau_{1/e}$	$\tau_{1.1}$	$\tau_{1/e}$	$\tau_{1.1}$	$\tau_{1/e}$	$\tau_{1.1}$
6000	DPE	0.0381	0.206				
	CE	0.0500	0.287				
	LTA	0.0383	0.209				
4000	DPE			0.0921	0.180		
	CE			0.1228	0.243		
	LTA			0.0929	0.182		
2000	DPE					n/a	0.0733
	CE					n/a	0.0977
	LTA					n/a	0.0739

Table 3.10: Timescales for the time evolution of the average energy of H⁺ for several H⁺-H cross sections. The temperatures of both hydrogen and the protons, in degrees Kelvin, are indicated in the table. The tabulated values are timescales, in dimensionless units, H⁺ being cooled by H (i.e. timescales are for the time evolution of the average energy of the protons). An entry of 'n/a' means that the particular timescale is not applicable for those particular temperatures. The timescales are defined in the text. The dimensionless time units are those of Clarke and Shizgal,⁷² $\tau = A t$, where A is defined in the text and is of the order of $2.04 - 3.53 \times 10^6 \text{ s}^{-1}$.

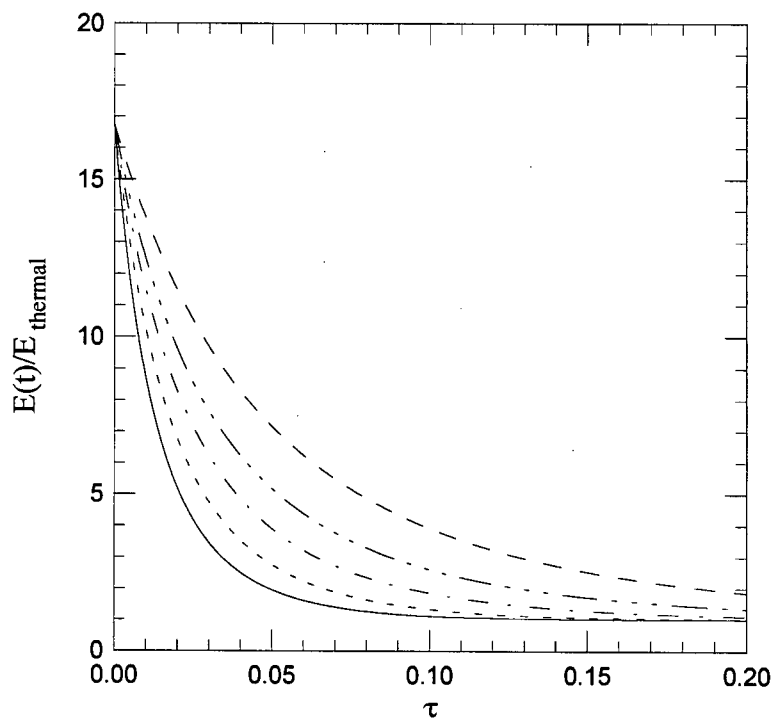


Figure 3.38: Comparison of the time evolution of the average proton energy. The average energy per proton divided by the average energy per proton at the bath temperature is plotted against dimensionless time units τ corresponding to those used by Clarke and Shizgal.⁷² In all cases, the initial average energy per proton is taken to be 0.646 eV (approx. 4993 K), and the (constant) background temperature is 298 K. The solid, short dashed, and long dashed curves represent the time evolution of the energy ratio for the DPE, CE, and direct (D) cross sections, respectively, as calculated using cross sections as defined in Clarke and Shizgal. The dash-dot and dash-dot-dot-dot curves represent the time evolution for DPE and CE cross sections, respectively, as calculated using cross sections as defined previously in this chapter.

	$E_o = 0.646 \text{ eV}$		$E_o = 1.27 \text{ eV}$	
	$\tau_{1/e}$	$\tau_{1.1}$	$\tau_{1/e}$	$\tau_{1.1}$
DPE	0.030	0.202	0.023	0.216
CE	0.040	0.291	0.029	0.309
LTA	0.031	0.205	0.023	0.219
DPE [†]	0.016	0.103	0.012	0.111
CE [†]	0.022	0.137	0.017	0.148
LTA2 [†]	0.006	0.050	0.004	0.053
DPE [‡]	0.016	0.080	0.012	0.077
CE [‡]	0.022	0.105	0.030	0.101
LTA2 [‡]	0.006	0.029	0.004	0.024

Table 3.11: Comparison of timescales for the time evolution of the average energy per proton for the H^+ -H system. The (constant) temperature of the background H is taken as 298 K, and the initial proton energy is 0.646 eV (approx. 4993 K). The values reported in the table are the timescales $\tau_{1/e}$ and $\tau_{1.1}$, defined in the text, for the DPE and CE cross sections defined previously. The DPE, CE, LTA entries are for calculations using cross sections from this work, DPE, CE, LTA2 entries marked [†] are calculations using cross sections from Clarke and Shizgal, and DPE, CE, LTA2 entries marked [‡] are the reported results from Clarke and Shizgal.⁷² All times are reported in the dimensionless time units of Clarke and Shizgal, $\tau = A t$, defined in the text.

3.4 Product Velocity Distribution Functions

3.4.1 Theory

The rate of production, Q , of fast moving particles depends on the rate of binary encounters between the two species involved in a collision and on the velocity distribution functions of the two species. We therefore write that²⁶

$$Q(r, c_1) = n_1(r)n_2(r) \iint f_1(r, \mathbf{c}'_1)f_2(r, \mathbf{c}'_2)g\sigma(g, \Omega') d\Omega' d\mathbf{c}_2 \quad (3.4.1)$$

where g , Ω' and $\sigma(g, \Omega')$ are as defined previously in Chapter 1. The units of $Q(r, c_1)$, above, are $\text{cm}^{-6} \text{s}^2$. The densities of the collision pair are $n_1(c)$ and $n_2(c)$ and their distribution functions are $f_1(r, \mathbf{c}'_1)$ and $f_2(r, \mathbf{c}'_2)$, respectively. Altitude dependence enters through the density profiles n_1 and n_2 and the temperature profiles, $T(r)$, contained in the distribution functions. The differential cross section, $\sigma(g, \Omega')$, is required in equation (3.4.1), and plays an important role in the velocity dependence of $Q(r, c_1)$. We call $Q(r, c_1)$ the product velocity distribution function (PVDF) for species 1.

It should also be noted that the distributions in equation (3.4.1) are for the incoming (or pre-collisional) particles, and the integration is over the velocity of the product ion (for a reaction of the type specified by processes (3.1.1) or (3.1.4), for example). With the kinematics of the collision, the velocities of the products ($\mathbf{c}_1, \mathbf{c}_2$) can be related to the velocities of the reactants ($\mathbf{c}'_1, \mathbf{c}'_2$) so that $Q(r, c_1)$ is a function of the velocity of the translationally energetic product. The hot atom production is thus due to 'inverse' collisions, with the primes denoting the atom velocities before collision. A schematic of the collision process is shown in Figure 3.39.

In fact, it is clear from equations (1.4.2) and (3.4.1) that the rate of production, $Q(r, c_1)$ is identical to the 'gain' (inverse) term of the Boltzmann collision operator. A difficulty in the calculation of $Q(r, c_1)$ is that in general the distribution functions

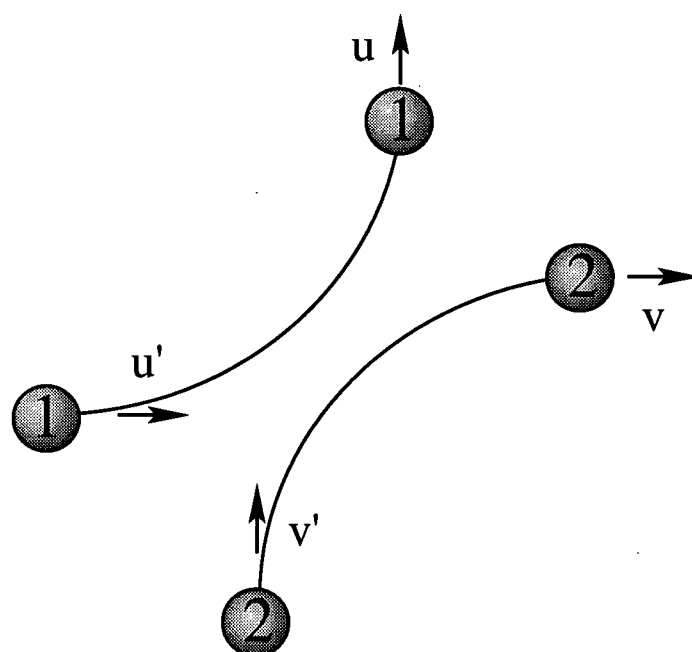


Figure 3.39: Schematic of an elastic binary collision. Particles 1 and 2 enter into an elastic collision with velocities u' and v' , and leave with velocities u and v , respectively.

of nonthermal species are far from equilibrium and are not Maxwellian. However, in order to render the problem tractable it is assumed that the two species are adequately described by Maxwellian distributions at different temperatures,

$$f_i(c'_i) = \left(\frac{m_i}{2\pi kT_i} \right)^{\frac{3}{2}} \exp \left[-\frac{m_i c'^2_i}{2kT_i} \right]$$

Substituting this form for the distribution functions in equation (3.4.1), we have, for some fixed altitude r ,

$$Q(c_1) = n_1 n_2 \left(\frac{\sqrt{\lambda_1 \lambda_2}}{\pi} \right)^3 \iint e^{-\lambda_1 c_1'^2 - \lambda_2 c_2'^2} g \sigma d\Omega' d\mathbf{c}_2 \quad (3.4.2)$$

where we have defined $\lambda_i = m_i/2kT_i$. For a fixed value of the velocity \mathbf{c}_1 , we have

$$\mathbf{c}_2 = \mathbf{g} + \mathbf{c}_1$$

$$d\mathbf{c}_2 = d\mathbf{g}$$

$$d\mathbf{g} = g^2 dg d\Omega$$

where $d\Omega$ is the solid angle about the direction of \mathbf{g} . With these changes, we may write

$$Q(c_1) = n_1 n_2 \left(\frac{\sqrt{\lambda_1 \lambda_2}}{\pi} \right)^3 K(c_1) \quad (3.4.3)$$

where

$$K(c_1) = \iint e^{-\lambda_1 c_1'^2 - \lambda_2 c_2'^2} g^3 \sigma d\Omega' d\Omega dg \quad (3.4.4)$$

As in the section detailing the calculation of the energy exchange rate coefficients, we have \mathbf{G} as the center of mass velocity, and \mathbf{g}' and \mathbf{g} as the relative velocities before and after a particle cross section. If we substitute for \mathbf{G} into the expressions for the particle velocities, as given by equation (3.3.6), we find

$$\mathbf{c}'_1 = \mathbf{c}_1 + M_2(\mathbf{g} - \mathbf{g}')$$

$$\mathbf{c}'_2 = \mathbf{c}_1 + M_1\mathbf{g}' + M_2\mathbf{g}$$

Squaring these expressions yields

$$\begin{aligned} c_1'^2 &= c_1^2 + M_2^2(g^2 + g'^2 - 2\mathbf{g} \cdot \mathbf{g}') + 2M_2(\mathbf{c}_1 \cdot \mathbf{g} - \mathbf{c}_1 \cdot \mathbf{g}') \\ c_2'^2 &= c_1^2 + (M_2^2g^2 + M_1^2g'^2 + 2M_1M_2\mathbf{g} \cdot \mathbf{g}') + 2(M_2\mathbf{c}_1 \cdot \mathbf{g} + M_1\mathbf{c}_1 \cdot \mathbf{g}') \end{aligned}$$

and so

$$\lambda_1 c_1'^2 + \lambda_2 c_2'^2 = Ac_1^2 + Bg^2 + \alpha\mathbf{c}_1 \cdot \mathbf{g} + \beta\mathbf{c}_1 \cdot \mathbf{g}' + \gamma\mathbf{g} \cdot \mathbf{g}' \quad (3.4.5)$$

where we have used conservation of energy, $g \equiv g'$, and made the definitions

$$\begin{aligned} A &= \lambda_1 + \lambda_2 \\ B &= 2M_2^2\lambda_1 + (M_1^2 + M_2^2)\lambda_2 \\ \alpha &= 2M_2(\lambda_1 + \lambda_2) \\ \beta &= 2(M_1\lambda_2 - M_2\lambda_1) \\ \gamma &= 2M_2(M_1\lambda_2 - M_2\lambda_1) \end{aligned} \quad (3.4.6)$$

Substituting equation (3.4.5) into equation (3.4.4), we have

$$K(c_1) = e^{-Ac_1^2} \int_0^\infty g^3 e^{-Bg^2} J(g, c_1) dg \quad (3.4.7)$$

where

$$\begin{aligned} J(g, c_1) &= \iint e^{-[\alpha\mathbf{c}_1 \cdot \mathbf{g} + \beta\mathbf{c}_1 \cdot \mathbf{g}' + \gamma\mathbf{g} \cdot \mathbf{g}']} \sigma^*(g, \Omega') d\Omega' d\Omega \\ &= \int_\Omega e^{-\alpha\mathbf{c}_1 \cdot \mathbf{g}} J_{\Omega'} d\Omega \end{aligned} \quad (3.4.8)$$

and

$$J_{\Omega'} = \int_{\Omega'} e^{-[\beta\mathbf{c}_1 \cdot \mathbf{g}' + \gamma\mathbf{g} \cdot \mathbf{g}']} \sigma(g, \Omega') d\Omega' \quad (3.4.9)$$

In equation (3.4.9), it should be noted that the solid angle $d\Omega'$ is about the direction of \mathbf{g}' , whereas $d\Omega$ is about the direction of \mathbf{g} . The geometry is illustrated in Figure 3.40.

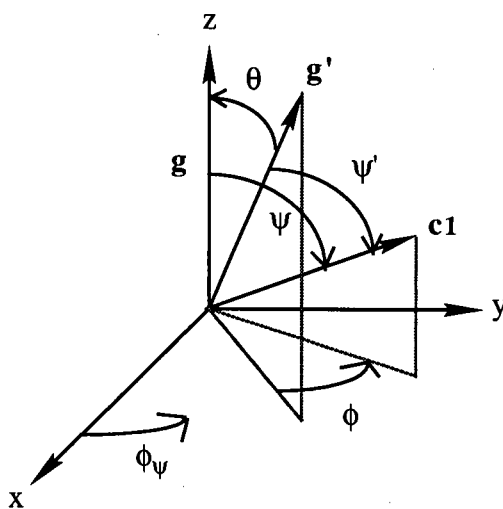


Figure 3.40: Coordinate system for the calculation of collisional production. The direction of g is taken as the polar direction.

Using the above geometry and the addition theory for non-coplanar angles,¹⁴⁹

$$\cos \psi' = \cos \theta \cos \psi + \sin \theta \sin \psi \cos \phi$$

we may write equation (3.4.9) as

$$J_{\Omega'} = \int_0^\pi J_\phi e^{-\gamma g^2 \cos \theta - \beta c_1 g \cos \theta \cos \psi} \sigma(g, \theta) d(\cos \theta) \quad (3.4.10)$$

where we have used the definition of the solid angle, $d\Omega' \equiv \sin \theta d\theta d\phi$, and made the definition

$$\begin{aligned} J_\phi &= \int_0^{2\pi} e^{-\beta c_1 g \sin \theta \sin \psi \cos \phi} d\phi \\ &= 2\pi I_0(\beta c_1 g \sin \theta \sin \psi) \end{aligned}$$

where $I_0(z)$, the modified Bessel function of order zero,¹⁵⁰ is given by

$$I_0(z) = \frac{1}{\pi} \int_0^\pi e^{\pm z \cos \theta} d\theta$$

If we substitute all of the above intermediate results into equation (3.4.8), and use the definition $d\Omega \equiv \sin \theta_\psi d\theta_\psi d\phi_{psi}$, we have

$$J(g, c_1) = (2\pi)^2 \int_0^\pi e^{-\gamma g^2 \cos \theta} \sigma(g, \theta) K_\psi d(\cos \theta) \quad (3.4.11)$$

where

$$\begin{aligned} K_\psi &= \int_0^\pi e^{-D_1 \cos \psi} I_0(D_2 \sin \psi) d(\cos \psi) \\ D_1 &= \alpha g c_1 + \beta g c_1 \cos \theta \\ D_2 &= \beta g c_1 \sin \theta \\ D_1^2 + D_2^2 &= g^2 c_1^2 (\alpha^2 + \beta^2 + 2\alpha\beta \cos \theta) \end{aligned}$$

The integral K_ψ may be done analytically,¹⁵¹ yielding

$$K_\psi = \frac{2 \sinh(\sqrt{D_1^2 + D_2^2})}{\sqrt{D_1^2 + D_2^2}}$$

If we now combine equations (3.4.12), (3.4.11), (3.4.7) and (3.4.3), we have

$$\begin{aligned}
 Q(c_1) &= n_1 n_2 \left(\frac{\sqrt{\lambda_1 \lambda_2}}{\pi} \right)^3 2(2\pi)^2 e^{-Ac_1^2} \frac{1}{c_1} \int_0^\infty g^3 e^{-Bg^2} \hat{J}(g, c_1) dg \\
 \hat{J}(g, c_1) &\equiv \frac{J(g, c_1)}{2(2\pi)^2 c_1} \\
 &= \int_0^\pi e^{-\gamma g^2 \cos \theta} \sigma(g, \theta) \frac{\sinh(g c_1 \sqrt{\alpha^2 + \beta^2 + 2\alpha\beta \cos \theta})}{g \sqrt{\alpha^2 + \beta^2 + 2\alpha\beta \cos \theta}} d(\cos \theta) \quad (3.4.12)
 \end{aligned}$$

Before implementing the result of equation (3.4.12), we wish to non-dimensionalize our various parameters. We define the velocity $v_o \equiv 2kT^*/m^*$, where T^*, m^* are arbitrary temperature and mass values, and then define dimensionless variables $x \equiv c_1/v_o$, $z \equiv g/v_o$, $A' \equiv Av_o^2$, $B' \equiv Bv_o^2$, $\alpha' \equiv \alpha v_o^2$, $\beta' \equiv \beta v_o^2$, $\gamma' \equiv \gamma v_o^2$, and $\sigma' \equiv \sigma/\sigma_o$, where $A, B, \alpha, \beta, \gamma$ are defined previously in equation (3.4.6), and σ_o is some factor chosen to non-dimensionalize the differential cross section. With these definitions we may now write equation (3.4.12) as

$$\begin{aligned}
 Q(x) &= v_o^4 n_1 n_2 \left(\frac{\sqrt{\lambda_1 \lambda_2}}{\pi} \right)^3 8\pi^2 \sigma_o \int_0^\infty z^3 e^{-B'z^2} \tilde{J}(z, x) dz \\
 \tilde{J}(z, x) &= \int_0^\pi e^{-A'x^2} e^{-\gamma'z^2 \cos \theta} \sigma'(z, \theta) \times \\
 &\quad \frac{\sinh(xz \sqrt{\alpha'^2 + \beta'^2 + 2\alpha'\beta' \cos \theta})}{xz \sqrt{\alpha'^2 + \beta'^2 + 2\alpha'\beta' \cos \theta}} d(\cos \theta) \quad (3.4.13)
 \end{aligned}$$

Since \tilde{J} is dimensionless, all the dimensions for $Q(x)$ are contained in the multiplicative factors in front of the integral; it is easy to verify that the units of $Q(x)$ are s^2cm^{-6} .

It is possible to perform the integrations in $Q(x)$ and \tilde{J} analytically for a suitable choice of differential cross section. For the hard sphere cross section (see Appendix C), $\sigma(z, \theta) = d^2/4$, we have

$$Q(x) = v_o^4 \pi^{3/2} n_1 n_2 \left(\frac{\sqrt{\lambda_1 \lambda_2}}{\pi} \right)^3 \frac{\pi d^2}{x \sqrt{A_2 \gamma'}} \{N(r, s, \hat{u}_+) - N(r, s, \hat{u}_-)\} \quad (3.4.14)$$

where

$$A_1 = \alpha'^2 + \beta'^2$$

$$\begin{aligned}
A_2 &= 2\alpha'\beta' \\
N(r, s, t) &= \frac{1}{r} \left[\operatorname{erf}(s) - \frac{t}{\sqrt{r+t^2}} \exp\left(-\frac{rs^2}{r+t^2}\right) \operatorname{erf}\left(\frac{st}{\sqrt{r+t^2}}\right) \right] \\
r &= B' - \gamma' \frac{A_1}{A_2} \\
s &= x \sqrt{\frac{A_2}{4\gamma'}} \\
t &= \hat{u}_{\pm} \\
\hat{u}_{\pm} &= \begin{cases} (\alpha' + \beta') \sqrt{\frac{\gamma'}{A_2}} & \text{for } + \\ (\alpha' - \beta') \sqrt{\frac{\gamma'}{A_2}} & \text{for } - \end{cases}
\end{aligned}$$

The details of the derivation are given in Appendix E.

3.4.2 Total Collision Rates

The preceding section described the rate of production of fast moving particles of speed c_1 by binary encounters between two species; that is, $Q(c_1)$ represents the rate at which collisions which create particles of species 1 with speed c_1 occur. In order to calculate the *total* number of collisions between species 1 and 2 we must integrate over all possible speeds c_1 . It should be noted that, in the absence of any particle sources or sinks, integration of the Boltzmann collision operator over $d\mathbf{c}_1$ must be equal to zero because of particle conservation;²⁹ that is, particles of species 1 and 2 may be moved between different elements of velocity space by elastic collisions, but the total number of particles remains constant. We have, from equation (1.4.2),

$$\iiint (f'_1 f'_2 - f_1 f_2) \sigma(g, \Omega) g d\Omega d\mathbf{c}_2 d\mathbf{c}_1 = 0$$

and so

$$\iiint f'_1 f'_2 \sigma(g, \Omega) g d\Omega d\mathbf{c}_2 d\mathbf{c}_1 = \iiint f_1 f_2 \sigma(g, \Omega) g d\Omega d\mathbf{c}_2 d\mathbf{c}_1$$

Either term above defines the total collision rate between species 1 and 2. Using the definition of the production rate, equation (3.4.1), and the definition of the collision

frequency,

$$\begin{aligned} Z(c_1) &\equiv \iint f_2 \sigma(g, \Omega) g d\Omega d\mathbf{c}_2 \\ &= \int f_2 \sigma_{tot}(g) g d\mathbf{c}_2 \end{aligned} \quad (3.4.15)$$

we may thus calculate the total collision rate using either of

$$Q_{tot} = \begin{cases} \int Q(c_1) d\mathbf{c}_1 \\ \int f_1 Z(c_1) d\mathbf{c}_1 \end{cases} \quad (3.4.16)$$

These total collision rates may also be compared with the work of Fitzpatrick and Shizgal¹⁴⁵ for the hard sphere case in order to verify the calculation of the product velocity distribution functions/collision frequencies.

3.4.3 Rate of Production of Escaping Atoms

Once we have calculated the product velocity distribution function, $Q(c_1)$, we are interested in making some statement about the number of hot atoms which are able to escape. A detailed discussion of the calculation of a rigorous, altitude dependent escape flux which includes the moderating effect of the ambient background atmosphere is discussed in Chapter 4. For the moment, we may use the product velocity distribution functions to compare the relative rates of production of escaping atoms. This incorporates the nonthermal production of hot atoms and the use of realistic collision cross sections.

It is assumed that any hot atom produced by nonthermal excitation (via any of the elastic collision mechanisms we have previously detailed in the calculation of the energy exchange rate coefficients: DIR, CE, or the LTA) with velocity greater than the escape velocity escapes from the planetary atmosphere. Thus, in order to calculate the rate of production of escaping atoms, we simply integrate the product velocity distribution function (or the gain term of the Boltzmann collision operator) normalized by the densities

of the colliding species, over all velocities c_1 greater than the escape velocity,

$$\alpha_{esc} = \frac{4\pi}{n_1 n_2} \int_{c_{esc}}^{\infty} Q(c_1) c_1^2 dc_1 \quad (3.4.17)$$

where $c_{esc} = \sqrt{2GM/r}$. It may be easily verified using equation (3.4.1) that α_{esc} has units of a rate, $\text{cm}^3 \text{s}^{-1}$. Equation (3.4.17) ignores reverse collisions, which reduce the overall rate at which escaping atoms are produced. We incorporate reverse collisions by adding the loss term of the Boltzmann collision operator to $Q(c_1)$ before integrating; that is,

$$\alpha_{esc} = \frac{4\pi}{n_1 n_2} \int_{c_{esc}}^{\infty} [Q(c_1) - f_1 Z(c_1)] c_1^2 dc_1 \quad (3.4.18)$$

where $Z(c_1)$ is the collision frequency between species 1 and 2, defined previously.

We may also utilize the PVDFs in order to estimate the fraction of hot atoms created by a nonthermal process which can escape from the atmosphere. This is given by

$$\alpha_{esc}^{frac} = \alpha_{esc} / \frac{4\pi}{n_1 n_2} \int_0^{\infty} Q(c_1) c_1^2 dc_1 \quad (3.4.19)$$

3.4.4 Results and Discussion

The calculation of the PVDF's in the present work follows closely the presentation and calculations done by Shizgal.⁷¹ It is a direct method in comparison to the Monte Carlo integration used by Hodges and Breig⁷³ to calculate the so-called 'differential scattering coefficients'. The calculation of the product velocity distributions (PVDFs), from equation (3.4.13), requires a double integration, over the scattering angle θ and reduced energy z . This integration requires the differential elastic cross section(s), $\sigma(g, \theta)$. The cross section(s) are calculated at 91 energies, from 1×10^{-4} to 10 eV, and at 361 angles (half degree increments), and are illustrated in Figures 3.23 and 3.24. In the calculation of the PVDFs, we use a Simpson's Rule with one-half degree spacing of grid points for the

θ integration. An interpolation scheme using z points located at the 91 energies used in calculating the differential cross section is used to perform the z integration (the scheme is detailed in Appendix E). The linear trajectory approximation adopted in the tables and graphs that follow is that given by equation (3.2.6), unless otherwise indicated.

Some examples of the product velocity distribution function normalized by the species' densities, $Q(c_1)/n_1n_2$, for H^+-H are illustrated in Figures 3.41-3.43. We have chosen the same pairs of temperatures as in the calculation of the energy exchange rate coefficients because they approximate ion and neutral temperatures approximating exospheric conditions on the terrestrial planets. For comparison with the work of Hodges and Breig,⁷³ we have also calculated and plotted the 'differential scattering rate coefficient' defined as

$$P(c_1) = \frac{4\pi c_1^2}{n_1n_2} J[f] \quad (3.4.20)$$

where $P(c_1)$ is equivalent to $\frac{\partial \alpha}{\partial v}$ calculated by Hodges and Breig. In equation (3.4.20), $J[f]$ is the Boltzmann collision operator, as defined by equation (1.4.2). The units of $P(c_1)$ and $Q(c_1)/n_1n_2$ in the figures are 10^{16} cm^2 and 10^{14} s^2 , respectively. In the calculation of the collision operator, we use equation (1.4.2), with the gain term given by the product velocity distribution function, $Q(c_1)$, as defined in equation (3.4.1), and the loss term given by the species 1 distribution function times the collision frequency, $Z(c_1)$, which is given by equation (3.4.15). For the collision frequency integration we use 400 Simpson's Rule points to ensure convergence for all values of c_1 . It should be noted that the vertical scale varies between figures in order to accentuate the details in the form of the PVDFs.

Figures 3.41-3.43 have similar features. The plots of $P(c_1)$ may be interpreted as indicative of the transfer of energy from the hot protons to the cold hydrogen. The negative portions of the curve are due to the removal of hydrogen for those velocities (the 'loss' term of the Boltzmann collision operator), while the positive portions are due to the addition of hot hydrogen for those velocities (the 'gain' term of the Boltzmann

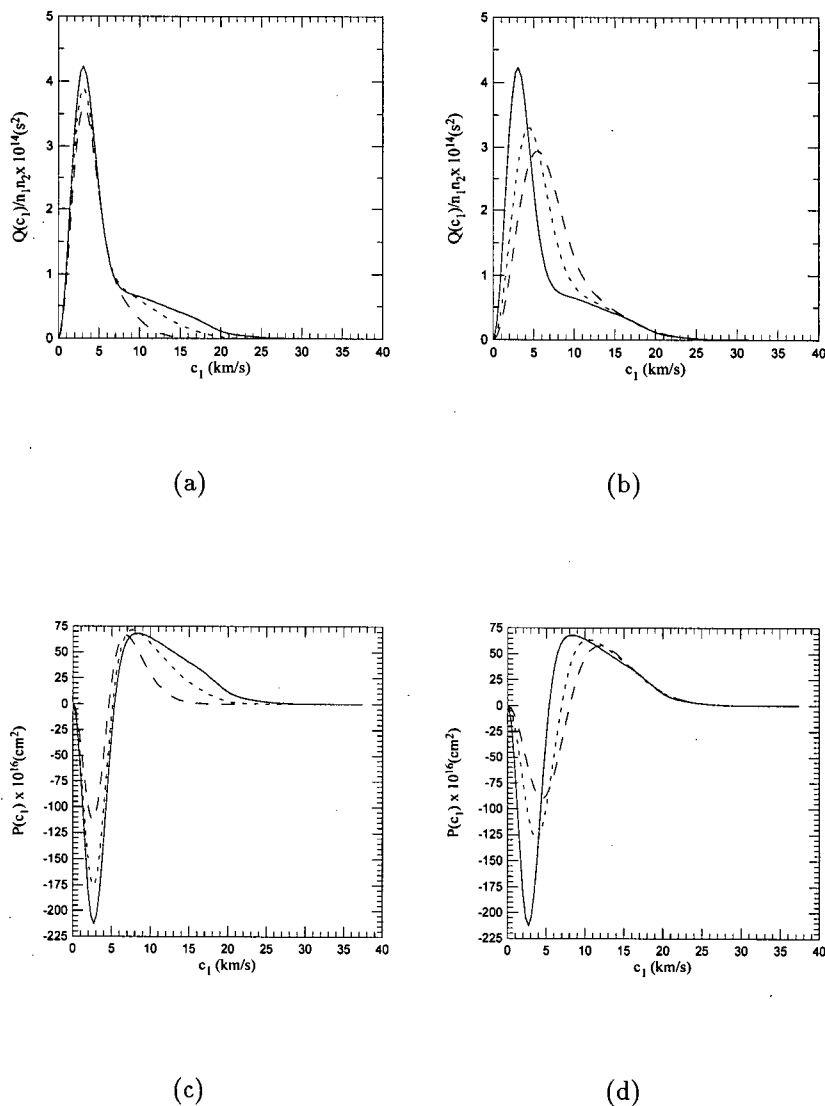


Figure 3.41: Product velocity distribution functions for the direct-plus-exchange (DPE) cross section for H^+-H . In (a), the hydrogen temperature is fixed at 500 K, and the proton temperature is varied, with values of 2000 K (long dashed), 4000 K (short dashed), and 6000 K (solid). In (b), the proton temperature is fixed at 6000 K, and the hydrogen temperature is varied, with values of 1500 K (long dashed), 1000 K (short dashed), and 500 K (solid). In (c) and (d) we have plotted $P(c_1)$, as defined in the text, for the same temperatures and with the same labeling as for (a) and (b), respectively.

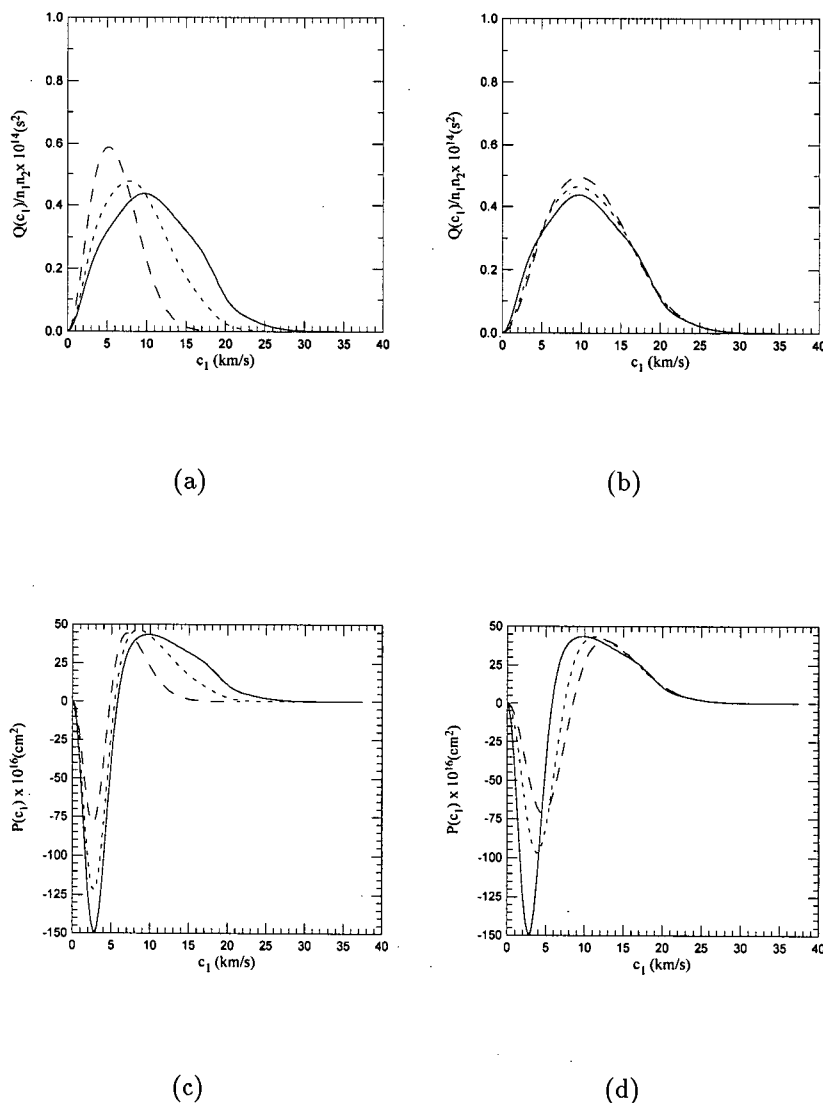


Figure 3.42: Product velocity distribution functions for the charge exchange (CE) cross section for $\text{H}^+\text{-H}$. In (a), the hydrogen temperature is fixed at 500 K, and the proton temperature is varied, with values of 2000 K (long dashed), 4000 K (short dashed), and 6000 K (solid). In (b), the proton temperature is fixed at 6000 K, and the hydrogen temperature is varied, with values of 1500 K (long dashed), 1000 K (short dashed), and 500 K (solid). In (c) and (d) we have plotted $P(c_1)$, as defined in the text, for the same temperatures and with the same labeling as for (a) and (b), respectively.

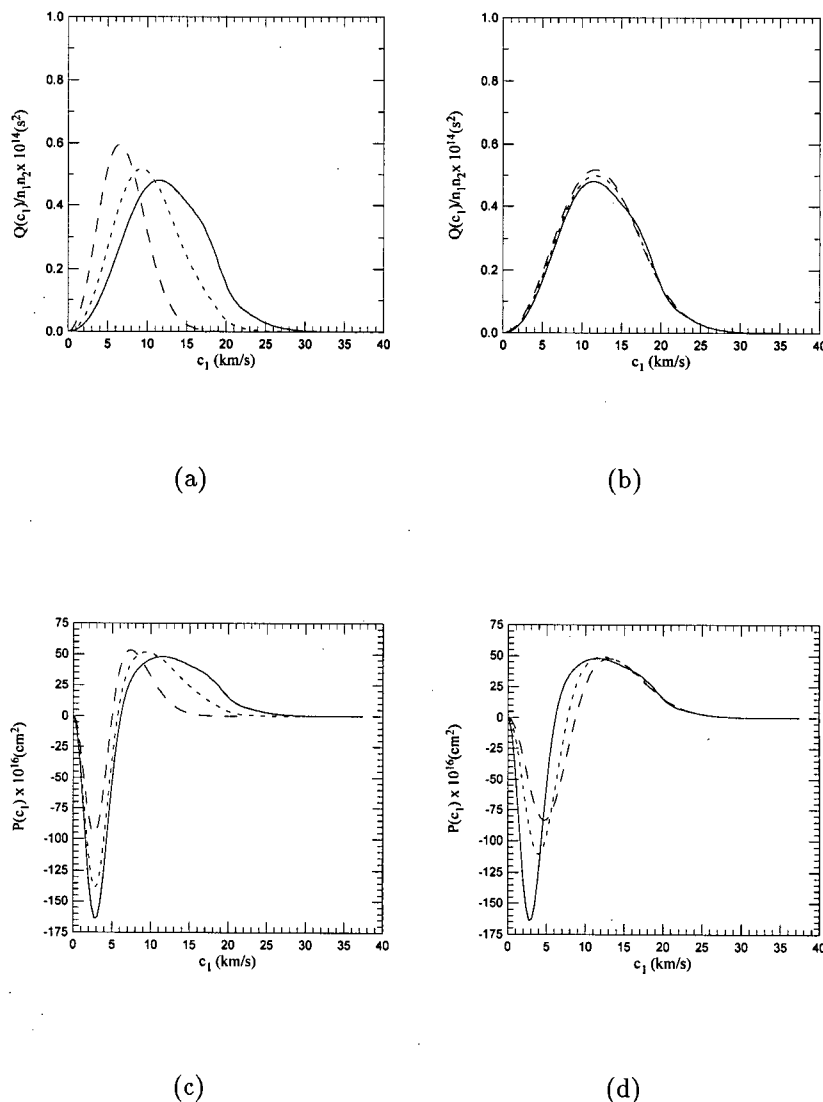


Figure 3.43: Product velocity distribution functions for the linear trajectory approximation (LTA) cross section for H^+-H . In (a), the hydrogen temperature is fixed at 500 K, and the proton temperature is varied, with values of 2000 K (long dashed), 4000 K (short dashed), and 6000 K (solid). In (b), the proton temperature is fixed at 6000 K, and the hydrogen temperature is varied, with values of 1500 K (long dashed), 1000 K (short dashed), and 500 K (solid). In (c) and (d) we have plotted $P(c_1)$, as defined in the text, for the same temperatures and with the same labeling as for (a) and (b), respectively.

collision operator). It is clear from subfigure (c) in Figures 3.41-3.43 that for a fixed hydrogen temperature, increasing the proton temperature increases the average energy of the cold hydrogen. Graphically, this is illustrated by the increase in the position of the peak and width of the positive portion of the $P(c_1)$ curve, respectively. From subfigure (d) in Figures 3.41-3.43, we see that for a fixed proton temperature, increasing the hydrogen temperature results in a smaller number of hydrogen atoms being energized, but with a greater average increase in energy. Graphically, this is illustrated by the decrease in the depth of the negative portion of the $P(c_1)$ curves and the change in position of the peak and width of the positive portion of the $P(c_1)$ curve, respectively.

The pattern of change with hydrogen and proton temperatures is the same for each of the DPE, CE and LTA cross sections; however, the relative magnitude of the changes varies between them. A comparison of the PVDFs for the three cross sections for fixed hydrogen and proton temperatures is shown in Figure 3.44. For subfigures (a) and (c), the proton temperature is 6000 K and the hydrogen temperature is 500 K, representing the largest difference in colliding partner temperatures. For subfigures (b) and (d), the proton temperature is 2000 K and the hydrogen temperature is 1500 K, representing the smallest difference in colliding partner temperatures. The difference between the large energy and small energy cases is evident by the difference in vertical scale between subfigures (a) and (b) or (c) and (d) and the change in shape of the PVDF's and differential scattering coefficients.

The DPE includes both direct elastic momentum transfer and charge exchange, and so the result that this cross section is most efficient at producing hot hydrogen is not unexpected. For only charge exchange, the effects are reduced by approximately 30-40% when considering the plots of $P(c_1)$; we may thus deduce that charge exchange is relatively efficient, as compared to direct elastic momentum transfer collisions, since the CE values are 60-70% of the magnitude of the DPE values. This roughly holds even

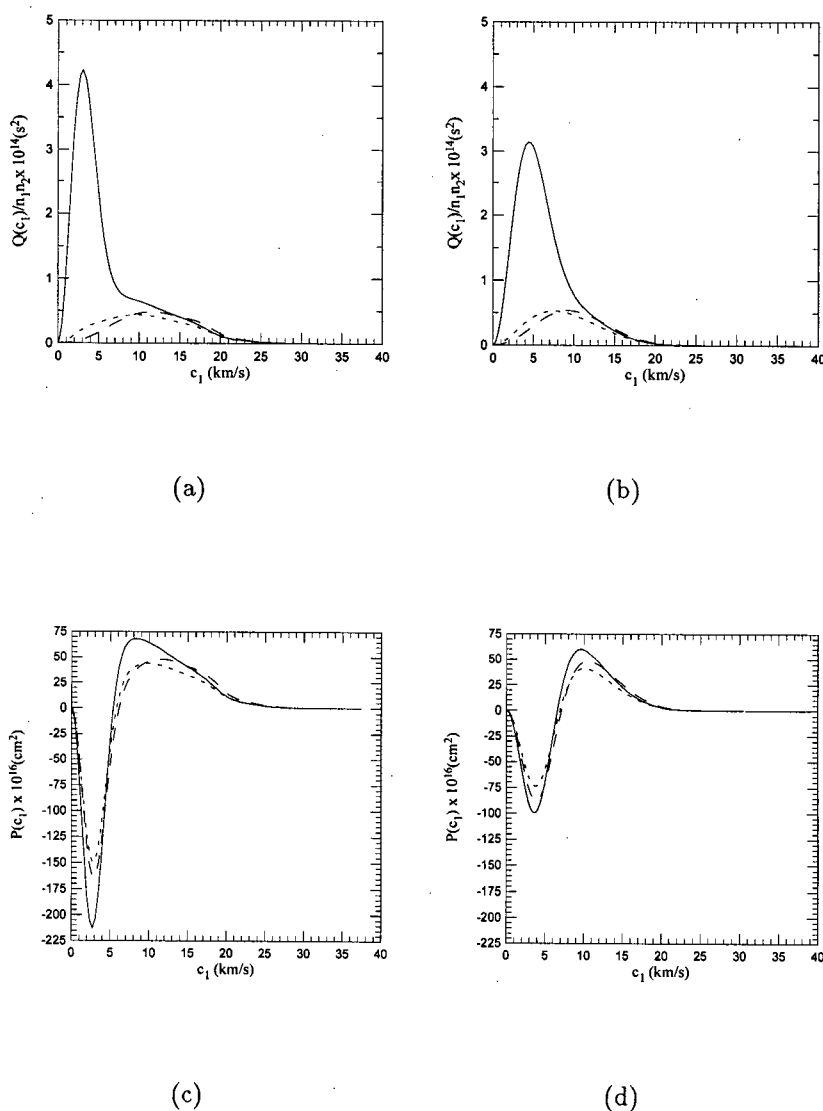


Figure 3.44: Product velocity distribution functions for the DPE, CE, and LTA cross sections for $\text{H}^+\text{-H}$. In (a), the hydrogen temperature is 500 K and the proton temperature is 6000 K. In (b), the hydrogen temperature is 1500 K and the proton temperature is 2000 K. For both cases, we show the resulting PVDFs for the LTA (long dashed), CE (short dashed), and DPE (solid) cross sections. In (c) and (d) we have plotted $P(c_1)$, as defined in the text, for the same temperatures and with the same labeling as for (a) and (b), respectively.

when considering the plots of the PVDFs, $Q(c_1)$, when considering the higher energy portion (greater than approximately 10 km/s). The LTA cross section behaves similarly to the CE one, except that it appears to overestimate both the rate at which energy is transferred from the protons to the hydrogen and the change in the average energy of the cold hydrogen. These overestimations are visible as a subtle shift toward higher velocities in the $Q(c_1)$ plots, and a change in the width and depth of the positive and negative portions of the $P(c_1)$ plots.

We also plot PVDFs and differential scattering coefficients for the deuterium-proton system. These are illustrated in Figures 3.45-3.46 for the DIR and CE interactions for a range of ion and neutral temperatures. The features of these curves are very similar to those for the hydrogen-proton curves, and most of the discussion for that system also applies to this one. The disparate masses of the two colliding partners makes energy transfer slightly less efficient for the deuterium-proton or deuterium ion-hydrogen systems than for the hydrogen-proton system. This is reflected in the vertical scale of the PVDF's compared to those for the hydrogen-proton system.

The PVDFs and differential scattering coefficients for the oxygen-hydrogen and oxygen-deuterium systems are shown in Figures 3.47-3.48. The figures represent results for the DIR interaction for a range of collision pair temperatures. The general shape and features of these curves are very similar to those of the previous systems. The magnitude of the PVDFs decrease as we move from D-H, O-D, and O-H, and we also note that the peak of the PVDFs shift toward higher velocities. For the case where the colliding partners are close in temperature the differential scattering coefficients, $P(c_1)$, show some structure for velocities below approximately 5 km/s.

There are several checks we may perform in order to verify that we are correctly calculating the PVDFs. One good initial check is that the condition given by equation (3.4.16) is satisfied; we have verified that this is correct within 2-7% depending on the

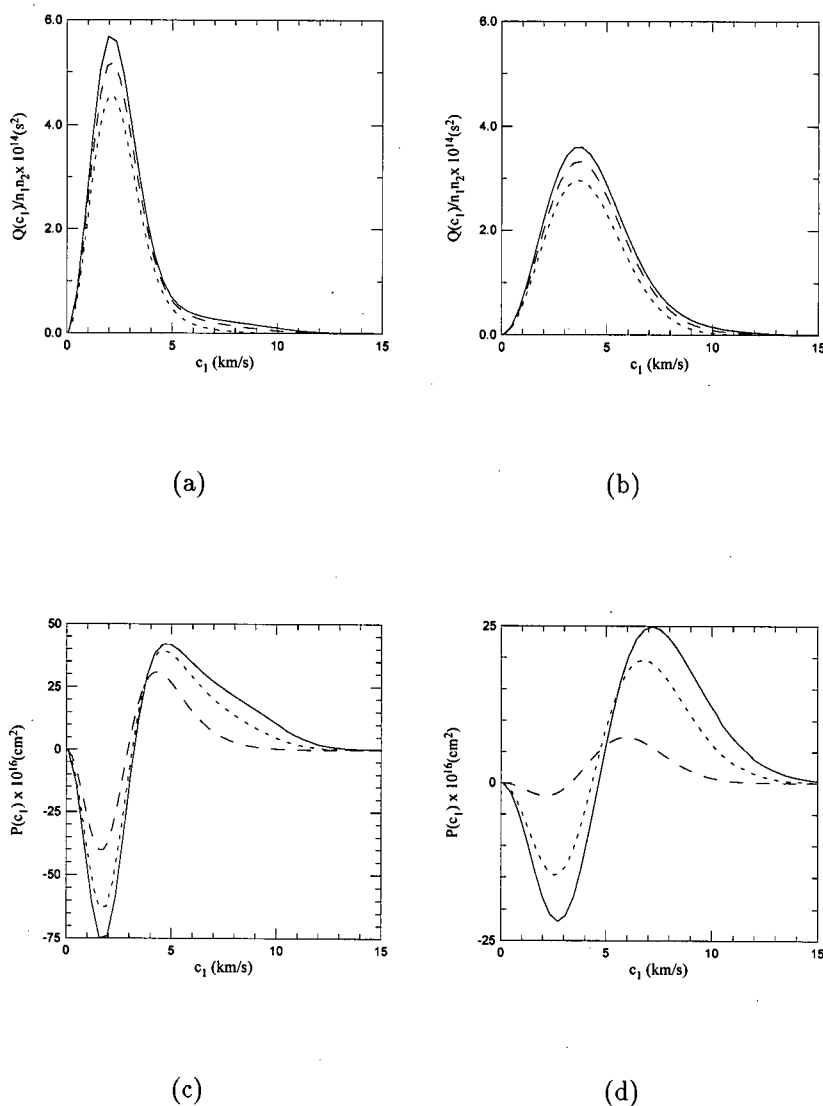


Figure 3.45: Product velocity distribution functions for the direct elastic (DIR) cross section for H^+-D . In (a), the deuterium temperature is fixed at 500 K, and the proton temperature is varied, with values of 1000 K (dot-dashed), 2000 K (short dashed), 4000 K (long dashed), and 6000 K (solid). In (b), the deuterium temperature is fixed at 1500 K, and the proton temperature is varied, with values of 1500 K (dot-dashed), 2000 K (short dashed), 4000 K (short dashed), and 6000 K (solid). In (c) and (d) we have plotted $P(c_1)$, as defined in the text, for the same temperatures and with the same labeling as for (a) and (b), respectively.

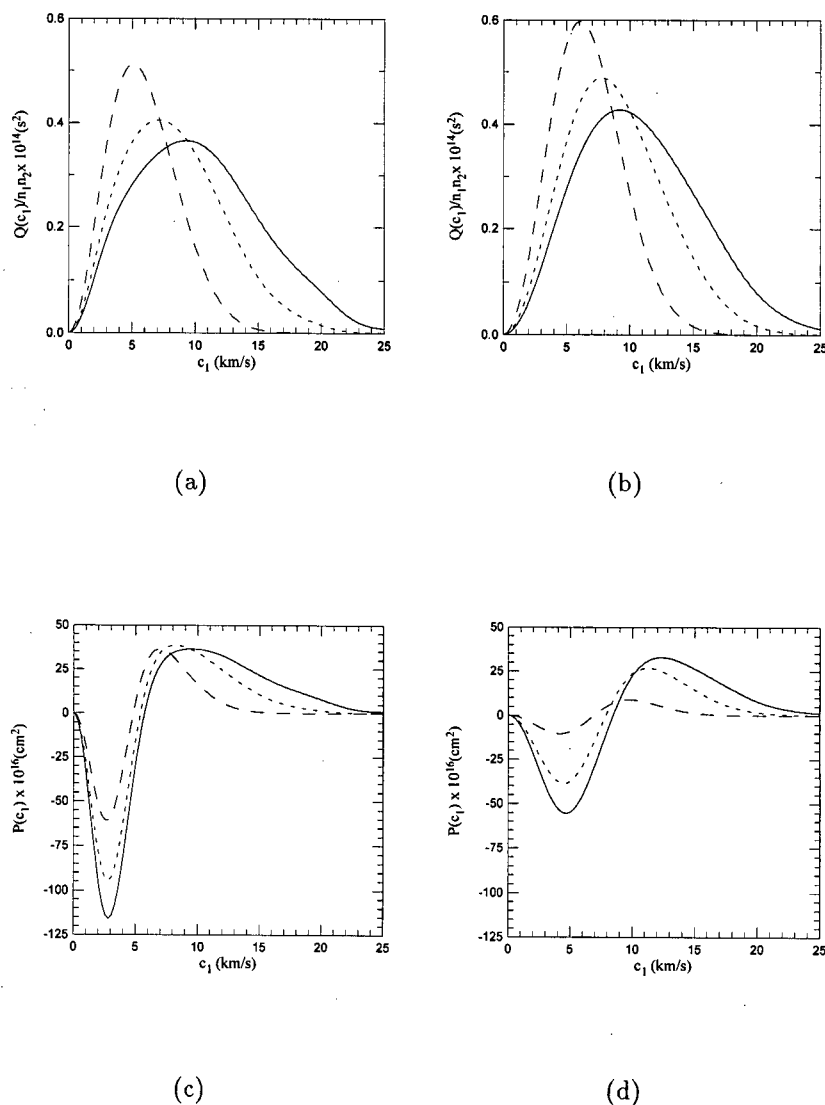


Figure 3.46: Product velocity distribution functions for the charge-exchange (CE) cross section for D^+-H . In (a), the hydrogen temperature is fixed at 500 K, and the deuterium ion temperature is varied, with values of 2000 K (long dashed), 4000 K (short dashed), and 6000 K (solid). In (b), the hydrogen temperature is fixed at 1500 K, and the deuterium ion temperature is varied, with values as in (a). In (c) and (d) we have plotted $P(c_1)$, as defined in the text, for the same temperatures and with the same labeling as for (a) and (b), respectively.

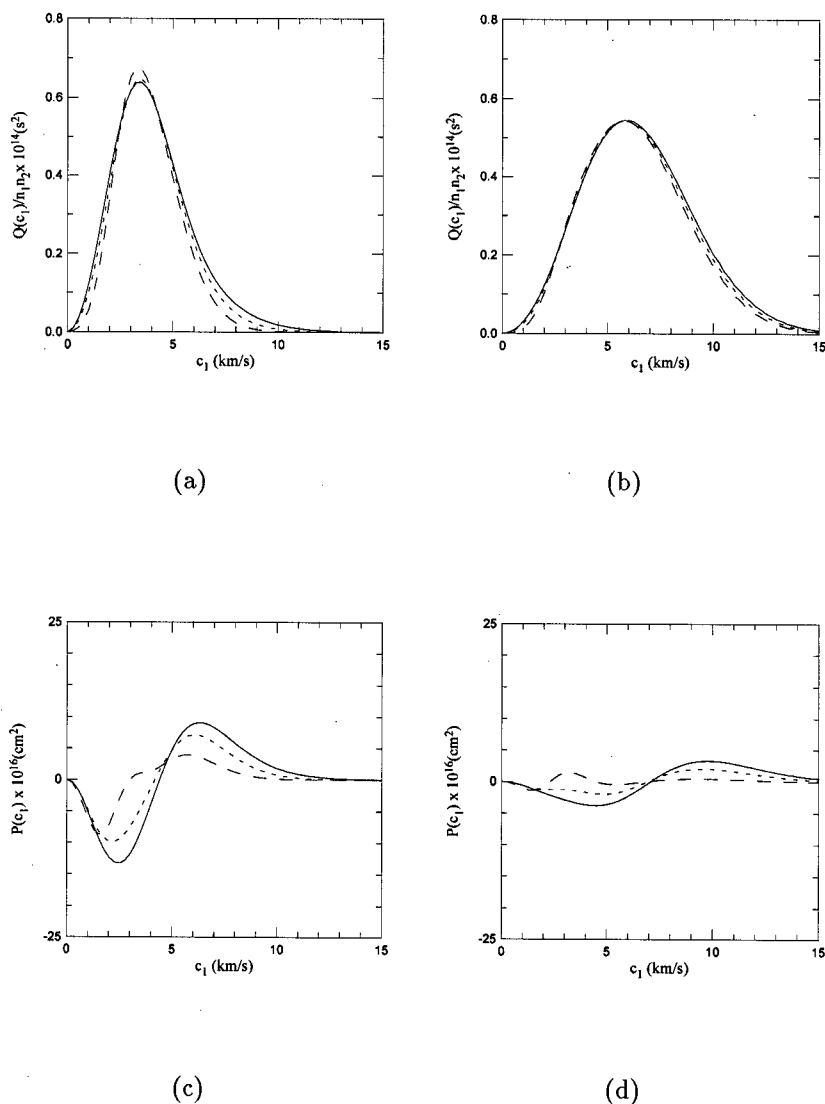


Figure 3.47: Product velocity distribution functions for the direct elastic (DIR) cross section for O-H. In (a), the hydrogen temperature is fixed at 500 K, and the oxygen temperature is varied, with values of 2000 K (long dashed), 4000 K (short dashed), and 6000 K (solid). In (b), the hydrogen temperature is fixed at 1500 K, and the oxygen temperature is varied, with values as in (a). In (c) and (d) we have plotted $P(c_1)$, as defined in the text, for the same temperatures and with the same labeling as for (a) and (b), respectively.

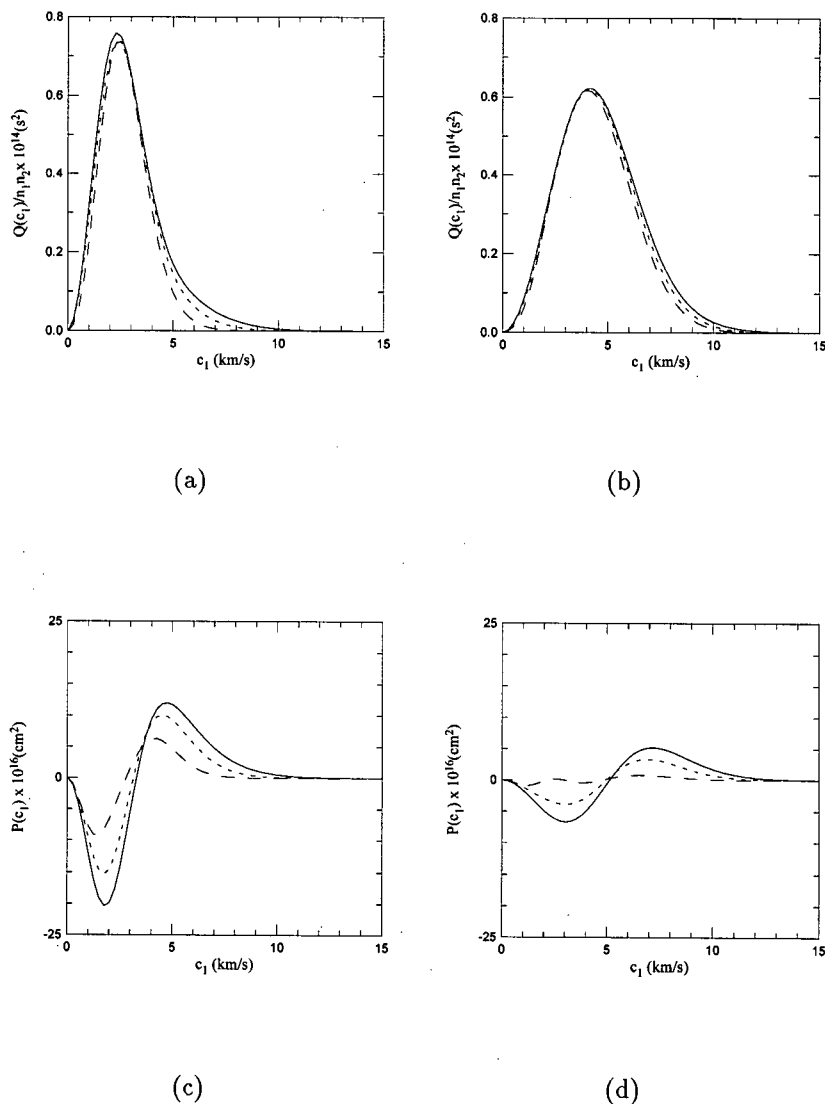


Figure 3.48: Product velocity distribution functions for the direct elastic (DIR) cross section for O-D. In (a), the deuterium temperature is fixed at 500 K, and the oxygen temperature is varied, with values of 2000 K (long dashed), 4000 K (short dashed), and 6000 K (solid). In (b), the deuterium temperature is fixed at 1500 K, and the oxygen temperature is varied, with values as in (a). In (c) and (d) we have plotted $P(c_1)$, as defined in the text, for the same temperatures and with the same labeling as for (a) and (b), respectively.

temperature ratio chosen. Graphically, from Figures 3.41-3.43, this means that the area under the negative and positive portions of the $P(c_1)$ curves must be equal, since particle conservation requires that the integral of the collision operator over all \mathbf{c}_1 must be zero.

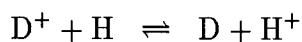
As a second check of the accuracy of our PVDFs, we use them to calculate the energy exchange rate coefficients calculated in a previous section of this chapter. That is, we calculate

$$R_E = \iiint \frac{1}{2} m_1 c_1^2 [Q(c_1) - f_1 Z(c_1)] d\Omega d\mathbf{c}_2 d\mathbf{c}_1 \quad (3.4.21)$$

We use equations 3.3.17 and (3.3.19) to obtain the energy exchange rate coefficient, k_E , from R_E as given above. The results of this calculation are given in Tables 3.12, 3.13 and 3.14. By comparison with the earlier results (using equation (3.3.16)), given in Tables 3.5, 3.7 and 3.8, we see that the two very different methods of calculation agree to better than 10% over most of the temperature ranges, and never differ by more than 20%.

To further quantify the relative accuracy of the two methods, we compare the results for the energy exchange rate coefficient for the hard sphere cross section (the hard sphere cross section is used because for this choice it is possible to calculate the analytic solution of equation (3.3.16), given by equation (3.3.17)). The results are summarized in Table 3.15 in the form of the ratio of k_E from equation (3.3.16) divided by the value from equation (3.4.21). For all pairs of temperatures, equation (3.3.16) reproduced the expected analytic solution given by equation (3.3.17) to better than 1%, and so the deviation from unity in Table 3.15 may be attributed entirely to the accuracy with which we are to calculate the triple integral of equation (3.4.21).

We perform another check on the PVDFs by calculating the charge exchange reaction rate. That is, we calculate the rate of both the forward and backward reaction for deuterium and hydrogen,



T[H ⁺]	Cross Section	T[H]		
		500	1000	1500
6000	DIR	2.47	2.58	2.72
	CE	8.94	9.26	9.57
	LTA	11.66	12.02	12.37
4000	DIR	2.42	2.61	2.91
	CE	7.78	8.25	8.73
	LTA	10.08	10.59	11.10
2000	DIR	2.18	2.50	2.62
	CE	5.90	6.48	7.32
	LTA	7.90	8.56	9.48

Table 3.12: Energy exchange rate coefficients for several H⁺-H cross sections, calculated by integration of the product velocity distribution functions. The temperatures of both H and the protons, in degrees Kelvin, are indicated in the table. The tabulated values of the energy exchange rate coefficients are in units of 10⁻⁹ cm³ s⁻¹.

T[ion]	Cross Section	T[neutral]					
		500		1000		1500	
		I	II	I	II	I	II
6000	DIR	1.897	1.874	1.987	1.994	2.101	2.145
	CE	8.388	6.301	8.577	6.748	8.772	7.170
	LTA	10.124	8.015	10.298	8.487	10.476	8.915
4000	DIR	1.953	1.770	2.109	1.950	2.345	2.238
	CE	7.026	5.328	7.275	5.851	7.548	6.372
	LTA	8.807	6.928	9.059	7.510	9.331	8.066
2000	DIR	1.797	1.670	2.094	1.928	3.065	2.908
	CE	5.139	4.233	5.485	4.756	6.052	5.376
	LTA	6.735	5.654	7.119	6.236	7.716	6.884

Table 3.13: Energy exchange rate coefficients for several H^+ -D cross sections, calculated by integration of the product velocity distribution functions. The temperatures of both deuterium and the protons, in degrees Kelvin, are indicated in the table. Values under columns marked 'I' are for reactions where the test particle is the deuterium atom, with a bath of hot protons; values under columns marked 'II' are for reactions where the test particle is hydrogen, with a bath of hot deuterium ions. The tabulated values of the energy exchange rate coefficients are in units of $10^{-9} \text{ cm}^3 \text{ s}^{-1}$.

T[O]	Cross Section	T[H] or T[D]		
		500	1000	1500
6000	OH	0.184	0.211	0.230
	OD	0.261	0.287	0.306
4000	OH	0.179	0.209	0.229
	OD	0.247	0.278	0.300
2000	OH	0.185	0.223	0.256
	OD	0.236	0.279	0.317

Table 3.14: Energy exchange rate coefficients for O-H and O-D direct elastic cross sections. The temperatures of O and H/D, in degrees Kelvin, are indicated in the table. The tabulated values of the energy exchange rate coefficients are in units of $10^{-9} \text{ cm}^3 \text{ s}^{-1}$.

T[H+]	T[H]		
	500	1000	1500
6000	0.95	0.95	0.94
4000	0.96	0.95	0.92
2000	0.98	0.96	0.88

Table 3.15: Comparison of energy exchange rate coefficients for the hard sphere cross section using equations (3.3.16) and (3.4.21). The temperatures of both H and the protons, in degrees Kelvin, are indicated in the table. The values reported in the table are the ratio of the result from equation (3.3.16) divided by that of equation (3.4.21).

The calculation is done both by direct integration of the the loss term and direct integration of the PVDF, as given by equation (3.4.16), and is illustrated in Figure 3.49. The results of Hodges⁷⁴ are also shown in the figure. It is noted that he calculates different rates for the forward/reverse charge exchange reaction, since he does not neglect the coupling coefficient in the calculation of the cross sections for DH^+ , although it is difficult to account for the magnitude of the difference between them given that the coupling coefficients are of the order of 10^{-4} the size of the coefficients of the primary channels. As mentioned previously, we have neglected the cross-coupling interaction, and so our rates for the forward and reverse reactions are identical. It is clear, however, that there is good agreement with Hodges' calculated rate coefficients. It should be noted that, as in most of the work done by Hodges, Monte Carlo integrations are used to perform all of the velocity integrals. Our calculation, in the form of a triple integral, does not have to resort to the Monte Carlo methodology in order to extract the rate coefficients.

The results of the calculation of the rate of production of escaping hot hydrogen atoms, α_{esc} , are given in Tables 3.16 -3.18. The same set of proton and hydrogen temperatures are used as in the calculations of the energy exchange rate coefficients. Values in columns marked A are calculations using equation (3.4.18) and include reverse collisions; values in columns marked B use equation (3.4.17), ignoring reverse collisions. We assume a hydrogen exobase altitude of 200 km for Venus,³⁵ 500 km for Earth,⁴⁴ and 250 km for Mars.⁶ The escape velocities for these altitudes are 10.2 km/s, 10.78 km/s, and 4.85 km/s, respectively.

We see several interesting trends in the values of the rate of production of escaping hot hydrogen for the terrestrial planets, as given in Tables 3.16 -3.18. The LTA cross section results overestimate the rate of production of hot atoms by 20-50% for Venus and Earth, and 5-30% for Mars, in good agreement with the discrepancy of 30-50% reported by Shizgal.¹³¹ This is observed for production of hot atoms including and excluding reverse

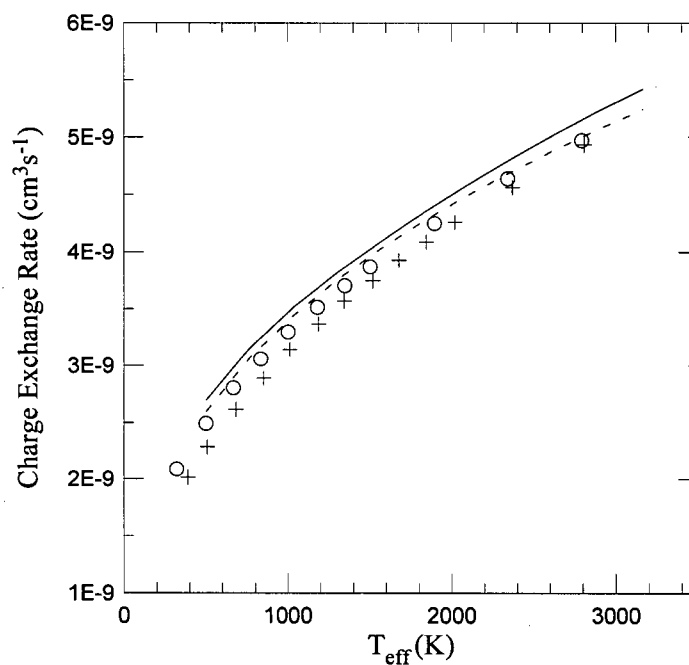


Figure 3.49: Dependence of charge exchange rate coefficients on the effective temperature for D^+H . The value of the charge exchange rate coefficients are plotted as a function of the effective temperature, T_{eff} . The solid curve is from integration of the PVDF, the dashed curve from integration of the Boltzmann collision operator loss term. The circle and plus symbols are the results of fits to Monte Carlo calculations by Hodges⁷⁴ for the rates of D^+H and $D-H^+$, respectively.

T[H ⁺]	Cross Section	T[H]					
		500		1000		1500	
		A	B	A	B	A	B
6000	DIR	0.850	0.851	0.934	1.040	0.966	1.706
	CE	3.282	3.282	3.385	3.426	3.289	3.572
	LTA	4.130	4.130	4.166	4.207	3.988	4.271
4000	DIR	0.475	0.475	0.544	0.644	0.574	1.273
	CE	1.894	1.894	1.986	2.024	1.901	2.166
	LTA	2.542	2.542	2.575	2.613	2.407	2.672
2000	DIR	0.092	0.092	0.120	0.214	0.116	0.773
	CE	0.404	0.404	0.428	0.463	0.307	0.552
	LTA	0.603	0.603	0.591	0.626	0.402	0.647

Table 3.16: Rate of production of escaping H on Venus for several H⁺-H cross sections. The temperatures of both hydrogen and the protons, in degrees Kelvin, are indicated in the table. The tabulated values of α_{esc} are in units of $10^{-9} \text{ cm}^3 \text{ s}^{-1}$. Columns marked 'A' are for production of hot atoms including the effect of reverse collisions; columns marked 'B' neglect reverse collisions.

T[H ⁺]	Cross Section	T[H]					
		500		1000		1500	
		A	B	A	B	A	B
6000	DIR	0.741	0.741	0.116	0.773	0.854	1.336
	CE	3.033	3.033	3.140	3.161	3.104	3.289
	LTA	3.859	3.859	3.906	3.927	3.796	3.981
4000	DIR	0.392	0.392	0.449	0.500	0.486	0.942
	CE	1.656	1.660	1.753	1.772	1.717	1.891
	LTA	2.256	2.256	2.299	2.318	2.193	2.366
2000	DIR	0.064	0.064	0.085	0.133	0.089	0.520
	CE	0.297	0.297	0.323	0.341	0.246	0.407
	LTA	0.450	0.450	0.450	0.468	0.322	0.484

Table 3.17: Rate of production of escaping H on Earth for several H⁺-H cross sections. The temperatures of both hydrogen and the protons, in degrees Kelvin, are indicated in the table. The tabulated values of α_{esc} are in units of $10^{-9} \text{ cm}^3 \text{ s}^{-1}$. Columns marked 'A' are for production of hot atoms including the effect of reverse collisions; columns marked 'B' neglect reverse collisions.

T[H ⁺]	Cross Section	T[H]					
		500		1000		1500	
		A	B	A	B	A	B
6000	DIR	2.196	4.311	1.582	8.630	1.211	11.466
	CE	4.597	5.385	3.044	5.675	2.072	5.914
	LTA	5.107	5.894	3.411	6.042	2.345	6.187
4000	DIR	1.703	3.626	1.179	7.624	0.881	10.310
	CE	3.622	4.322	2.308	4.666	1.486	4.953
	LTA	4.183	4.883	2.696	5.053	1.756	5.223
2000	DIR	0.971	2.653	0.541	6.248	0.308	8.740
	CE	2.171	2.764	1.127	3.154	0.465	3.485
	LTA	2.711	3.304	1.427	3.455	0.592	3.612

Table 3.18: Rate of production of escaping H on Mars for several H⁺-H cross sections. The temperatures of both hydrogen and the protons, in degrees Kelvin, are indicated in the table. The tabulated values of α_{esc} are in units of $10^{-9} \text{ cm}^3 \text{ s}^{-1}$. Columns marked 'A' are for production of hot atoms including the effect of reverse collisions; columns marked 'B' neglect reverse collisions.

collisions.

As may be expected given their similar size and escape velocities, the results for α_{esc} for Venus and Earth are very similar. From Tables 3.16 and 3.17 the data for both planets indicate that for cases where a large separation occurs between the temperatures of the protons and hydrogen that the LTA cross section yields larger α_{esc} values than either the CE or the DIR cross sections; as the temperature of the hydrogen increases, the temperature discrepancy diminishes, and the LTA predicted α_{esc} values fall below those using the DIR cross section, although they continue to exceed α_{esc} values using the CE cross section. We observe a monotonic increase of the values of α_{esc} with an increase in hydrogen temperatures, for fixed proton temperature, for calculations of α_{esc} excluding reverse collisions. Physically, this is reasonable; imparting some fixed amount of energy to a distribution of particles of higher average energy results in more particles reaching the escape energy. The situation is roughly reversed when we include reverse collisions, where α_{esc} decreases as we increase the hydrogen temperature, for a fixed proton temperature. For low hydrogen temperatures the rate of reverse collisions is insufficient to offset the rate of transfer of nonthermal energy, and so the values for α_{esc} including and excluding reverse collisions are roughly identical. However, as the hydrogen temperature increases, the rate of reverse collisions increases, and so the discrepancy between the values of α_{esc} including and excluding reverse collisions increases. It is important to note that even for the highest value of the hydrogen temperature considered here, 1500 K, the most probable hydrogen speed is still only approximately 5 km/s, less than the escape speed. We would expect that even with the aid of nonthermal energy exchange, the number of hot hydrogen atoms produced which avoid thermalization to escape is relatively modest, given the high escape velocity.

The situation is much different for Mars, primarily because of its much lower escape speed. From Table 3.18 the predicted values of α_{esc} are 1.5-3 times that for Venus or

Earth. When reverse collisions are neglected, we observe a monotonic increase of the values of α_{esc} with an increase in hydrogen temperatures, for fixed proton temperature. However, when we include reverse collisions, the observed values of α_{esc} increase and then decrease with increasing hydrogen temperature for fixed proton temperature. This behaviour is most likely related to a change in the balance between the rate of production, the rate of thermalization, and the value of the mean thermal hydrogen speed relative to the escape speed. As for Venus and Earth, for low hydrogen temperatures, the rate of reverse collisions is insufficient to offset the rate of production, and the values of α_{esc} including and excluding reverse collisions are approximately the same. As the hydrogen temperature increases, the mean thermal hydrogen speed begins to exceed the escape speed, and so we sample more of the hydrogen distribution when we calculate the rate of production of escaping hydrogen. That is, the peak of the hydrogen distribution is very close to the escape speed, and the bulk of the hydrogen atoms are involved in the integration of the reverse collision term. As the hydrogen speed increases further, even more of the hydrogen distribution is sampled, and the mean thermal hydrogen speed is in excess of the escape speed. The rate of reverse collisions is now calculated integrating over the bulk of the hydrogen distribution (as opposed to the tail of the distribution when the mean thermal speed of the hydrogen is less than the escape speed, as for Venus and Earth), and so the rate of reverse collisions increases faster than the rate of production of hot atoms, slowing the overall rate of production of hot hydrogen atoms. For a species with a much heavier mass, such as oxygen, we would expect that the mean thermal speed would be much lower for a given temperature, and that the values of α_{esc} would be similar to that of Venus and Earth for hydrogen.

We may again compare our results with those of Hodges and Breig,⁷³ whose results for the production of hot hydrogen for Earth are summarized in Table 3.19. Once again we see a (variable) discrepancy between our results and their work, similar but not identical

T[H ⁺]	Cross	T[H]		
	Section	500	1000	1500
6000	DIR	6.79	6.60	6.26
	LTA	7.34	6.88	6.43
4000	DIR	3.56	3.54	3.25
	LTA	4.18	3.86	3.49
2000	DIR	0.58	0.55	0.43
	LTA	0.78	0.67	0.50

Table 3.19: Rate of production of escaping H on Earth for several H⁺-H cross sections taken from the results of Hodges and Breig.⁷³ The temperatures of both hydrogen and the protons, in degrees Kelvin, are indicated in the table. The tabulated values of α_{esc} are in units of $10^{-9} \text{ cm}^3 \text{ s}^{-1}$.

to the discrepancy in the values of the energy exchange rate coefficients. As before, it is difficult to comment on the source of this discrepancy.

The same calculation of rates of production of escaping particles is done for deuterium-proton systems. These results are reported in Tables 3.21-3.22. The interpretation is similar to those done for hydrogen-proton collisions. We can see from the tables that it is more difficult to produce escaping deuterium than escaping hydrogen, regardless of the type of interaction considered. The values in the tables of rate of escape production of hot deuterium by collisions with protons are roughly a factor of 2-10 times smaller than those for hydrogen-proton collisions. In addition, direct elastic collisions are much less efficient at production of hot neutrals than charge exchange reactions. This is because although some momentum is transferred in each charge exchange collision, the pre-collisional ion keeps most of its energy when it becomes a post-collisional neutral.

The same calculation of rates of production of escaping particles is done for oxygen-hydrogen systems, and oxygen-deuterium systems. These results are reported in Tables

T(ion)	Cross Section	T[(neutral)]					
		500		1000		1500	
		A	B	A	B	A	B
6000	DIR	0.117	0.117	0.145	0.145	0.176	0.191
	CE	1.340	1.340	1.370	1.370	1.394	1.400
4000	DIR	0.042	0.042	0.055	0.055	0.071	0.085
	CE	0.450	0.450	0.465	0.465	0.484	0.489
2000	DIR	0.184	0.184	0.310	0.333	0.520	1.800
	CE	0.018	0.018	0.020	0.021	0.021	0.026

Table 3.20: Rate of production of escaping D on Venus for several H^+ -D cross sections. The temperatures of both deuterium and the protons, in degrees Kelvin, are indicated in the table. The tabulated values of α_{esc} are in units of $10^{-9} \text{ cm}^3 \text{ s}^{-1}$. Columns marked 'A' are for production of hot atoms including the effect of reverse collisions; columns marked 'B' neglect reverse collisions.

T(ion)	Cross Section	T(neutral)					
		500		1000		1500	
		A	B	A	B	A	B
6000	DIR	0.072	0.072	0.096	0.096	0.122	0.127
	CE	1.069	1.069	1.102	1.103	1.132	1.135
4000	DIR	0.023	0.023	0.033	0.033	0.044	0.050
	CE	0.314	0.314	0.330	0.330	0.350	0.351
2000	DIR	7.3×10^{-4}	7.3×10^{-4}	1.3×10^{-3}	1.4×10^{-3}	2.5×10^{-3}	7.7×10^{-3}
	CE	0.009	0.009	0.010	0.010	0.011	0.013

Table 3.21: Rate of production of escaping D on Earth for several H^+ -D cross sections. The temperatures of both deuterium and the protons, in degrees Kelvin, are indicated in the table. The tabulated values of α_{esc} are in units of $10^{-9} \text{ cm}^3 \text{ s}^{-1}$. Columns marked 'A' are for production of hot atoms including the effect of reverse collisions; columns marked 'B' neglect reverse collisions.

T(ion)	Cross Section	T(neutral)					
		500		1000		1500	
		A	B	A	B	A	B
6000	DIR	1.45	1.61	1.39	3.49	1.17	5.90
	CE	4.51	4.57	3.95	4.73	3.11	4.89
4000	DIR	1.04	1.18	0.99	2.92	0.82	5.17
	CE	3.23	3.29	2.77	3.47	2.07	3.65
2000	DIR	0.43	0.56	0.38	2.09	0.25	4.11
	CE	1.38	1.43	1.04	1.63	0.50	1.85

Table 3.22: Rate of production of escaping D on Mars for several H^+ -D cross sections. The temperatures of both deuterium and the protons, in degrees Kelvin, are indicated in the table. The tabulated values of α_{esc} are in units of $10^{-9} \text{ cm}^3 \text{ s}^{-1}$. Columns marked 'A' are for production of hot atoms including the effect of reverse collisions; columns marked 'B' neglect reverse collisions.

3.24-3.25. The values here are smaller by several orders of magnitude than rate of production for hydrogen-proton or deuterium-proton systems, mainly due to the disparate masses of the collisional pair. It should be noted that for all of the terrestrial planets, the production of deuterium is only approximately 1/10th that of hydrogen due to direct elastic collisions with hot oxygen. While energy transfer overall is more efficient for collision partners with similar masses, the lighter hydrogen has more particles created with velocities in the high energy 'tail' of the PVDF, which is the portion that contributes to the rate of production of escaping hot product atoms.

We may utilize equation (3.4.19) in order to approximate the fraction of escaping hot atoms produced by a given nonthermal process. This estimate does not account for thermalization effects or reverse collisions. We assume that the hot oxygen atoms have an initial velocity of 5.6 km/s, corresponding to approximately 2.5 eV, and that the hydrogen

T[O]	Cross Section	T[H] & T[D]					
		500		1000		1500	
		A	B	A	B	A	B
6000	OH	0.0203	0.0204	0.0598	0.0916	0.0906	0.3159
	OD	0.0047	0.0047	0.0101	0.0102	0.0196	0.0240
4000	OH	0.0060	0.0061	0.0290	0.0606	0.0470	0.2704
	OD	0.0006	0.0006	0.0024	0.0025	0.0067	0.0111
2000	OH	0.0006	0.0007	0.0069	0.0382	0.0082	0.2257
	OD	6.0×10^{-5}	6.0×10^{-5}	0.0001	0.0002	0.0007	0.0050

Table 3.23: Rate of production of escaping H on Venus for direct elastic collisions between O-H and O-D. The temperatures of the hydrogen, deuterium, and oxygen atoms, in degrees Kelvin, are indicated in the table. The tabulated values of α_{esc} are in units of $10^{-9} \text{ cm}^3 \text{ s}^{-1}$. Columns marked 'A' are for production of hot atoms including the effect of reverse collisions; columns marked 'B' neglect reverse collisions.

T[O]	Cross Section	T[H] & T[D]					
		500		1000		1500	
		A	B	A	B	A	B
6000	OH	0.0128	0.0129	0.0425	0.0592	0.0728	0.2228
	OD	0.0027	0.0027	0.0060	0.0060	0.0122	0.0140
4000	OH	0.0033	0.0033	0.0193	0.0359	0.0367	0.1856
	OD	0.0003	0.0003	0.0012	0.0012	0.0037	0.0055
2000	OH	0.0002	0.0003	0.0043	0.0207	0.0063	0.1518
	OD	1.4×10^{-5}	1.5×10^{-5}	1.5×10^{-5}	1.5×10^{-5}	0.0003	0.0021

Table 3.24: Rate of production of escaping H on Earth for direct elastic collisions between O-H and O-D. The temperatures of the hydrogen, deuterium, and oxygen atoms, in degrees Kelvin, are indicated in the table. The tabulated values of α_{esc} are in units of $10^{-9} \text{ cm}^3 \text{ s}^{-1}$. Columns marked 'A' are for production of hot atoms including the effect of reverse collisions; columns marked 'B' neglect reverse collisions.

T[O]	Cross Section	T[H] & T[D]					
		500		1000		1500	
		A	B	A	B	A	B
6000	OH	0.330	0.781	0.189	1.789	0.081	2.497
	OD	0.250	0.283	0.256	0.714	0.194	1.262
4000	OH	0.226	0.668	0.117	1.677	0.036	2.327
	OD	0.152	0.185	0.164	0.612	0.117	1.162
2000	OH	0.102	0.533	0.034	1.489	0.001	1.956
	OD	0.052	0.084	0.057	0.493	0.024	1.031

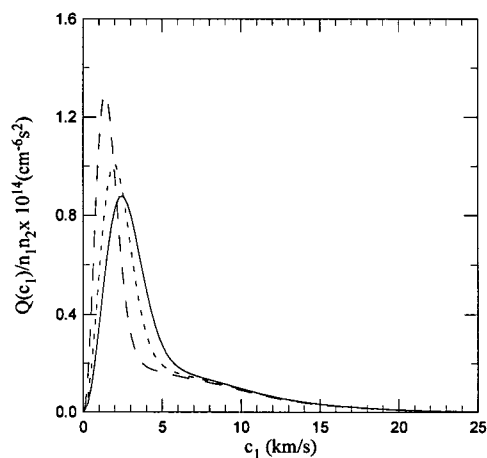
Table 3.25: Rate of production of escaping H on Mars for direct elastic collisions between O-H and O-D. The temperatures of the hydrogen, deuterium, and oxygen atoms, in degrees Kelvin, are indicated in the table. The tabulated values of α_{esc} are in units of $10^{-9} \text{ cm}^3 \text{ s}^{-1}$. Columns marked 'A' are for production of hot atoms including the effect of reverse collisions; columns marked 'B' neglect reverse collisions.

is at a temperature of 0, 100, 200 and 300 K. We summarize the results of the production of hot hydrogen from elastic O-H collisions on Venus in Table 3.26, along with results calculated by Cooper et al.,⁷⁵ McElroy et al.³⁵ and Gurwell and Yung.⁷⁶ It should be noted that the results of McElroy et al. assume isotropic scattering in their calculations. Cooper et al. perform calculations for both 'real' and isotropic scattering systems, and assume a Maxwellian distribution for the hot hydrogen product. Gurwell and Yung use a Henyey-Greenstein (HG) functional fit to the integrated angular distribution functions derived from the cross section calculations of Cooper et al. for a relative impact energy of 0.15 eV. They assume that the same fit is applicable to the OD system. They modify the anisotropy parameter in the HG function to approximate forward and isotropic scattering. They use several different approximations to the branching ratios for the O_2^+ dissociative recombination process, noting that while there is fairly large variation in the values of

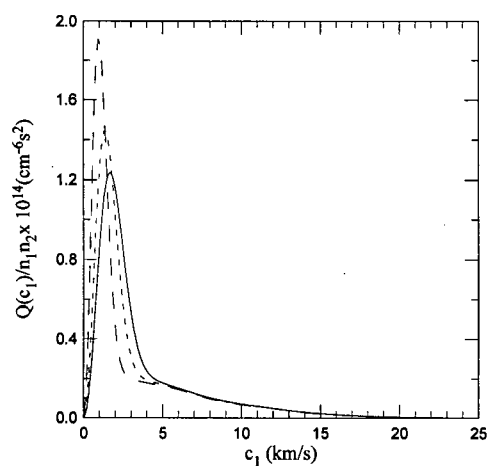
the branching ratios the average energy of the final hot oxygen distribution is generally fairly uniform. Their final calculation of product hot atom velocity distributions is done by Monte Carlo.

Our calculation assumes that the hot oxygen distribution function is Maxwellian, with a peak about the energy of the main dissociation branch (+5 eV). We also assume that the product hot atoms are Maxwellian. We utilize the (anisotropic) quantum mechanical differential cross sections directly for our calculation. As can be seen from the table, our calculated escape fractions lie between those of Cooper et al. and Gurwell and Yung, using anisotropic scattering, and those of McElroy et al. and Gurwell and Yung using isotropic scattering. Gurwell and Yung note the discrepancy between their results and those of Cooper and co-workers, especially for the case of anisotropic scattering, especially since they used the cross section data of Cooper et al. in the HG fit. However, as has been mentioned previously, published values for O-H cross sections in Cooper et al. are most likely in error, and it would therefore seem likely that calculations based on them would also be in error. The product velocity distribution functions $Q(c_1)$ for both O-H and O-D for various initial hydrogen and deuterium temperatures are shown in Figure 3.50). The results for both systems show a distribution of production of hot product speeds dominated by a peak at lower speeds and with a long tail which slowly decays with increasing speed. Their form is remarkably similar to the results of Gurwell and Yung, as given in their Figure 5.

The same calculations may be performed for O-D. Escaping production fractions for both O-H and O-D direct elastic collisions for all three terrestrial planets are given in Table 3.27. McElroy et al.³⁵ predicted that deuterium escape resulting from collisions with hot oxygen was negligible compared to hydrogen escape resulting from the same process. This was because their scattering model resulted in a maximum scattered product velocity which was less than the escape velocity on Venus for all branches of the O_2^+



(a)



(b)

Figure 3.50: Product velocity distribution functions for O-H and O-D due to direct elastic scattering. The O-H results are illustrated in (a), O-D results in (b). Initial oxygen most probable velocity is 5.6 km/s. In both figures, the hydrogen/deuterium temperatures are 100 K (long-dashed), 200 K (short-dashed), and 300 K (solid), respectively.

T[H] (K)	Present Work	C1	C2	Mc	GY1	GY2
0	9.73			6.0		
100	9.91	5.1	11.6			
200	10.16	6.9	15.5			
300	10.41	8.5	18.8	15.0	4.6	15.8

Table 3.26: Escape fraction for hot H from O-H elastic collisions on Venus. The results of Cooper et al.⁷⁵ for forward and isotropic scattering are given in C1 and C2; results of McElroy et al.³⁵ in Mc; and results of Gurwell and Young⁷⁶ for forward and isotropic scattering, in GY1 and GY2, respectively. The pre-collisional hot oxygen atom is assumed to have a velocity of 5.6 km/s.

T[H] or T[D] (K)	Venus		Earth		Mars	
	H	D	H	D	H	D
0	9.73	6.91	8.38	5.95	27.62	22.71
100	9.91	6.97	8.62	6.01	28.36	23.02
200	10.16	7.04	8.84	6.06	29.54	23.37
300	10.41	7.12	15.0	9.07	32.00	23.82

Table 3.27: Escape fraction for hot H and hot D from elastic collisions with O. Columns marked H are results for hot product hydrogen, D are results for hot product deuterium. The pre-collisional hot oxygen atom is assumed to have a most probable velocity of 5.6 km/s.

dissociative recombination reaction.⁷⁶ From the table it is clear that while the production of deuterium with velocities at or above the escape velocity for any of the terrestrial planets is not as efficient as for hydrogen, it is hardly negligible, especially for Mars where the escape energy for deuterium is only 0.25 eV. We agree with the assessment of Gurwell and Yung that the differential production of hot H and D on Venus is insufficient to account for the observed fractionation observed by the Pioneer Venus Orbiter. The magnitude of the D/H fractionation on Venus would require a mechanism which is much more selective in removal of hydrogen.

3.5 Summary

Product velocity distribution functions describing the rate of production of hot atoms for a variety of nonthermal processes, including direct-elastic and charge-exchange collisions were calculated using realistic, quantum-mechanical collision cross sections. The atomic systems H-H^+ , D-H^+ , O-H , and O-D were examined. The product velocity distribution functions for the various systems and nonthermal processes were compared and contrasted.

The product velocity distribution functions were used to yield a direct estimate of the escaping fractions of H and D as a result of nonthermal direct elastic energization by hot oxygen atoms. These kinetic theory calculations were compared to work done by other workers. Some discrepancies were found in the magnitude and form of the collision cross sections used in this work and that of some other workers. It was found that the current calculations, incorporating quantum mechanical cross sections, were in reasonably good agreement with predictions of other workers based on anisotropic cross sections. They agreed with more the more recent works in that the fraction of hot deuterium produced via direct energization by hot oxygen is not negligible, though less than the escape fraction

of hot hydrogen produced in the same way. In the current calculations, no fitting was required in the extraction of the escape fractions, nor was it necessary to fix the relative impact energy or approximate the differential collision cross section using functional fits.

Energy exchange rate coefficients were calculated using both a direct hydrodynamic approach and integration of the product velocity distribution functions calculated previously. The results of these calculations for H-H^+ were compared with results obtained using a more complicated Monte Carlo approach. It was found that while roughly similar in magnitude, the current approach correctly predicted the overestimation of energy exchange by the hot ion in the linear-trajectory approximation to the charge-exchange process. A similar calculation of charge exchange rate coefficients was carried out for D-H^+ , and it was found that the current results were in good agreement with the Monte Carlo results of other workers, but required no fitting or smoothing of statistical fluctuations.

Chapter 4

Kinetic Theory Calculations of Nonthermal Escape Fluxes

The exospheric escape problem has been examined by many previous workers for a variety of different species and for a large number of different planetary bodies. The standard collisionless approach^{9,16} to the escape of atmospheric species assumes that an equilibrium Maxwellian velocity distribution function exists at the exobase. This distribution is integrated over all upward directed velocities of magnitude equal to or greater than the escape speed, as illustrated in equation (1.2.8), in order to yield the escape flux. The result is the well known Jeans' flux, given by equation (1.2.9). Other similar approaches to the calculation of the escape flux include examinations of the steady-state, collisionless solution ($\delta f / \delta t = 0$, $J = 0$) of the Boltzmann equation, reviewed by Chamberlain¹⁶ and others.^{9,1}

The problem of non-Maxwellian effects associated with thermal escape was examined by Lindenfeld and Shizgal.^{26,152} They studied the escape of hydrogen from Earth, and found that the perturbation of the escaping minor constituents distribution function leads to an escape flux somewhat less than that predicted by Jeans theory. The steady-state case of the Boltzmann equation, where the gravitational term is explicitly ignored (but incorporated as a boundary condition) was examined by Shizgal and Blackmore.²⁷ They used a plane-parallel model for the atmosphere, and performed an altitude dependent kinetic theory calculation for escape of hydrogen and helium from Earth, and hydrogen escape from Mars, and found good agreement with Monte Carlo calculations. Lindenfeld and Shizgal⁴⁵ employed a simple collisional model to obtain an expression of the charge

exchange induced flux that can be compared with the thermal escape flux. They calculated a charge exchange rate coefficient for Earth with a value of $4.8 \times 10^{-6} \text{ s}^{-1}$, close to the estimate of $5 \times 10^{-6} \text{ s}^{-1}$ obtained by Bertaux,⁴² and showed that the total of the charge exchange and Jeans' hydrogen escape flux was roughly constant. This was consistent with the results of Liu and Donahue,³⁸⁻⁴⁰ who demonstrated that the escape flux should be approximately $1.8 \times 10^8 \text{ cm}^{-2} \text{ s}^{-1}$. A more realistic model which includes the actual density and temperature profiles was carried out by Maher and Tinsley.⁷⁷ Their estimates of hydrogen escape fluxes for low and middle latitudes on Earth are $1.5 \times 10^8 \text{ cm}^{-2} \text{ s}^{-1}$. A comprehensive assessment of terrestrial hydrogen and deuterium fluxes was carried out by Yung et al.⁷⁸ They used a one-dimensional photochemical model extending from the middle atmosphere to the exobase to model sources and sinks of both hydrogen and deuterium. They calculated net and charge-exchange escape fluxes for hydrogen of $3.02 \times 10^8 \text{ cm}^{-2} \text{ s}^{-1}$ and $1.41 \times 10^8 \text{ cm}^{-2} \text{ s}^{-1}$. The same calculations for deuterium yielded values of $3.5 \times 10^4 \text{ cm}^{-2} \text{ s}^{-1}$ and $5.4 \times 10^3 \text{ cm}^{-2} \text{ s}^{-1}$, respectively.

It has been estimated³⁷ that the average escape flux for proton charge-exchange produced hot hydrogen on Venus is $1.7 \times 10^7 \text{ cm}^{-2} \text{ sec}^{-1}$, although it may have been as much as 1000 times larger in an early atmosphere much richer in hydrogen. Deuterium escape is thought to be approximately one-tenth as efficient. McElroy et al.^{79,35} examined the nonthermal energization of hydrogen and deuterium via the dissociative recombination processes involving O_2^+ using a radiative transfer formulation. They found fluxes of approximately $8 \times 10^6 \text{ cm}^{-2} \text{ sec}^{-1}$ for hydrogen, while concluding that the analogous process for deuterium was negligible. Kumar et al.¹⁵³ estimated that the hydrogen escape flux due to charge exchange with hot protons was $1.2 \times 10^6 \text{ cm}^{-2} \text{ sec}^{-1}$. A Monte Carlo simulation of hydrogen escape on Venus by Hodges and Tinsley¹⁵⁴ estimated the planetary average escape rate due to charge exchange was $2.8 \times 10^7 \text{ cm}^{-2} \text{ s}^{-1}$. Shizgal⁷¹ performed a kinetic

theory calculation of escape rates for nonthermal hydrogen on Venus using quantum collision cross sections for hydrogen-proton charge exchange collisions. He found escape rates of 1.1 and $6.2 \times 10^7 \text{ cm}^{-2}\text{s}^{-1}$ for the dayside and nightside exosphere. These values were smaller than those reported by Kumar et al.,¹²³ who performed a simpler rate calculation to find escape fluxes of 2.7 and $13.3 \times 10^7 \text{ cm}^{-2}\text{s}^{-1}$, respectively.

Calculations of hydrogen escape for Mars are few, as temperature and density data are poor for hydrogen. Using Mariner observations, Barth et al.¹²¹ and Anderson¹²⁰ estimate a value between $(1-2) \times 10^8 \text{ cm}^{-2}\text{s}^{-1}$. Lammer and Bauer⁸ employed a Monte Carlo technique to simulate the thermalization and transport of hot oxygen atoms produced by dissociative recombination of O_2^+ on Mars. They estimated an escape flux of $6 \times 10^6 \text{ cm}^{-2}\text{s}^{-1}$, corresponding to a mass loss of oxygen atoms at a rate of 0.14 kg/s . Other estimates of the oxygen escape rate are given by Fox⁸⁰ at $3 \times 10^6 \text{ cm}^{-2}\text{s}^{-1}$, and by McElroy⁸¹ at $(6-7) \times 10^6 \text{ cm}^{-2}\text{s}^{-1}$.

In Chapter 3, we considered the result of the nonthermal charge exchange process, employing realistic differential cross sections. Others^{71,76} have also considered the production of hot atoms from charge exchange processes. However, it is notable that distributions of hot atoms calculated in this way for Venus do not yield temperatures in tremendous agreement with the observed two temperature exosphere.⁷¹ An important consideration may involve the partial thermalization of the energetic atoms produced owing to collisions with other ambient species, something not incorporated into the models of Chapter 3. Due to thermalization, it is expected that the escape rate will be reduced, bringing the theory into better agreement with observations. To account for the competition between thermalization and reactive processes in a rigorous fashion requires an altitude dependent kinetic theory treatment of the Boltzmann equation, and is currently beyond the scope of this work. However, it is possible to make approximations of the thermalization process in order to yield escape fluxes which reflect the effect of

the ambient neutral atmosphere on hot atom escape rates. This is addressed in further detail in the theory section of this chapter.

It is also clear that the theoretical structure of the exosphere must be reconsidered in order to include the effect of escape due to collisional nonthermal processes. The collisionless picture is not a true reflection of the actual exosphere, although one could consider the exosphere as almost collisionless with infrequent nonthermal collisional processes as a first order deviation from the collisionless state.^{122,5} However, in order to properly describe the transition between the collision dominated and collisionless regimes properly, the notion of a sharp discontinuity at the exobase that divides the atmosphere between hydrodynamic kinetic regimes has to be abandoned. Instead, the escape process should be considered as occurring from a range of altitudes above and below the exobase.^{26,1} This concept originates in the older works of Biutner,¹⁵⁵ Jensen¹⁵⁶ and Jockers,¹⁵⁷ and has been considered by Shizgal and Lindenfeld^{26,45} and Shizgal⁷¹ and more recently by Johnson.^{158,159} It forms the basis for the treatment of the escape process used in this chapter.

4.1 Theory

The basic concept of the model proposed by Lindenfeld and Shizgal²⁶ is that translationally energetic species are produced by elastic or reactive collisions. These energetic particles are moving in all directions but only those moving radially outward can escape, provided they do not suffer further collisions that change the direction and magnitude of their velocity so as to prevent it. Since the density decreases approximately barometrically (see equation (1.2.4)), the rate of collisions decreases with increasing altitude, and hence the population of translationally energized particles decreases. However, with the decrease in the density the mean free path increases and the probability of escape

increases. Thus, the rate of escape as a function of altitude attains a maximum value occurring in the vicinity of the exobase. The net escape flux may be written as an integral over radial position,

$$F_{net} = \int_{r_0}^{r_1} F(r) dr \quad (4.1.1)$$

The units of F_{net} are those of a flux, $\text{cm}^{-2} \text{s}^{-1}$. In equation (4.1.1), r_0 is some reference level deep enough in the atmosphere that the escape probability is zero while r_1 is the altitude above which the atmosphere can be considered 'collisionless' and there is no collisional production of hot, nonthermal atoms. $F(r)$, the rate of production of energetic atoms per unit volume escaping from radial position r , is given by

$$F(r) = \int p(r, c_1) Q(r, c_1) d\mathbf{c}_2 \quad (4.1.2)$$

where $Q(r, c_1)$ is the velocity dependent production rate of energetic particles at radial position r and $p(r, c_1)$, is the probability that a particle with speed c_1 at position r will escape. The explicit form of $p(r, c_1)$ exhibits a very weak dependence on the speed.²⁶ The probability for escape, $p(r, c_1)$, increases to approximately 1/2 with altitude while $Q(r, c_1)$, the production of energetic particles through collisions, decreases with altitude. The units of $F(r)$ are $\text{cm}^{-3} \text{s}^{-1}$.

It is assumed that F_{net} represents the net escape flux from the entire range of altitudes, but only along the direction $d\hat{\mathbf{r}}$. If it is further assumed that the flux from the atmosphere or system is isotropic, then the overall planetary escape rate is found by multiplying F_{net} by the area of the spherical shell defining the uppermost boundary of the system.

We consider a system with two species. Particles of type 1 are the escaping, collisionally energized species, while particles of type 2 comprise the (thermal) background. Collisions occur only between the two different types; non-linear self collisional types of processes are not considered. If we choose a 'plane parallel' atmosphere, with geometry as shown in Figure 4.51, the probability of escape of a particle with speed c_1 , moving in a

direction making an angle θ with the zenith direction and which suffered its last collision at an altitude r is given by^{160,26}

$$P(r, c_1, \theta) = \exp \left[-\sec \theta Z(c_1) \int_r^{r_1} n_b(r') dr' \right] \quad (4.1.3)$$

where $Z(c_1)$ is the dimensionless collision frequency for particles of species 1 with the background, $n_b(r')$ is the density of the background gas, and the range of θ for escaping particles is taken as $0 \leq \theta \leq \pi/2$. The velocity dependence of equation (4.1.3) arises through the collision frequency, $Z(c_1)$, which is defined as

$$Z(c_1) = \frac{1}{A} \iint f_2(\mathbf{c}_2) \sigma g d\Omega d\mathbf{c}_2 \quad (4.1.4)$$

where A is the non-dimensionalizing factor for $Z(c_1)$, \mathbf{g} is the relative velocity, Ω is the solid angle about the scattering direction, and σ is the differential scattering cross section.

If the total elastic collision cross section for collisions between the two particle types is assumed to be the hard sphere cross section, πd^2 , where d is the mean diameter of the colliding pair, $d \equiv (d_1 + d_2)/2$, it can be shown (see Appendix F) that the collision frequency is given by

$$Z(x) = \frac{A}{\sqrt{\gamma}} \left[e^{-\gamma x} + \frac{\sqrt{\pi}}{2} \left\{ \frac{1}{\sqrt{\gamma x}} + 2\sqrt{\gamma x} \right\} \text{erf}(\sqrt{\gamma x}) \right] \quad (4.1.5)$$

where $A = d^2 \left(\frac{2\pi k T_2}{m_1} \right)^{\frac{1}{2}}$, and where we have defined a dimensionless energy $x \equiv \frac{m_1 c_1^2}{2kT}$, the mass ratio $\gamma = m_2/m_1$, and used the standard definition of the error function $\text{erf}(x)$.

The escape probability $p(r, c_1)$ from equation (4.1.2) is given by the *average* of $P(r, c_1, \theta)$ over all possible escape angles θ , that is

$$\begin{aligned} p(r, c_1) &= \int_0^{\pi/2} \frac{1}{2} \sin \theta P(r, c_1, \theta) d\theta \\ &= \frac{1}{2} E_2(\gamma Z(x)/\sqrt{\pi x}) \end{aligned} \quad (4.1.6)$$

where we have defined

$$E_2(s) = \int_1^\infty e^{-st} t^{-2} dt$$

and where y is the vertical optical depth,

$$y = \pi d^2 \int_r^{r_1} n_2(r') dr' \quad (4.1.7)$$

Equation (3.4.1) gives the rate of production of particles of type 1, with speed c_1 , due to collisions. Only those particles with speeds exceeding the escape speed will permanently escape the planetary atmosphere. Thus, in calculating the net escape flux, equation (4.1.1), we want to include only those particles of type 1 which have speeds exceeding the escape speed. Thus, the rate of production of hot atoms with speeds exceeding the escape speed becomes²⁶

$$Q(r, c_1) = H(c_1 - C_{esc}) n_1(r) n_2(r) \iint f_1(r, \mathbf{c}'_1) f_2(r, \mathbf{c}'_2) g \sigma d\Omega d\mathbf{c}_2 \quad (4.1.8)$$

where

$$H(c_1 - C_{esc}) = \begin{cases} 0 & c_1 \leq C_{esc} \\ 1 & c_1 > C_{esc} \end{cases}$$

is simply the standard Heavyside function. If it is assumed that the velocity distribution functions of both the background and the escaping species have reached equilibrium, we get the equilibrium rate of production of hot atoms,

$$Q^{eq}(r, c_1) = H(c_1 - C_{esc}) n_1(r) n_2(r) \iint f_1^M(c'_1) f_2^M(c'_2) g \sigma d\Omega d\mathbf{c}_2$$

where

$$f_1^M(c'_1) = \left(\frac{m_1}{2\pi kT} \right)^{3/2} \exp \left[-\frac{m_1 c'^2_1}{2kT} \right]$$

$$f_2^M(c'_2) = \left(\frac{m_2}{2\pi kT} \right)^{3/2} \exp \left[-\frac{m_2 c'^2_2}{2kT} \right]$$

In this case, it is possible to easily replace the velocities $(\mathbf{c}'_1, \mathbf{c}'_2)$ with $(\mathbf{c}_1, \mathbf{c}_2)$ in the velocity distribution functions using simple conservation of energy, $m_1 c_1'^2 + m_2 c_2'^2 = m_1 c_1^2 + m_2 c_2^2$; that is,

$$\begin{aligned} f_1^M(\mathbf{c}'_1) f_2^M(\mathbf{c}'_2) &= \left(\frac{m_1}{2\pi kT} \right)^{3/2} \left(\frac{m_2}{2\pi kT} \right)^{3/2} \exp \left[-\frac{m_1 c_1'^2 + m_2 c_2'^2}{2kT} \right] \\ &= \left(\frac{m_1}{2\pi kT} \right)^{3/2} \left(\frac{m_2}{2\pi kT} \right)^{3/2} \exp \left[-\frac{m_1 c_1^2 + m_2 c_2^2}{2kT} \right] \\ &= f_1^M(\mathbf{c}_1) f_2^M(\mathbf{c}_2) \end{aligned}$$

and so we have

$$Q^{eq}(r, c_1) = H(c_1 - C_{esc}) n_1(r) n_2(r) f_1^M(c_1) AZ(x) \quad (4.1.9)$$

where we have simply used the definition of the collision frequency, equation (4.1.4). With equations (4.1.9) and (4.1.6) in equation (4.1.1), we find that the net equilibrium escape flux is given by

$$\begin{aligned} F_{net}^{eq} &= \frac{A}{2} \int f_1^M(c_1) Z(x) H(c_1 - C_{esc}) \times \\ &\quad \int_{r_0}^{r_1} E_2(y(r) Z(x) / \sqrt{\pi x}) n_1(r) n_2(r) dr d\mathbf{c}_1 \end{aligned} \quad (4.1.10)$$

Using the definition of y from equation (4.1.7) to change the variable of integration from r to $y' = yZ/\sqrt{\pi x}$, and with r_0 and r_1 taken as 0 and ∞ respectively, it is possible to show that equation (4.1.10) reduces to the Jeans flux, F_J , defined by equation (1.2.9).

If we rewrite equations (4.1.1) and (4.1.2) using the PVDFs from the previous chapter, we can see that our net escape flux is given by

$$F_{net}^{eq} = \int_{C_{esc}}^{\infty} \int_{r_0}^{r_1} n_1(r) n_2(r) p(r, c_1) Q(c_1) dr d\mathbf{c}_1 \quad (4.1.11)$$

where $Q(c_1)$ is the product velocity distribution function given in Chapter 3. We note that the calculation is carried out only over those speeds in excess of the escape speed;

in effect, we sample only the 'tail' of the PVDFs. The PVDFs are calculated using the realistic, quantum mechanical cross sections for H^+-H , H^+-D , $O-H$ or $O-D$ as illustrated in the previous chapter. The probability of escape, $p(r, c_1)$, is given by equation (4.1.6). As mentioned previously, it depends only weakly on the velocity, and is not particularly sensitive to the energy dependence of the total cross section. It is thus calculated using a hard-sphere cross section representing collisions between species 1 and the background gas (not necessarily species 2) which dictates the probability of escape. We may add the reverse collision term to equation (4.1.11) in order to estimate the effect of reverse collisions in reducing the production of hot atoms. It should be noted, however, that this is not strictly correct, as the reverse collision term is calculated with the assumption that the hot atom distribution function is Maxwellian (and as we saw in Chapter 3, the PVDF is clearly indicative of non-Maxwellian hot atom distributions).

In order to calculate net escape fluxes, we require some estimate of the temperature and density profiles of species 1 and 2, in addition to the density profile of the escape inhibiting background and the species 1-background total cross section. Especially for Mars, most of these parameters are, at best, poorly known or poorly constrained. The choices for our input profiles are shown in Figures 4.52- 4.55 for Venus and Earth. The predominant gas at exospheric altitudes is atomic oxygen for all three planets, and so it is adopted as the background in each case. We estimate a total hard sphere cross section for species 1-background collisions from our quantum calculations; we choose a value of $33 \times 10^{-16} \text{ cm}^2$ for $O-H$ and for $O-D$.

The escape flux for hydrogen on Venus was calculated for both day- and night-side conditions. The integration was carried out from a starting altitude of 120 km up to the level of the ionopause, the base of the ionosphere, assumed to be 800 km.¹⁵³ For day-side conditions where the probability of escape, $p(r)$ was neglected, the calculated net escape fluxes for direct elastic and charge-exchange produced hot hydrogen were $2.8 \times 10^5 \text{ cm}^{-2}$

s^{-1} and $2.6 \times 10^5 \text{ cm}^{-2} \text{ s}^{-1}$, respectively. When $p(r)$ was included, the net escape flux was reduced to $9.7 \times 10^3 \text{ cm}^{-2} \text{ s}^{-1}$ and $8.9 \times 10^3 \text{ cm}^{-2} \text{ s}^{-1}$, respectively. For night-side conditions where the probability of escape, $p(r)$ was neglected, the calculated net escape fluxes for direct elastic and charge-exchange produced hot hydrogen were $7.0 \times 10^6 \text{ cm}^{-2} \text{ s}^{-1}$ and $5.0 \times 10^6 \text{ cm}^{-2} \text{ s}^{-1}$, respectively. When $p(r)$ was included, the net escape flux was reduced to $3.0 \times 10^6 \text{ cm}^{-2} \text{ s}^{-1}$ and $2.0 \times 10^6 \text{ cm}^{-2} \text{ s}^{-1}$, respectively. The calculated values are slightly lower than most values reported by other workers, as given in the introduction to this chapter. If we consider only the night-side values for charge-exchange, the calculated fluxes are of roughly the correct magnitude. It also appears, from our results, that direct collisional excitation of hydrogen by hot protons may also provide a reasonable enhancement to the net escape of hydrogen.

The escape flux for hydrogen from the Earth's atmosphere was calculated for a background oxygen temperature of 917 K. The integration was carried out from a starting altitude of 100 km up to an altitude of 6000 km. For the case where the probability of escape, $p(r)$ was neglected, the calculated net escape fluxes for direct elastic and charge-exchange produced hot hydrogen were $1.3 \times 10^9 \text{ cm}^{-2} \text{ s}^{-1}$ and $1.1 \times 10^9 \text{ cm}^{-2} \text{ s}^{-1}$, respectively. When $p(r)$ was included, the net escape flux was reduced to $1.9 \times 10^7 \text{ cm}^{-2} \text{ s}^{-1}$ and $1.4 \times 10^7 \text{ cm}^{-2} \text{ s}^{-1}$, respectively. These values without $p(r)$ appear slightly higher than those predicted by other workers, while those with $p(r)$ are slightly lower.

The current calculation calculates a rate of production of hot hydrogen with speeds in excess of the escape speed only. Inclusion of the probability of escape $p(r)$ reduces the net escape flux substantially; this is because $p(r)$ is near zero at lower altitudes (where the production of hot atoms is highest) and grows to a maximal value of $\frac{1}{2}$ at high altitudes where densities are lower and production of hot hydrogen is much lower.

4.2 Summary

An altitude dependent, kinetic theory approach was used to calculate the rate of escape of atmospheric constituents. This was approached in the context of escape resulting from energization of neutral atmospheric species via nonthermal processes, with the kinematics described by realistic, quantum mechanical collision cross sections. The reduction of the escape rate by the ambient atmosphere was included through an altitude dependent probability of escape, $p(r)$, although the effect of thermalization via collisions with the background was neglected. Temperature and density profiles used in the calculations were taken from available atmospheric data and from atmospheric models, and escape fluxes of hydrogen were estimated for Venus and Earth due to direct elastic collisions and charge-exchange.

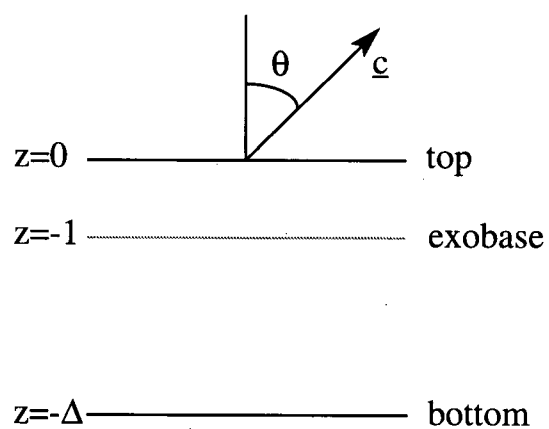


Figure 4.51: Geometry for a plane-parallel atmosphere.

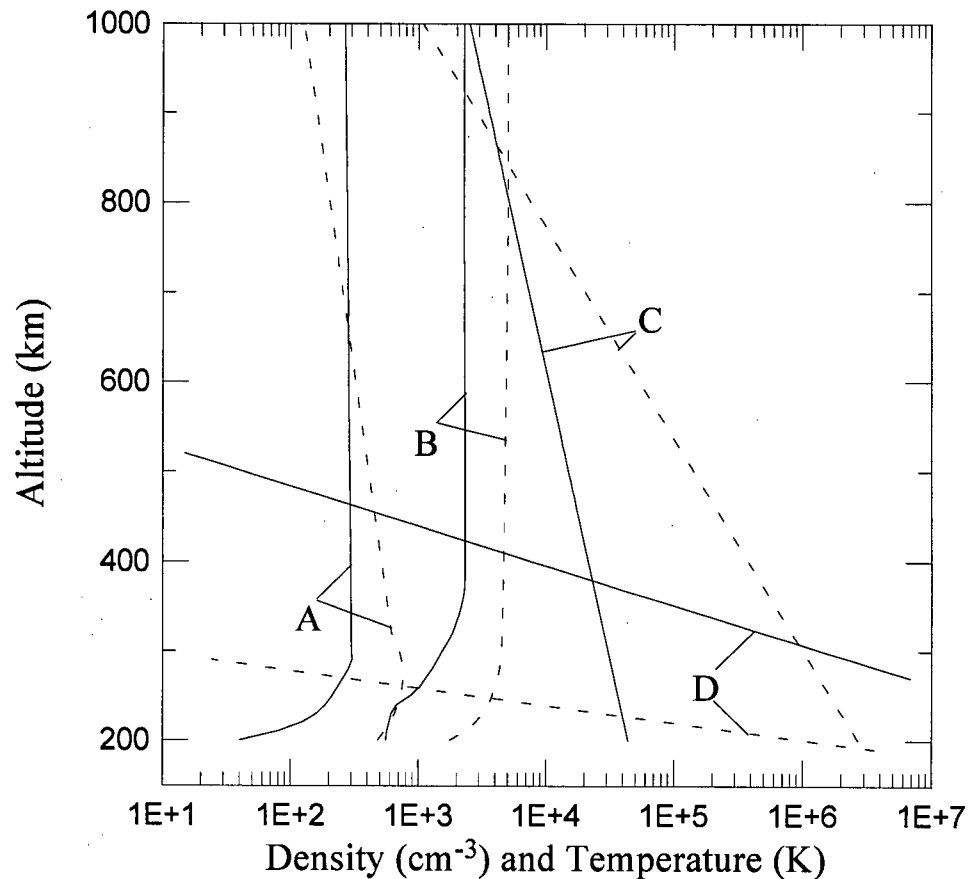


Figure 4.52: Temperature and density profiles used as input for flux calculations on Venus. The labels A, B, C, and D denote the proton density, proton temperature, atomic hydrogen density, and background oxygen density, respectively. Solid curves represent dayside values and dashed curves represent nightside values. The data are taken from Pioneer Venus orbiter measurements as reported by Brinton and workers¹⁶¹ and Kumar and workers.¹⁵³ The dayside/nightside hydrogen temperature is assumed to be constant, with a value of 300/110 K as deduced from Pioneer Venus orbiter measurements.

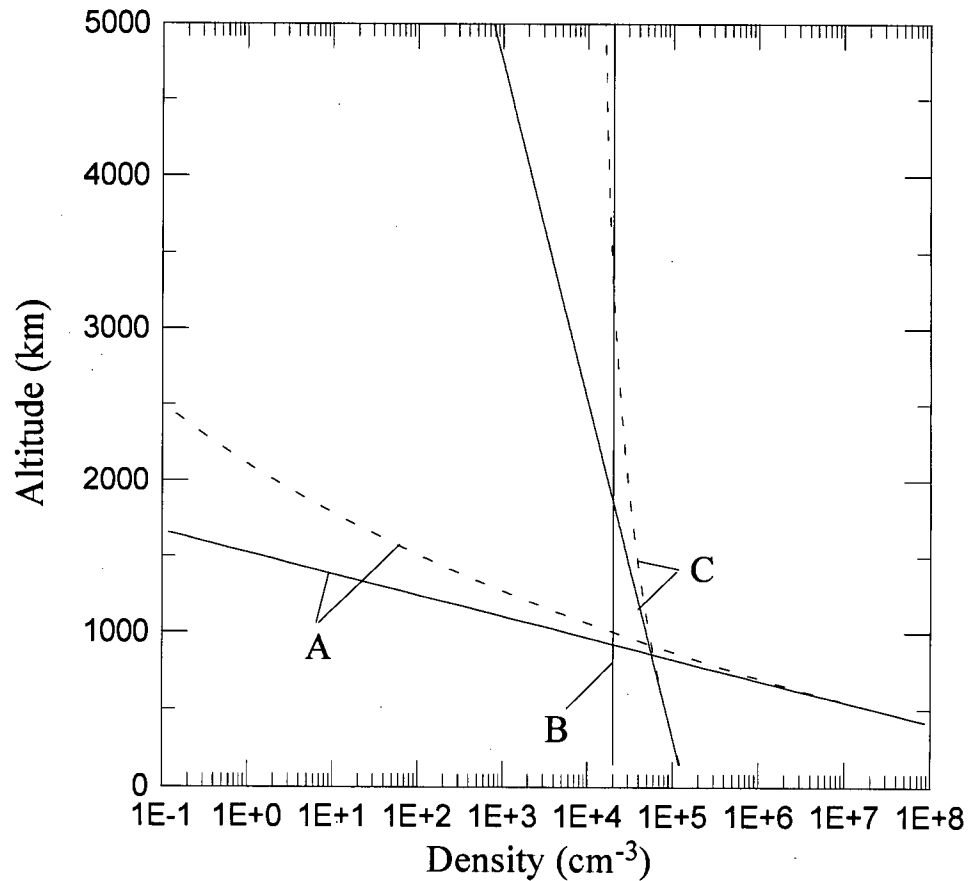


Figure 4.53: Density profiles used as input for flux calculations on Earth. The values are taken from the work of Shizgal and Lindenfeld,⁴⁵ and are shown for an exospheric temperature of 1000 K. The labels A, B, and C denote the background oxygen density, proton density, and atomic hydrogen density, respectively. The proton density is assumed to be constant, with a value of $2.0 \times 10^{-4} \text{ cm}^{-3}$. The solid/dashed curves for the oxygen and hydrogen profiles are barometric, with a constant/altitude varying scale height.

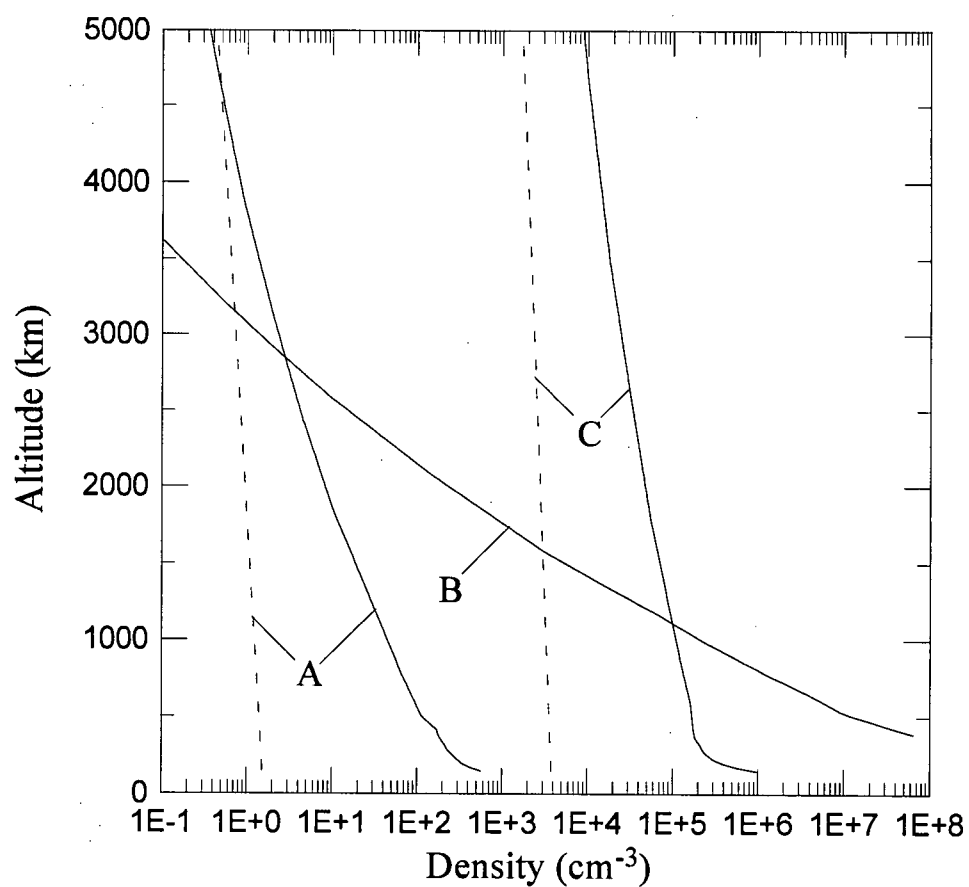


Figure 4.54: Density profiles used as input for flux calculations on Earth. The values are taken from Yung and workers.⁷⁸ The labels A, B, and C denote deuterium, oxygen, and hydrogen density profiles. The solid curves represent densities for the neutral species and the dashed curve represents the density of the ion of that particular species.

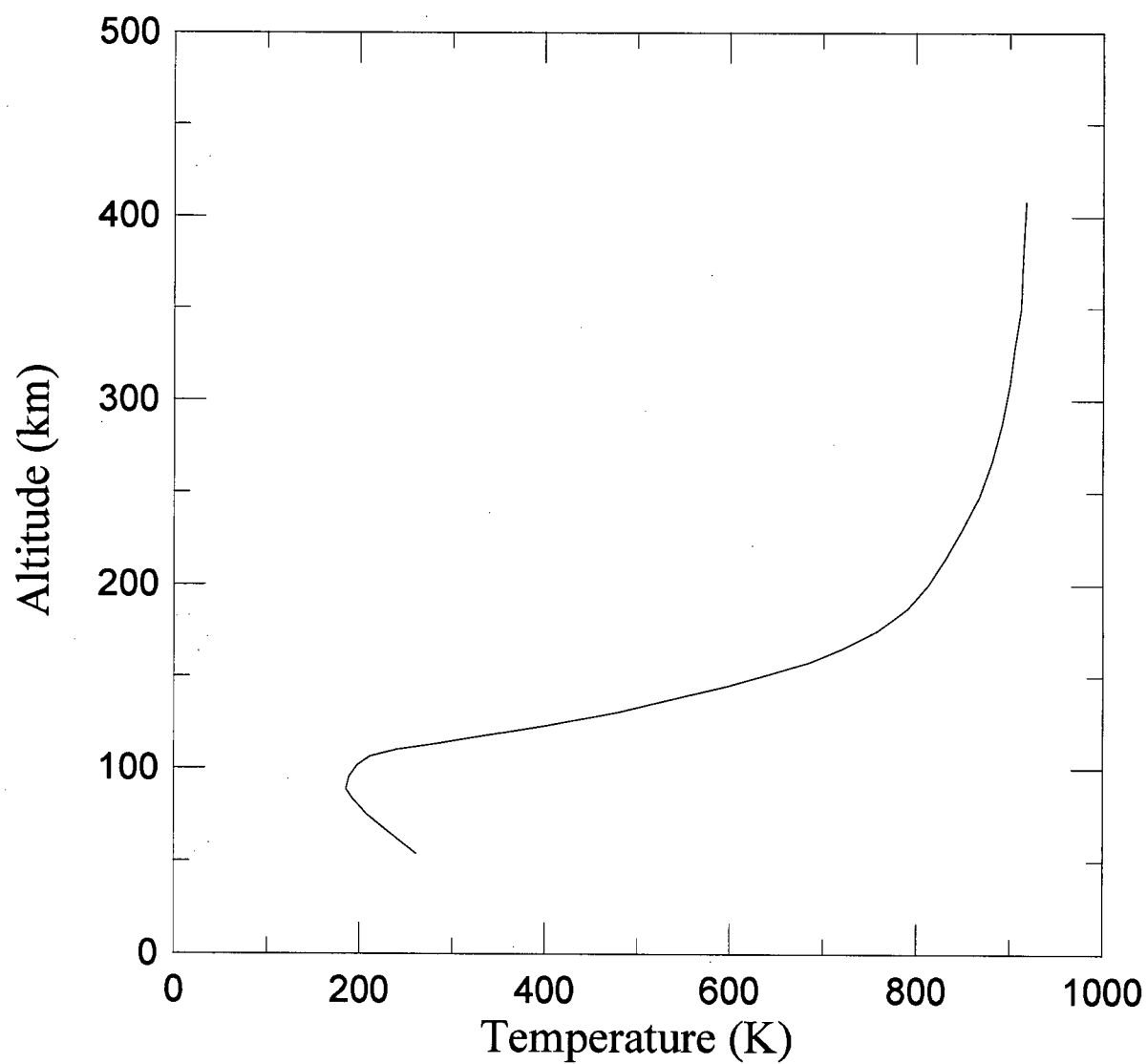


Figure 4.55: Temperature profile used as input for flux calculations on Earth. The data are taken from Yung and workers,⁷⁸ and are representative of exospheric neutral temperatures.

Chapter 5

Summary and Suggestions for Future Research

This work was intended to examine the importance of nonthermal processes in the exospheres of the terrestrial planets. Specifically, the role of nonthermal processes in the production of hot oxygen and generation of extended coronae was examined. Nonthermal processes such as charge-exchange and direct elastic energization were described using a kinetic theory approach, and were contrasted for several atomic systems. The kinetic theory description of hot atom production was extended to calculate escape fluxes from the terrestrial planets.

The formation of hot oxygen coronae in the atmospheres of Venus and Mars via the nonthermal process of dissociative recombination of O_2^+ was examined using both hydrodynamic and kinetic theory approaches. It was found that an extended hot oxygen corona could be predicted from either approach. The magnitude and extent of the predicted coronae were found to vary greatly. For the hydrodynamic constant temperature model the choice of the hot product atom temperature profile had great impact on the hot oxygen densities at altitudes well above the exobase, although variation of the temperature did not affect the qualitative prediction of sizable enhancement of oxygen densities over the thermal background. The kinetic theory model included the effect of thermalizing collisions with the cold background and yielded the time dependent distribution function for the hot oxygen atoms. The time dependence was transformed to altitude dependence, and the distribution function at the exobase was used to calculate hot oxygen densities in the exosphere. It was found that the assumptions made in this

model caused an overestimation of the effect of thermalizing collisions, and density profiles extracted in this manner were on the order of an order of magnitude lower at an altitude of approximately 1600 km than those predicted by workers using other methods, although still far above thermal densities.

Product velocity distribution functions describing the rate of production of hot atoms for the atomic systems H-H^+ , D-H^+ , O-H , and O-D were calculated for a variety of nonthermal processes, including direct-elastic and charge-exchange collisions. The calculations were carried out using a kinetic theory approach, and were done utilizing direct numerical integration techniques. The calculations incorporated realistic, quantum-mechanical collision cross sections for each system. Energy exchange rate coefficients were calculated in a similar manner, and compared with results obtained using a more complicated Monte Carlo approach. Timescales describing the time evolution of the average energy of a test particle in a bath were calculated using the energy exchange rate coefficients. The overestimation of energy exchange by the hot ion in the linear-trajectory approximation to the charge-exchange process was re-confirmed by both these studies. The product velocity distribution functions were also used to estimate the escaping fractions of H and D as a result of nonthermal direct elastic energization by hot oxygen atoms. These kinetic theory calculations were compared to work done by other workers using Monte Carlo methods incorporating approximate and quantum mechanical cross sections, and were found to be in good agreement with predictions based on anisotropic cross sections. The calculations also showed that the fraction of hot deuterium produced via direct energization by hot oxygen, while less than the fraction of hot hydrogen, is not negligible.

An altitude dependent, kinetic theory approach was used to calculate the rate of escape of atmospheric constituents. This was approached in the context of escape resulting from energization of neutral atmospheric species via nonthermal processes, with

the kinematics described by realistic, quantum mechanical collision cross sections. The reduction of the escape rate by the ambient atmosphere was included through an altitude dependent probability of escape, $p(r)$, although the effect of thermalization via collisions with the background was neglected. Temperature and density profiles used in the calculations were taken from available atmospheric data and from atmospheric models, and escape fluxes of hydrogen were estimated for Venus and Earth, and were in reasonable agreement with estimates obtained by other workers.

There are many possible future research topics which could follow up on and extend the work done in this thesis. One of the more important immediate research objectives would be the rigorous incorporation of thermalization of hot atom products by the ambient atmosphere. In full generality, this would involve the solution of the full, altitude dependent Boltzmann equation, given previously by equation (1.4.1). This problem is extremely formidable as it stands. It could be made tractable by assuming that all species except for the hot atoms are in equilibrium. In a first instance, the problem could be further simplified by assuming a spatially homogeneous distribution function and a plane-parallel atmosphere. A problem similar to this was examined by Shizgal and Blackmore,²⁷ where they examined the nonequilibrium escape flux and calculated density and temperature profiles. In their model, time dependence and the external force (gravity) term in the Boltzmann equation were explicitly neglected, although the effect of gravity was incorporated into boundary conditions in their discretization procedure. In that work, nonthermal production of hot atoms was not examined and a hard sphere cross section was used to describe the collision process. It would be of interest to, as a first step, extend their work with the incorporation of the nonthermal processes and realistic cross sections examined in this thesis. A further improvement to the model could include the inclusion of spherical geometry.

Other immediate extensions to this present work are also possible. A set of coupled

Boltzmann equations examining modification of the ambient neutral velocity distribution function by interaction with a hot atom source, based on the Boltzmann equation work done in Chapter 2, would be an obvious choice. An example of this would be the differential effect of hot oxygen, produced by dissociative recombination, on hydrogen and deuterium in the atmosphere of Venus. Such a study would show the time dependent development of the the distribution functions as a result of nonthermal collisional processes and thermalization.

Of great importance, especially for Mars, is the accumulation of more extensive and accurate temperature and density profiles. Many of the uncertainties in the models are a result of poor spatial or temporal resolution of these parameters. The accumulation of further data on the atmospheric composition of Mars by instruments aboard planetary missions en-route to the planet (or planned for the near future) could also do much to extend the work done on escape fluxes in this thesis. The availability of solar cycle dependent temperature and density profiles for major ions and neutrals would provide much needed constraints on the modeling of nonthermal collisional production of hot atoms in the upper atmosphere. Further measurements of the extent of isotopic fractionation patterns on the terrestrial planets would greatly aid in models of the strength and importance of nonthermal processes in the early evolution of the planetary atmospheres.

Appendix A

Density Profiles in a Collisionless Exosphere

The calculation of densities for a collisionless exosphere has been examined in many different ways.^{16,22,43,11} In this appendix, the terminology and notation of the review article by Fahr and Shizgal¹ is adopted.

In the absence of collisions, particles moving through an exosphere follow trajectories determined by the direction and magnitude of their velocities and the strength of the gravitational field. This may be quantified by considering the parameterization of any given particle by its total energy E and its angular momentum L . We define c and r as the speed and radial position, with their exobase (or critical level) values denoted by c_c and r_c . The conservation of energy and angular momentum yield

$$\begin{aligned} E_r^{tot} = T + V &= E_c^{tot} \\ \Rightarrow \frac{1}{2}mc^2 - (GMm/r) &= \frac{1}{2}mc_c^2 - (GMm/r_c) \end{aligned}$$

and

$$\begin{aligned} L_r = \mathbf{r} \times m\mathbf{c} &= L_c \\ \Rightarrow rc \sin \theta &= r_c c_c \sin \theta_c \end{aligned}$$

respectively, coupling the values at the exobase with the values higher in the exosphere. The quantities G and M are the universal gravitational constant and the planetary mass, and m is the particle mass. Transforming to dimensionless units $X = c/c_{esc}$ and $y = r_c/r$, where $c_{esc} \equiv \sqrt{(2GM/r_c)}$ is the exobase escape speed, yields

$$X_c^2 - 1 = X^2 - y \tag{A.0.1}$$

$$yX_c \sin \theta_c = X \sin \theta \quad (\text{A.0.2})$$

The angle θ is the interior angle between the outward radial direction \mathbf{r} and \mathbf{c} . The various types of particle classes and trajectories, detailed by Chamberlain,¹⁶ can be identified by the values of X and θ for any given particle.

Escaping particles are those with energies $E > 0$; that is, they have translational energy exceeding the gravitational potential 'well' of the planet. Those that are non-escaping have $E < 0$, with the value $E = 0$ marking the division between the two classes. If we define

$$X_t = X \sin \theta$$

$$X_r = X \cos \theta$$

we see from equation (A.0.1) that the boundary $E = 0$ is equivalent to

$$X^2 = X_r^2 + X_t^2 = y$$

or a circle of radius \sqrt{y} in (X_r, X_t) phase space. Particles with (X_r, X_t) inside this circle execute closed, elliptical orbits while particles with (X_r, X_t) outside the circle execute open hyperbolic ones. The other important concept in the division of particle classes is whether or not a particle trajectory intersects the exobase level, r_c . A particle whose trajectory touches the exobase at only one point (a "glancing" trajectory) will have $\theta_c = \pi/2$; that is, from equation (A.0.2), X_c is perpendicular to \mathbf{r} . Any trajectory crossing r_c must have $\theta_c \neq \pi/2$. If we substitute $\theta_c = \pi/2$ into equation (A.0.2), square it, and then substitute for X_c^2 from equation (A.0.1), we have after some simplification that

$$X_t^2 - \frac{y^2}{1 - y^2} X_r^2 = X_b^2 \quad (\text{A.0.3})$$

where

$$X_b \equiv \frac{y^2}{1+y}$$

Equation (A.0.3) defines the particle trajectories which do not cross the exobase; it is of the form

$$\frac{X_t^2}{a^2} - \frac{X_r^2}{b^2} = 1$$

which defines a hyperbola with foci at $c = a^2 + b^2 = \pm X_b/y$ and eccentricity $e = c/a = 1/y$. If we define the polar angle of the hyperbola as θ_p , we have for any point on the hyperbola that

$$X_t = X \sin \theta_p$$

$$X_r = X \cos \theta_p$$

or, substituting into equation (A.0.3) and simplifying,

$$\sin \theta_p = \frac{y}{X} (X^2 + 1 - y)^{\frac{1}{2}} \quad (\text{A.0.4})$$

The various classes of particles are listed in Table A.28, and may be graphically illustrated for fixed values of y , as in Figure A.56 (which corresponds to a radial position giving $y = 1.5$).

The densities of particular classes of particle at altitudes above the exobase are calculated by assuming that the distribution function at the exobase is a Maxwellian. From equation (1.2.7), we have

$$\begin{aligned} n_k &= \int_{\text{partial}} f^M(c_c) dc \\ &= 2\pi n_c \left(\frac{m}{2\pi k T_c} \right)^{\frac{3}{2}} \iint_{\theta, c \text{ partial}} \exp \left[-\frac{mc^2}{2kT_c} \right] c^2 dc \sin \theta d\theta \end{aligned} \quad (\text{A.0.5})$$

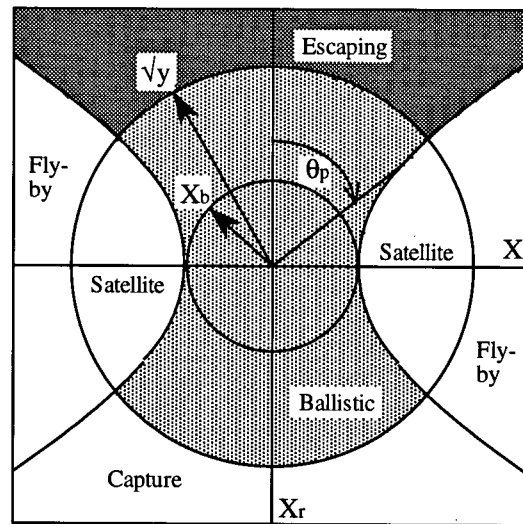


Figure A.56: A graphical illustration of exospheric particle classes in the phase plane of (X_r, X_t) . The altitude used for this particular figure corresponds to a value of $y = 1.5$. The quantities y , X_b and θ_p are defined in the text of this Appendix. The escaping and ballistic particle regions are shaded to clarify the regions of phase space represented by those particle classes. Based on figures by Fahr and Shizgal.¹

Particle Class	Orbit	X limits	θ limits	Region of (X_r, X_t)
(B)allistic & (S)atellite	elliptic (b)	$0 \leq X \leq \sqrt{y}$	$0 \leq \theta \leq \pi$	inside large circle
(E)scaping & (I)ncoming	hyperbolic (nb)	$X > \sqrt{y}$	$0 \leq \theta \leq \pi$	outside large circle
(B)allistic	elliptic (b) and cross r_c	$0 \leq X \leq X_b$ $X_b < X \leq \sqrt{y}$	$0 \leq \theta \leq \pi$ $0 \leq \theta \leq \theta_p$	inside small circle between circles & inside hyperbola
(E)scaping	hyperbolic (nb) and cross r_c	$X > \sqrt{y}$	$0 \leq \theta \leq \theta_p$	outside large circle & inside hyperbola

Table A.28: Exospheric particle classes. The incoming particles are sometimes divided into a flyby and capture component. The abbreviations 'b' and 'nb' under the 'Orbit' column refer to bound or non-bound orbits of the type specified. Based on Fahr and Shizgal.¹

If we use the definition of the escape parameter from equation (1.2.10),

$$\begin{aligned}\lambda_c &= \frac{E_{esc}}{kT_c} \\ &= \frac{GMm}{kT_c r_c}\end{aligned}$$

change to dimensionless variables y, X as previously, and use equation (A.0.1), equation (A.0.5) becomes

$$n_k = 2\pi n_{bar} \left(\frac{\lambda_c}{\pi}\right)^{\frac{3}{2}} \iint_{\theta, X_{partial}} e^{-\lambda_c X} X^2 dX \sin \theta d\theta \quad (\text{A.0.6})$$

where $n_{bar} = n_c \exp[-\lambda_c(1-y)]$ is the barometric density, equivalent to that given in equation (1.2.4). If the integration in equation (A.0.6) is carried out over all (θ, X) the total density n_{tot} is given by the barometric density, n_{bar} . The densities of the various particle classes are given by performing partial integrations over (θ, X) based on the

limits given in Table A.28. For the ballistic and satellite (B&S) components we have

$$n_{bs} = 2\pi n_{bar} \left(\frac{\lambda_c}{\pi} \right)^{\frac{3}{2}} \int_0^\pi \int_0^{\sqrt{y}} e^{-\lambda_c X} X^2 dX \sin \theta d\theta$$

If we make the change of variable $s = \lambda_c X^2$, and also use $\int_0^\pi \sin \theta d\theta = \int_{-1}^1 d(\cos \theta) = 2$, this becomes

$$\begin{aligned} n_{bs} &= \frac{2}{\sqrt{\pi}} n_{bar} \int_0^{\lambda_c y} e^{-s} s^{\frac{3}{2}-1} ds \\ &= \frac{2}{\sqrt{\pi}} n_{bar} \gamma(3/2, \lambda_c y) \end{aligned} \quad (\text{A.0.7})$$

where we have used the ‘incomplete’ gamma function

$$\gamma(a, z) = \int_0^z e^{-t} t^{a-1} dt$$

Since the total density is simply the some of all the components, we can easily find the escaping and incoming (E&S) components with the relation

$$\begin{aligned} n_{ei} &= n_{tot} - n_{bs} \\ &= n_{bar} \left[1 - \frac{2}{\sqrt{\pi}} \gamma(3/2, \lambda_c y) \right] \end{aligned} \quad (\text{A.0.8})$$

The ballistic (B) component requires partial integrations over different two ranges. Taking the limits of each integration from Table A.28, and making note of the angular symmetry of the second integration region, we have

$$\begin{aligned} n_b &= 2\pi n_{bar} \left(\frac{\lambda_c}{\pi} \right)^{\frac{3}{2}} \left[\int_0^\pi \int_0^{X_b} e^{-\lambda_c X} X^2 dX \sin \theta d\theta \right. \\ &\quad \left. + 2 \int_0^{\theta_P(X)} \int_{X_b}^{\sqrt{y}} e^{-\lambda_c X} X^2 dX \sin \theta d\theta \right] \end{aligned}$$

We may carry out the integrals over θ to yield

$$n_b = 4\pi n_{bar} \left(\frac{\lambda_c}{\pi} \right)^{\frac{3}{2}} \left[\int_0^{X_b} e^{-\lambda_c X} X^2 dX + \int_{X_b}^{\sqrt{y}} e^{-\lambda_c X} X^2 (1 - \cos \theta_p) dX \right]$$

Treating the first integral as we did the integral in the n_{bs} case, with the change of variable $s = \lambda_c(X^2 - X_c^2)$ in the second term and with equation (A.0.4) to substitute for $\cos\theta_p$ we have

$$n_b = 4\pi n_{bar} \left(\frac{\lambda_c}{\pi}\right)^{\frac{3}{2}} \left[\frac{\gamma(3/2, \lambda_c y)}{2\lambda_c^{3/2}} - \frac{1}{2\lambda_c} \int_0^{\lambda_c y/(1+y)} e^{-s} e^{-\lambda_c X^2} \sqrt{X^2(1-y^2) - y^2(1-y)} dX \right]$$

After some further simplification, we find that our expression for n_b becomes

$$n_b = \frac{2}{\sqrt{\pi}} n_{bar} \left\{ \gamma(3/2, \lambda_c y) - \sqrt{1-y^2} \exp\left[\frac{-\lambda_c y^2}{1+y}\right] \gamma(3/2, \lambda_c y/(1+y)) \right\} \quad (\text{A.0.9})$$

Using equations (A.0.7) and (A.0.9), one can determine the satellite component, n_s .

The density for the escaping particles is given by

$$\begin{aligned} n_e &= 2\pi n_{bar} \left(\frac{\lambda_c}{\pi}\right)^{\frac{3}{2}} \int_0^{\theta_p} \int_{\sqrt{y}}^{\infty} e^{-\lambda_c X} X^2 dX \sin\theta d\theta \\ &= 2\pi n_{bar} \left(\frac{\lambda_c}{\pi}\right)^{\frac{3}{2}} \int_{\sqrt{y}}^{\infty} e^{-\lambda_c X} X^2 (1 - \cos\theta_p) dX \\ &= 2\pi n_{bar} \left(\frac{\lambda_c}{\pi}\right)^{\frac{3}{2}} \int_{\sqrt{y}}^{\infty} e^{-\lambda_c X} X^2 \left(1 - \sqrt{1-y^2(X^2+1-y)/X^2}\right) dX \end{aligned}$$

Splitting the integral we have

$$\begin{aligned} n_e &= 2\pi n_{bar} \left(\frac{\lambda_c}{\pi}\right)^{\frac{3}{2}} \left\{ \int_{\sqrt{y}}^{\infty} e^{-\lambda_c X} X^2 dX \right. \\ &\quad \left. - \int_{\sqrt{y}}^{\infty} e^{-\lambda_c X} X^2 \sqrt{1-y^2(X^2+1-y)/X^2} dX \right\} \end{aligned}$$

Performing some manipulations and substitutions similar to the ballistic case yields

$$n_e = \frac{n_{bar}}{\sqrt{\pi}} \{ [\Gamma(3/2) - \gamma(3/2, \lambda_c y)] \quad (\text{A.0.10})$$

$$- \sqrt{1-y^2} \exp\left[\frac{-\lambda_c y^2}{1+y}\right] [\Gamma(3/2) - \gamma(3/2, \lambda_c y/(1+y))] \} \quad (\text{A.0.11})$$

where Γ is the gamma function, defined as

$$\Gamma(z) = \int_0^{\infty} e^{-t} t^{z-1} dt$$

The incoming component n_i can be determined from equations (A.0.8) and (A.0.11).

Appendix B

Details from Chapter 2

B.1 Modified Fourier's Law

A modified form of Fourier's Law used to specify the heat flow is given by,⁹⁸

$$\mathbf{q}_s = -K_{st}\nabla T_t - K'_{ts}\nabla T_s + R_{st}(\mathbf{u}_s - \mathbf{u}_t)$$

where the coefficients K_{st} , K'_{ts} , and R_{st} are strongly dependent on the form of the interaction between the species of the gas mixture. The general form of the coefficients is given by

$$K_{st} = C_{st}J_t/H_{st}$$

$$K'_{ts} = -F_{st}J_t/H_{st}$$

$$R_{st} = (C_{st}A_{ts} + F_{ts}A_{st})/H_{st}$$

where

$$\begin{aligned} A_{st} &= \frac{p_s \nu_{st} \mu_{st}}{m_t} \left\{ \frac{5}{2} \left[\frac{T_t}{T_{st}} + \frac{m_t}{m_s} \frac{T_{st}}{T_s} (1 - z_{st}) \right] + y_{st} \left(1 - \frac{T_t}{T_s} \right) - \frac{5}{2} \left(\frac{m_t}{\mu_{st}} \right) \right\} \\ F_{ts} &= - \left\{ \frac{2z''_{ss}}{5} \nu_{ss} + \nu_{st} \left[3 \left(\frac{\mu_{st}}{m_t} \right)^2 \left(\frac{T_t}{T_{st}} \right)^2 + B_{st}^{(3)} \left(z'_{st} - \frac{5}{2} z_{st} \right) - B_{st}^{(1)} \right. \right. \\ &\quad \left. \left. + \frac{\mu_{st}}{(m_s + m_t)} \frac{T_t}{T_{st}} \left(\frac{4}{5} z''_{st} - \frac{5}{2} \frac{T_s}{T_{st}} z_{st} \right) + \frac{5}{2} \frac{\mu_{st}}{m_s} \frac{T_s}{T_{st}} z_{st} \right] \right\} \\ C_{st} &= \nu_{st} \frac{n_s m_s}{n_t m_t} \left[3 \left(\frac{\mu_{st}}{m_s} \right)^2 \left(\frac{T_s}{T_{st}} \right)^2 + B_{st}^{(3)} \left(z'_{st} - \frac{5}{2} z_{st} \right) + B_{st}^{(2)} \right. \\ &\quad \left. - \frac{\mu_{st}}{(m_s + m_t)} \frac{T_s}{T_{st}} \left(\frac{4}{5} \frac{m_t}{m_s} z''_{st} + \frac{5}{2} \frac{T_t}{T_{st}} z_{st} \right) + \frac{5}{2} \frac{\mu_{st}}{m_s} \frac{T_s}{T_{st}} z_{st} \right] \end{aligned}$$

$$J_s = \frac{5kp_s}{2m_s}$$

$$H_{st} = F_{st}F_{ts} + C_{st}C_{ts}$$

with ν_{st} , T_{st} , and μ_{st} as defined previously in the 'Transport Equations' section. We have also made the definitions

$$\nu_{ss} = \frac{8n_s}{3\sqrt{\pi}} \left(\frac{kT_s}{m_s} \right)^{\frac{1}{2}} \sigma_{HS}$$

$$y_{st} = \frac{m_t}{m_s + m_t} \left[2z''_{st} - 5\frac{T_s}{T_{st}} - \frac{15}{2} \frac{m_s(1 - z_{st})(T_t - T_s)}{m_s + m_t} \frac{1}{T_{st}} \right]$$

$$B_{st}^{(1)} = \frac{m_t \mu_{st}}{(m_s + m_t)^2} \frac{(T_t - T_s)}{T_{st}} \left[\frac{4}{5} z'''_{st} - 2z''_{st} + \frac{m_s}{m_t} \frac{T_t}{T_{st}} (6 - 11z_{st}) \right]$$

$$B_{st}^{(2)} = \frac{m_t \mu_{st}}{(m_s + m_t)^2} \frac{(T_t - T_s)}{T_{st}} \left[-\frac{4}{5} z'''_{st} + 2z''_{st} + \frac{T_s}{T_{st}} (6 - 11z_{st}) \right]$$

$$B_{st}^{(3)} = \frac{m_t^2}{(m_s + m_t)^2} \left[1 + \frac{3m_s^2}{(m_s + m_t)^2} \frac{(T_t - T_s)^2}{T_{st}^2} \right]$$

The coefficients z_{st} , z'_{st} , z''_{st} , and z'''_{st} are given by⁹⁷

$$z_{st} = 1 - \frac{2}{5} \frac{\Omega_{st}^{(1,2)}}{\Omega_{st}^{(1,1)}}$$

$$z'_{st} = \frac{5}{2} - \frac{2}{5} \frac{\Omega_{st}^{(1,3)} - 5\Omega_{st}^{(1,2)}}{\Omega_{st}^{(1,1)}}$$

$$z''_{st} = \frac{\Omega_{st}^{(2,2)}}{\Omega_{st}^{(1,1)}}$$

$$z'''_{st} = \frac{\Omega_{st}^{(2,3)}}{\Omega_{st}^{(1,1)}}$$

where $\Omega_{st}^{(i,j)}$ are the Chapman-Cowling collision integrals,²⁹ defined as

$$\Omega_{st}^{(i,j)} = \left(\frac{kT_{st}}{2\pi\mu_{st}} \right)^{\frac{1}{2}} \int_0^\infty \exp(-\gamma_{st}^2) \gamma_{st}^{2j-3} Q_{st}^i d\gamma_{st}$$

$$Q_{st}^i = 2\pi \int_0^\infty (1 - \cos^i \theta) \sigma_{st}(g_{st}, \theta) \sin \theta d\theta$$

$$\gamma_{st} = \left(\frac{\mu_{st}}{2kT_{st}} \right)^{\frac{1}{2}} g_{st}$$

where σ is the differential cross section and g is the relative velocity between particles s and t . For hard spheres, we have⁶⁸

$$\begin{aligned} {}^{HS}\Omega_{st}^{(i,j)} &= {}^{HS}Q_{st}^i \left(\frac{kT_{st}}{2\pi\mu_{st}} \right)^{\frac{1}{2}} \frac{(s+1)!}{2} \\ {}^{HS}Q_{st}^i &= \sigma_{HS} \left[1 - \frac{1}{2} \frac{1}{(i+1)} (1 + (-1)^i) \right] \end{aligned}$$

B.2 Symmetrization of the Collision Kernel

For a hard sphere collision model, we had from equation (2.4.11) that

$$\begin{aligned} K^{ns}(x, x') &= \frac{1}{2} A Q^2 \sqrt{\frac{\pi}{x}} \{ \text{erf}(Q\sqrt{x'} + R\sqrt{x}) + e^{x-x'} \text{erf}(R\sqrt{x'} + Q\sqrt{x}) \\ &\quad \pm [\text{erf}(Q\sqrt{x'} - R\sqrt{x}) + e^{x-x'} \text{erf}(R\sqrt{x'} - Q\sqrt{x})] \} \end{aligned} \quad (\text{B.2.1})$$

where the $+(-)$ sign refers to $x > x'$ ($x < x'$), and

$$\begin{aligned} Q &\equiv \frac{1}{2} \left[\frac{1}{\sqrt{\gamma}} + \sqrt{\gamma} \right] \\ R &\equiv \frac{1}{2} \left[\frac{1}{\sqrt{\gamma}} - \sqrt{\gamma} \right] \\ \gamma &\equiv m_{back}/m_{hot} \\ A &\equiv \sigma_{tot}^{hs} n_{back} \sqrt{\frac{2kT_{back}}{\pi m_{hot}}} \end{aligned}$$

This is multiplied by the symmetrizing factor

$$\begin{aligned} F_s &= \sqrt{\frac{\sqrt{x}}{\sqrt{x'}}} e^{(x-x')/2} \\ &= \sqrt{\frac{\sqrt{x}}{\sqrt{x'}}} e^{-(x-x')} \end{aligned}$$

so that

$$K^s(x, x') \equiv F_s \cdot K^{ns}(x, x')$$

or

$$K^s(x, x') = \frac{1}{2}AQ^2\sqrt{\frac{\pi}{\sqrt{x'}x}}\{e^{(x'-x)/2}[\text{erf}(Q\sqrt{x'}+R\sqrt{x})\pm\text{erf}(Q\sqrt{x'}-R\sqrt{x})] + e^{(x-x')/2}[\text{erf}(R\sqrt{x'}+Q\sqrt{x})\pm\text{erf}(R\sqrt{x'}-Q\sqrt{x})]\} \quad (\text{B.2.2})$$

is symmetric in its arguments. The $+$ ($-$) sign refers to $x > x'$ ($x < x'$), or in terms of the magnitude and order of the arguments, $+$ ($-$) where the first argument is larger (smaller) than the second. If $K^s(x, x')$ is symmetric in its arguments then

$$K^s(x, x') \equiv K^s(x', x)$$

Exchanging the arguments of equation (B.2.2) yields

$$K^s(x', x) = \frac{1}{2}AQ^2\sqrt{\frac{\pi}{\sqrt{x}x'}}\{e^{(x-x')/2}[\text{erf}(Q\sqrt{x}+R\sqrt{x'})\pm\text{erf}(Q\sqrt{x}-R\sqrt{x'})] + e^{(x'-x)/2}[\text{erf}(R\sqrt{x}+Q\sqrt{x'})\pm\text{erf}(R\sqrt{x}-Q\sqrt{x'})]\} \quad (\text{B.2.3})$$

If we recognize that the error function is anti-symmetric in its argument, i.e. $\text{erf}(-z) \equiv -\text{erf}(z)$, and then rearrange equation (B.2.3), we have

$$K^s(x', x) = \frac{1}{2}AQ^2\sqrt{\frac{\pi}{\sqrt{x}x'}}\{e^{(x'-x)/2}[\text{erf}(Q\sqrt{x'}+R\sqrt{x})\pm-\text{erf}(Q\sqrt{x'}-R\sqrt{x})] + e^{(x-x')/2}[\text{erf}(R\sqrt{x'}+Q\sqrt{x})\pm-\text{erf}(R\sqrt{x'}-Q\sqrt{x})]\} \quad (\text{B.2.4})$$

where $+$ ($-$) sign refers to $x < x'$ ($x > x'$), or in terms of the magnitude and order of the arguments, $+$ ($-$) where the second argument is smaller (larger) than the first. This is exactly opposite to what we had in equation (B.2.2). To synchronize the sign convention between the two equations we *choose* the convention that the $+$ ($-$) sign refers to $x > x'$ ($x < x'$) *irrespective* of the actual order of the arguments. With this convention equation (B.2.4) becomes

$$K^s(x', x) = \frac{1}{2}AQ^2\sqrt{\frac{\pi}{\sqrt{x}x'}}\{e^{(x'-x)/2}[\text{erf}(Q\sqrt{x'}+R\sqrt{x})\pm\text{erf}(Q\sqrt{x'}-R\sqrt{x})] + e^{(x-x')/2}[\text{erf}(R\sqrt{x'}+Q\sqrt{x})\pm\text{erf}(R\sqrt{x'}-Q\sqrt{x})]\} \quad (\text{B.2.5})$$

and comparison with equation (B.2.2) verifies that K^s as defined in equation (B.2.2) is indeed symmetric in its arguments. The non-symmetric kernel K^{ns} may thus be replaced by

$$K^{ns}(x, x') = \sqrt{\frac{\sqrt{x'}}{\sqrt{x}}} e^{(x-x')} K^s(x, x')$$

or, re-written in terms of speed quadrature points,

$$K^{ns}(y_l^2, y_m^2) = \sqrt{\frac{y_m}{y_l}} e^{(y_l^2 - y_m^2)} K^s(y_l^2, y_m^2)$$

B.3 Symmetrization of the Discretized Collision Operator

From Chapter 2, we had the equation

$$\frac{\partial f}{\partial t} = \mathbf{M} \cdot \mathbf{f} + \mathbf{S} \quad (\text{B.3.6})$$

We first define a dimensionless ‘time’

$$\tau \equiv At$$

where A is the quantity defined in equation (2.4.11), yielding

$$\frac{\partial f}{\partial \tau} = \hat{\mathbf{M}} \cdot \mathbf{f} + \hat{\mathbf{S}} \quad (\text{B.3.7})$$

where $\hat{\mathbf{M}}$ and $\hat{\mathbf{S}}$ are simply \mathbf{M} and \mathbf{S} divided by A . The eigenvalue problem corresponding to the equation (B.3.7) is

$$\hat{\mathbf{M}}\psi^{(n)} = \lambda_n \psi^{(n)} \quad (\text{B.3.8})$$

or

$$\int_0^\infty dx \hat{M}(x, x') \psi^{(n)}(x) = \lambda_n \psi^{(n)}(x') \quad (\text{B.3.9})$$

where

$$\begin{aligned}\hat{M} &\equiv \int_0^\infty dx \hat{M}(x, x') \\ \hat{M}(x, x') &\equiv [K^{ns}(x, x') - Z(x')\delta(x - x')] / A\end{aligned}$$

Our goal is to transform this eigenvalue problem into one of the form

$$B\phi^{(n)} = \lambda_n \phi^{(n)} \quad (\text{B.3.10})$$

where B is a real, symmetric matrix. We know the symmetrizing factor for the kernel from equation (2.4.12), and so we define

$$\hat{M}(x, x') \equiv \sqrt{\frac{(x')^{\frac{1}{2}}}{x^{\frac{1}{2}}}} e^{x-x'} B(x, x') \quad (\text{B.3.11})$$

and then substitute this into equation (B.3.9) to yield

$$\int_0^\infty dx \sqrt{\frac{(x')^{\frac{1}{2}}}{x^{\frac{1}{2}}}} e^{x-x'} B(x, x') \psi^{(n)}(x) = \lambda_n \psi^{(n)}(x')$$

We then transform to a quadrature in speed, with $x' = y_i^2$ and $x = y_j^2$,

$$\sum_{j=1}^N 2y_j W_j \sqrt{\frac{y_i}{y_j}} e^{y_j^2 - y_i^2} B_{j,i} \psi_j^{(n)} = \lambda_n \psi_i^{(n)}$$

or

$$\sum_{j=1}^N 2\sqrt{y_i y_j W_i W_j} \sqrt{\frac{W_j e^{-y_i^2}}{W_i e^{-y_j^2}}} B_{j,i} \psi_j^{(n)} = \lambda_n \psi_i^{(n)}$$

Rearranging, we finally have

$$\sum_{j=1}^N \hat{B}_{i,j} \sqrt{\frac{W_j}{e^{-y_j^2}}} \psi_j^{(n)} = \lambda_n \sqrt{\frac{W_i}{e^{-y_i^2}}} \psi_i^{(n)} \quad (\text{B.3.12})$$

where

$$\hat{B}_{i,j} = 2\sqrt{y_i y_j W_i W_j} B_{j,i} \quad (\text{B.3.13})$$

is, by inspection, symmetric in (i, j) (since \mathbf{B} is a symmetric matrix). Comparing equations (B.3.10) and (B.3.12), we see that

$$\phi_i^{(n)} = \sqrt{\frac{W_i}{e^{-y_i^2}}} \psi_i^{(n)} \quad (\text{B.3.14})$$

If we redefine our original eigenvectors according to equation (B.3.14),

$$\hat{f}_i = \sqrt{\frac{W_i}{e^{-y_i^2}}} f_i \quad (\text{B.3.15})$$

we find after some manipulation that equation (B.3.7) becomes

$$\frac{\partial \hat{f}}{\partial \tau} = \hat{\mathbf{B}} \cdot \hat{\mathbf{f}} + \tilde{\mathbf{S}} \quad (\text{B.3.16})$$

where $\hat{\mathbf{B}}$ is a symmetric matrix defined by equations (B.3.11) and (B.3.13), and

$$\tilde{\mathbf{S}} \equiv \sqrt{\frac{W_i}{e^{-y_i^2}}} \hat{\mathbf{S}}$$

B.4 Solution of the Eigenvalue Problem

From equation (2.4.14), we had

$$\frac{\partial \hat{f}}{\partial \tau} = \hat{\mathbf{B}} \cdot \hat{\mathbf{f}} + \tilde{\mathbf{S}} \quad (\text{B.4.17})$$

This is analagous to the eigenvalue problem of the form^{162, 163}

$$\hat{\mathbf{B}} \mathbf{U} = \tilde{\lambda} \cdot \mathbf{U} \quad (\text{B.4.18})$$

where $\hat{\mathbf{B}}$ is a symmetric matrix and \mathbf{U} is the matrix of eigenvectors of $\hat{\mathbf{B}}$. If we make the definition

$$\hat{\mathbf{f}} \equiv \mathbf{U} \cdot \mathbf{F}$$

in equation (B.4.17), we find that

$$\mathbf{U} \frac{\partial \mathbf{F}}{\partial \tau} = \hat{\mathbf{B}} \mathbf{U} \cdot \mathbf{F} + \tilde{\mathbf{S}}$$

or after multiplication by U^{-1} from the right-hand side

$$\frac{\partial F}{\partial \tau} = D \cdot F + Q \quad (\text{B.4.19})$$

where

$$\begin{aligned} Q &\equiv U^{-1} \tilde{S} \\ D &= U^{-1} \hat{B} U \end{aligned}$$

The matrix D is a diagonal matrix of the eigenvalues of \hat{B} . It can be shown that all the eigenvalues are inherently negative, except for $\tilde{\lambda}_1$ which we expect to be zero since it represents the equilibrium eigenfunction. We choose to redefine the eigenvalues with the negative sign explicitly shown, i.e. $\tilde{\lambda} \equiv -\lambda$. We then have

$$\lambda_1 = 0 < \lambda_2 < \lambda_3 < \dots < \lambda_n$$

With this convention we may write the j^{th} component of equation (B.4.19) as

$$\frac{\partial F_j}{\partial \tau} = -\lambda_j F_j + Q_j$$

If we use an integrating factor, this may be rewritten as

$$e^{-\lambda_j \tau} \frac{\partial}{\partial \tau} [e^{\lambda_j \tau} F_j] = Q_j$$

or integrating both sides

$$e^{\lambda_j \tau} F_j \Big|_0^\tau = \int_0^\tau e^{\lambda_j \tau} Q_j d\tau$$

Carrying out the integration on the right-hand side and rearranging yields

$$F_j(\tau) = F_j(0)e^{-\lambda_j \tau} + Q_j \left[\frac{1 - e^{-\lambda_j \tau}}{\lambda_j} \right]$$

With our previous definition of $\hat{\mathbf{f}} \equiv \mathbf{U} \cdot \mathbf{F}$, or $\hat{f}_j \equiv \sum_{i=1}^N U_{i,j} F_j$, we finally arrive at

$$\hat{f}_i(\tau) = U_{i,1} [F_1(0) + Q_1 \tau] + \sum_{j=2}^N U_{i,j} \left(F_j(0) e^{-\lambda_j \tau} + Q_j \frac{[1 - e^{-\lambda_j \tau}]}{\lambda_j} \right)$$

where we have used L'Hôpital's Rule to account for the indeterminacy caused by the zero eigenvalue in the $j = 1$ term.

Appendix C

The Differential Collision Cross Section

The scattering cross section is of great importance in any detailed analysis involving the Boltzmann equation. It appears explicitly in the definition of the collision operator in equation (1.4.1), and describes the physics of the binary collisions for the system. The physical meaning of the cross section is made clear by considering a typical scattering configuration, such as is illustrated in Figure C.57, where a uniform beam of particles is incident on a (repulsive) scattering center. For the particular case of a two-body collision, both the incident beam and the target become single particles, but the description of the process remains the same.

The incident beam is characterized by its intensity I , also called the incident flux density, which gives the number of particles per unit time which cross a unit area perpendicular to the incident direction. There is a finite region of interaction over which the incident beam is deflected (or scattered) from its incident direction after which the effect of the scatterer diminishes and the scattered beam continues linearly in the scattered direction.

Referring again to Figure C.57, we may quantify this process as follows.^{132,133} For a central force type of potential (i.e., dependent only on radial distance), there is symmetry about the axis of the incident beam, and the element of solid angle may be written as

$$d\Omega = 2\pi \sin(\theta) d\theta \quad (\text{C.0.1})$$

The angle θ is the angle between the incident and scattered directions, and is not surprisingly known as the scattering angle. For any given incident particle, the amount of

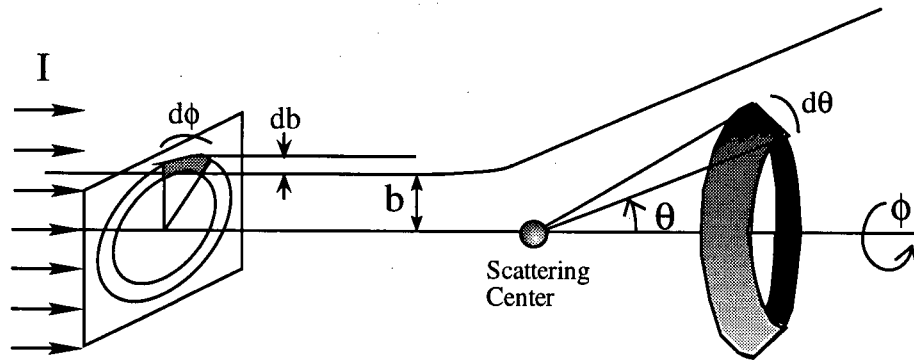


Figure C.57: A typical scattering configuration. An incident beam of particles interacts with a scattering center, and part of the beam is scattered through an angle θ into a solid angle $d\Omega$.

scattering is determined by the impact parameter b (the perpendicular distance between the direction of incidence and the scattering body) and the energy E of the particle. If the incident intensity or flux is given as I , the number of particles per second scattered into the solid angle $d\Omega$ (that is, between $\theta, \theta + d\theta$) will be proportional to both I and $d\Omega$,

$$\Delta N = \sigma I d\Omega \quad (\text{C.0.2})$$

where σ is a constant of proportionality, and is called the differential cross section. We assume that different values of b cannot lead to the same scattering angle (that is, that θ is single valued function of b). Thus, the particles scattered into $\theta, \theta + d\theta$ are those incident particles with an impact parameter between $b, b + db$,

$$\Delta N = 2\pi I b db \quad (\text{C.0.3})$$

Equating equations (C.0.2) and (C.0.3), and making use of the definition of the solid

angle from equation (C.0.1), we find that the differential cross section is given by

$$\sigma = \frac{b}{\sin(\theta)} \left| \frac{db}{d\theta} \right| \quad (\text{C.0.4})$$

The absolute value signs are used in equation (C.0.4) because b and θ may vary in opposite directions despite the fact that particle number ΔN must always be positive. Physically, the differential cross section is the collisional obstacle or area presented by the scatterer to the incident beam. The term 'cross section' is appropriate since the dimensions of σ are length-squared or area. The total scattering cross section is simply the integral of equation (C.0.4) over all directions,

$$\begin{aligned} \sigma_{tot} &= \int \sigma d\Omega \\ &= 2\pi \int_0^\pi \sigma \sin(\theta) d\theta \end{aligned} \quad (\text{C.0.5})$$

A special form of the differential cross section that is regularly used in kinetic theory is the hard-sphere cross section, often also referred to as the "billiard ball" model. It approximates each scattering particle as a rigid sphere of a fixed radius r_o with an interaction potential defined as

$$V(r) = \begin{cases} \text{constant} & \geq 2r_o \\ \infty & < 2r_o \end{cases}$$

The hard-sphere differential cross section arising from this potential is

$$\sigma_{diff}^{HS} = \frac{(2r_o)^2}{4}$$

An important feature of the hard-sphere differential cross section is its independence of both energy and angle. The total cross section is found by integrating over all solid angles,

$$\begin{aligned} \sigma_{tot}^{HS} &= \int \sigma_{diff}^{HS} d\Omega \\ &= 2\pi \int_0^\pi \sin(\theta) d\theta \\ &= \pi d^2 \end{aligned}$$

where $d \equiv 2r_o$, the hard-sphere diameter.

Though not a particularly realistic model of particle interaction, the hard-sphere cross section is useful. It is often used to reduce the complexity of the collision operator in the Boltzmann equation, and is also useful in the examination (analytically) of cross section dependent properties that would be extremely difficult or impossible to calculate with a more realistic model. Finally, it can be useful as a test of computer codes, since there are many results for a large class of problems utilizing the hard-sphere cross section.

Appendix D

Scattering Theory

D.1 Quantum Mechanical Scattering

The description of the scattering (or collision) process is well described in most standard texts on quantum mechanics.¹³²⁻¹³⁴ In this section we give an outline of the theory describing QM scattering, and the procedure for the calculation of the phase shifts and hence the differential and total elastic collision cross sections.

We are interested in finding the wave function $\psi(\mathbf{r})$ for a particle with a given energy E moving in a potential field $V(\mathbf{r})$. This problem involves solving the Schrödinger equation,^{132,133}

$$H\psi(\mathbf{r}) = E\psi(\mathbf{r}) \quad (\text{D.1.1})$$

where

$$H \equiv \frac{\hat{\mathbf{p}}^2}{2\mu} + V(\mathbf{r})$$

is the Hamiltonian operator and represents the total energy. If we substitute for the linear momentum operator, $\hat{\mathbf{p}} \equiv -i\hbar\nabla$, and use the definitions

$$\begin{aligned} k &\equiv \frac{2\pi}{\lambda} \\ \lambda &\equiv \frac{h}{p} \\ \hbar &\equiv \frac{h}{2\pi} \\ p &= k\hbar \end{aligned}$$

$$E = \frac{1}{2}\mu g^2 = \frac{p^2}{2\mu} = \frac{\hbar^2 k^2}{2\mu}$$

the Schrödinger equation can be rewritten as

$$\left[\frac{-\hbar^2}{2\mu} \nabla^2 + V(\mathbf{r}) \right] \psi(\mathbf{r}) = \frac{\hbar^2 k^2}{2\mu} \psi(\mathbf{r}) \quad (\text{D.1.2})$$

In equation (D.1.2), μ is the reduced mass and k is the wave number. If we assume that the potential $V(r)$ is spherical, and define

$$U(r) = \frac{2\mu}{\hbar^2} V(r) \quad (\text{D.1.3})$$

then equation (D.1.2) becomes

$$[\nabla^2 + k^2 - U(r)] \psi(\mathbf{r}) = 0 \quad (\text{D.1.4})$$

At large radial distances we expect the potential $V(r)$ to fall off to zero, and the effect of a scattering body on another particle is assumed to be negligible. If the potential term of equation (D.1.4) is set to zero we have the 'free-motion' Schrödinger equation

$$[\nabla^2 + k^2] \psi(\mathbf{r}) = 0 \quad (\text{D.1.5})$$

A solution of equation (D.1.5) is

$$\psi_{in}(\mathbf{r}) = A e^{i\mathbf{k} \cdot \mathbf{r}} \quad (\text{D.1.6})$$

which is a plane wave (that is, $\mathbf{k} \cdot \mathbf{r}$, the phase of the wave, is a constant). We expect that in the absence of a scatterer that the wave function would be of this form, and that the inclusion of a scattering potential simply adds an additional component to the incident wave function. We approximate the effect of a collision by examining the change in the incident particle wave function after interaction with the potential field of the central scattering body. This is similar to the treatment of diffraction effects in optics or

acoustics.¹³² As the incident particle, in the form of a plane wave as given by equation (D.1.6), approaches the scatterer it begins to feel the potential field of the scatterer. We assume that scattering from a point target produces a spherical wave of the form

$$\psi_{sc}(\mathbf{r}) = \mathcal{F}(\theta) \cdot \frac{e^{ikr}}{r} \quad (\text{D.1.7})$$

where the $\mathcal{F}(\theta)$ is the scattering angle dependent scattering amplitude, and allows for angular anisotropy in the scattered wave function. The total scattered wave function is a superposition of the wave functions in equations (D.1.6) and (D.1.7),

$$\psi_{tot}(\mathbf{r}) = A e^{i\mathbf{k} \cdot \mathbf{r}} + \mathcal{F}(\theta) \cdot \frac{e^{ikr}}{r} \quad (\text{D.1.8})$$

Since the scattered spherical wave decays as $1/r$ as we move away from the collision interaction region, the total wave function asymptotically approaches a plane wave again. The effect of a the scattering body on the incident wave function is illustrated by Figure D.58.

We may now relate the quantum mechanical wave function terminology with the classical derivation of the collision cross section given in Appendix C. The intensity of the incident beam is defined as

$$\begin{aligned} I_{in} &= |\psi_{in}|^2 g \\ &= |A|^2 \frac{\hbar k}{\mu} \end{aligned} \quad (\text{D.1.9})$$

and that of the scattered beam as

$$\begin{aligned} I_{sc} &= |\psi_{sc}|^2 g \\ &= \frac{|\mathcal{F}(\theta)|^2 \hbar k}{r^2 \mu} \end{aligned} \quad (\text{D.1.10})$$

where $g = p/\mu$ is the relative velocity of collision. The number of particles per second scattered through an angle θ into an area dS (perpendicular to the scattered beam) is

$$\Delta N = I_{sc} dS$$

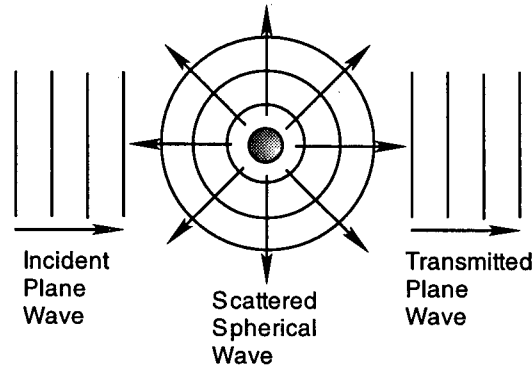


Figure D.58: Wave function scattering by a central potential. An incoming plane wave is partially transmitted/reflected as another plane wave and partially scattered as a spherical wave by the potential field due to the scattering body.

$$= \frac{|\mathcal{F}(\theta)|^2 \hbar k}{r^2 \mu} dS \quad (\text{D.1.11})$$

If the incident beam is normalized such that $|A|^2 \equiv 1$, then

$$I_{in} = \frac{\hbar k}{\mu} \quad (\text{D.1.12})$$

If we put equation (D.1.12) into equation (D.1.11), and use the definition that $dS/r^2 \equiv d\Omega$, we find that

$$\Delta N = |\mathcal{F}(\theta)|^2 I_{in} d\Omega \quad (\text{D.1.13})$$

Comparing this with the form of equation (C.0.2), we immediately find that the quantum mechanical differential cross section is given by

$$\sigma = |\mathcal{F}(\theta)|^2 \quad (\text{D.1.14})$$

D.2 Calculation of the Phase Shifts

To calculate the scattering amplitude \mathcal{F} , we must match equation (D.1.8) to the asymptotic form of the solution of the Schrödinger equation including the interaction potential, equation (D.1.4), which was written as

$$\left[\nabla^2 + k^2 - U(r)\right] \psi(\mathbf{r}) = 0$$

The solution for the wave function may be written as an expansion of the form

$$\psi(\mathbf{r}) = \sum_{l=0}^{\infty} C_l \psi_l(r, \theta)$$

where we assume that

$$\psi_l(r, \theta) = R_l(r) P_l(\cos \theta)$$

The l th term in the expansion of ψ is known as the l th partial wave. In general, the solution of equation (D.1.4) is a three dimensional problem, where $\psi = \psi(r, \theta, \phi)$. However, with a spherical potential, there is spherical symmetry (that is, there is no dependence of σ on the angle ϕ as one looks along the incident beam axis), and so the problem reduces to a two dimensional one. We may thus write

$$\nabla^2 \psi_l(r, \theta) = \left[\frac{1}{r^2} \frac{\partial}{\partial r} \left(r^2 \frac{\partial R_l}{\partial r} \right) \right] P_l + \frac{R_l}{r^2} \hat{L}^2 P_l$$

where \hat{L}^2 is the quantum mechanical angular momentum operator¹³³ with the ϕ dependence omitted. If the P_l 's are chosen to be the Legendre polynomials, then they are the eigenvectors of the angular momentum operator, that is

$$\hat{L}^2 P_l = \frac{1}{\sin(\theta)} \frac{\partial}{\partial \theta} \left(\sin(\theta) \frac{\partial P_l}{\partial \theta} \right) = -l(l+1) P_l$$

If this is substituted into equation (D.1.4), the original problem reduces to determining the R_l 's from the radial Schrödinger equation,

$$\frac{1}{r^2} \frac{\partial}{\partial r} \left(r^2 \frac{\partial R_l}{\partial r} \right) + (k^2 - U_{eff}(r)) R_l(r) = 0 \quad (\text{D.2.15})$$

where we have defined an 'effective potential'

$$U_{eff} \equiv U(r) + \frac{l(l+1)}{r^2}$$

If we consider the 'free motion' ($U(r) \equiv 0$) version of equation (D.2.15),

$$\frac{1}{r^2} \frac{\partial}{\partial r} \left(r^2 \frac{\partial R_l}{\partial r} \right) + \left(k^2 - \frac{l(l+1)}{r^2} \right) R_l(r) = 0$$

we may rewrite it in the form of Bessel's equation of half-integral order,

$$r^2 \frac{\partial^2 R_l}{\partial r^2} + 2r \frac{\partial R_l}{\partial r} + (k^2 r^2 + l(l+1)) R_l(r) = 0$$

The general solution is of the form of a linear combination of two independent solutions,

$$R_l(r) = C_{1l} j_l(kr) + C_{2l} n_l(kr)$$

where j_l is the spherical bessel function, n_l is the spherical Neumann function, and C_{1l} and C_{2l} are coefficients to be determined by boundary conditions. Since the spherical Neumann functions diverge at the origin, and we require that R_l be finite everywhere, we set $C_{2l} = 0$. Our 'free motion' solution is thus

$$\psi_l = C_{1l} j_l(kr) P_l(\cos \theta) \quad (\text{D.2.16})$$

It can be shown¹³⁴ that this is exactly equivalent to an expansion in Legendre polynomials of our plane wave 'free motion' solution of equation (D.1.6). Since we are interested in the form of ψ as $r \rightarrow \infty$ (that is, far from the interaction region), we examine the asymptotic behaviour of the radial portion of equation (D.2.16),

$$R_l(r \rightarrow \infty) = C_{1l} \frac{\sin(kr - l\pi/2)}{kr} \quad (\text{D.2.17})$$

We now consider the case where the potential in equation (D.2.15) is not zero. If we restrict ourselves to the region far from the interaction region, $r \gg 0$, and assume

that the potential $U(r)$ is negligible in this region, then we find that equation (D.2.15) again reduces to Bessel's equation of half-integral order. The general solution is a linear combination of spherical Bessel and Neumann functions, as previously. However, we cannot simply exclude n_l as before since the origin is no longer included in the region of interest. Setting

$$\begin{aligned} C_{1l} &= \gamma_l \cos \delta_l \\ C_{2l} &= -\gamma_l \sin \delta_l \end{aligned}$$

we have the solution

$$R_l(r) = \gamma_l [j_l(kr) \cos \delta_l - n_l(kr) \sin \delta_l] \quad (\text{D.2.18})$$

For $r \rightarrow \infty$, this takes the form

$$R_l(r \rightarrow \infty) = \gamma_l \frac{\sin(kr - l\pi/2 + \delta_l)}{kr}$$

and thus the asymptotic wave function is given by

$$\psi_l = \gamma_l \frac{\sin(kr - l\pi/2 + \delta_l)}{kr} P_l(\cos \theta) \quad (\text{D.2.19})$$

Comparing equations (D.2.17) and (D.2.19), we see that the inclusion of the potential causes a small shift δ_l in the phase of the radial part of the asymptotic wave function. This phase difference between asymptotic solutions of the radial wave equation with and without the potential is known as the phase shift. In general, the phase shifts are calculated by finding the nodes r_o of R_l from equation (D.2.18), yielding

$$\tan \delta_l = \frac{j_l(kr_o)}{n_l(kr_o)} \quad (\text{D.2.20})$$

In order to finally find the scattering amplitude \mathcal{F} , we now match the expected form of the asymptotic wave function, equation (D.1.8), to equation (D.2.19).^{133, 134} If we express

the sine function as a sum of exponentials,

$$\sin z \equiv \frac{1}{2i}(e^{iz} - e^{-iz})$$

this yields

$$\begin{aligned} \sum_{l=0}^{\infty} \frac{C_{1l}}{2i kr} \left[e^{ikr} e^{-il\pi/2} - e^{-ikr} e^{il\pi/2} \right] P_l(\cos \theta) + \mathcal{F}(\theta) \cdot \frac{e^{ikr}}{r} = \\ \sum_{l=0}^{\infty} \frac{\gamma_l}{2i kr} \left[e^{ikr} e^{-il\pi/2} e^{i\delta_l} - e^{-ikr} e^{il\pi/2} e^{-i\delta_l} \right] P_l(\cos \theta) \end{aligned}$$

Since e^{-ikr} and e^{ikr} are linearly independent, the coefficients of these terms must separately be equal. For the terms involving e^{-ikr} , we have

$$\sum_{l=0}^{\infty} C_{1l} P_l(\cos \theta) = \sum_{l=0}^{\infty} \gamma_l P_l(\cos \theta) e^{-i\delta_l}$$

If we multiply by $P_{l'}(\cos \theta)$, integrate over $d(\cos \theta)$, and use the orthogonality condition for the Legendre polynomials,

$$\int_{-1}^{+1} P_l P_{l'} d(\cos \theta) = \frac{2}{2l+1} \delta_{ll'}$$

we find

$$\gamma_l = C_{1l} e^{i\delta_l} \quad (\text{D.2.21})$$

If we make use of the fact that the asymptotic expansion of the plane wave in equation (D.1.6) is given by equation (D.2.16), we have

$$\begin{aligned} \psi &= \psi_{in}(\mathbf{r}) = e^{i\mathbf{k} \cdot \mathbf{r}} \\ &= \sum_l C_{1l} j_l(kr) P_l(\cos \theta) \end{aligned}$$

If we multiply by $P_{l'}(\cos \theta)$ and integrate over $d(\cos \theta)$, again using the orthogonality condition for Legendre polynomials, and then make use of the definition for the spherical

Bessel functions, we have

$$\begin{aligned} C_{1l} j_l(kr) \frac{2}{2l+1} \delta_{ll'} &= \int_{-1}^{+1} e^{ikr \cos \theta} P_l(\cos \theta) d(\cos \theta) \\ &= 2i^l j_l(kr) \end{aligned}$$

or

$$C_{1l} = (2l+1) i^l \quad (\text{D.2.22})$$

We are now (finally!) ready to solve for the scattering amplitude itself. Equating the coefficients of the e^{ikr} terms yields

$$\sum_{l=0}^{\infty} C_{1l} P_l(\cos \theta) e^{-il\pi/2} + 2ik\mathcal{F}(\theta) = \sum_{l=0}^{\infty} \gamma_l P_l(\cos \theta) e^{-i(l\pi/2 - \delta_l)}$$

If we substitute for C_{1l} and γ_l from equations (D.2.22) and (D.2.21), and simplify as for the e^{-ikr} case, we find

$$\mathcal{F}(\theta) = \frac{1}{2ik} \sum_{l=0}^{\infty} (2l+1) P_l(\cos \theta) [e^{i2\delta_l} - 1]$$

After taking a factor $e^{i\delta_l}$ out of the brackets and using the definition of the sine function, we finally arrive at the form

$$\mathcal{F}(\theta) = \frac{1}{k} \sum_{l=0}^{\infty} (2l+1) P_l(\cos \theta) e^{i\delta_l} \sin \delta_l \quad (\text{D.2.23})$$

It should be noted that the phase shifts $\delta_l = \delta_l(k)$ are energy dependent. From equation (D.1.14), the differential cross section is thus

$$\sigma(\theta) = \frac{1}{k^2} \left| \sum_{l=0}^{\infty} (2l+1) P_l(\cos \theta) e^{i\delta_l} \sin \delta_l \right|^2 \quad (\text{D.2.24})$$

and from equation (C.0.5), the total cross section is

$$\sigma(\theta) = \frac{4\pi}{k^2} \sum_{l=0}^{\infty} (2l+1) \sin^2 \delta_l \quad (\text{D.2.25})$$

D.3 Semi-Classical (WKB) Phase Shift Approximation

For systems with many interaction potentials or with ‘heavy’ collision partners, the number of phase shifts required to accurately construct the collision cross sections may be very large, and the computer time required for rigorous quantum mechanical calculations may be on the order of days. It is thus desirable to be able to find an approximate form for the phase shifts δ_l . Such a form is given by the Wentzel-Kramers-Brillouin (WKB) or semi-classical approximation.^{164,133} In general, the WKB approximation is appropriate for those energies above the centrifugal barrier for the effective potential (see equation (D.2.18), where there is no orbiting and only a single classical turning point.¹³³ A brief outline of the WKB formulation for the phase shifts is given here; further detail is available in many standard textbooks^{164,133} and papers.^{165–167} The WKB phase shift is given by

$$\delta_l^{WKB} = \frac{(l + 1/2)}{2}\pi - kr_o + \int_{r_o}^{\infty} [k_l(r) - k] dr \quad (D.3.26)$$

$$k_l(r) \equiv \sqrt{k^2 - \frac{(l + 1/2)^2}{r^2} - U(r)}$$

where k is the wave number, $U(r)$ is the potential given by equation (D.1.3), and r_o is the classical turning point. There is no inherent restriction as to the size of the WKB phase shifts given by equation (D.3.26), unlike other approximations (e.g. Born phase shifts). From a computational point of view, it is much quicker to compute the phase shifts using equation (D.3.26), which involves a single integration, than to perform the integration of the radial Schrödinger equation, equation (D.2.15), involved in the QM calculation of the phase shifts.

We may put equation into a computationally more convenient form. Using the definitions

$$b = \frac{(l + 1/2)}{k}$$

$$k^2 = \frac{2\mu E}{\hbar^2}$$

where E is the energy of the colliding particle, equation (D.3.26) becomes

$$\delta_l^{WKB} = \frac{kb}{2}\pi - kr_o + \int_{r_o}^{\infty} k \left[\sqrt{1 - \frac{b^2}{r^2} - \frac{V(r)}{E}} - 1 \right] dr$$

If we now make the change of variable $y = r_o/r$, we have

$$\begin{aligned} \delta_l^{WKB} &= \frac{kb}{2}\pi - kr_o + k \int_0^1 \left[\sqrt{1 - \frac{b^2 y^2}{r_o^2} - \frac{V(r)}{E}} - 1 \right] / y^2 dy \\ &= k \left\{ \frac{b}{2}\pi + r_o \left(\int_0^1 \frac{\left[\sqrt{1 - \frac{b^2 y^2}{r_o^2} - \frac{V(r)}{E}} - 1 \right]}{y^2} dy - 1 \right) \right\} \end{aligned}$$

To perform the integral, which is of the form

$$\int_0^1 g(x) dx$$

we make the transformation $x = (y + 1)/2$, yielding

$$\int_{-1}^1 \frac{1}{2} g\left(\frac{y+1}{2}\right) dy$$

Using a standard Gauss-Legendre quadrature, with points and weights y_i and w_i , we thus have

$$\int_{-1}^1 \frac{1}{2} g\left(\frac{y+1}{2}\right) dy = \sum_{i=1}^n W_i g(p_i)$$

where we have simply defined a 'new' set of points and weights, $p_i = (y_i + 1)/2$ and $W_i = w_i/2$.

Appendix E

Details of the Production of Hot Atoms

E.1 Derivation of $\xi_1'^2 - \xi_1^2$

From equation (3.3.12) we have

$$\begin{aligned} \xi_1'^2 = & \mathcal{M}_1 \Xi^2 + \mathcal{M}_2(1 + \alpha)^2 \xi'^2 + \mathcal{M}_2 \alpha^2 \xi^2 - 2\sqrt{\mathcal{M}_1 \mathcal{M}_2}(1 + \alpha) \xi' \cdot \Xi + \\ & 2\sqrt{\mathcal{M}_1 \mathcal{M}_2} \alpha \xi \cdot \Xi - 2\mathcal{M}_2(1 + \alpha) \alpha \xi' \cdot \xi \end{aligned} \quad (\text{E.1.1})$$

where we have used $\Xi' \equiv \Xi$ from conservation of momentum and energy and equation (3.3.8). Now, using equation (3.3.8) for ξ , and the analagous expression for ξ' , we have (since $g = g'$ for elastic collisions) that

$$\xi' = \xi \quad (\text{E.1.2})$$

From equations (3.3.8) and (3.3.10) we have

$$\xi' = \xi - 2\mathbf{k}(\mathbf{k} \cdot \xi) \quad (\text{E.1.3})$$

Substituting equations (E.1.2) and (E.1.3) into equation (E.1.1),

$$\begin{aligned} \xi_1'^2 = & \mathcal{M}_1 \Xi^2 + \mathcal{M}_2(1 + \alpha)^2 \xi^2 + \mathcal{M}_2 \alpha^2 \xi^2 - 2\sqrt{\mathcal{M}_1 \mathcal{M}_2}(1 + \alpha) \xi \cdot \Xi + \\ & 4\sqrt{\mathcal{M}_1 \mathcal{M}_2}(1 + \alpha)(\mathbf{k} \cdot \xi)(\xi \cdot \Xi) + 2\sqrt{\mathcal{M}_1 \mathcal{M}_2} \alpha \xi \cdot \Xi + \\ & -2\mathcal{M}_2(1 + \alpha) \alpha \xi^2 + 4\mathcal{M}_2(1 + \alpha) \alpha (\mathbf{k} \cdot \xi)^2 \end{aligned} \quad (\text{E.1.4})$$

Similarly, we have from equation (3.3.9) that

$$\xi_1^2 = \mathcal{M}_1 \Xi^2 + \mathcal{M}_2 \xi^2 - 2\sqrt{\mathcal{M}_1 \mathcal{M}_2} \xi \cdot \Xi \quad (\text{E.1.5})$$

Thus, combining equations (E.1.4) and (E.1.5), and simplifying, we have

$$\begin{aligned}
 \xi_1'^2 - \xi_1^2 &= \mathcal{M}_2(1 + \alpha^2 + 2\alpha)\xi^2 + \mathcal{M}_2\alpha^2\xi^2 + \\
 &\quad 4\sqrt{\mathcal{M}_1\mathcal{M}_2}(1 + \alpha)(\mathbf{k} \cdot \boldsymbol{\xi})(\boldsymbol{\xi} \cdot \boldsymbol{\Xi}) + \\
 &\quad -2\mathcal{M}_2(1 + \alpha)\alpha\xi^2 + 4\mathcal{M}_2(1 + \alpha)\alpha(\mathbf{k} \cdot \boldsymbol{\xi})^2 - \mathcal{M}_2\xi^2 \\
 &= 4\sqrt{\mathcal{M}_1\mathcal{M}_2}(1 + \alpha)(\boldsymbol{\xi} \cdot \mathbf{k})(\boldsymbol{\Xi} \cdot \mathbf{k}) + 4\mathcal{M}_2\alpha(1 + \alpha)(\boldsymbol{\xi} \cdot \mathbf{k})^2
 \end{aligned}$$

E.2 Derivation of $\xi_1^2 + \xi_2^2$

From equation (3.3.9) we have

$$\begin{aligned}
 \xi_1^2 + \xi_2^2 &= \mathcal{M}_1\Xi^2 + \mathcal{M}_2\xi^2 + \mathcal{M}_1\xi^2 + \\
 &\quad \left(2\sqrt{\mathcal{M}_1\mathcal{M}_2} - 2\sqrt{\mathcal{M}_1\mathcal{M}_2}\right)(\boldsymbol{\xi} \cdot \boldsymbol{\Xi}) \\
 &= (\mathcal{M}_1 + \mathcal{M}_2)(\Xi^2 + \xi^2)
 \end{aligned}$$

By equation (3.3.8), $\mathcal{M}_1 + \mathcal{M}_2 \equiv 1$, and so we obtain the desired result,

$$\xi_1^2 + \xi_2^2 = \Xi^2 + \xi^2$$

E.3 Transformation from $d\xi_1 d\xi_2$ to $d\Xi d\xi$

We wish to make a transformation of coordinates from the reduced variables $d\xi_1 d\xi_2$ to $d\Xi d\xi$. As for equation (3.3.4), we use the standard definition of the Jacobian for coordinate transformations,

$$\begin{aligned}
 J d\xi_1 d\xi_2 &= d\Xi d\xi \\
 J &\equiv \frac{\partial(\Xi, \xi)}{\partial(\xi_1, \xi_2)} \\
 &= \begin{vmatrix} \frac{\partial\Xi}{\partial\xi_1} & \frac{\partial\Xi}{\partial\xi_2} \\ \frac{\partial\xi}{\partial\xi_1} & \frac{\partial\xi}{\partial\xi_2} \end{vmatrix}
 \end{aligned}$$

We use equations (3.3.7) and (3.3.8) and vector differentiation to obtain

$$\begin{aligned} J &= \begin{vmatrix} \sqrt{\mathcal{M}_1} & \sqrt{\mathcal{M}_2} \\ -\sqrt{\mathcal{M}_2} & \sqrt{\mathcal{M}_1} \end{vmatrix} \\ &= \mathcal{M}_1 + \mathcal{M}_2 \\ &= 1 \end{aligned}$$

E.4 Transformation from χ to the scattering angle θ

The geometry of the dynamics of an elastic collision process is illustrated in Figure E.59, where θ is the scattering angle and χ is the angle between \mathbf{k} and $\boldsymbol{\xi}$ (or, equivalently, since \mathbf{k} is the external bisector of the scattering angle, between \mathbf{k} and $\boldsymbol{\xi}'$). From the figure, we have

$$\cos \chi = \cos \left(\frac{1}{2}(\pi - \theta) \right)$$

From basic trigonometric identities,¹⁵⁰ we know that

$$\cos^2 z = \frac{\cos(2z) + 1}{2}$$

so

$$\begin{aligned} \cos^2 \chi &= \frac{\cos(\pi - \theta) + 1}{2} \\ &= \frac{1}{2}(1 - \cos \theta) \end{aligned}$$

where we have used standard trigonometric identities for angle addition,¹⁵⁰ and the fact that $\cos(-z) \equiv -\cos(z)$.

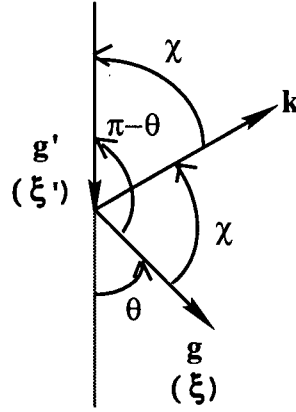


Figure E.59: Geometry of the dynamics of an elastic collision.

E.5 Derivation of the hard sphere product velocity distribution function

We wish to calculate the product velocity distribution function $Q(x)$ for the case where the differential cross section is given by the hard sphere approximation. From equation (3.4.13), this requires us to integrate

$$I_z = \int_0^\infty z^3 e^{-B'z^2} I_\theta(z) dz \quad (\text{E.5.6})$$

where

$$I_\theta(z) = \frac{1}{z} \int_{-1}^1 e^{-\gamma' z^2 \mu} \sigma' \frac{\sinh(xz\sqrt{A_1 + A_2\mu})}{\sqrt{A_1 + A_2\mu}} d\mu \quad (\text{E.5.7})$$

and where we have defined

$$A_1 \equiv \alpha'^2 + \beta'^2$$

$$A_2 \equiv 2\alpha'\beta'$$

$$\mu \equiv \cos \theta$$

For the hard sphere differential cross section, we have (see Appendix C) that

$$\begin{aligned}\sigma(z, \theta) &= \frac{d^2}{4} \\ \sigma' &= 1\end{aligned}$$

To carry out the integration over μ in equation (E.5.7), we make a change of variable

$$\begin{aligned}u^2 &\equiv \alpha'^2 + \beta'^2 + 2\alpha'\beta'\mu \\ \mu &= \frac{u^2 - (\alpha'^2 + \beta'^2)}{2\alpha'\beta'} \\ d\mu &= \frac{u}{\alpha'\beta'} du\end{aligned}$$

and so

$$\begin{aligned}I_\theta(z) &= \frac{1}{z} \int_{\alpha'-\beta'}^{\alpha'+\beta'} \exp \left[-\gamma' z^2 \left(\frac{u^2 - (\alpha'^2 + \beta'^2)}{2\alpha'\beta'} \right) \right] \frac{\sinh(xzu)}{u} \frac{u}{\alpha'\beta'} du \\ &= \frac{1}{2} \frac{1}{\alpha'\beta'z} \exp \left[\gamma' z^2 \left(\frac{(\alpha'^2 + \beta'^2)}{2\alpha'\beta'} \right) \right] \times \\ &\quad \int_{\alpha'-\beta'}^{\alpha'+\beta'} \exp \left[-\gamma' z^2 \left(\frac{u^2}{2\alpha'\beta'} \right) \right] \sinh(xzu) du\end{aligned}\quad (\text{E.5.8})$$

This is of the form

$$\begin{aligned}K_u &= \int e^{-Au^2} \sinh(Bu) du \\ &= \frac{1}{2} \int e^{-Au^2} (e^{Bu} - e^{-Bu}) du \\ &= \frac{1}{2} \int e^{-Au^2} e^{Bu} du - \frac{1}{2} \int e^{-Au^2} e^{-Bu} du \\ &= K_u^+ - K_u^-\end{aligned}\quad (\text{E.5.9})$$

If we complete the square in the argument of the exponential of equation (E.5.9) we have for the first term

$$\begin{aligned}K_u^+ &= \frac{1}{2} e^{B^2/4A} \int e^{-(Au^2 + Bu + B^2/4A)} du \\ &= \frac{1}{4} \sqrt{\frac{\pi}{A}} e^{B^2/4A} \operatorname{erf} \left(u\sqrt{A} + \frac{B}{2\sqrt{A}} \right)\end{aligned}$$

where the final form follows directly from integral tables.¹⁵⁰ Similarly,

$$K_u^- = \frac{1}{4} \sqrt{\frac{\pi}{A}} e^{B^2/4A} \operatorname{erf} \left(u\sqrt{A} - \frac{B}{2\sqrt{A}} \right)$$

From equations (E.5.8) and (E.5.9) we may identify

$$\begin{aligned} A &= \frac{\gamma' z^2}{2\alpha' \beta'} \\ B &= xz \\ B^2/4A &= \frac{\alpha' \beta'}{2\gamma'} x^2 \\ B/2\sqrt{A} &= x \sqrt{\frac{\alpha' \beta'}{2\gamma'}} \\ u\sqrt{A} &= uz \sqrt{\frac{\gamma'}{2\alpha' \beta'}} \end{aligned}$$

Putting it all together, we thus may write equation (E.5.8) as

$$I_\theta(z) = N_\theta \left[K(\sqrt{A_1 + A_2}) - K(\sqrt{A_1 - A_2}) \right] \quad (\text{E.5.10})$$

where we have collected coefficients and defined

$$\begin{aligned} N_\theta &\equiv \frac{1}{2} \frac{1}{z^2} \sqrt{\frac{\pi}{A_2 \gamma'}} e^{C^2} e^{\gamma' z^2 A_1/A_2} \\ K(u) &\equiv \operatorname{erf}(\hat{u}z + C) - \operatorname{erf}(\hat{u}z - C) \\ \hat{u} &\equiv \sqrt{\frac{\gamma'}{A_2}} u \\ C &\equiv x \sqrt{\frac{A_2}{4\gamma'}} \end{aligned} \quad (\text{E.5.11})$$

Substituting equation (E.5.10) into (E.5.6),

$$\begin{aligned} I_z &= \frac{1}{2} \sqrt{\frac{\pi}{A_2 \gamma'}} e^{C^2} \int_0^\infty z e^{-(\gamma' A_1/A_2 - B')z^2} \times \\ &\quad \left[K(\sqrt{A_1 + A_2}) - K(\sqrt{A_1 - A_2}) \right] dz \end{aligned} \quad (\text{E.5.12})$$

With equation (E.5.11) giving the form of $K(u)$, equation (E.5.12) thus reduces to the form (ignoring factors in front of the integrals)

$$I_z \approx \left[I(\sqrt{A_1 + A_2}) - I(\sqrt{A_1 - A_2}) \right] \quad (\text{E.5.13})$$

where

$$I(\eta_{\pm}) \equiv \int_0^{\infty} y e^{-\xi y^2} [\text{erf}(\eta_{\pm} y + \delta) - \text{erf}(\eta_{\pm} y - \delta)] dy$$

and

$$\eta = \begin{cases} \sqrt{A_1 + A_2} = \alpha' + \beta' & \text{for } + \\ \sqrt{A_1 - A_2} = \alpha' - \beta' & \text{for } - \end{cases}$$

Since the two terms in $I(\eta_{\pm})$ differ only by the sign of the argument of the $\text{erf}()$ function, we really only have to do the integral

$$I_+(\eta) = \int_0^{\infty} y e^{-\xi y^2} \text{erf}(\eta y + \delta) dy$$

We do this integral by parts; let $u = \text{erf}(\eta y + \delta)$, $dv = y e^{-\xi y^2}$ so $du = \frac{2}{\sqrt{\pi}} \eta e^{-(\eta y + \delta)^2} dy$ and $v = -e^{-\xi y^2} / 2\xi$, and thus

$$I_+(\eta) = -\frac{e^{-\xi y^2}}{2\xi} \text{erf}(\eta y + \delta) \Big|_0^{\infty} + \frac{1}{\sqrt{\pi}} \int_0^{\infty} \exp \left[-((\xi + \eta^2)y^2 + 2\eta\delta y + \delta^2) \right] dy$$

The integral is of a standard form, and may be done using integral tables.¹⁵⁰ Noting that $\text{erf}(\infty) = 1$, we find that

$$I_+(\eta) = \frac{\text{erf}(\delta)}{2\xi} - C_1 \text{erf} \left(\frac{\eta\delta}{\sqrt{\xi + \eta^2}} \right) + C_1$$

where

$$C_1 = \frac{\eta}{2\xi} \frac{1}{\sqrt{\xi + \eta^2}} \exp \left[\frac{\eta^2 \delta^2 - (\xi + \eta^2) \delta^2}{\xi + \eta^2} \right]$$

Similarly, with $\text{erf}(-z) \equiv -\text{erf}(z)$, we find

$$\begin{aligned} I_-(\eta) &= \int_0^\infty y e^{-\xi y^2} \text{erf}(\eta y - \delta) dy \\ &= -\frac{\text{erf}(\delta)}{2\xi} + C_1 \text{erf}\left(\frac{\eta\delta}{\sqrt{\xi + \eta^2}}\right) + C_1 \end{aligned}$$

Thus, combining our results for I_+ and I_- , we have

$$I(\eta_\pm) = \frac{1}{\xi} \left[\text{erf}(\delta) - \frac{\eta_\pm}{\sqrt{\xi + \eta_\pm^2}} \exp\left[\frac{\eta_\pm^2 \delta^2 - (\xi + \eta_\pm^2) \delta^2}{\xi + \eta_\pm^2}\right] \text{erf}\left(\frac{\eta\delta}{\sqrt{\xi + \eta^2}}\right) \right]$$

Defining $r \equiv \xi$, $s \equiv \delta$, and $t \equiv \eta$, we thus have

$$\begin{aligned} N(r, s, t(\hat{u}_\pm)) &\equiv I(\eta_\pm) \\ &= \frac{1}{r} \left[\text{erf}(s) - \frac{t}{\sqrt{r + t^2}} \exp\left[\frac{rs^2}{r + t^2}\right] \text{erf}\left(\frac{st}{\sqrt{r + t^2}}\right) \right] \end{aligned} \quad (\text{E.5.14})$$

where, from equations (E.5.11) and (E.5.13), we identify

$$\begin{aligned} r &= -\left[\frac{\gamma' A_1}{A_2} - B'\right] \\ s &= x \sqrt{\frac{A_2}{4\gamma'}} \\ t(\hat{u}_\pm) &= u_\pm \sqrt{\frac{\gamma'}{A_2}} \end{aligned}$$

With equation (E.5.12) and (E.5.14), we thus have

$$I_z = \frac{1}{2} \sqrt{\frac{\pi}{A_2 \gamma'}} e^{x^2 \frac{A_2}{4\gamma'}} [N(r, s, t(\hat{u}_+)) - N(r, s, t(\hat{u}_-))] \quad (\text{E.5.15})$$

We can substitute this into equation (3.4.13), and find that the product velocity distribution for the hard sphere interaction is given by

$$Q(x) = v_o^4 \pi^{3/2} n_1 n_2 \left(\frac{\sqrt{\lambda_1 \lambda_2}}{\pi}\right)^3 \frac{\pi d^2}{x \sqrt{A_2 \gamma'}} \{N(r, s, \hat{u}_+) - N(r, s, \hat{u}_-)\}$$

where we have eliminated the exponentials since $A' = A_2/4\gamma'$.

E.6 Interpolation scheme for the calculation of integrals over reduced energy

We are faced with integrals over reduced energy $z^2 = E/E_o$, of the form

$$I(z) = \int_0^\infty z^n f(z) dz \quad (\text{E.6.16})$$

where $f(z)$ may represent a differential cross section, a momentum transfer cross section, or some other function of the reduced energy. To avoid having to interpolate values for $f(z)$, as would occur with a Simpson's Rule or Gaussian quadrature based integration scheme, we instead choose our integration points to coincide with the tabulated energy values at which $f(z)$ is known. We then assume that $f(z)$ varies *linearly* with energy over each integration interval. Thus, we write

$$\int_0^\infty z^n f(z) dz \approx \sum_i I_i(z) \quad (\text{E.6.17})$$

where

$$\begin{aligned} I_i(z) &= \int_i^{i+1} z^n f dz \\ f &= \alpha_i + \beta_i E \end{aligned}$$

and where $z_i^2 \equiv E_i/E_o$. The coefficients α_i and β_i are constants for any given interval i , chosen such that f_i is equal to the tabulated values on the boundary intervals, that is

$$\begin{aligned} f(z_i) &= \alpha_i + \beta_i E_i \\ f(z_{i+1}) &= \alpha_i + \beta_i E_{i+1} \end{aligned} \quad (\text{E.6.18})$$

Subtracting the two equations yields

$$\beta_i = \frac{f_{i+1} - f_i}{E_{i+1} - E_i}$$

where $f_i \equiv f(E_i)$. We may then substitute β_i back into either of equation (E.6.18) to give

$$\alpha_i = \frac{f_i E_{i+1} - f_{i+1} E_i}{E_{i+1} - E_i}$$

Transforming equation (E.6.17) to energy, and using our linear approximation for $f(z)$ over the interval i , we have, for interval i ,

$$\begin{aligned} \int_{z_i}^{z_{i+1}} z^n f_i dz &= \frac{1}{2E_o} \int_i^{i+1} \left(\frac{E}{E_o} \right)^{(n-1)/2} f_i dE \\ &= \frac{1}{2E_o^{(n+1)/2}} \int_i^{i+1} E^{(n-1)/2} (\alpha_i + \beta_i E) dE \\ &= \frac{1}{2E_o^{(n+1)/2}} \left(\alpha_i \int_i^{i+1} E^{(n-1)/2} dE + \beta_i \int_i^{i+1} E^{(n+1)/2} dE \right) \end{aligned}$$

The final integral above may easily be evaluated analytically, yielding

$$I_i(z) = \frac{1}{2E_o^{(n+1)/2}} \left(\alpha_i \frac{2}{(n+1)} [E_{i+1}^{(n+1)/2} - E_i^{(n+1)/2}] + \beta_i \frac{2}{(n+3)} [E_{i+1}^{(n+3)/2} - E_i^{(n+3)/2}] \right)$$

We choose the boundaries of the intervals to coincide with the values E_i at which $f(E)$ is tabulated. This method can be extended to other forms similar to equation (E.6.16), including (for example)

$$I(z) = \int_0^\infty \exp[-z^2] z^n f(z) dz$$

Appendix F

Derivation of the Hard Sphere Collision Frequency

The definition of the velocity dependent collision frequency between two species is defined by²⁹ as

$$\nu(c_1) = \iint f_2(c_2) \sigma g d\Omega dc_2 \quad (\text{F.0.1})$$

where σ is the differential scattering cross section describing the physics of the interaction between the two species, g is the magnitude of the relative velocity between the particles, $d\Omega$ is the solid angle describing the orientation of the collision process, and f_2 is the velocity distribution function for the 'background' species (labelled 2). Hence, $\nu(c_1)$ is the collision frequency for 'test' particles (labelled 1) of speed c_1 with the background. For an arbitrary or unknown differential cross section and background velocity distribution function, it is necessary to numerically compute the collision frequency.

It is possible, however, to simplify equation (F.0.1) if a few assumptions are made about the type of interaction and the distribution of the background particle velocities. As most workers are primarily interested in obtaining information about the velocity distribution, density, or temperature of the 'test' particles, it is common practice to assume that the background distribution is in local equilibrium and is given by an isotropic Maxwellian distribution,

$$\begin{aligned} f_2^M(c_2) &= \left(\frac{m_2}{2\pi kT_2} \right)^{3/2} \exp \left[-\frac{m_2 c_2^2}{2kT_2} \right] \\ &= N_2 \exp \left[-\frac{\gamma c_2^2}{v_{th}^2} \right] \end{aligned}$$

where we have defined

$$\begin{aligned} v_{th} &= \sqrt{2kT_2/m_1} \\ \gamma &= m_2/m_1 \\ N_2 &= \frac{\gamma^{3/2}}{\pi^{3/2}v_{th}^{3/2}} \end{aligned}$$

Since the background distribution is isotropic we may rewrite equation (F.0.1) in the form

$$\nu(c_1) = \int f_2(c_2) \sigma_{tot} g d\mathbf{c}_2 \quad (\text{F.0.2})$$

where we have simply used the definition of the total scattering cross section from Appendix C to eliminate the integration over the solid angle.

In addition, if the form of the interaction between the two species is poorly known or poorly constrained, it is often assumed that the particles interact as 'hard spheres' during the collision process. Substituting for the total hard sphere cross section from Appendix C we have

$$\nu(c_1) = \pi d^2 \int f_2(c_2) g d\mathbf{c}_2 \quad (\text{F.0.3})$$

We may now make a change to spherical coordinates, where \mathbf{g} is taken to lie along the polar axis, making an angle θ with the velocity of the test particle, \mathbf{c}_1 . Thus, we have for a constant c_1 that

$$\begin{aligned} \mathbf{g} &= \mathbf{c}_2 - \mathbf{c}_1 \\ d\mathbf{g} &= d\mathbf{c}_2 \\ &= g^2 \sin \theta d\theta d\phi dg \\ c_2^2 &= \mathbf{c}_2 \cdot \mathbf{c}_2 \\ &= g^2 + c_1^2 + 2gc_1 \cos \theta \end{aligned} \quad (\text{F.0.4})$$

Making the change of variable of integration from \mathbf{c}_2 to \mathbf{g} , and using the results in equation (F.0.4), we now have

$$\nu(c_1) = N_2 \pi d^2 \iiint \exp \left[-\frac{\gamma}{v_{th}^2} (g^2 + c_1^2 + 2gc_1 \cos \theta) \right] g^3 \sin \theta d\theta d\phi dg$$

Since there is azimuthal symmetry, the integration over ϕ simply yields a factor of 2π . If we make the change of variable $\mu = \cos \theta$, we have

$$\nu(c_1) = 2N_2 \pi^2 d^2 \int_0^\infty \exp \left[-\frac{\gamma}{v_{th}^2} (g^2 + c_1^2) \right] g^3 \int_{-1}^1 \exp \left[-\frac{\gamma}{v_{th}^2} (2gc_1 \mu) \right] d\mu dg$$

The integral over μ is simply an exponential and may be done easily, yielding

$$\nu(c_1) = \frac{2N_2 \pi^2 d^2 v_{th}^2}{2\gamma c_1} \int_0^\infty \exp \left[-\frac{\gamma}{v_{th}^2} (g^2 + c_1^2) \right] \left(\exp \left[\frac{2\gamma g c_1}{v_{th}^2} \right] - \exp \left[-\frac{2\gamma g c_1}{v_{th}^2} \right] \right) g^2 dg$$

If we make the change of variable from velocity to reduced speed,

$$x = c_1/v_{th}$$

$$y = g/v_{th}$$

we then have

$$\nu(x) = \frac{N_2 \pi^2 d^2 v_{th}^4}{\gamma x} \int_0^\infty \exp \left[-\gamma(x^2 + y^2) \right] (\exp [2\gamma xy] - \exp [-2\gamma xy]) y^2 dy$$

We may rewrite this as

$$\nu(x) = \frac{N_2 \pi^2 d^2 v_{th}^4}{\gamma x} \int_0^\infty \left(\exp \left[-\gamma(x-y)^2 \right] - \exp \left[-\gamma(x+y)^2 \right] \right) y^2 dy \quad (\text{F.0.5})$$

The integral over y in equation (F.0.5) may be performed using ??, yielding

$$\nu(x) = \frac{N_2 \pi^2 d^2 v_{th}^4}{\gamma x} \left[\frac{x e^{-\gamma x^2}}{\gamma} + \sqrt{\pi} \left\{ \frac{1}{2\gamma^{3/2}} + \frac{x^2}{\sqrt{\gamma}} \right\} \text{erf}(\sqrt{\gamma} x) \right]$$

where $\text{erf}(x)$ is the standard error function,

$$\text{erf}(x) = \frac{2}{\sqrt{\pi}} \int_0^x e^{-s^2} ds$$

Substituting back in the definition of N_2 , and simplifying the result in the brackets, we finally have

$$\nu(x) = \frac{\sqrt{\pi}d^2v_{th}}{\sqrt{\gamma}} \left[e^{-\gamma x^2} + \frac{\sqrt{\pi}}{2} \left\{ \frac{1}{\sqrt{\gamma}x} + 2x\sqrt{\gamma} \right\} \operatorname{erf}(\sqrt{\gamma}x) \right] \quad (\text{F.0.6})$$

If we wish instead to express the collision frequency as a function of reduced energy,

$$\begin{aligned} x^* &= m_1 c_1^2 / 2kT_2 \\ &= c_1^2 / v_{th}^2 \\ &= x^2 \end{aligned}$$

we have

$$\nu(x^*) = \frac{A}{\sqrt{\gamma}} \left[e^{-\gamma x^*} + \frac{\sqrt{\pi}}{2} \left\{ \frac{1}{\sqrt{\gamma}x^*} + 2\sqrt{\gamma}x^* \right\} \operatorname{erf}(\sqrt{\gamma}x^*) \right] \quad (\text{F.0.7})$$

where we have defined

$$\begin{aligned} A &= \sqrt{\pi}d^2v_{th} \\ &= d^2 \left(\frac{2\pi kT_2}{m_1} \right)^{\frac{1}{2}} \end{aligned}$$

It should be noted that since the background distribution is normalized to 1, the units of the collision frequency ν are not sec^{-1} , but rather cm^3/sec . A dimensionless collision frequency may be readily defined as

$$\nu^*(x^*) = \frac{\nu(x^*)}{A}$$

Bibliography

- [1] H.J. Fahr and B. Shizgal. Modern exospheric theories and their observational relevance. *Rev. Geop. & Sp. Phys.*, 21:75-124, 1983.
- [2] D.E. Anderson. The Mariner 5 UV photometer experiment: An analysis of H Lyman- α data. *J. Geophys. Res.*, 81:1213-1216, 1976.
- [3] J.L. Bertaux and et al. Lyman- α observations of Venera 9 and 10. i. the nonthermal hydrogen population in the exosphere of Venus. *Plan. Sp. Sci.*, 26:817-831, 1978.
- [4] A.I. Steward, D.E. Anderson, L.W. Esposito, and C.A. Barth. Ultraviolet spectroscopy of Venus: Initial results from the Pioneer Venus orbiter. *Science*, 203:777-779, 1979.
- [5] R.R. Hodges and B.A. Tinsley. Charge exchange in the Venus ionosphere as the source of the hot exospheric hydrogen. *J. Geophys. Res.*, 86:7649-7656, 1981.
- [6] W.H. Ip. On a hot oxygen corona of Mars. *Icarus*, 76:135-145, 1988.
- [7] A.F. Nagy and T.E. Cravens. Hot oxygen atoms in the upper atmosphere of Venus and Mars. *Geop. Res. Lett.*, 15:433-435, 1988.
- [8] H. Lammer and S.J. Bauer. Nonthermal atmospheric escape from Mars and titan. *J. Geophys. Res.*, 96:1819-1825, 1991.
- [9] J.H. Jeans. *The Dynamical Theory of Gases*. Cambridge University Press, fourth edition, 1925.
- [10] K.D. Cole. Theory of some quiet magnetospheric phenomena related to the geomagnetic tail. *Nature*, 211:1385-1387, 1966.
- [11] J.H. Yee. *A Theoretical and Experimental Study on the Atomic Oxygen Corona in the Earth's Atmosphere*. PhD thesis, University of Michigan, 1980.
- [12] A.E. Hedin. Hot oxygen geocorona as inferred from neutral exospheric models and mass spectrometer measurements. *J. Geophys. Res.*, 94:5523-5529, 1989.
- [13] C.A. Barth and et al. Ultraviolet emissions observed near Venus from Mariner 5. *Science*, 158:1675-1678, 1967.
- [14] G. Kotova et al. Study of the solar wind deceleration upstream of the Martian terminator bow-shock. *J. Geophys. Res.*, 102:2165-2173, 1997.

- [15] B. D. Shizgal and G. Arkos. Nonthermal escape of the atmospheres of Venus, Earth, and Mars. *Rev. Geophys.*, 34(4):483–505, 1996.
- [16] J.W. Chamberlain. Planetary coronae and atmospheric evaporation. *Plan. Sp. Sci.*, 11:901–960, 1963.
- [17] D.M. Hunten and T.M. Donahue. Hydrogen loss from the terrestrial planets. *Ann. Rev. Earth & Plan. Sci.*, 4:265–292, 1976.
- [18] B.A. Tinsley. Effects of charge exchange involving H and H^+ in the upper atmosphere. *Plan. Sp. Sci.*, 26:847–853, 1978.
- [19] D.M. Hunten. Thermal and nonthermal escape mechanisms for terrestrial bodies. *Plan. Sp. Sci.*, 8:773–783, 1982.
- [20] D.M. Hunten. Escape of atmospheres, ancient and modern. *Icarus*, 85:1–20, 1990.
- [21] K.K. Mahajan and J. Kar. A comparative study of Venus and Mars: Upper atmospheres, ionospheres, and solar wind interactions. *Indian Journal of Radio & Space Phys.*, 19:444–465, 1990.
- [22] P.M. Banks and G. Kockarts. *Aeronomy, Parts A & B*. Academic Press, 1973.
- [23] T.M. Donahue. Fractionation of noble gases by thermal escape from accreting planetesimals. *Icarus*, 66:195–210, 1986.
- [24] H.B. Niemann, W.T. Kaspizak, A.E. Hedin, D.M. Hunten, and N.W. Spencer. Mass spectrometric measurements of the neutral gas composition of the thermosphere and exosphere of Venus. *J. Geophys. Res.*, 85:7817–7827, 1980.
- [25] J.L. Fox and A. Dalgarno. Ionization, luminosity, and heating of the upper atmosphere of Mars. *J. Geophys. Res.*, 84:7315–7333, 1979.
- [26] M.J. Lindinfeld and B. Shizgal. Non-maxwellian effects associated with the thermal escape of a planetary atmosphere. *Plan. Sp. Sci.*, 27:739–751, 1979.
- [27] B. Shizgal and R. Blackmore. A collisional kinetic theory of a plane parallel evaporating planetary atmosphere. *Plan. Sp. Sci.*, 34:279–291, 1986.
- [28] P.K. Kundu. *Fluid Mechanics*. Academic Press, 1990.
- [29] S. Chapman and T.G. Cowling. *The Mathematical Theory of Non-Uniform Gases*. Cambridge at the University Press, 1964.
- [30] P.G. Richards, M.P. Hickey, and D.G. Torr. New sources for the hot oxygen geocorona. *Geop. Res. Lett.*, 21:657–660, 1994.

- [31] Y.H. Yee, J.W. Meriwether, and P.B. Hays. Detection of a corona of fast oxygen atoms during solar maximum. *J. Geophys. Res.*, 85:3396–3400, 1980.
- [32] A.F. Nagy, J. Kim, and T.E. Cravens. Hot hydrogen and oxygen atoms in the upper atmospheres of Venus and Mars. *Annal. Geop.*, 8:251–256, 1990.
- [33] W.H. Ip. The fast atomic oxygen corona extent of Mars. *Geop. Res. Lett.*, 17:2289–2292, 1990.
- [34] V.I. Shematovich, D.V. Bisikalo, and J.C. Gerard. A kinetic model of the formation of the hot oxygen geocorona 1. quiet geomagnetic conditions. *J. Geophys. Res.*, 99:23,217–23,228, 1994.
- [35] M.B. McElroy, M.J. Prather, and J.M. Rodriguez. Escape of hydrogen from Venus. *Science*, 215:1614–1615, 1982.
- [36] T.E. Donahue, J.H. Hoffman, R.R. Hodges, and A.J. Watson. Venus was wet: A measurement of the ratio of D to H. *Science*, 216:630–633, 1982.
- [37] J.F. Kasting and J.B. Pollack. Loss of water from Venus. I. hydrodynamic escape of hydrogen. *Icarus*, 53:479–508, 1983.
- [38] S.C. Liu and T.M. Donahue. The aeronomy of hydrogen in the atmosphere of the Earth. *J. Atmos. Sci.*, 31:1118–1136, 1974.
- [39] S.C. Liu and T.M. Donahue. Mesospheric hydrogen related to exospheric escape mechanisms. *J. Atmos. Sci.*, 31:1466–1470, 1974.
- [40] S.C. Liu and T.M. Donahue. Realistic model of hydrogen constituents in the lower atmosphere and the escape flux from the upper atmosphere. *J. Atmos. Sci.*, 31:2238–2242, 1974.
- [41] D.M. Hunten and D.F. Strobel. Production and escape of terrestrial hydrogen. *J. Atmos. Sci.*, 31:305–317, 1974.
- [42] J.L. Bertaux. Observed variations of the exospheric hydrogen density with the exospheric temperature. *J. Geophys. Res.*, 80:639–642, 1975.
- [43] J.W. Chamberlain. Charge exchange in a planetary corona; its effect on the distribution and escape of hydrogen. *J. Geophys. Res.*, 82:1–9, 1977.
- [44] R.R. Hodges, R.P. Rohrbaugh, and B.A. Tinsley. The effect of charge exchange source on the velocity and ‘temperature’ distributions and their anisotropies in the Earth’s exosphere. *J. Geophys. Res.*, 86:6917–6925, 1981.

- [45] B. Shizgal and M. J. Lindinfeld. A simple kinetic theory calculation of terrestrial atomic hydrogen escape induced by charge exchange collisions. *J. Geophys. Res.*, 87:853–860, 1982.
- [46] D.R. Bates and M.R.C. McDowell. Escape of helium. *J. Atmos. & Terr. Phys.*, 16:393–395, 1959.
- [47] O. Svendsen, M. H. Rees, and K. Stamnes. Helium escape from the Earth's atmosphere: the charge exchange mechanism revisited. *Plan. Sp. Sci.*, 40:1639–1662, 1992.
- [48] T. Torgerson. Terrestrial helium degassing fluxes and the atmospheric helium budget: Implications with respect to the degassing processes of continental crust. *Chem. Geol.*, 79:1–14, 1989.
- [49] O. Svendsen, M. H. Rees, and K. Stamnes. Helium ion outflow from the Earth's atmosphere. *EOS Trans. AGU*, 75:490, 1994.
- [50] W.B. Maier. Reactions of He^+ with N_2 and O_2 in the upper atmosphere. *Plan. Sp. Sci.*, 16:477–493, 1968.
- [51] T.E. Donahue. Evolution of water reservoirs on Mars from D/H ratios in the atmosphere and crust. *Nature*, 374:432–434, 1995.
- [52] T.E. Donahue. Water on Mars and Venus. *Proc. of the Conference on Deep Earth and Planetary Volatiles*, 1995.
- [53] S.W. Squyres and J.F. Kasting. Early Mars: How warm and how wet? *Science*, 265:744–749, 1994.
- [54] J.B. Pollack, J.F. Kasting, S.M. Richardson, and K. Poliakoff. The case for a wet, warm climate on early Mars. *Icarus*, 71:203–224, 1987.
- [55] T. Owen, J.P. Maillard, C. De Bergh, and B.J. Lutz. Deuterium on Mars: The abundance of DHO and the value of D/H. *Science*, 240:1767–1770, 1988.
- [56] R.O. Pepin. On the origin and early evolution of terrestrial planet atmospheres and meteoritic volatiles. *Icarus*, 92:2–79, 1991.
- [57] H.Y. McSween. What we have learned about Mars from SNC meteorites. *Meteoritics*, 29:757–779, 1994.
- [58] D.M. Hunten. Atmospheric evolution of the terrestrial planets. *Science*, 259:915–920, 1993.
- [59] D.M. Hunten, R.O. Pepin, and J.C.G. Walker. Mass fractionation in hydrodynamic escape. *Icarus*, 69:532–549, 1987.

- [60] J.L. Fox. The production and escape of nitrogen atoms on Mars. *J. Geophys. Res.*, 98:3297–3310, 1993.
- [61] M.B. McElroy and Y.L. Yung. Oxygen isotopes in the Martian atmosphere: Implications for the evolution of volatiles. *Plan. Sp. Sci.*, 24:1107–1113, 1976.
- [62] K. Zahnle, J.F. Kasting, and J.B. Pollack. Mass fractionation of noble gases in diffusion-limited hydrodynamic hydrogen escape. *Icarus*, 84:502–527, 1990.
- [63] R.R. Hodges. Isotopic fractionation of hydrogen in planetary exospheres due to ionosphere-exosphere coupling: Implications for Venus. *J. Geophys. Res.*, 98:10833–10838, 1993.
- [64] R.O. Pepin. Evolution of the Martian atmosphere. *Icarus*, 111:289–304, 1994.
- [65] Jakosky, R.O. Pepin B.M., R.E. Johnson, and J.L. Fox. Mars atmospheric loss and isotopic fractionation by solar-wind induced sputtering and photochemical escape. *Icarus*, 111:271–288, 1994.
- [66] X. He. *Hydrogen Escape from the Earth's Atmosphere*. PhD thesis, Boston University, 1995.
- [67] F.F. Chen. *Introduction to Plasma Physics and Controlled Fusion: Volume 1*. Plenum Press, second edition, 1984.
- [68] D.A. McQuarrie. *Statistical Mechanics*. Harper Collins Publishers, 1976.
- [69] A.F. Nagy, T.E. Cravens, J. H. Yee, and A.I.F Stewart. Hot oxygen atoms in the upper atmosphere of Venus. *Geop. Res. Lett.*, 8:629–632, 1981.
- [70] D.V. Bisikalo, V.I. Shematovich, and J.C. Gerard. A kinetic model of the formation of the hot oxygen geocorona 2. influence of O^+ ion precipitation. *J. Geophys. Res.*, 100:3715–3720, 1995.
- [71] B. Shizgal. Hot hydrogen and deuterium in the exosphere of Venus. *Adv. Sp. Res.*, 7:73–77, 1987.
- [72] A.S. Clarke and B.D. Shizgal. Relaxation dynamics of hot protons in a thermal bath of atomic hydrogen. *Phys. Rev. E.*, 49:347–358, 1994.
- [73] R.R. Hodges and E.L. Breig. Ionosphere-exosphere coupling through charge exchange and momentum transfer in hydrogen-proton collisions. *J. Geophys. Res.*, 96:7697–7708, 1991.
- [74] R.R. Hodges and E.L. Breig. Charge transfer and momentum exchange in exospheric $D-H^+$ and $H-D^+$ collisions. *J. Geophys. Res.*, 98:1581–1588, 1993.

- [75] D.L. Cooper, Y.H. Yee, and A. Dalgarno. Energy transfer in oxygen-hydrogen collisions. *Plan. Sp. Sci.*, 32:825–830, 1984.
- [76] M.A. Gurwell and Y.H. Yung. Fractionation of hydrogen and deuterium on Venus due to collisional ejection. *Plan. Sp. Sci.*, 41:91–104, 1993.
- [77] L.J. Maher and B.A. Tinsley. Atomic hydrogen escape rate due to charge exchange with hot plasmaspheric ions. *J. Geophys. Res.*, 82:689–695, 1977.
- [78] Y.L. Yung, J.S. Wen, J.I. Moses, B.M. Landry, M. Allen, and K.J. Hsu. Hydrogen and deuterium loss from the terrestrial atmosphere: A quantitative assessment of nonthermal escape fluxes. *J. Geophys. Res.*, 94:14,971–14,989, 1989.
- [79] M.B. McElroy, M.J. Prather, and J.M. Rodriguez. Loss of oxygen from Venus. *Geop. Res. Lett.*, 9:649–651, 1982.
- [80] J.L. Fox. On the escape of oxygen and hydrogen from Mars. *Geop. Res. Lett.*, 20:1847–1850, 1993.
- [81] M.B. McElroy. Mars: An evolving atmosphere. *Science*, 175:443–445, 1972.
- [82] M.G. Shepherd, J.C. McConnell, W.K. Tobiska, G.R. Gladstone, S. Chakrabati, and G. Schmidtke. Inference of atomic oxygen concentration from remote sensing of optical aurora. *J. Geophys. Res.*, 100:17,415–17,428, 1995.
- [83] D.M. Cotton, G.R. Gladstone, and S. Chakrabarti. Sounding rocket observations of a hot atomic oxygen geocorona. *J. Geophys. Res.*, 98:21,651–21,657, 1993.
- [84] R.P. Rohrbaugh and J.S. Nisbet. Effects of energetic oxygen atoms on neutral density models. *J. Geophys. Res.*, 78:6768–6772, 1973.
- [85] B. Shizgal and M.J. Lindenfeld. Energy distribution function of translationally hot $O(^3p)$ atoms in the atmosphere of Earth. *Plan. Sp. Sci.*, 27:1321–1332, 1979.
- [86] G.A. Schmitt, V.J. Abreu, and P.B. Hays. Nonthermal $O(^1d)$ produced by dissociative recombination of O_2^+ : A theoretical model and observational results. *Plan. Sp. Sci.*, 29:1095–1099, 1981.
- [87] A.L. Broadfoot, S. Kumar, M.J.S. Belton, and M.B. McElroy. Ultraviolet observations of Venus from Mariner 10: Preliminary results. *Science*, 183:1315–1318, 1974.
- [88] P.Z. Takacs, A.L. Broadfoot, G.R. Smith, and S. Kumar. Mariner 10 observations of hydrogen Lyman alpha emission from the Venus exosphere: Evidence of a complex structure. *Plan. Sp. Sci.*, 28:687–701, 1980.

- [89] J.L. Bertaux and et al. Venera 11 and Venera 12 observations of EUV emissions from the upper atmosphere of Venus. *Plan. Sp. Sci.*, 29:149–166, 1981.
- [90] L.J. Paxton. *Atomic Carbon in the Venus Thermosphere: Observations and Theory*. PhD thesis, University of Colorado, Boulder, 1983.
- [91] J.G. Luhmann and L.H. Brace. Near-Mars space. *Rev. Geophys.*, 28:121–140, 1991.
- [92] S.L. Guberman. The production of $O(^1S)$ in dissociative recombination of O_2^+ . *Nature*, 327:408–409, 1987.
- [93] S.L. Guberman. The production of $O(^1D)$ from dissociative recombination of O_2^+ . *Plan. Sp. Sci.*, 36:47–53, 1988.
- [94] S.L. Guberman and A. Giusti-Suzor. The generation of $O(^1S)$ from the dissociative recombination of O_2^+ . *J. Chem. Phys.*, 95:2602–2613, 1991.
- [95] W.B. Hanson, S. Sanatani, and D.R. Zuccaro. The Martian ionosphere as observed by the Viking retarding potential analyzers. *J. Geophys. Res.*, 82:4351–4363, 1977.
- [96] S. Kumar, D.M. Hunten, and H.A. Taylor. H_2 abundance in the atmosphere of Venus. *Geop. Res. Lett.*, 8:237–240, 1981.
- [97] R.W. Schunk. Mathematical structure of transport equations for multispecies flows. *Rev. Geop. & Sp. Sci.*, 15(4):429–445, 1977.
- [98] J.R. Conrad and R.W. Schunk. Diffusion and heat flow equations with allowance for large temperature differences between interacting speices. *J. Geophys. Res.*, 84(A3):811–822, 1979.
- [99] E. Kreyszig. *Advanced Engineering Mathematics*. John Wiley & Sons, Inc., sixth edition, 1988.
- [100] E.N. Parker. Dynamical theory of the solar wind. *Space Sci. Rev.*, 4:666–708, 1965.
- [101] J.C. Brandt. *Introduction to the Solar Wind*. W.H. Freeman, 1970.
- [102] E.N. Parker. Dynamics of the interplanetary gas and magnetic fields. *Astrophys. J.*, 128:664–676, 1958.
- [103] F. Yasseen and J.M. Retterer. Critical points in the 16-moment approximation. *J. Geophys. Res.*, 96:1827–1830, 1991.
- [104] M.H. Rees. *Physics and chemistry of the upper atmosphere*. Cambridge University Press, 1989.
- [105] J.R. Conrad and R.W. Schunk. On the validity of the navier-stokes equations for thermosphere dynamics calculations. *J. Geophys. Res.*, 84:5355–5360, 1979.

- [106] S. Glasstone and M.C. Edlund. *The Elements of Nuclear Reactor Theory*. D. Van Nostrand Company, Inc., 1952.
- [107] K. Kowari. Validity of the continuous slowing-down approximation in electron degradation, with numerical results for argon. *Phys. Rev. A.*, 41:2500–2505, 1989.
- [108] K. Kowari, L. Demeio, and B. Shizgal. Electron degradation and thermalization in CH_4 gas. *J. Chem. Phys.*, 97:2061–2074, 1992.
- [109] K. Anderson and K.E. Shuler. On the relaxation of the hard-sphere Rayleigh and Lorentz gas. *J. Chem. Phys.*, 40:633–650, 1964.
- [110] R. Kapral and J. Ross. Relaxation in a dilute binary gas mixture. *J. Chem. Phys.*, 52:1238–1243, 1970.
- [111] B. Shizgal. A gaussian quadrature procedure for use in the solution of the boltzmann equation and related problems. *J. Comput. Phys.*, 41:309–328, 1981.
- [112] M.R. Hoare and C.H. Kaplinsky. Linear hard-sphere gas: variational eigenvalue spectra of the energy kernel. *J. Chem. Phys.*, 52:3336–3353, 1970.
- [113] R.R. Meier and P. Mange. Geocoronal hydrogen: An analysis of the Lyman-alpha airglow and related atomic hydrogen distribution. *Plan. Sp. Sci.*, 18:803–821, 1970.
- [114] R.R. Meier and P. Mange. Spatial and temporal variations of the Lyman-alpha airglow and related atomic hydrogen distribution. *Plan. Sp. Sci.*, 21:309–327, 1970.
- [115] D.E. Anderson, L.J. Paxton, R.P. McCoy, R.R. Meier, and S. Chakrabati. Atomic hydrogen and solar Lyman-alpha flux deduced from STP 78-1 UV observations. *J. Geophys. Res.*, 92:78759–8766, 1987.
- [116] D.E. Anderson, R.R. Meier, R.R. Hodges, and B.A. Tinsley. Hydrogen Balmer-alpha intensity distributions and line profiles from multiple scattering theory using realistic geocoronal models. *J. Geophys. Res.*, 92:7619–7642, 1987.
- [117] R.B. Kerr, S.K. Atreya, J.W. Meriwether, C.A. Tepley, and R.G. Burnside. Simultaneous H_α line profile and radar measurements at Arecibo. *J. Geophys. Res.*, 91:4491–4512, 1986.
- [118] X. He, R.B. Kerr, J. Bishop, and C.A. Tinsley. Determining exospheric hydrogen density by reconciliation of H_α measurements with radiative transfer theory. *J. Geophys. Res.*, 98:21,611–21,626, 1993.
- [119] D.E. Anderson and C.W. Hord. Mariner 6 and 7 ultraviolet spectrometer experiment: Analysis of hydrogen Lyman-alpha data. *J. Geophys. Res.*, 76:6666–6673, 1971.

- [120] D.E. Anderson. Mariner 6, 7 and 9 ultraviolet spectrometer experiment: Analysis of hydrogen Lyman-alpha data. *J. Geophys. Res.*, 79:1513-1528, 1974.
- [121] C.A. Barth, A.I. Stewart, and C.W. Hord. Mariner 9 ultraviolet spectrometer experiment: Mars airglow spectroscopy and variations in Lyman alpha. *Icarus*, 17:7457-468, 1972.
- [122] J.W. Chamberlain and G.R. Smith. Comments on the rate of evaporation of a non-maxwellian atmosphere. *Plan. Sp. Sci.*, 19:675-684, 1971.
- [123] S. Kumar, D.M. Hunten, and A.L. Broadfoot. Nonthermal hydrogen in the Venus exosphere: The ionospheric source and the hydrogen budget. *Plan. Sp. Sci.*, 26:1063-1075, 1978.
- [124] R.B. Kerr, J. Noto, and X. He. Deriving exospheric escape flux of atomic hydrogen from h_α line profile measurements (abstract). *EOS Trans. AGU*, 74:471, 1993.
- [125] A.J. Watson, T.M. Donahue, and J.C.G. Walker. The dynamics of a rapidly escaping atmosphere: Applications to the evolution of Earth and Venus. *Icarus*, 48:150-166, 1981.
- [126] S.M. Richardson, J.B. Pollack, and R.T. Reynolds. Water loss on Venus: The role of carbon monoxide. *Icarus*, 60:307-316, 1984.
- [127] M.B. McElroy, M.J. Prather, and J.M. Rodriguez. Loss of oxygen from Venus. *Geop. Res. Lett.*, 9:649-651, 1982.
- [128] R.T. Brinkmann. Departures from Jeans escape rate for H and He in the Earth's atmosphere. *Plan. Sp. Sci.*, 18:449-478, 1970.
- [129] R.R. Hodges. Collision cross sections and diffusion parameters for h and d in atomic oxygen. *J. Geophys. Res.*, 98:3799-3805, 1993.
- [130] R.M. Goody and Y.L. Yung. *Atmospheric Radiation*. Oxford University Press, 1989.
- [131] B. Shizgal. Analysis of the dynamics of (H^+ , H) charge exchange collisions in the production of nonthermal H (abstract). *EOS Trans. AGU*, 66:1002, 1985.
- [132] E.E. Anderson. *Modern Physics and Quantum Mechanics*. W.B. Saunders Company, 1971.
- [133] R.L. Liboff. *Introductory Quantum Mechanics*. Addison-Wesley Publishing Company, first edition, 1980.
- [134] J.B. Marion and M.A. Heald. *Classical Electromagnetic Radiation*. Academic Press, second edition, 1980.

- [135] G. Hunter and M. Kuriyan. Proton collisions with hydrogen atoms at low energies: Quantum theory and integrated cross sections. *Proc. R. Soc. London Ser. A.*, 353:575–588, 1977.
- [136] J.P. Davis and W.R. Thorson. Very low energy scattering in HH^+ and HD^+ . *Can. J. Phys.*, 56:996–1020, 1977.
- [137] W.D. Pesnell, K. Omidvar, and W.R. Hoegy. Momentum transfer collision frequency of O^+ -O. *Geop. Res. Lett.*, 20:1343–1346, 1993.
- [138] J.A. Peek. Eigenparameters for the $1s_{\sigma_g}$ and $2p_{\sigma_u}$ orbitals of H_2^+ . *J. Chem. Phys.*, 43(9):3004–3006, 1965.
- [139] H. Wind. Electron energy for rmh_2^+ in the ground state. *J. Chem. Phys.*, 42(7):2371–2373, 1965.
- [140] E.F. van Dishoeck and A. Dalgarno. Photodissociation processes in the O-H molecule. *J. Chem. Phys.*, 79:873–888, 1983.
- [141] E.F. van Dishoeck, S.R. Langhoff, and A. Dalgarno. The low-lying $^2\sigma^-$ states of O-H. *J. Chem. Phys.*, 78:4552–4561, 1983.
- [142] J.S. Wright and D.J. Donaldson. Potential energy and vibrational levels for local modes in water and acetylene. *Chem. Phys.*, 94:15–23, 1985.
- [143] M.V. Korolkov, J. Manz, G.K. Paramonov, and B. Schmidt. Vibrationally state-selective photodissociation by infrared sub-picosecond laser pulses: model simulations for $\text{O}+\text{H} \rightarrow \text{OH}$. *Chem. Phys. Lett.*, 260:604–610, 1996.
- [144] B. Shizgal and J.M. Fitzpatrick. Matrix elements of the linear boltzmann collision operator for systems of two components at different temperatures. *Chem. Phys.*, 63:54–65, 1974.
- [145] J.M. Fitzpatrick and B. Shizgal. Temperature relaxation in a binary gas. I. steady state solution. *J. Chem. Phys.*, 63(1):131–137, 1975.
- [146] B. Shizgal and J.M. Fitzpatrick. Temperature relaxation in a binary gas. ii. time dependent solution. *J. Chem. Phys.*, 63(1):138–142, 1975.
- [147] B. Shizgal. Nonequilibrium time dependent theory of hot atom reactions. ii. the hot $^{18}\text{F}+\text{H}_2$ reaction. *J. Chem. Phys.*, 72(5):3156–3162, 1980.
- [148] B.A. Tinsley, R.R. Hodges, and R.P. Rohrbaugh. Monte Carlo methods for the terrestrial exosphere over a solar cycle. *J. Geophys. Res.*, 91:13631–13647, 1986.
- [149] G. Arfken. *Mathematical Methods for Physicists*. Academic Press, third edition, 1985.

- [150] M. Abramowitz and I.A. Stegun. *Handbook of Mathematical Functions*. Dover Publications, 1972.
- [151] I.S. Gradshteyn and I.M. Ryzhik. *Table of Integrals, Series and Products*. Academic Press, fourth edition, 1965.
- [152] B. Shizgal and M.J. Lindenfeld. Further studies of non-maxwellian effects associated with the thermal escape of a planetary atmosphere. *Plan. Sp. Sci.*, 28:159-163, 1980.
- [153] S. Kumar, D.M. Hunten, and J.B. Pollack. Nonthermal escape of hydrogen and deuterium from Venus and implications for loss of water. *Icarus*, 55:369-389, 1983.
- [154] R.R. Hodges and B.A. Tinsley. The influence of charge exchange on the velocity distribution of hydrogen in the Venus exosphere. *J. Geophys. Res.*, 91:13,649-13,658, 1986.
- [155] E.K. Biutner. The dissipation of gas from planetary atmospheres, I. the dissipation of a gas in a central field of gravitation. *Sov. Astr.*, 2:528-537, 1958.
- [156] E. Jensen. Mass losses through evaporation from a completely ionized atmosphere with applications to the solar corona. *Astrophysica Norvegica*, 8:99-126, 1963.
- [157] K. Jockers. Solar wind models based on exospheric theory. *Astron. Astrophys.*, 6:219-239, 1970.
- [158] R.E. Johnson. Dayside pick-up oxygen ion precipitation at Venus and Mars. *J. Geophys. Res.*, 97:911-913, 1992.
- [159] R.E. Johnson. Plasma-induced sputtering of an atmosphere. *Space Sci. Rev.*, 69:215-253, 1994.
- [160] E.K. Biutner. Gas dissipation from planetary atmospheres, ii. the total velocity of gas dissipation from a planetary atmosphere. the problem of terrestrial helium. *Sov. Astr.*, 3:92-102, 1959.
- [161] H.C. Brinton, H.A. Taylor, H.B. Niemann, and H.G. Mayr. Venus nighttime hydrogen bulge. *Geop. Res. Lett.*, 7:865-868, 1980.
- [162] B. Shizgal. Nonequilibrium time dependent theory of hot atom reactions. ii. comparison with estrup-wolfgang theory. *J. Chem. Phys.*, 15:1401-1408, 1981.
- [163] B. Shizgal and A.S. Clarke. The dynamics of hot F atoms in low pressure plasma etching reactors. *Chem. Phys.*, 166:317-328, 1992.
- [164] L.S. Rodberg and R.M. Thaler. *Introduction to the Quantum Theory of Scattering*. Academic Press, 1967.

- [165] F.J. Smith. The numerical evaluation of the classical angle of deflection and of the JWKB phase shift. *Physica*, 30:497-504, 1964.
- [166] M. Kennedy and F.J. Smith. The efficient computation of JWKB phase shifts. *Mol. Phys.*, 13(5):443-448, 1967.
- [167] J.S. Cohen. Rapid accurate calculation of JWKB phase shifts. *J. Chem. Phys.*, 68(4):1841-1843, 1978.